Phase-Field Modeling of Electro-Chemo-Mechanical Behavior of Li-ion Battery Electrodes

Zur Erlangung des akademischen Grades Doktor-Ingenieur (Dr.-Ing.)
genehmigte Dissertation von M.Eng. Ying Zhao aus Dangyang, Hubei, China
Tag der Einreichung: 01. November 2016, Tag der Prüfung: 16. Januar 2017
Darmstadt 2017 — D 17

1. Gutachten: Prof. Dr. Bai-Xiang Xu
2. Gutachten: Prof. Dr.-Ing. Kerstin Weinberg

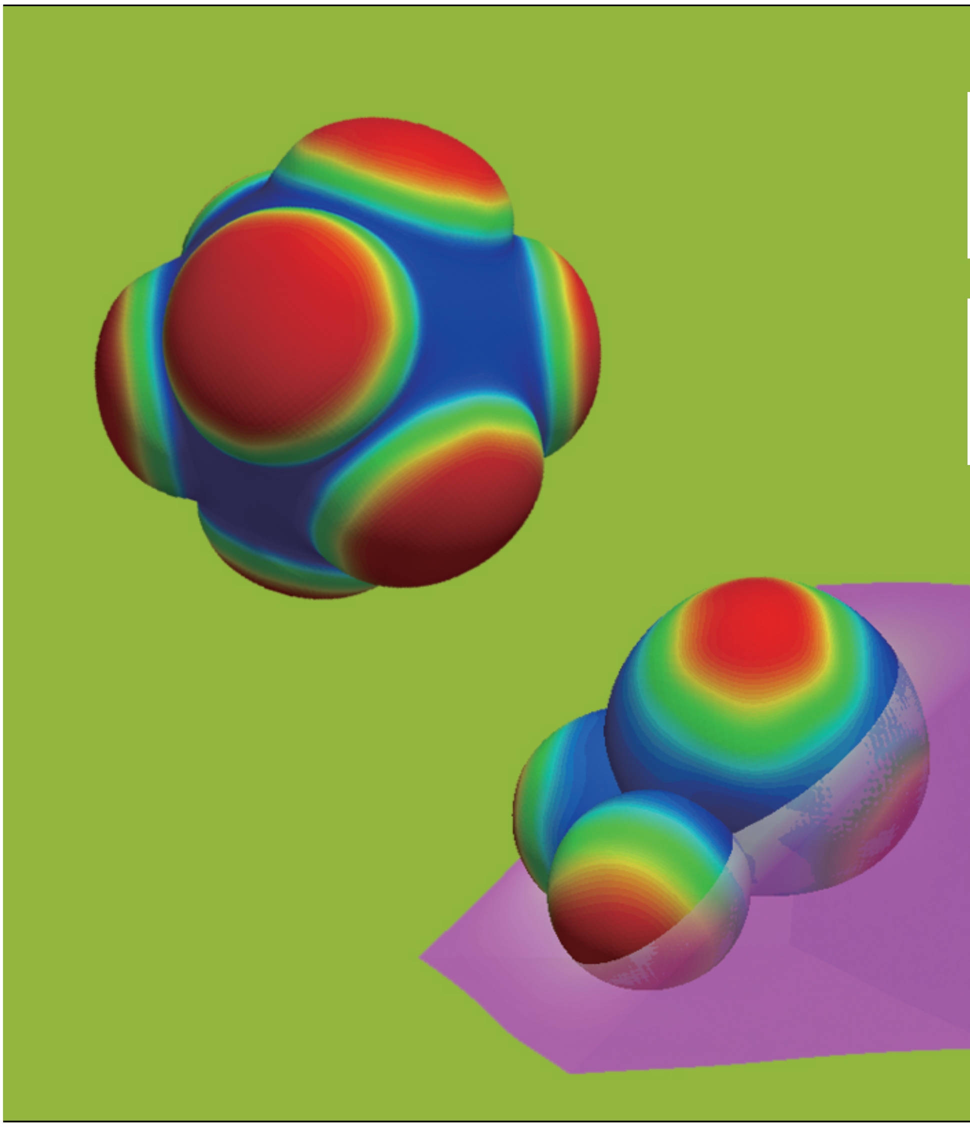

TECHNISCHE
UNIVERSITÄT
DARMSTADT

Fachbereich
Material- und Geowissenschaften
Fachgebiete
Mechanik funktionaler Materialien

Phase-Field Modeling of Electro-Chemo-Mechanical Behavior of Li-ion Battery Electrodes

Genehmigte Dissertation von M.Eng. Ying Zhao aus Dangyang, Hubei, China

1. Gutachten: Prof. Dr. Bai-Xiang Xu
2. Gutachten: Prof. Dr.-Ing. Kerstin Weinberg

Tag der Einreichung: 01. November 2016
Tag der Prüfung: 16. Januar 2017

Darmstadt 2017 — D 17

Bitte zitieren Sie dieses Dokument als:
URN: urn:nbn:de:tuda-tuprints-62735
URL: http://tuprints.ulb.tu-darmstadt.de/6273

Erklärung zur Dissertation

Hiermit versichere ich, die vorliegende Dissertation ohne Hilfe Dritter nur mit den angegebenen Quellen und Hilfsmitteln angefertigt zu haben. Alle Stellen, die aus Quellen entnommen wurden, sind als solche kenntlich gemacht. Diese Arbeit hat in gleicher oder ähnlicher Form noch keiner Prüfungsbehörde vorgelegen.

Darmstadt, den 30. Juni 2017

(Y. Zhao)

一叶知秋。

From a single falling leaf one realizes the coming autumn.

Acknowledgements

First and foremost, I would like to sincerely thank my advisor Prof. Dr. Bai-Xiang Xu, who has been a mentor and a friend during my doctoral study in Darmstadt. I will always remember the tense but productive time we have worked so intensively together before every publication and presentation, as well as the completion of the thesis. I have benefited and learned a great deal from her knowledge, intelligence and diligence. I am also very proud and delighted to have witnessed both her achievements in the professional career and her happiness in the personal life.

I would also like to acknowledge the three-year funding from the "Excellence Initiative" of the German Federal and State Governments and the Graduate School of Computational Engineering (GSC CE) at Technische Universität Darmstadt. Their support for my three-month academic visit to the University of Minnesota is also greatly acknowledged.

I would like to thank Prof. Kerstin Weinberg for her kindness to be my second reviewer of the thesis. In addition, I would also like to thank Prof. Karsten Albe and Prof. Jens Lang for being part of the examination commission.

Dr. Peter Stein has introduced me the whole world of isogeometric analysis, without whose help I couldn't proceed with my topic as far and quickly as I do now. His patience in explaining all details of the numerical aspects, painstaking help with my computer administration have greatly benefited me. Moreover, he also kindly offers to help with the translation of the abstract of my thesis into German. I owe him a huge debt of gratitude.

It is my great pleasure to have worked with Prof. Dominik Schillinger for three months in the University of Minnesota in the United States. We worked almost everyday together during that time. He tutored me to implement my own codes for the finite cell method, and encouraged and helped me to realize my idea into one journal paper. I have been so moved by his enthusiasm on research. I have enjoyed a lot during my stay in Minneapolis, together with the colleagues and friends I made there, Lam Nguyen and Stein Stoter. I still remember the time Stein and I explored the local restaurants and breweries together, exchanging our funny and weird ideas.

I would also like to acknowledge my colleagues in the research group of Mechanics of Functional Materials (MFM). Thank Habib Pouriayevali for the insightful knowledge of the cars (although I am not very much interested), the free pistachios, and the help with the correction of my thesis. The grammar and format checking of my thesis from Mamun Al-Siraj is also acknowledged. My thanks to Yangbin Ma for always inviting me to go out together with his family, especially during the first days of my stay in Germany. I thank Dr. Min Yi for his vast knowledge of many scientific topics and information about scientific journals, which helps me to find a

proper journal to publish. I would also like to thank all the help from Shuai Wang and other members in our group for creating such a comfortable atmosphere to work in.

The kind help from Dr. Markus Lazanowski and Carina Schuster about the admission and daily life in GSC CE is also acknowledged.

I would also like to thank the friends in the Department of Materials Science. Hairui Liu always brings presents to me whenever she comes back from other places. Her thoughtfulness and kind heart is very much valued. My gratitude to Na Liu and Pan Hu, for inviting me to their places for lunches and dinners.

My special thanks to my flatmates. I am very grateful that my first flatmate is Danny Menz, who is so gentle, reliable and helpful. Alexandre Ferraz brought so much joy to our apartment. Marius Dajbog helped me many times to repair my bicycle. Thank you all so much!

Last but never the least, I would like to thank my parents and my boyfriend, who have always been by my side, although not physically, during my stay in Germany. Your support makes me to feel so secured that I could concentrate on my research.

Ying Zhao
Darmstadt, June, 2017

Abstract

Lithium-ion batteries, with their high energy densities and light-weight designs, have found broad applications in portable electronics and electric vehicles. However, their mechanisms and operation are not yet fully understood, which has motivated a wide span of multi-physical models from different disciplines. In this thesis, a thermodynamically consistent phase-field framework is presented, to investigate the electro-chemo-mechanical behavior of lithium-ion battery electrode materials. Within this framework, a series of coupled models is developed sequentially towards the more realistic modeling. Firstly, a mechanically coupled two-phase model of a single particle is proposed, based on a thorough study of the chemical phase separation of this particle. Thereby, the effect of large strains and the concentration-dependent elastic properties are considered, which has been proved in this thesis to have a great impact on the phase separation. A more comprehensive model is formulated, which deals additionally with the electrochemical reaction on the particle surface and the orthotropic phase separation. The reaction rate is governed by a modified Butler–Volmer equation, which takes both chemical and mechanical states into account. Based on this model, we further investigate the fracture in the particle by the phase-field approach, where the reaction on the newly cracked surfaces is also taken into consideration. Finally, the model of the particle embedded in a polymer matrix is presented to study the interaction between the particle and the surrounding materials.

For the implementation two novel finite element methods are used: isogeometric analysis and the B-Spline based finite cell method. Isogeometric analysis is employed in order to treat the fourth-order Cahn–Hilliard equation and the third-order drifting term in a straightforward fashion. To deal with the additional boundary constraint, which states that the normal gradient of the concentration equals to zero, and which arises from the Cahn–Hilliard equation, we propose two variational formulations based on the Lagrange multiplier method and the Nitsche method, respectively, as the weak imposition. Moreover, we also employ finite cell method with Cartesian B-Spline meshes to simulate the composite electrode with complex geometries.

In this thesis, the chemical and mechanical fields are fully resolved in a variety of three-dimensional simulations. These simulations demonstrate the influence of the phase separation on the stress field, the fracture and the reaction rate. We find that the phase separation results in, among others, an intensified stress field and enhanced reaction rate near the phase interface, and in severe cases it also leads to crack propagation and branching. Moreover, intensive discussions are carried out to explore the factors that contribute to phase separation and suppression, such as the particle size, charge rate and material stiffness.

Zusammenfassung

Bedingt durch ihre hohe Energiedichte und leichte Designs haben Lithium-Ionen-Batterien breite Anwendung für tragbare Elektronik und Elektroautos gefunden. Die ihnen zugrundeliegenden Mechanismen sind jedoch noch nicht vollkommen nachvollzogen. Dies hat die Entwicklung einer Reihe multiphysikalischer Modelle aus verschiedenen Fachdisziplinen motiviert. Diese Dissertation befasst sich mit der Entwicklung eines thermodynamisch konsistenten Phasenfeldmodells zur Untersuchung des elektro-chemo-mechanischen Verhaltens der Elektrodenmaterialien von Lithium-Ionen-Batterien. Im Rahmen der Arbeit wird dazu schrittweise eine Reihe gekoppelter Modelle mit dem Ziel einer realistischeren Beschreibung formuliert. Zunächst wird dazu ein mechanisch gekoppeltes Zweiphasen-Modell für freistehende Elektrodenpartikel entwickelt und für umfassende Studien der chemische Phasenseparation innerhalb des Partikels angewandt. Dabei werden Effekte aus großen Verformungen und konzentrationsabhängigen elastischen Eigenschaften berücksichtigt, was, wie die Arbeit zeigt, großen Einfluss auf die Phasenseparation besitzt. Im nächsten Schritt wird das Modell um elektrochemische Reaktionen auf der Partikeloberfläche sowie um orthotrope Phasenseparation erweitert. Die Reaktionsrate wird dabei durch ein modifiziertes Butler-Volmer-Modell beschrieben, in dem sowohl chemische als auch mechanische Beiträge berücksichtigt werden. Auf Basis dieses Modells werden dann Bruchphänomene des Partikels mittels eines Phasenfeld-Ansatzes untersucht, wobei frische Bruchflächen wiederum chemischen Reaktionen ausgesetzt werden. Schließlich wird ein Modell für in einer Polymermatrix eingebettete Partikel aufgestellt, um die Interaktion zwischen Partikel und umgebendem Material zu beleuchten.

Die Implementation dieser Modelle macht sich zwei neuartige Finite-Elemente-Methoden zunutze: das Konzept der Isogeometrischen Analyse und die B-Spline-basierte Finite-Cell-Methode. Der isogeometrische Ansatz wird zur direkten Behandlung der Cahn-Hilliard-Gleichung und der damit verbundenen Kopplungsterme verwendet, die von vierter beziehungsweise dritter Ordnung sind. Aus der Herleitung der Cahn-Hilliard-Gleichung resultiert eine zusätzliche Randbedingung, die erfordert, dass der Normalgradient der Konzentration entlang der Oberfläche verschwindet. Zur Erfassung dieser Bedingung werden zwei Variationsformulierungen entwickelt, basierend auf Lagrangeschen Multiplikatoren und der Nitsche-Methode (für eine Berücksichtigung im schwachen Sinn). Die Finite-Cell-Methode mit kartesischen B-Spline-Netzen hingegen wird für die Simulation von Kompositelektroden mit komplexer Geometrie angewandt.

Chemische und mechanische Felder werden im Rahmen dieser Dissertation in einer Vielzahl dreidimensionaler Simulationen vollständig aufgelöst. Diese demonstrieren den Einfluss von Phasenseparation auf Spannungen, Bruchinitiation und -propagation, sowie auf chemische Reaktionsraten. Demnach führt Phasenseparation unter Anderem zu erhöhten Spannungsfeldern und verstärkten Reaktionsraten entlang der Phasengrenzen, und in extremen Fällen zu Rissfortschritt und -verzweigung. Die Arbeit diskutiert eingehend jene Faktoren, die Phasenseparation begünstigen beziehungsweise unterdrücken, zum Beispiel Partikelgröße, Ladungsrate und Materialsteifigkeit.

Contents

List of Figures

List of Tables

Chapter 1

Introduction

1.1 Motivation

Electric energy plays a crucial role in the modern society. It can be easily converted to other forms of energy through all kinds of electrical appliances. The huge energy demand not only drives people to generate electricity in a more economical and sustainable manner, but also poses the challenge of storing electricity more efficiently. Renewable energy sources such as solar, wind, tide energy are developing rapidly since they are clean and inexhaustible, in contrast to traditional fossils. In 2015, they maintained a robust grow and contributed to 3% of the global primary energy consumption [1]. However, these renewables are mostly intermittent energy sources and can not provide a stable supply. To effectively make use of these renewables, one way is to integrate them into the electric grid with the help of storage devices, which can store electricity when it is abundant and provide it later when needed. On the off-grid level, electricity can be directly supplied to end products, for instance, electric vehicles. In both cases the requirement for energy storage has to be fulfilled [2].

Storing energy means to convert the energy into another form of energy (or itself). Based on the energy form it is converted to, storage can be mainly classified in five categories: mechanical, electrochemical, chemical, electrical and thermal (Fig. 1.1). Mechanical storage systems such as the pumped hydro storage power plants represent by far most of the world-wide installed electrical storage. Flywheels also show a promising capability as fast storage. Nevertheless, mechanical storage systems in general share the drawbacks of inflexibility on the configuration (either have enormous volume or require a certain shape) and the low efficiency due to friction and resistance. Double-layer capacitors, or super-capacitors are highly promising due to their unlimited cycle life and ultra-fast charge/discharge rate. However, limited by its low energy density and high self discharge, those capacitors are more used as electric buffers in hybrid power designs. Batteries, including fuel cells, usually serve as a supplementary to the traditional mechanical storage as the emergency power supply. They are also major energy supplier for portable end products. They are technologically mature and reliable, with an adequate energy density. Most importantly, they are flexible in configurational designs, which can be tailored to fit different products.

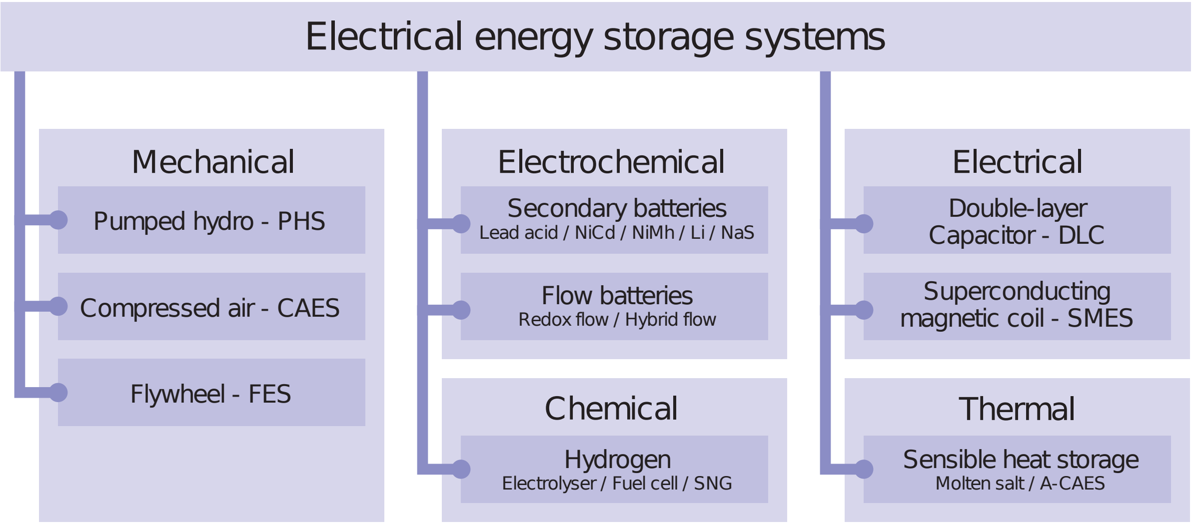

FIGURE 1.1. *Classification of electrical energy storage system according to energy form [2].*

Batteries are devices that convert chemical energy contained in its active materials directly into electric energy by means of an electrochemical reduction/oxidation (redox) reaction [3]. Depending on the rechargeability, batteries fall into two different systems: primary and secondary batteries. The former can only convert the chemical energy into electricity once. The latter, also known as rechargeable batteries, are designed for repeated discharges and charges, thus requiring reversible electrochemical reactions. The last half of the twentieth century has witnessed a great advancement in battery technology. As shown in Fig. 1.2, first and secondary batteries always develop at a comparable pace, with primary batteries showing around doubled energy density as the rechargeable competitors. The primary ones are attractive for portable electric devices requiring a higher energy density with a limited size such as watches, the sec-

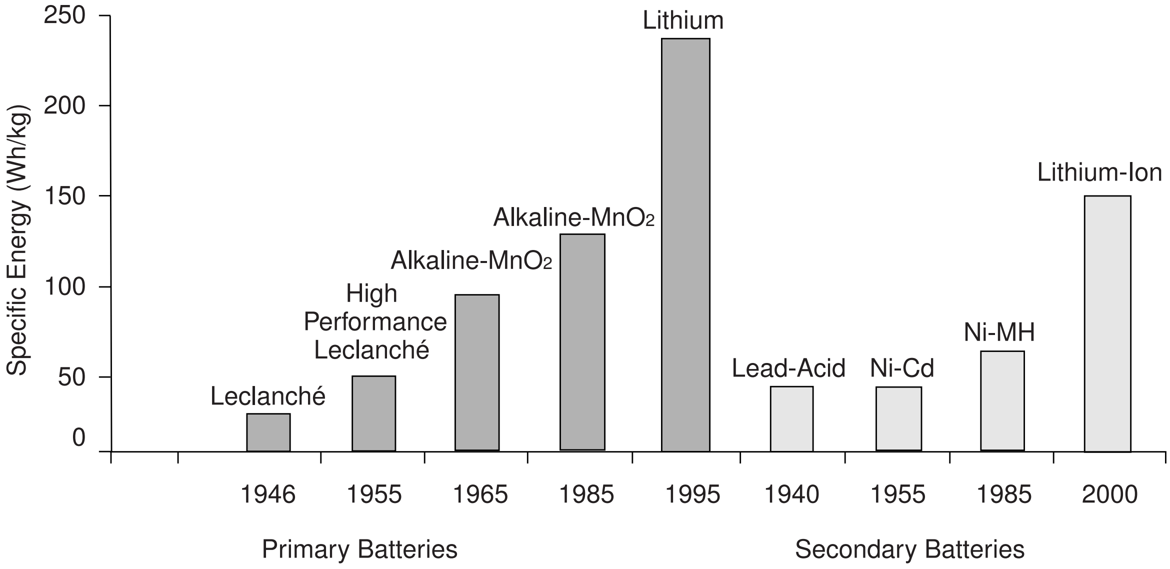

FIGURE 1.2. *Advances in the battery performance for portable applications [3].*

ondary batteries are more appealing for almost all applications, especially after the availability of lithium-ion batteries. Lithium-based batteries have some obvious advantages. Li metal is the most electro-positive (−3.04 V v.s. standard hydrogen electrode) and the lightest metal ($0.53\,\mathrm{g\,cm^{-3}}$), which insures the high voltage and high energy density of a lithium metal battery (Fig. 1.3). However, uncontrollable dendritic Li growth during Li deposition will lead to an internal short-circuit and thus failure of the battery. This has prevented the use of metallic Li as the anode in rechargeable batteries. While efforts are still invested in the research on Li metal rechargeable batteries [5], carbon-based anodes first harvested a commercial success in the rechargeable lithium-ion battery by Sony in 1991 and until now they are still the unbeatable anode material in the market. Recent studies have shown that it is the carbonaceous anode that has held down the overall lithium-ion battery capacity given the cathode materials as $LiMn_{1-x}Mi_xO_2$, $Li[Ni_xCo_{(1-2x)}Mn_x]O_2$, defective Li-Mn-O spinels, olivine $LiFePO_4$, and related materials with the specific capacity between 140 and $200\,\mathrm{mA\,h\,g^{-1}}$ [6]. Alloy anodes such as aluminum, silicon, tin, antimony are very promising candidates for the next generation of lithium-ion battery because of their high theoretical energy density, relatively low cost, safe operation potentials [7, 8]. The lithium–silicon system can reach a theoretical specific insertion capacity of $4010\,\mathrm{mA\,h\,g^{-1}}$, making the silicon a very attractive alternative to the carbons. However, a severe volumetric swelling of 238% will occur when the alloying process runs to the last stage with the composition of $Li_{22}Si_5$ [9]. Moreover, phase transformations cause the occurrence of strain gradients [10]. All these factors give rise to cracking and contact loss, thus leading to an irreversible capacity fade of the battery. Although many attempts have been made and pro-

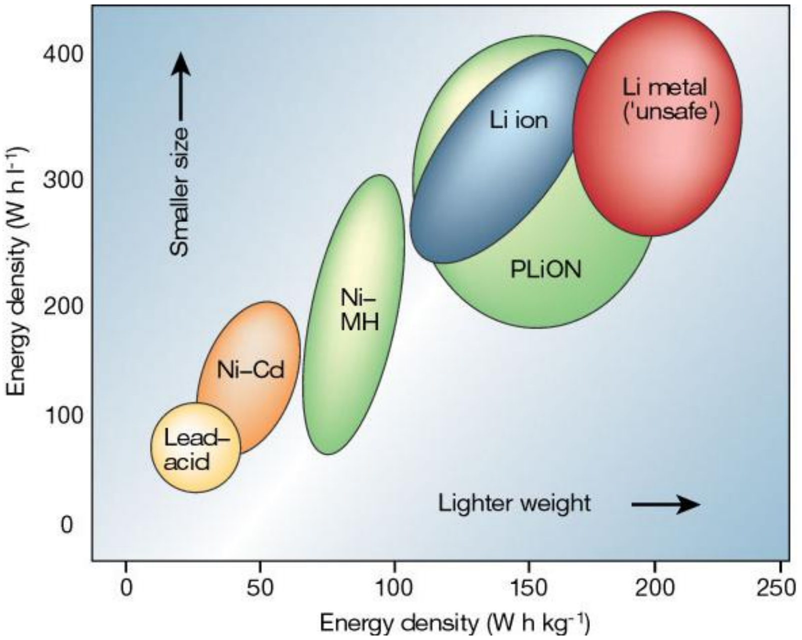

Figure 1.3. *Comparison of the different battery technologies in terms of volumetric and gravimetric energy density. The share of world wide sales for Ni–Cd, Ni–MeH and Li-ion portable batteries is 23%, 14% and 63%, respectively (in the year 2000) [4].*

gresses achieved in the past few years, the commercial silicon-based anodes in replacement of carbonaceous and graphitic anodes are still not yet ready.

To gain an understanding of the mechanisms and operation of the lithium-ion batteries, multi-physical models are extensively and intensively studied by researchers from different disciplines [11–16]. Multi-physics models of lithium-ion batteries involve the interplay between e.g. the electrochemical reaction, the charge and mass transport, the heat generation and transfer, as well as the mechanical fracture and fatigue. As shown in Fig. 1.4, various processes are described by their corresponding mathematical models based on well defined assumptions. Moreover, models are formulated and simulated at different scales for specific purposes [17]. At the system level (macro-scale), models based on complex electrochemical transport equations help to, among others, predict the impact of cell design, improve the packing technique and optimize the electrode morphology. At the particle level (meso-scale), electro-chemo-mechanical models provide more insights in the understanding of the capacity fade, power loss and the SEI formation. They also offer optimization suggestions of the particle size, shape and distribution. In order to measure the properties of the target materials and to estimate the parameters of these models, research tools at lower scales such as molecular dynamics (atomic scale) and the density functional theory (electronic scale) play a key role. These methods can give parameters such as transport, kinetic and mechanical properties, which are not easy to obtain through experiments, especially through *in situ* measurements.

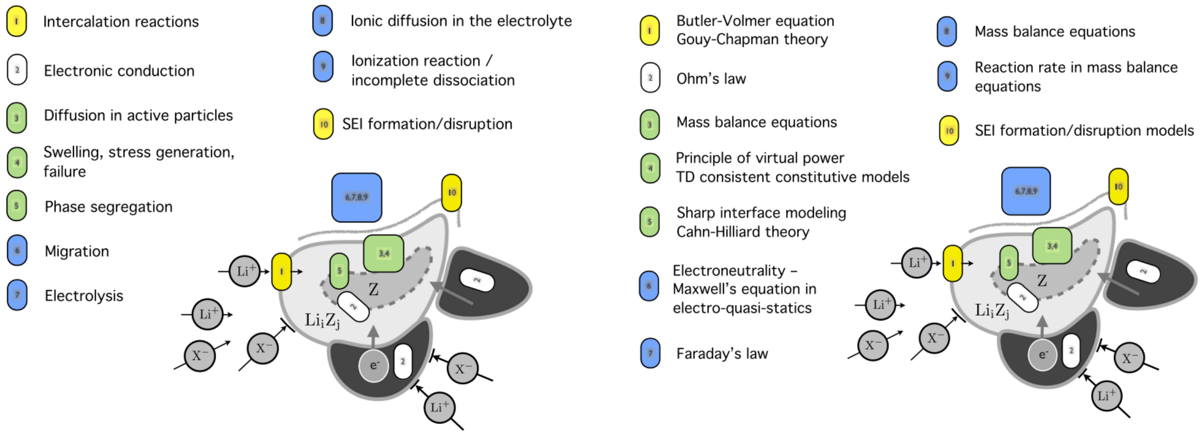

(a) *Processes* **(b)** *Models*

FIGURE **1.4.** *Examples of processes and the corresponding models in a battery during normal operation [16].*

1.2 Goal and outline

The goal of this thesis is to understand the electro-chemo-mechanical behavior of lithium-ion battery electrodes at the meso-scale, and to predict the stress evolution and fracture propagation in electrode particles. To that end, in this thesis, a thermodynamically consistent framework for the active particle and the interactive surrounding matrix is built, with fully consideration of large deformation, phase separation, reaction and diffusion, and crack propagation. In particular, the originality of the model in this thesis includes the following three aspects:

- The phase-separation is coupled with large deformation;
- The electrochemical reaction is modeled through a modified Butler-Volmer equation, which takes both chemical and mechanical states into account;
- The electrochemical reaction front can track the newly created crack surface during simulation through a phase-field model.

Furthermore, several numerical difficulties are also tackled in this thesis:

- The fourth-order Cahn–Hilliard equation, which is employed for the description of the phase-separation, is solved by a finite element method with higher continuous shape functions;
- The complex geometry of the embedded particle and the embedding matrix is described by recursively created computational points in the framework of the finite cell method.

The remaining part of the thesis is organized as follows. In Chapter 2 and Chapter 3, fundamentals of the related theoretical and numerical aspects are briefly reviewed, respectively. Thereupon four models are presented in the following four chapters.

In Chapter 4, the chemical phase separation is discussed, where the Cahn–Hilliard equation is solved. Since the Cahn–Hilliard equation is a fourth-order partial differential equation, the inherent numerical difficulty is addressed and handled. B-Spline based finite element methods—isogeometric analysis and finite cell method—are employed to achieve a global C^1-continuity required by the fourth-order Cahn–Hilliard equation. To deal with the additional essential boundary term arising from the variational derivation, two methods are proposed: the Lagrange multiplier method and the Nitsche method.

In Chapter 5, as a further attempt, a chemo-mechanical model with phase separation in a single particle is proposed and simulated. Thereby, phase-dependent elastic properties are also taken into account. The calculated phase separation behavior in a bar is validated by analytical results. In particular, the influence of the phase-dependent elastic properties on the phase separation and the thickness of the phase interface is demonstrated. Thereafter, the phase separation and the mechanical stresses state in particles with different geometries are studied.

In Chapter 6, a more comprehensive model which deals additionally with the fracture in the particle, is formulated based on the phase-field method. The electrochemical reaction on the surface, phase interface and crack surface is modeled by the modified Butler–Volmer equation. In particular, the reaction on the crack surface is considered through adding a source term regularized by the fracture order parameter. Based on the model, characteristic examples are considered to reveal the material behavior. The results show that both the anisotropy and the ratio between the timescales of reaction and diffusion have a significant influence on the phase separation behavior. In turn, the distribution of the lithium concentration strongly influences the reaction on the surface, especially when the phase interfaces appear on exterior surfaces or crack surfaces. Moreover, the simulations demonstrate that the separation of a Li-rich and a Li-poor phase during delithiation can drive the cracks to propagate. The results indicate that the model can capture the electrochemical reaction on the freshly cracked surfaces.

In Chapter 7, a study of the composite electrode is conducted, where the matrix surrounding the particle is also considered. For the sake of simplicity, the two-material-coupled model presented in this chapter is formulated in the small deformation regime. For a more flexible adaptivity of the particle shape, boundary-unfitted finite cell method is employed, where the interface between the particle and the matrix is represented by a layer of quadrature points. Weak formulations based on the Nitsche method is thus employed for the mechanical and chemical boundary conditions. In order to reduce the computational cost, parallel threading with OpenMP is implemented in the code to achieve the parallelization in the assembly of the global matrix. Composite electrodes with different embedding particles are simulated in this chapter.

In Chapter 8, we bring this thesis to an end with the final conclusion and the outlook.

Chapter 2

Theoretical background

In this chapter, theoretical preliminaries are summarized. The electrochemistry of a lithium-ion battery is firstly reviewed, followed by the basics of continuum mechanics. Finally, the concept of phase-field modeling is introduced.

2.1 Electrochemical system of Li-ion battery

A battery consists of several electrochemical cells, connected in series or parallel, or both, to achieve the desired output voltage and capacity [3]. A typical lithium-ion battery cell is depicted in Fig. 2.1 [18]. *Electrode active particles* are mostly electronic conductors, which can perform an electrochemical reaction with an adjacent material on the particle surface. *Binders* are conductive medium between the electrodes which will transfer electrons and provide mechanical integrity at the same time. The *electrolyte* is the solution that has charged species, of which the most important are lithium cations. Those charged species can diffuse in response to electrochemical potential and concentration differences. Between composite anode and cathode is *the separator* which, in the ideal case, is an ionic conductor and electronic insulator. The *current collector* will conduct the electrons to the external circuit.

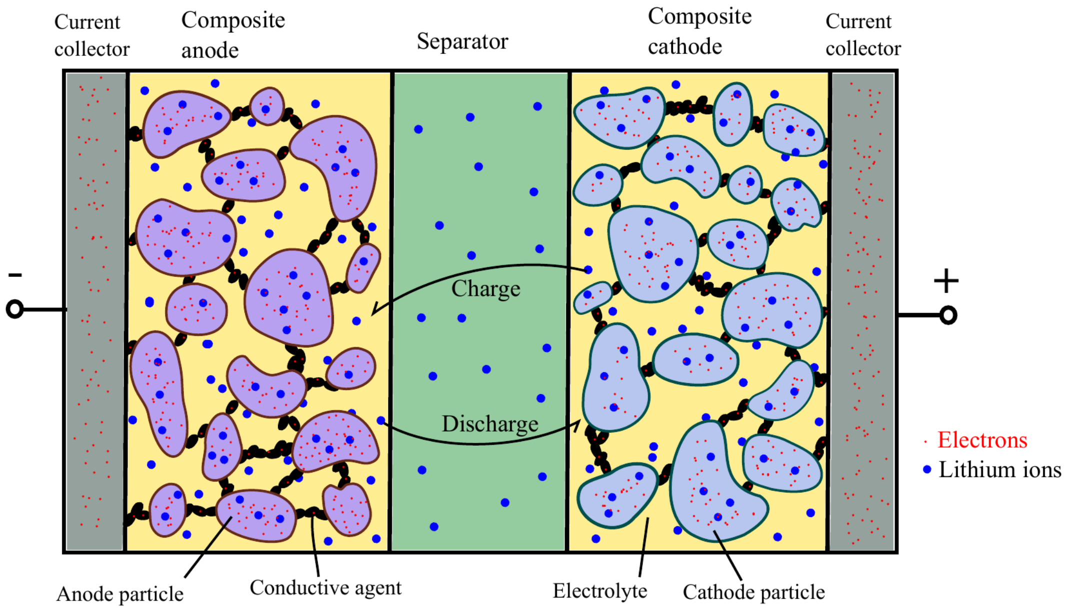

FIGURE 2.1. *Schematic of a lithium-ion battery cell.*

To explain the working principle, a Li-ion battery cell with a graphite-anode and a $LiCoO_2$-cathode is presented [9]. The electrolyte is an organic solvent with fixed background charge. During charge, lithium cations dissolve into the electrolyte on the cathode via the oxidation reaction

$$\mathrm{LiCoO_2} \rightarrow x\mathrm{Li}^+_{(\mathrm{ely})} + x\mathrm{e}^- + \mathrm{Li}_{1-x}\mathrm{CoO_2}. \tag{2.1}$$

Electrons will flow through the binder and current collectors to the external circuit, while lithium cations migrate in the electrolyte and arrive at the anode through the separator. At the anode, lithium cations insert into the active particle via the reduction reaction

$$x\mathrm{Li}^+_{(\mathrm{ely})} + x\mathrm{e}^- + \mathrm{C_6} \rightarrow \mathrm{Li}_x\mathrm{C_6}. \tag{2.2}$$

An exactly reverse reaction occurs during the discharge process. During the whole process, the lithium remains as cations to prevent a destructive dendritic Li growth. For hosts made of alloys or metals, intermetallic insertion exists [19, 20].

The ionic transport of Li^+ in the whole cell plays a crucial role in the charge/discharge rate of the battery. While there are different models for the Li^+ transport [14], Li-ions in an electrolyte move generally in response to concentration gradients, an electric field and bulk fluid motion. In the absence of the solvent velocity, the transport of lithium cations in an electrolyte is governed by the Nerst–Planck equation

$$\frac{\partial c_{\mathrm{Li}^+}}{\partial t} = \boldsymbol{\nabla} \cdot \left[D_{\mathrm{Li}^+} \boldsymbol{\nabla} c_{\mathrm{Li}^+} + \frac{M_{\mathrm{Li}^+} \mathrm{F} c_{\mathrm{Li}^+}}{\mathrm{RT}} (\boldsymbol{\nabla}\phi) \right], \tag{2.3}$$

where D_{Li^+} and M_{Li^+} are the diffusivity and mobility of Li^+ in the electrolyte, R, T, F are gas constant, absolute temperature and Faraday constant, respectively. ϕ is the electric potential. The diffusion inside the particles is studied more intensively later in this thesis.

Since the electronic transport is typically fast enough [21], the key limitation in the charge rate is the availability of Li^+ in the electrolyte, the reaction rate on the particle surface and the diffusion of the lithium inside the electrode particle. The mechanical stresses come into play when the particle experiences strain mismatch due to an uneven deformation. This will lead to cracks or even isolated fragments of particles, which will never been involved in the functioning of the battery, resulting in a capacity fade. Particles may deform unevenly when the distribution of the lithium is not homogeneous. In the electrochemical system of a battery, the reaction rate is a key issue since it is directly related to the charge/discharge performance of a battery. The phenomenological Butler–Volmer equation is thus proposed [22], which define the basis form for the reaction rate R_{BV}

$$R_{\mathrm{BV}} = R_0 \left[\exp\left(-\beta \frac{\mathrm{F}\eta^s}{\mathrm{RT}} \right) - \exp\left((1-\beta) \frac{\mathrm{F}\eta^s}{\mathrm{RT}} \right) \right]. \tag{2.4}$$

The parameter β is an apparent transfer coefficient, representing a favor of the overpotential for a back- or forward reaction. This equation states that the chemical reaction is controlled by the overpotential η^s. However, since the Butler–Volmer equation is based on a dilute solution model, the overpotential is often referred to as the electro-static overpotential, not being able to account for a separation of phases with different Li concentrations. Furthermore, the mechanical contribution is also ignored. Therefore, in this thesis we derive a modified Butler–Volmer equation [23–25], which defines the overpotential based on the electrochemical potential. This electrochemical potential involves

- the electro-static potential,
- the chemical potential at different phases, and
- the mechanical stresses.

Moreover, in the model, the electrochemical reaction front also tracks the newly created crack surfaces. More details are discussed in Chapter 6.

2.2 Basics of mechanics of continua

2.2.1 Mathematical notations

In this section, vectors are denoted by bold-face lowercase Latin and Greek letters

$$\boldsymbol{a}, \boldsymbol{b}, \boldsymbol{c}, \dots, \boldsymbol{\alpha}, \boldsymbol{\beta}, \boldsymbol{\chi}, \dots, \tag{2.5}$$

second-order tensors by bold-face uppercase Latin letters

$$\mathbf{A}, \mathbf{B}, \mathbf{C}, \dots, \tag{2.6}$$

and fourth-order tensors by uppercase blackboard Latin letters

$$\mathbb{A}, \mathbb{B}, \mathbb{C}, \dots. \tag{2.7}$$

Remark: In the entire thesis, since there are certain conventional notations in the theory of continuum mechanics, the above-mentioned notations are sometimes violated, especially the difference between the vector and the matrix notation. However, the bold face letters—Latin or Greek, upper- or lowercase—denote the vectors and matrices, while the letters without bold styling are representing scalars, of which italic letters are variables and roman letters are parameters.

The model is built in the three-dimensional Euclidean space with the Cartesian basis $\mathbf{e}_1$, $\mathbf{e}_2$, $\mathbf{e}_3$. Vectors can thus be represented by a linear combination of the basis vectors as

$$\boldsymbol{a} = \sum_{i=1}^{3} a_i \mathbf{e}_i = a_i \mathbf{e}_i, \tag{2.8}$$

where a repeated subscript i invokes the Einstein summation. $\boldsymbol{a}$ can be then expressed as

$$\boldsymbol{a} = \begin{bmatrix} a_1 & a_2 & a_3 \end{bmatrix}^{\mathrm{T}}, \tag{2.9}$$

where $[\cdot]^{\mathrm{T}}$ denotes transpose of a vector/matrix. The dot product is given by

$$\boldsymbol{a} \cdot \boldsymbol{b} = a_i b_i = \boldsymbol{a}^{\mathrm{T}} \boldsymbol{b}, \tag{2.10}$$

and the norm of a vector is

$$|\boldsymbol{a}| = \sqrt{\boldsymbol{a} \cdot \boldsymbol{a}} = \sqrt{a_i a_i}. \tag{2.11}$$

The tensor product is given by

$$\boldsymbol{a} \otimes \boldsymbol{b} = a_i b_j \mathbf{e}_i \otimes \mathbf{e}_j = \boldsymbol{a} \boldsymbol{b}^{\mathrm{T}}. \tag{2.12}$$

The second-order tensor (matrix) is expressed as

$$\mathbf{A} = \sum_{i,j=1}^{3} A_{ij} \mathbf{e}_i \otimes \mathbf{e}_j. \tag{2.13}$$

Analogically, the fourth-order tensors is given by

$$\mathbb{A} = \sum_{i,j,k,l=1}^{3} A_{ijkl} \mathbf{e}_i \otimes \mathbf{e}_j \otimes \mathbf{e}_k \otimes \mathbf{e}_l. \tag{2.14}$$

The double dot product between two tensors is defined as

$$\mathbf{A} : \mathbf{B} = A_{ij} B_{ij} = \mathrm{tr}\left(\mathbf{A}^{\mathrm{T}} \mathbf{B}\right), \tag{2.15}$$

$$\mathbb{A} : \mathbf{B} = A_{ijkl} B_{kl}, \tag{2.16}$$

where $\mathrm{tr}(\cdot)$ denotes the trace of the matrix. The determinant of a matrix is given by $\det(\cdot)$. The second-order identity tensor is denoted by

$$\mathbf{1} = \delta_{ij} \mathbf{e}_i \otimes \mathbf{e}_j, \tag{2.17}$$

where δ_{ij} is the Kronecker delta. The fourth-order identity tensor $\mathbb{I}$ is defined such that

$$\mathbf{A} = \mathbb{I} : \mathbf{A}. \tag{2.18}$$

The fourth-order identity tensor is then expressed as

$$\mathbb{I} = I_{ijkl} \mathbf{e}_i \otimes \mathbf{e}_j \otimes \mathbf{e}_k \otimes \mathbf{e}_l, \tag{2.19}$$

where

$$I_{ijkl} = \frac{\partial A_{ij}}{\partial A_{kl}} = \begin{cases} \delta_{ik}\delta_{jl}, & \mathbf{A} \neq \mathbf{A}^{\mathrm{T}}, \\ \frac{1}{2}\left(\delta_{ik}\delta_{jl} + \delta_{il}\delta_{jk}\right), & \mathbf{A} = \mathbf{A}^{\mathrm{T}} \, \text{(Symmetric)}, \\ \frac{1}{2}\left(\delta_{ik}\delta_{jl} - \delta_{il}\delta_{jk}\right), & \mathbf{A} = -\mathbf{A}^{\mathrm{T}} \, \text{(Skew symmetric)}. \end{cases} \tag{2.20}$$

$\partial\,(\cdot)\,/\partial\,(\cdot)$ denotes a partial derivative.

2.2.2 Kinematics and stress tensors

In accordance with the literature convention on continuum mechanics (e.g. [26, 27]), a three-dimensional body B occupies continuous sequences of configurations in the Euclidean space in a given open time-interval $t \in [0, +\infty)$. A reference state is chosen at a fixed reference time, with the body denoted by $\mathrm{B_R}$. The choice of the reference state is arbitrary, while usually an undeformed body is preferred and this also coincides with the initial state at $t = 0$. The material point of the body $\mathrm{B_R}$ are labeled as Cartesian coordinates $\mathbf{X} = [\mathrm{X}_1, \mathrm{X}_2, \mathrm{X}_3]^{\mathrm{T}}$. The motion of B is described by a continuous mapping from the material points $\mathbf{X}$ to the spatial coordinates $\mathbf{x}$ at time t

$$\mathbf{x} = \boldsymbol{\chi}(\mathbf{X}, t). \tag{2.21}$$

The deformation gradient at a given time is then defined as

$$\mathbf{F} = \nabla_{\mathrm{R}}\, \boldsymbol{\chi}, \tag{2.22}$$

in which ∇_{R} denotes the gradient with respect to the material point $\mathbf{X}$ in the reference (material) configuration. Considering a neighboring material point $\mathbf{X}'$ and its mapped spatial point $\mathbf{x}'$ at time t, which allows $|\mathrm{d}\mathbf{X}| = \left|\mathbf{X}' - \mathbf{X}\right| \to 0$, the Taylor expansion of $\mathrm{d}\mathbf{x} = \mathbf{x}' - \mathbf{x}$ then can be expressed as

$$\mathrm{d}\mathbf{x} = \boldsymbol{\chi}(\mathbf{X}', t) - \boldsymbol{\chi}(\mathbf{X}, t) = \mathbf{F}\mathrm{d}\mathbf{X} + O\left(|\mathrm{d}\mathbf{X}|^2\right). \tag{2.23}$$

The deformation gradient $\mathbf{F}$ is the mapping of an infinitesimal neighborhood of $\mathbf{X}$ to an infinitesimal neighborhood of $\mathbf{x}$. Consider a polar decomposition of $\mathbf{F}$

$$\mathbf{F} = \mathbf{R}\mathbf{U} = \mathbf{V}\mathbf{R}, \tag{2.24}$$

where $\mathbf{R}$ is an orthogonal matrix, representing the rotation, and $\mathbf{U}$, $\mathbf{V}$ are positive-definite symmetric tensors, representing the stretch. By introducing the right and left Cauchy–Green deformation tensor $\mathbf{C} = \mathbf{U}^2$ and $\mathbf{B} = \mathbf{V}^2$, the following expressions hold:

$$\mathbf{C} = \mathbf{F}^{\mathrm{T}}\mathbf{F}, \quad \mathbf{B} = \mathbf{F}\mathbf{F}^{\mathrm{T}}. \tag{2.25}$$

From Eq. (2.23) and Eq. (2.25), ignoring the higher-order terms, one can arrive at the following relations:

$$|\mathrm{d}\mathbf{x}|^2 = \mathrm{d}\mathbf{x} \cdot \mathrm{d}\mathbf{x} = \mathrm{d}\mathbf{X} \cdot \mathbf{C}\mathrm{d}\mathbf{X}, \quad |\mathrm{d}\mathbf{X}|^2 = \mathrm{d}\mathbf{X} \cdot \mathrm{d}\mathbf{X} = \mathrm{d}\mathbf{x} \cdot \mathbf{B}\mathrm{d}\mathbf{x}. \tag{2.26}$$

The Green–Lagrange strain tensor $\mathbf{E}$ is then defined through the relation:

$$\frac{1}{2}\left(|\mathrm{d}\mathbf{x}|^2 - |\mathrm{d}\mathbf{X}|^2\right) = \mathrm{d}\mathbf{X} \cdot \mathbf{E}\mathrm{d}\mathbf{X}, \quad \mathbf{E} = \frac{1}{2}\left(\mathbf{C} - \mathbf{1}\right). \tag{2.27}$$

The mapping from infinitesimal reference volume dV to the current state dv can be expressed as

$$\mathrm{dv} = J\mathrm{dV}, \quad J = \det \mathbf{F}. \tag{2.28}$$

The mapping of the infinitesimal surface $\mathrm{d}\mathbf{S}$ to the current surface $\mathrm{d}\mathbf{s}$,

$$\mathrm{d}\mathbf{s} = J\mathbf{F}^{-\mathrm{T}}\mathrm{d}\mathbf{S}, \tag{2.29}$$

can be derived based on Eq. (2.23) and the observation of the following relation

$$\mathrm{dv} = \mathrm{d}\mathbf{s} \cdot \mathrm{d}\mathbf{x} = J\mathrm{dV} = J\mathrm{d}\mathbf{S} \cdot \mathrm{d}\mathbf{X}, \tag{2.30}$$

where

$$\mathrm{d}\mathbf{S} = \mathrm{dS}\mathbf{N}, \quad \mathrm{d}\mathbf{s} = \mathrm{ds}\mathbf{n}, \tag{2.31}$$

with $\mathbf{N}$ and $\mathbf{n}$ being the unit normal of the surfaces in the reference and current configurations, respectively.

The tractions $\mathbf{T}$ and $\mathbf{t}$ are defined on the two infinitesimal surfaces such that the infinitesimal force $\mathrm{d}\mathbf{f}$ is

$$\mathrm{d}\mathbf{f} = \mathbf{T}\mathrm{dS} = \mathbf{t}\mathrm{ds}. \tag{2.32}$$

The second-order *first Piola-Kirchhoff stress tensor* $\mathbf{P}$ and *Cauchy stress tensor* $\boldsymbol{\sigma}$ are defined from

$$\mathbf{T} = \mathbf{P}\mathbf{N}, \quad \mathbf{t} = \boldsymbol{\sigma}\mathbf{n} \tag{2.33}$$

such that

$$\mathrm{d}\mathbf{f} = \mathbf{P}\mathbf{N}\mathrm{d}S = \mathbf{P}\mathrm{d}\mathbf{S} = \boldsymbol{\sigma}\mathbf{N}\mathrm{d}s = \boldsymbol{\sigma}\mathrm{d}\mathbf{s}. \tag{2.34}$$

This can further give the relation between the two stress tensors as

$$\mathbf{P} = J\boldsymbol{\sigma}\mathbf{F}^{-\mathrm{T}}. \tag{2.35}$$

Since $\mathbf{P}$ is not symmetric, the *second Piola-Kirchhoff stress tensor* $\mathbf{S}$ is introduced through a pull-back operator $\mathbf{F}^{-1}$ performed on $\mathbf{P}$

$$\mathbf{S} = \mathbf{F}^{-1}\mathbf{P} = J\mathbf{F}^{-1}\boldsymbol{\sigma}\mathbf{F}^{-\mathrm{T}}. \tag{2.36}$$

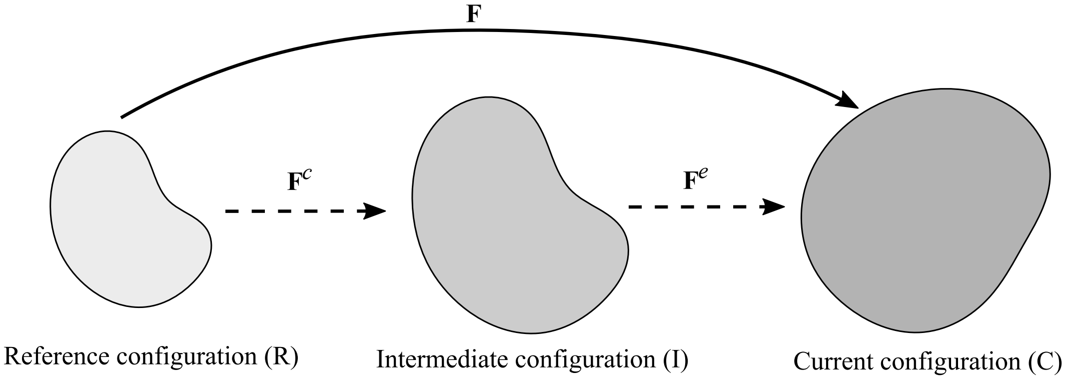

FIGURE 2.2. *Multiplicative decomposition of the total deformation gradient* $\mathbf{F} = \mathbf{F}^e\mathbf{F}^c$.

In this thesis, the inelastic deformation due to the insertion of the chemical species is considered together with the elastic deformation due to the stresses. Therefore, as shown in Fig. 2.2, a multiplicative decomposition of the total deformation gradient is assumed

$$\mathbf{F} = \mathbf{F}^e\mathbf{F}^c, \tag{2.37}$$

where $\mathbf{F}^e$ denotes the elastic distortion and $\mathbf{F}^c$ the (de-)intercalation-induced deformation. It is usually assumed that a continuum body undergoes a uniform dilation under (de-)intercalation, and the deformation is further defined as

$$\mathbf{F}^c = (J^c)^{\frac{1}{3}}\,\mathbf{1} \quad \text{with } J^c = 1 + \Omega c_{\mathrm{R}}, \tag{2.38}$$

in which $c_{\mathrm{R}}(\mathbf{X}, t)$ is the molar concentration per unit volume in the reference configuration and Ω is the constant partial molar volume. In this thesis, entities with subscript R indicate those defined per volume of the reference configuration. Applying the normalization with respect to the maximum concentration $\mathrm{c}_{\max}$,

$$c = c_\mathrm{R}/\mathrm{c}_{\max}, \quad \Omega^* = \Omega \mathrm{c}_{\max}. \tag{2.39}$$

one has

$$J^c = 1 + \Omega^* c. \tag{2.40}$$

On the other hand, one can also define the volumetric part and the right Cauchy-Green deformation tensor of the elastic contribution $\mathbf{F}^e$,

$$J^e = \det \mathbf{F}^e = J/J^c, \tag{2.41}$$

$$\mathbf{C}^e = (\mathbf{F}^e)^\mathrm{T}\mathbf{F}^e = (J^c)^{-\frac{2}{3}}\,\mathbf{C}. \tag{2.42}$$

Due to the volumetric feature of $\mathbf{F}^c$, the deviatoric part of the total deformation equals that of the elastic deformation, i.e.,

$$\bar{\mathbf{C}} = \bar{\mathbf{C}}^e, \quad \text{with } \bar{\mathbf{C}} = J^{-\frac{2}{3}}\mathbf{C} \text{ and } \bar{\mathbf{C}}^e = (J^e)^{-\frac{2}{3}}\mathbf{C}^e. \tag{2.43}$$

It follows that

$$\bar{I}_1 = \bar{I}_1^e, \quad \text{with } \bar{I}_1 = \mathrm{tr}(\bar{\mathbf{C}}) \text{ and } \bar{I}_1^e = \mathrm{tr}(\bar{\mathbf{C}}^e). \tag{2.44}$$

In the linear elastic framework, the *infinitesimal strain* $\boldsymbol{\epsilon}$ is defined as the symmetric part of the displacement gradient

$$\boldsymbol{\epsilon} = \frac{1}{2}\left[\boldsymbol{\nabla}_\mathrm{R}\mathbf{u} + (\boldsymbol{\nabla}_\mathrm{R}\mathbf{u})^\mathrm{T}\right], \quad \mathbf{u} = \mathbf{x} - \mathbf{X}. \tag{2.45}$$

It follows that

$$\boldsymbol{\epsilon} = \frac{1}{2}\left(\mathbf{F} + \mathbf{F}^\mathrm{T}\right) - \mathbf{1}. \tag{2.46}$$

The following relation can be observed from the Eq. (2.27) and Eq. (2.46) that

$$\frac{1}{2}\boldsymbol{\nabla}_\mathrm{R}\mathbf{u} \cdot \boldsymbol{\nabla}_\mathrm{R}\mathbf{u} = \frac{1}{2}\left(\mathbf{F}^\mathrm{T}\mathbf{F} - \mathbf{F} - \mathbf{F}^\mathrm{T} + \mathbf{1}\right) = \mathbf{E} - \boldsymbol{\epsilon}, \tag{2.47}$$

which implies that the two strain tensors $\mathbf{E}$, $\boldsymbol{\epsilon}$ are equal in the limit of $|\boldsymbol{\nabla}_\mathrm{R}\mathbf{u}|^2 \to 0$.

2.3 Phase-field method

Phase-field method is based on a diffuse-interface description proposed in 1894 by van der Waals to derive an expression for the surface tension [28]. Early as it emerged, its major revival was several decades later, when independent works employing phase-field method to describe the microstructure evolution in different physical systems were carried out by Landau and his coworkers [29, 30] and later Cahn and his coworkers [31, 32]. These theories were later generalized for two groups of field variables: non-conserved and conserved variables. Up till now, it has been employed to describe, among other phenomena, the solidification of liquids [33], the condensation of vapor and the evaporation of liquid [34], solid-state transformation [35], the grain growth and coarsening [36], the spinodal decomposition of binary mixture [37], as well as the propagation of cracks under mechanical loading [38–42]. And there are even more to come [43–47].

Microstructures are usually compositional and structural heterogeneous by nature, and can also transform with time. To distinguish different microstructures, or phases, a continuum field variable called *order parameter* is defined in the whole material that bears different values in different phases. The microstructures are thus naturally defined by the order parameter, which varies with space and time. The order parameter can be an existing field with a physical significance such as polarization [48], concentration [31] or magnetization [49]. It can also be a dummy field, only identifying different phases. For instance, in the material with a crack, the crack zone can be identified as 0, while the unbroken region can be set as 1 [39]. Contrary to the sharp-interface model, in the phase-field description, the interface between different phases is diffuse (Fig. 2.3). The total free energy then consists of two contributions: the local free energy and the nonlocal (or gradient) free energy. As an example, a closed multi-phase system in a body B with volume V is considered. The order parameter is denoted by ϕ_i, with i running

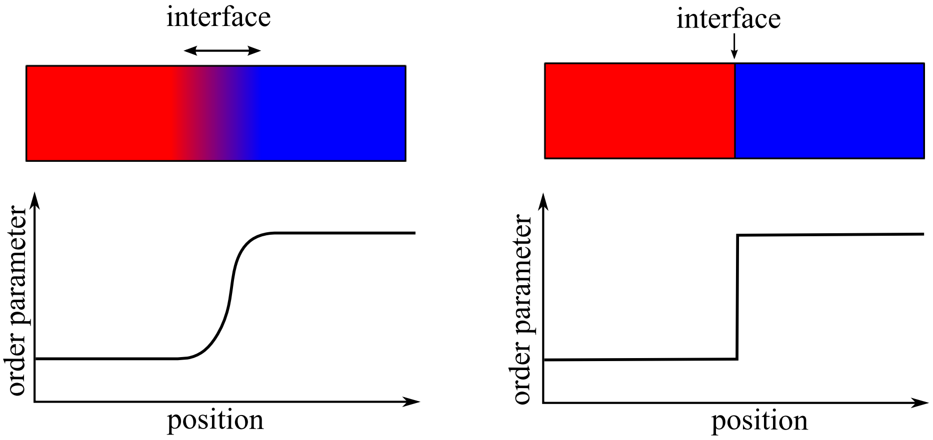

FIGURE 2.3. *Illustration of the diffuse-interface and sharp-interface model.*

from 1 to $\mathrm{n}_{\mathrm{total}}$, which is the total number of order parameters

$$\mathrm{n}_{\mathrm{total}} = \mathrm{n}_{\mathrm{non}} + \mathrm{n}_{\mathrm{con}}, \tag{2.48}$$

with $\mathrm{n}_{\mathrm{non}}$ and $\mathrm{n}_{\mathrm{con}}$ being number of non-conserved and conserved order parameters, respectively. The total free energy Ψ_{total} is expressed as

$$\Psi_{\mathrm{total}} = \int_{\mathrm{B}} \psi_{\mathrm{local}} + \psi_{\mathrm{grad}} \,\mathrm{dV} = \int_{\mathrm{B}} \psi_{\mathrm{local}}(\phi_i) + \sum_{i=1}^{\mathrm{n}} \frac{1}{2}\kappa_i \left|\nabla\phi_i\right|^2 \mathrm{dV}. \tag{2.49}$$

ψ_{local} can be a multi-well function of ϕ_i, having multiple local minima, thus allowing for the coexistence of multiple phases. In certain cases it is also a single well function. For example, in the phase-field fracture models, ψ_{local} is often single-well function in order to prevent a non-physical crack [41, 42]. In the expression of ψ_{grad}, the first order derivative of ϕ_i is used. But one can also use higher-order derivatives to reach a higher convergence rate in the numerical treatment [50]. Let ζ_i denote the variational derivative of Ψ_{total} with respect to the i-th order parameter ϕ_i, one can obtain the following relation

$$\zeta_i = \frac{\delta\Psi_{\mathrm{total}}}{\delta\phi_i} = \frac{\partial\psi_{\mathrm{local}}}{\partial\phi_i} - \kappa_i\Delta\phi_i, \tag{2.50}$$

where $\Delta(\cdot)$ denotes the Laplacian. Please note that the Einstein summation doesn't apply in this section.

After the construction of the free energy functional, the equilibrium state system can be achieved by minimizing the total free energy Ψ_{total}. Different types of order parameters are subject to different evolution equations, arriving at different final state. The non-conserved order parameters ϕ_i^{non} will simply relax so as to minimize overall energy, viz.,

$$\min_{\phi_1^{\mathrm{non}},\ldots,\phi_{\mathrm{n}}^{\mathrm{non}}} \quad \Psi_{\mathrm{total}}. \tag{2.51}$$

The stationary solution can be obtained by enforcing that the variation of Ψ_{total} vanishes,

$$\delta\Psi_{\mathrm{total}} = 0, \tag{2.52}$$

which means that for each independent order parameter ϕ_i^{non} the following equation needs to be fulfilled in equilibrium

$$\zeta_i^{\mathrm{non}} = \frac{\partial\psi_{\mathrm{local}}}{\partial\phi_i^{\mathrm{non}}} - \kappa_i^{\mathrm{non}}\Delta\phi_i^{\mathrm{non}} = 0. \tag{2.53}$$

To describe the evolution of ϕ_i^{non} towards equilibrium, the *Allen–Cahn equation* (or *time-dependent Ginzburg–Landau equation*) is thus proposed as

$$\frac{\partial \phi_i^{\mathrm{non}}}{\partial t} = -\mathrm{M}_i \zeta_i^{\mathrm{non}} = -\mathrm{M}_i \left[\frac{\partial \psi_{\mathrm{local}}}{\partial \phi_i^{\mathrm{non}}} - \kappa_i^{\mathrm{non}} \Delta \phi_i^{\mathrm{non}} \right], \quad i = 1, \ldots, \mathrm{n}_{\mathrm{non}}, \tag{2.54}$$

where M_i is a positive mobility [51].

In the case of conserved order parameters ϕ_i^{con}, they should additionally be subject to the mass conservation:

$$\begin{aligned} &\min_{\phi_1^{\mathrm{con}}, \ldots, \phi_{\mathrm{n}}^{\mathrm{con}}} && \Psi_{\mathrm{total}}, \\ &\text{subject to} && \frac{1}{\mathrm{V}} \int_{\mathrm{B}} \phi_i^{\mathrm{con}} \, \mathrm{dV} = \bar{\phi}_i^{\mathrm{con}} = \mathrm{Const.}, \quad i = 1, \ldots, \mathrm{n}_{\mathrm{con}}, \end{aligned} \tag{2.55}$$

in the absence of flux on the boundary [52]. To obtain the equilibrium state, we perform a variational analysis by formulating a Lagrange function [53]

$$\mathscr{L} = \Psi_{\mathrm{total}} - \sum_{i=1}^{\mathrm{n}_{\mathrm{con}}} \lambda_i^{\mathrm{con}} \int_{\mathrm{B}} \left(\phi_i^{\mathrm{con}} - \bar{\phi}_i^{\mathrm{con}} \right) \mathrm{dV} \tag{2.56}$$

where Lagrange multipliers λ_i^{con} are introduced. Since the Lagrange multipliers are introduced in the global sense and not dependent on the spatial position, it is constant over the field at equilibrium. Performing variations of $\mathscr{L}$ with respect to each ϕ_i^{con} yields

$$\frac{\delta \mathscr{L}}{\delta \phi_i^{\mathrm{con}}} = \frac{\partial \psi_{\mathrm{local}}}{\partial \phi_i^{\mathrm{con}}} - \kappa_i^{\mathrm{con}} \Delta \phi_i^{\mathrm{con}} - \lambda_i^{\mathrm{con}} = \zeta_i^{\mathrm{con}} - \lambda_i^{\mathrm{con}} = 0, \tag{2.57}$$

which gives

$$\zeta_i^{\mathrm{con}} = \lambda_i^{\mathrm{con}} = \mathrm{Const.} \tag{2.58}$$

at equilibrium. Here, ζ_i^{con} is energetically conjugate with ϕ_i^{con} defined in Eq. (2.50). When ϕ_i^{con} denotes the concentration, ζ_i^{con} represents the chemical potential. As for the evolution of ϕ_i^{con} with time, the *Cahn–Hilliard equation* thus applies

$$\frac{\partial \phi_i^{\mathrm{con}}}{\partial t} = \boldsymbol{\nabla} \cdot \left(\mathrm{M}_i \boldsymbol{\nabla} \zeta_i^{\mathrm{con}} \right) = \boldsymbol{\nabla} \cdot \left[\mathrm{M}_i \boldsymbol{\nabla} \frac{\partial \psi_{\mathrm{local}}}{\partial \phi_i^{\mathrm{con}}} - \mathrm{M}_i \boldsymbol{\nabla} \left(\kappa_i^{\mathrm{con}} \Delta \phi_i^{\mathrm{con}} \right) \right], \quad i = 1, \ldots, \mathrm{n}_{\mathrm{con}}. \tag{2.59}$$

Remark: There is a third type which is usually not recognized: the magnetization field to describe the processional switching of the magnetization. It can not be categorized as conserved or non-conserved order parameter. But rather it has its own constraints, making the stationary state and the evolution equation totally different from the other two. In a 3D setup, the magnetization field is denoted by a vector $\boldsymbol{\phi}^{\mathrm{mag}}$ with three components: ϕ_1^{mag}, ϕ_2^{mag}, ϕ_3^{mag}. The equilibrium state below Curie temperature is obtained by finding the solution of

$$\begin{aligned} &\min_{\phi_1^{\mathrm{mag}},\phi_2^{\mathrm{mag}},\phi_3^{\mathrm{mag}}} \quad \Psi_{\mathrm{total}}, \\ &\text{subject to} \quad |\boldsymbol{\phi}^{\mathrm{mag}}| = \left[\sum_{i=1}^{3}\left(\phi_i^{\mathrm{mag}}\right)^2\right]^{\frac{1}{2}} = \mathrm{Const.}. \end{aligned} \tag{2.60}$$

The motion of the magnetization field is then derived as being governed by *Landau–Lifshitz–Gilbert equation*

$$\frac{\partial \boldsymbol{\phi}^{\mathrm{mag}}}{\partial t} = -\gamma \boldsymbol{\phi}^{\mathrm{mag}} \times \left[\frac{\partial \psi_{\mathrm{local}}}{\partial \boldsymbol{\phi}^{\mathrm{mag}}} - \kappa^{\mathrm{mag}} \Delta \boldsymbol{\phi}^{\mathrm{mag}}\right] - \frac{\alpha}{|\boldsymbol{\phi}^{\mathrm{mag}}|} \boldsymbol{\phi}^{\mathrm{mag}} \times \frac{\partial \boldsymbol{\phi}^{\mathrm{mag}}}{\partial t}, \tag{2.61}$$

where γ and α are gyromagnetic and damping parameters. For more details the readers are referred to Refs. [29, 49, 54, 55].

The phase-field method recently has found more and more applications in different contexts for the following reasons:

- The phase-field method is derived from the free energy, which can be estimated from experimental data through the Calphad method [56, 57], or from the atomistic simulation results such as first-principles and molecular dynamics.
- It also allows for the coupling of different physical fields which can be achieved by modifying the free energy with additional terms. Attentions should be paid when a new physical effect is introduced. The convergence of the diffuse interface model to the sharp interface model needs to be examined.
- The phase-field method offers a much simpler tracking of the interface than the sharp interface model in numerical simulations, since in the former model, different phases with interfaces are only represented by field variables, while in the latter model, it has to be explicitly indicated by the simulation geometry.

Nevertheless, since the interfacial thickness is usually very thin compared to the bulk dimensions, phase-field simulations are computationally expensive. Thus, the urge for large-scale simulations and thinner interfaces drives the researchers to improve the numerical efficiency, through e.g. smarter spatial and temporal adaptivity, more efficient and larger-scale parallelization method, as well as the employment of more powerful supercomputers [58].

In this thesis, conserved and non-conserved order parameters are employed to describe phase separation and crack propagation during (de-)lithiation, respectively.

Chapter 3

Numerical background

In order to simulate the model, a set of partial/ordinary differential equations is required to be solved under given geometrical and physical conditions. The intuitive way is to find analytical solutions for these differential equations [59]. However, analytical solutions are not always available, especially for highly nonlinear differential equations, which is always the case for real physical systems. Numerical approximations are thus put forward to solve these differential equations. While many standard models are already available in commercial software based on different optimized numerical methods, newly developed models, especially models with high-order and nonlinear differential equations, still require a careful treatment.

The models in this thesis are Initial-Boundary Value Problems (IBVP). Spatially, the partial differential order is up to fourth-order, and the complete boundary values are specified for all time (Boundary Value Problem); temporally, they are first-order partial differential problems with specified initial field value for every point (Initial Value Problem). Numerically, different methods are employed for the handling of partial differential operators in space and time. In this chapter, the finite element method is introduced to handle the spatial boundary value problem in Section 3.1. In particular, two advanced numerical methods are briefly introduced: isogeometric analysis in Section 3.1.1 and the finite cell method in Section 3.1.2. The former is introduced for the treatment of the fourth-order partial differential Cahn–Hilliard equation, and it is applied in the simulations in Chapter 4, Chapter 5 and Chapter 6. The latter method is employed to treat the irregular geometry of the electrode particles in the composition electrodes in Chapter 7. Finally, in Section 3.2, the finite difference method is introduced for the treatment of the partial differential in time.

3.1 Finite element framework in space

The finite element method is a numerical method to approximate solutions to partial differential equations, with special emphasize on boundary value problems. As a prototype example to introduce the finite element method, we consider the Poisson equation defined in a 3D body B:

$$\Delta u + f = 0 \quad \text{in} \quad \mathrm{B} \tag{3.1}$$

where $f(\boldsymbol{x})$ is a given function and $u(\boldsymbol{x})$ is the unknown field to be solved. For the boundary, we consider the following equations,

$$\boldsymbol{\nabla} u \cdot \boldsymbol{n} = \hat{h} \qquad \text{on} \quad \mathrm{S_N}, \tag{3.2}$$

$$u = \hat{u} \qquad \text{on} \quad \mathrm{S_D}, \tag{3.3}$$

where $\mathrm{S_N}$ and $\mathrm{S_D}$ are two complementary surfaces of the complete boundary surface $\partial\mathrm{B}$. Eq. (3.2) is called *Neumann boundary condition*, where the flux of the unknown is specified and $\boldsymbol{n}$ is the normal vector of the surface. Eq. (3.3) is called *Dirichlet boundary condition* where the solution field itself is specified.

The process of the finite element method begins with the weighted residual method performed on the governing equation. Multiplying Eq. (3.1) with a weighting function δu and integrating over the complete domain yields

$$\int_{\mathrm{B}} (\Delta u + f)\, \delta u \,\mathrm{dV} = 0. \tag{3.4}$$

After the integration by parts and the application of divergence theorem, we obtain

$$-\int_{\mathrm{B}} \boldsymbol{\nabla} u \cdot \boldsymbol{\nabla} \delta u \,\mathrm{dV} + \int_{\mathrm{B}} f\, \delta u \,\mathrm{dV} + \int_{\partial\mathrm{B}} \boldsymbol{\nabla} u \cdot \boldsymbol{n} \delta u \,\mathrm{dS} = 0. \tag{3.5}$$

Substituting the corresponding surface term of Eq. (3.5) with Eq. (3.2) gives

$$-\int_{\mathrm{B}} \boldsymbol{\nabla} u \cdot \boldsymbol{\nabla} \delta u \,\mathrm{dV} + \int_{\mathrm{B}} f\, \delta u \,\mathrm{dV} + \int_{\mathrm{S_D}} \boldsymbol{\nabla} u \cdot \boldsymbol{n} \delta u \,\mathrm{dS} + \int_{\mathrm{S_N}} \hat{h} \delta u \,\mathrm{dS} = 0. \tag{3.6}$$

In this way, we have built Eq. (3.1) and Eq. (3.2) into Eq. (3.6). The Dirichlet boundary condition of Eq. (3.3) is often imposed pointwise on the boundary, whereas the weighting function δu is enforced in such a way that it vanishes on $\mathrm{S_D}$. The Eq. (3.6) is thus further derived as

$$\int_{\mathrm{B}} \boldsymbol{\nabla} u \cdot \boldsymbol{\nabla} \delta u \,\mathrm{dV} = \int_{\mathrm{B}} f\, \delta u \,\mathrm{dV} + \int_{\mathrm{S_N}} \hat{h} \delta u \,\mathrm{dS}. \tag{3.7}$$

Eq. (3.7) is called the *weak form* of the Poisson problem, in comparison with the *strong form* of Eq. (3.1)–Eq. (3.3). The solution of Eq. (3.7) is exactly the solution of the corresponding strong formulation. As the next step, the partition of the continuum B into finite pieces of domains B_e called *elements* is performed, viz.,

$$\mathrm{B} \approx \sum_e \mathrm{B}_e, \tag{3.8}$$

and similarly for the boundary

$$\partial \mathrm{B} \approx \sum_e \mathrm{S}_{\mathrm{N}e} + \sum_e \mathrm{S}_{\mathrm{D}e}. \tag{3.9}$$

Hence, Eq. (3.7) is discretized as

$$\sum_e \int_{\mathrm{B}_e} \nabla u \cdot \nabla \delta u \, \mathrm{dV} = \sum_e \int_{\mathrm{B}_e} f \, \delta u \, \mathrm{dV} + \sum_e \int_{\mathrm{S}_{\mathrm{N}e}} \hat{h} \delta u \, \mathrm{dS}. \tag{3.10}$$

Since the surface integration involves no unknown variables to be solved, the last term of Eq. (3.10) is often taken care of independently in a global sense. Each element has *nodes*, which are typically points of geometric significance such as vertices of the element. The local basis functions, mostly polynomials, are associated with each node, so that each position $\boldsymbol{x}$ in the body B can be interpolated as

$$\boldsymbol{x}(\xi) = \boldsymbol{x}^{\mathrm{I}} \mathrm{N}^{\mathrm{I}}(\xi), \tag{3.11}$$

where $\boldsymbol{x}^{\mathrm{I}}$ is the physical spatial position of the I-th node and N^{I} is the interpolation function, or *the shape function*. ξ is the coordinate of $\boldsymbol{x}$ in the parametric space, which is usually defined in a closed range of $[-1,1] \times [-1,1] \times [-1,1]$ for later convenience of integration. But exceptions also apply, for instance in the case of isogeometric analysis to be introduced in Section 3.1.1. The simplest basis function of N^{I} is the piece-wise linear function, which bears the value of 1 when it hits the corresponding node and zero at other nodes. The solution field u employs the same basis functions as the position field $\boldsymbol{x}$,

$$u(\xi) = u^{\mathrm{I}} \, \mathrm{N}^{\mathrm{I}}(\xi), \tag{3.12}$$

where u^{I} is the I-th nodal unknown, also known as degree of freedom (DOF). The idea to use the same set of shape functions for the representation of the element geometry and called *isoparametric concept*. The weighting function also shares the same basis functions

$$\delta u = \delta u^{\mathrm{I}} \, \mathrm{N}^{\mathrm{I}}(\xi), \tag{3.13}$$

which is called *the Galerkin method*. There are also other choices of weighting functions, which leads to other numerical methods such as collocation methods [60]. The gradients of the solution and the weighting function are thus

$$\nabla u = u^{\mathrm{I}} \, \nabla \mathrm{N}^{\mathrm{I}} \tag{3.14}$$

$$\nabla \delta u = \delta u^{\mathrm{I}} \, \nabla \mathrm{N}^{\mathrm{I}}. \tag{3.15}$$

Please note that $\nabla \mathrm{N}^{\mathrm{I}}$ is the gradient of N^{I} with respect to the physical coordinates $\boldsymbol{x}$, which is derived as

$$\frac{\partial \mathrm{N}^{\mathrm{I}}}{\partial \boldsymbol{x}} = \frac{\partial \mathrm{N}^{\mathrm{I}}}{\partial \xi} \frac{\partial \xi}{\partial \boldsymbol{x}}. \tag{3.16}$$

Putting Eq. (3.12)–Eq. (3.15) into Eq. (3.10) yields

$$\sum_e \int_{\mathrm{B}_e} u^{\mathrm{J}} \nabla \mathrm{N}^{\mathrm{J}} \cdot \nabla \mathrm{N}^{\mathrm{I}} \, \delta u^{\mathrm{I}} \, \mathrm{dV} = \sum_e \int_{\mathrm{B}_e} f \, \mathrm{N}^{\mathrm{I}} \delta u^{\mathrm{I}} \, \mathrm{dV} + \sum_e \int_{\mathrm{S}_{\mathrm{N}e}} \hat{h} \mathrm{N}^{\mathrm{I}} \delta u^{\mathrm{I}} \, \mathrm{dS}. \tag{3.17}$$

Since Eq. (3.17) should hold for every δu^{I}, the residual

$$R^{\mathrm{I}} = \sum_e u^{\mathrm{J}} \int_{\mathrm{B}_e} \nabla \mathrm{N}^{\mathrm{J}} \cdot \nabla \mathrm{N}^{\mathrm{I}} \, \mathrm{dV} - \sum_e \int_{\mathrm{B}_e} f \, \mathrm{N}^{\mathrm{I}} \, \mathrm{dV} + \sum_e \int_{\mathrm{S}_{\mathrm{N}e}} \hat{h} \mathrm{N}^{\mathrm{I}} \, \mathrm{dS} \tag{3.18}$$

should be equal to zero for all I. Thanks to the fact that shape functions N^{I} are highly local, only limited shape functions N^{I} are non-zero at each physical position and they are accessible locally within one element. The residual in each element integral can thus be computed as

$$R_e^{\mathrm{A}} = u^{\mathrm{B}} \int_{\mathrm{B}_e} \nabla \mathrm{N}^{\mathrm{B}} \cdot \nabla \mathrm{N}^{\mathrm{A}} \, \mathrm{dV} - \int_{\mathrm{B}_e} f \, \mathrm{N}^{\mathrm{A}} \, \mathrm{dV}. \tag{3.19}$$

Here A and B run from 1 to total number of nodes per element. The integration of Eq. (3.19) is done by quadrature rules, of which the most widely used one is *the Gaussian quadrature rule*. The integral is replaced by the weighted sum of the integrand at *the Gauss points*,

$$R_e^{\mathrm{A}} = u^{\mathrm{B}} \sum_{\mathrm{g}} \nabla \mathrm{N}^{\mathrm{B}}(\xi_{\mathrm{g}}) \cdot \nabla \mathrm{N}^{\mathrm{A}}(\xi_{\mathrm{g}}) w_{\mathrm{g}} J_{\mathrm{g}}^{e} - \sum_{\mathrm{g}} f(\boldsymbol{x}(\xi_{\mathrm{g}})) \mathrm{N}^{\mathrm{A}}(\xi_{\mathrm{g}}) w_{\mathrm{g}} J_{\mathrm{g}}^{e}, \tag{3.20}$$

where the Gauss points ξ_{g} and the corresponding weight w_{g} are chosen according to the polynomial order of the integrand. J_{g}^{e} is the determinant of the Jacobian transformation and is computed as the volume change from the physical space to the parametric space:

$$J_{\mathrm{g}}^{e} = \det\left(\frac{\partial \boldsymbol{x}}{\partial \xi}(\xi_{\mathrm{g}}) \right). \tag{3.21}$$

Since the parametric domain we have defined coincides with the Gaussian integration domain $[-1,1] \times [-1,1] \times [-1,1]$, no further mapping is needed. However, if the parametric domain is defined other than the integration domain, a mapping from the parametric domain to the bi-unit integration domain is required. Based on the connection of the local nodal index and the global nodal index, the global residual vector is assembled, with dimension of the total DOF.

Rewriting Eq. (3.18) in the vector format and ignoring the surface integration yields the linear algebraic equation

$$\boldsymbol{R} = \boldsymbol{K}\boldsymbol{u} - \boldsymbol{f} = \boldsymbol{0}, \tag{3.22}$$

with

$$\boldsymbol{K} = \left[K^{\mathrm{IJ}}\right], \quad K^{\mathrm{IJ}} = \sum_{e}\left[\sum_{\mathrm{g}} \nabla \mathrm{N}^{\mathrm{J}}(\xi_{\mathrm{g}}) \cdot \nabla \mathrm{N}^{\mathrm{I}}(\xi_{\mathrm{g}}) w_{\mathrm{g}} J_{\mathrm{g}}^{e}\right], \tag{3.23}$$

$$\boldsymbol{f} = \left[f^{\mathrm{I}}\right], \quad f^{\mathrm{I}} = \sum_{e}\left[\sum_{\mathrm{g}} f(\boldsymbol{x}(\xi_{\mathrm{g}}))\mathrm{N}^{\mathrm{I}}(\xi_{\mathrm{g}}) w_{\mathrm{g}} J_{\mathrm{g}}^{e}\right]. \tag{3.24}$$

If the Eq. (3.22) are not linear, certain root-finding algorithms are invoked to search the correct root iteratively. In the thesis the Newton–Raphson iteration procedure is employed, where the solution for the next iteration $\boldsymbol{u}_{(k+1)}$ is updated from the current k-th iteration through

$$\boldsymbol{u}_{(k+1)} = \boldsymbol{u}_{(k)} + \mathrm{d}\boldsymbol{u}_{(k)} \tag{3.25}$$

recursively until the convergence is reached. The update $\mathrm{d}\boldsymbol{u}_{(k)}$ is computed from the tangent matrix $\boldsymbol{S}_{(k)}$ and the residual $\boldsymbol{R}_{(k)}$ at the current iteration through the equation

$$\boldsymbol{R}_{(k+1)} = \boldsymbol{R}_{(k)} + \boldsymbol{S}_{(k)}\mathrm{d}\boldsymbol{u}_{(k)} = \boldsymbol{0} \tag{3.26}$$

where

$$\boldsymbol{S}_{(k)} = -\left(\frac{\partial \boldsymbol{R}}{\partial \boldsymbol{u}}\right)_{(k)}. \tag{3.27}$$

Newton-Raphson iteration gives a quadratic rate of convergence. Finally, one need to solve the linear equation system of either Eq. (3.22) or Eq. (3.26). Since the basis functions are highly localized, the stiffness matrix $\boldsymbol{K}$ (or tangent matrix $\boldsymbol{S}$) is sparse. While iterative solver is recommended for large problems, for small problem with ill-conditioned stiffness matrix, a direct solver can give a more reliable result. In this thesis, a direct solver is used. In particular, a built-in profile solver from FEAP [61] and the MKL-Pardiso solver from Intel are used [62].

In this thesis, two advanced numerical methods will be employed: isogeometric analysis and the finite cell method. The former employs higher-order splines as the basis functions; the exact geometry representation will give a higher accuracy in the solution. The latter represents the geometry with an adaptively calculated quadrature points, with a structured background mesh. For the completeness, the two methods are reviewed here briefly.

3.1.1 Isogeometric analysis

The concept of IsoGeometric Analysis (IGA) was proposed more than one decade ago [60, 63], whose target was to bridge the gap between Computer Aided Design (CAD) and Computer Aided Engineering (CAE) by employing the same spline basis functions that used in CAD for finite element simulations, unlike Lagrange polynomials employed by traditional finite element methods. In that way, the geometric representation is faithfully retained in the numerical simulation and the communicational cost between the CAD and CAE are saved once the first coarse but exact geometric model is built. Furthermore, isogeometric analysis has turned out to offer significant additional benefits. For problems with smooth solutions, it exhibits increased accuracy and robustness on a per-degree-of-freedom basis [64–66]. Unlike C^0-continuous basis functions, the higher modes of spline basis functions do not diverge with increasing degree, but achieve almost spectral accuracy that improves with degree [67–69]. Approximations of derivative fields are smooth and their degree can be adjusted to what is required by the primal variational formulation [70–72]. It is also noted that the higher-order continuity of spline basis functions has triggered interest beyond finite element analysis, e.g., in collocation methods [66, 73, 74].

In this section, a brief review of the most common basis function, Non-Uniform Rational B-Splines (NURBS) will be given. Its application in IGA will then be introduced.

A B-splines curve is defined by a *knot vector* and *control points*, where the former determines the basis functions and latter mark the locations. They are defined independently, provided that the number of basis functions from the knot vector equals the number of control points. In one dimension, let n and p denote the number and the polynomial order of the basis functions, a knot vector consists of a non-decreasing set of coordinates, or knots

$$\varXi = \left[\xi_1, \xi_2, \ldots, \xi_{n+p+1}\right], \tag{3.28}$$

which defines the B-spline basis functions through the Cox-de Boor recursion formula

$$N_{i,0}(\xi) = \begin{cases} 1 & \text{if } \xi_i \leq \xi < \xi_{i+1}, \\ 0 & \text{otherwise.} \end{cases} \tag{3.29}$$

$$N_{i,p}(\xi) = \frac{\xi - \xi_i}{\xi_{i+p} - \xi_i} N_{i,p-1}(\xi) + \frac{\xi_{i+p+1} - \xi}{\xi_{i+p+1} - \xi_{i+1}} N_{i+i,p-1}(\xi). \tag{3.30}$$

Fig. 3.1 shows cubic B-spline basis functions defined by the open knot vector $\varXi = [0,0,0,0,1,2,2,3,4,4,4,4]$. We can observe that the basis functions are very smooth accross elements. Furthermore, in order to describe conic curves such as circles, an additional weight vector

$$[w_1, w_2, \ldots, w_n] \tag{3.31}$$

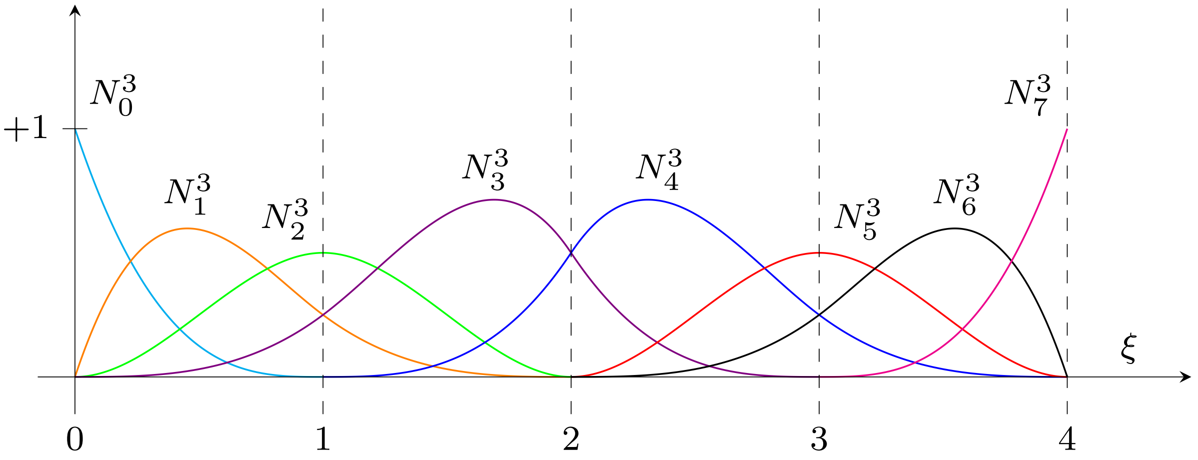

Figure 3.1. *Cubic B-spline functions with knot vector* $\varXi = [0,0,0,0,1,2,2,3,4,4,4,4]$ *[75].*

associated to each basis functions is introduced, which leads to the NURBS basis functions defined as

$$R_i^p(\xi) = \frac{w_i N_i^p(\xi)}{\sum_{j=1}^n w_j N_j^p(\xi)}. \tag{3.32}$$

Note that in this subsection, no Einstein summation is used. All summations are expressed explicitly with the summation symbol. A NURBS curve can thus be given by

$$\mathbf{C}(\xi) = \sum_{i=1}^{n} R_i^p(\xi)\mathbf{P}_i, \tag{3.33}$$

where $\mathbf{P}_i$ is the control point associated with the i-th NURBS basis function. When the weight $w_i = 1$ holds for all basis functions, the curve will be degenerated to the B-splines curve. The three dimensional NURBS solid can be defined analogously by three knot vectors

$$\begin{aligned} \boldsymbol{\varXi} &= \left[\xi_1, \xi_2, \dots, \xi_{n+p+1}\right], \\ \boldsymbol{H} &= \left[\eta_1, \eta_2, \dots, \eta_{m+q+1}\right], \\ \boldsymbol{Z} &= [\zeta_1, \zeta_2, \dots, \zeta_{l+r+1}] \end{aligned} \tag{3.34}$$

and the control lattice $\mathbf{P}_{ijk}$, together with the corresponding weights w_{ijk}. The basis functions are given as

$$R_{ijk}^{pqr}(\xi,\eta,\zeta) = \frac{w_{ijk} N_i^p(\xi) N_j^q(\eta) N_k^r(\zeta)}{\sum_{a=1}^n \sum_{b=1}^m \sum_{c=1}^l w_{abc} N_a^p(\xi) N_b^q(\eta) N_c^r(\zeta)} \tag{3.35}$$

and the solid is

$$\mathbf{S}(\xi,\eta,\zeta) = \sum_{i=1}^{n}\sum_{j=1}^{m}\sum_{k=1}^{l} R_{ijk}^{pqr}\mathbf{P}_{ijk}. \tag{3.36}$$

Recalling Eq. (3.10), as a generalized notation of Eq. (3.33) and Eq. (3.36), the geometry of dimension d is described by the mapping $\mathbf{G}$,

$$\mathbf{x} = \mathbf{G}(\xi) = \sum_{\mathrm{I}} \mathrm{N}^{\mathrm{I}}(\xi)\mathbf{x}^{\mathrm{I}}, \quad \mathbf{x} \in \mathbb{R}^d,\ \xi \in \mathbb{R}^d, \quad d = 1, 2 \text{ or } 3, \tag{3.37}$$

where $\mathbf{x}$, ξ are the coordinates in the physical and the parametric domain, respectively. In 3-dimensional solids, we have

$$\boldsymbol{x} = [x, y, z], \quad \xi = [\xi, \eta, \zeta]. \tag{3.38}$$

N^{I} is the I-th basis function, representing R_i^p and R_{ijk}^{pqr} in Eq. (3.33) and Eq. (3.36), respectively. $\mathbf{x}^{\mathrm{I}}$ is the coordinates of the I-th control point $\mathbf{P}^{\mathrm{I}}$. The inverse of the mapping is thus

$$\xi = \mathbf{G}^{-1}(\mathbf{x}). \tag{3.39}$$

Recalling Eq. (3.12), the solution field u is then approximated by the map

$$u = \mathbf{A}(\xi) = \sum_{\mathrm{I}} \mathrm{N}^{\mathrm{I}}(\xi) u^{\mathrm{I}} \tag{3.40}$$

in which u^{I} is the field unknown at the I-th control point. By combining Eq. (3.39) and Eq. (3.40) one can obtain the solution field in the physical space

$$u = \mathbf{A}\left(\mathbf{G}^{-1}(\mathbf{x})\right). \tag{3.41}$$

3.1.2 Finite cell method

The Finite Cell Method (FCM) is an embedded domain method. The latter is also known as immersed boundary or fictitious domain methods [76]. The main idea is to employ a structured background mesh with higher-order basis functions to approximate the solution field, while the geometry is represented with adaptive quadrature points [65, 77]. Thanks to the flexibility of the quadrature based geometry approximation, the FCM can operate with almost any geometric model, ranging from a boundary representation from CAD to a voxel representation obtained from scanned images. There are three main components of the FCM, which make it different from a standard higher-order finite element method. They are the concept of fictitious domain approach, the procedure of adaptive quadrature points, and the weak constraint of the essential boundary condition. In this section, the three differences will be introduced. The basis functions in this thesis are B-splines since the mesh is structured.

The fictitious domain concept is illustrated in Fig. 3.2. The embedding domain Ω consists

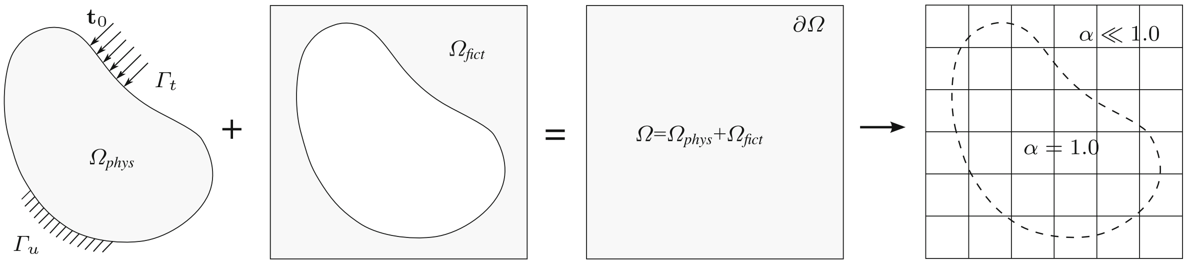

FIGURE 3.2. *The fictitious domain approach: the physical domain Ω_{phys} is extended by the fictitious domain Ω_{fict} into an embedding domain Ω to allow easy meshing of complex geometries. The influence of Ω_{fict} is penalized by α [76].*

of the physical domain of interest Ω_{phys} and the fictitious domain extension Ω_{fict}. The weak formulation is the same as in the finite element method, with the embedding area as the integration area. In the fictitious domain, the material parameters are weighted by a scalar factor α, which leaves the material behavior unchanged in the physical domain, and makes the contribution of the fictitious domain low enough. The parameter α is not chosen as exactly zero in the fictitious domain to prevent extreme ill-conditioning of the stiffness matrix.

The volume quadrature approach of the finite cell method employs composed Gauss quadrature, based on a hierarchical decomposition of the original element into quadrature sub-cells [78]. Fig. 3.3 illustrates the generation of the sub-cell structure in two dimensions following the procedure of recursive bisection, also called quadtree. It is emphasized again that basis functions for the approximation of the solution fields are still defined exclusively on the original mesh, while the sub-cell structure exists only for defining adaptive quadrature points, aggregated around the geometric boundary. The recursive subdivision approach can be easily

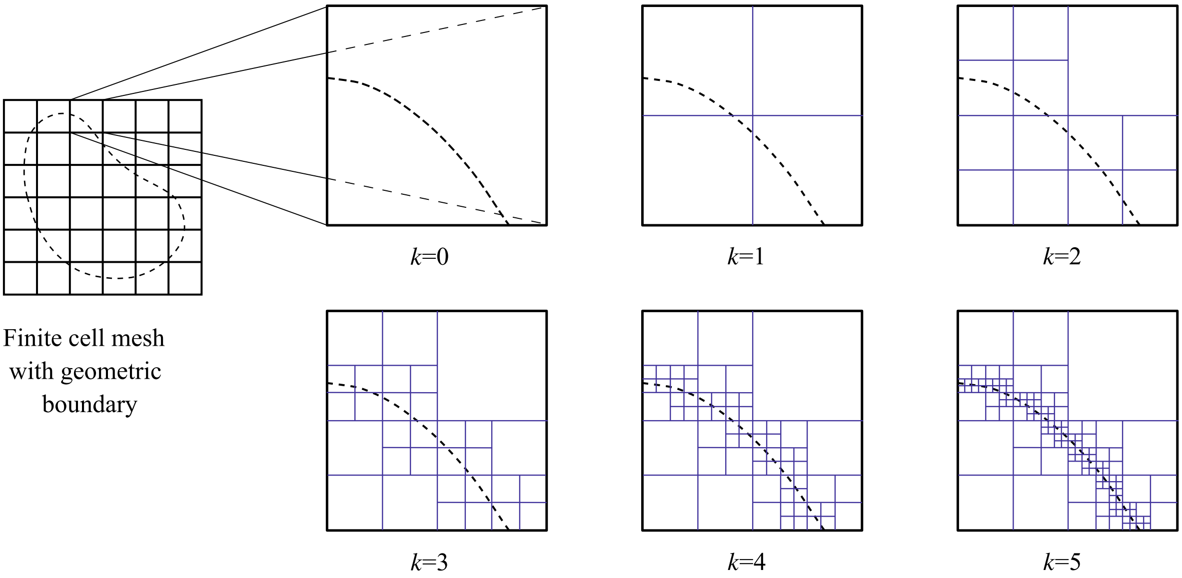

FIGURE 3.3. *2D sub-cell structure (thin blue lines) for adaptive integration of finite cells (bold black lines) that are cut by the geometric boundary (dashed line) [76].*

adjusted to one or three dimensions in the sense of binary or octrees, respectively. A three dimensional octree with the producing quadrature points in a three dimensional geometric with two contacted materials are illustrated in Fig. 3.4. It can also easily be generalized to other element shapes such as tetrahedral [79, 80] or polygonal elements [81].

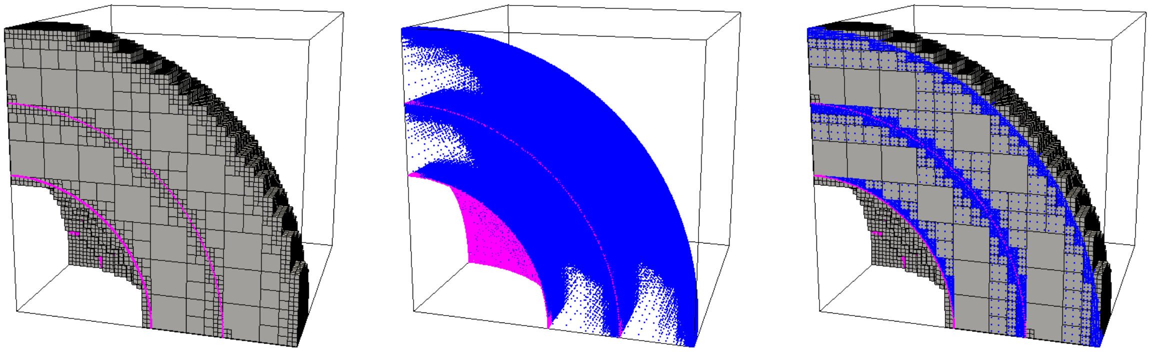

(a) *Cells* **(b)** *Quadrature points.* **(c)** *Cells and the quadratures.*

FIGURE **3.4.** *3D sub-cell structure and adaptive integration points in the double layered thick spherical shell. An octree sub-division starts from a* $8\times8\times8$ *mesh and it goes to the sub-cell level of three. Volume quadrature points are in blue and surface quadrature points are in magenta.*

The fictitious domain method inherently satisfies flux-free and traction-free boundary condition. For evaluating surface integrals of non-zero Neumann boundary conditions in this paper, we simply introduce a fine triangulation of each embedded boundary. Each triangle serves as the basis for generating independent quadrature points based on standard monomial rules [82, 83] (see the magenta points in Fig. 3.4). Each quadrature point can be related to a specific element via its global coordinate. When essential boundary conditions are to be satisfied, special efforts are required. Those essential boundary conditions need to be built in the weak formulation through Lagrange multiplier, penalty, or Nitsche's method. In this work, the non-symmetric Nitsche method is employed, where the mechanical compatibility condition needs to be satisfied between two materials (see the interfacial layer between the two shells in Fig. 3.4). More details are given in Chapter 7.

3.2 Finite difference framework in time

Since the problem addressed in this work is also time dependent, the discretization of time is also necessary. For an initial condition problem, common treatment is the finite difference method. This method works directly on the strong forms of the partial/ordinary differential equations, by approximating the differential operators by finite differences in the discretized space. In this section, a short introduction to two simplest methods is given: forward and backward Euler method.

For simplicity, consider a first-order ordinary differential problem

$$\frac{\mathrm{d}y}{\mathrm{d}t} = f(t,y), \quad t \in (0,+\infty), \tag{3.42}$$

$$y(t=0) = y_0. \tag{3.43}$$

First the continuous time is divided by a set of time intervals $t_0, t_1, \ldots, t_n, t_{n+1}, \ldots$ with the interval size $\triangle t = t_{n+1} - t_n$. Integrating Eq. (3.42) from t_n to t_{n+1} yields

$$y(t_{n+1}) - y(t_n) = \int_{t_n}^{t_{n+1}} f(t,y)\,\mathrm{d}t. \tag{3.44}$$

A *forward Euler method* is obtained when the right hand side integration is approximated by the rectangular method with the integrand computed from t_n

$$y(t_{n+1}) = y(t_n) + f(t_n, y(t_n))\triangle t. \tag{3.45}$$

Similarly, the *backward Euler method* is obtained when the integrand is computed from t_{n+1}

$$y(t_{n+1}) - y(t_n) = f(t_{n+1}, y(t_{n+1}))\triangle t. \tag{3.46}$$

Care should be taken when the backward method is used since the quantities at $t = t_{n+1}$ is yet unknown, and a Newton-Raphson iteration is necessary to solve the equation. Since this method is unconditionally convergent, in this thesis, the backward-Euler method is employed.

Chapter 4

Chemical behavior of electrode particles: phase separation

Phase separation often occurs during (de-)lithiation in the electrode particles made of materials such as crystalline silicon (Si) [84], tin (Sn), antimony (Sb) and their oxides [8, 85] for anodes, as well as cathode material i.e. Li_xFePO_4 [10, 86] and $Li_xMn_2O_4$ [87]. In this regard, the Cahn–Hilliard phase-field model proposed in [31, 37] has attracted increasing attention in describing the chemical phase separation in lithium-ion batteries. Han et al. [88] simulated galvanostatic and potentiostatic intermittent titration technique experiments and gave reliable predictions for the chemical diffusion coefficient. Apart from that, they also showed a way to approximate an interfacial parameter from the nearest-neighbor interaction and the lattice spacing of the material. Further, Singh et al. [89] developed a Cahn–Hilliard-type diffusion into an anisotropic ionic mobility in the crystal and considered surface reaction. The mathematical study of the Cahn–Hilliard equation has long been carried out to discuss the existence and uniqueness of its solution [90, 91]. On the other hand, different numerical methods are employed to solve the equation, among which are finite difference methods [92], spectral methods [93], and finite volume methods [94]. The finite element method emerges as a very strong tool to solve Cahn–Hilliard equation since it offers greater flexibility of the geometry. In this section, simulations based on the finite element method is employed.

As the Cahn–Hilliard equation is a fourth-order partial differential equation spatially, it is accompanied by numerical difficulties in dealing with higher-order operators. In the context of finite element methods, this usually requires globally C^1-continous basis functions. Previous treatments include mixed formulations, where the Cahn–Hilliard equation is rewritten into two coupled equations, by introducing an additional variable, which can be a nonlocal species concentration [95], or the chemical potential [96]. Alternatively, Wells et al. [97] formulated the Cahn–Hilliard equation in the framework of a discontinuous Galerkin method. Both methods reduce the requirement of continuity of the elements and standard C^0-continuous shape functions are used. However, the convenience of employing these shape functions comes with the cost of extra degrees of freedom in addition to the prime unknowns.

To treat the high-order operator straightforwardly, isogeometric analysis was employed by Gomez et al. [70] to solve the Cahn–Hilliard equation. A comparison between different numerical schemes with an emphasis on C^1-continuous methods has been recently carried out by

Kaessmair and Steinmann [98]. The B-spline based finite cell method is also suitable to handle this equation. The employment of B-splines or NURBS as basis functions provides global C^1 or even higher-order continuity. However, when the Cahn–Hilliard is to be dealt with directly, a special effort has to be made to an essential boundary term $\nabla c \cdot \boldsymbol{n} = 0$, which states as normal gradient of concentration to be zero. This term arises from a thermodynamic derivation but does not fit directly into the weak formulation of the finite element method. In the context of isogeometric analysis, Gomez et al. [70] avoided this problem by imposing periodic boundary conditions with periodic B-spline basis functions. Liu et al. [99] imposed this boundary term by setting two consecutive boundary control values to be equal in the rectangular/cuboid grid with quadratic shape functions. Dalcin et al. [100] developed an unclamping algorithm to adapt higher-order open knot vector for a desired continuity at the boundary, so as to enforce the periodic boundary conditions. However, those strong impositions of the essential boundary conditions are limited by the geometry, where there should be a control axis perpendicular to the surface when it intersects with the surface. Moreover, a strong imposition is not even possible in the finite cell method, where the surface is represented by a layer of quadrature points.

Therefore, in this chapter, two new ways are proposed to treat the essential boundary condition: the Lagrange multiplier and the Nitsche method. Anders et al. [101] used Lagrange multiplier to impose this boundary term. However, they also introduced a new space for the Lagrange multiplier on the surface, which is not straightforward. The Lagrange multiplier method we propose requires no much effort to implement since it shares the same basis functions as the solution field, but it increases the computational cost. The Nitsche method, on the other hand, introduces no additional degrees of freedom, while maintains the flexibility of the Lagrange multiplier method, since it is also built into the weak formulation [102]. Nitsche's method has been widely used in discontinuous Galerkin method [103] and introduced also in continuous Galerkin to impose Dirichlet boundary condition in second-order or fourth-order problems [104], and embedded interface problems [105, 106].

In this chapter, the derivation of the Cahn–Hilliard equation is reviewed in order to introduce to the reader the problem as well as the essential boundary condition. The weak formulations, based on the Lagrange multiplier and the Nitsche method, are derived in Section 4.2 and Section 4.4, respectively. The representative examples are performed in Section 4.3 and Section 4.5. More applications of these two methods in the mechanically coupled problems are presented in the following chapters. In particular, in Chapter 5 and Chapter 6, the Lagrange multiplier method is employed; while in Chapter 7, the Nitsche method in combination with the finite cell method is used.

4.1 Derivation of Cahn–Hilliard equation from thermodynamics

The physical derivation of the Cahn–Hilliard equation from the thermodynamics has two main approaches. The traditional derivation is through a variational formulation, following Cahn and

Hilliard [31, 37, 43, 107]. Alternatively, Gurtin et al. [51, 108] asserted that a derivation from a microforce balance is physically more sound. The equivalence of these two will be discussed in Chapter 5. Since the emphasis of this section is to introduce the Cahn–Hilliard equation, only the classic derivation based on the variational approach is reviewed. We consider a binary solution system in the body $\tilde{\mathrm{B}}$, which has been normalized as B. For simplicity, the Cahn–Hilliard equation is derived with the quantities in their normalized form. The normalization and the necessary parameters are listed in Table 4.1 and Table 4.2.

Table 4.1. *Normalization of the Cahn–Hilliard equation.*

Physical quantities	Normalization
Length ($\tilde{\boldsymbol{x}}$)	$\boldsymbol{x} = \tilde{\boldsymbol{x}}/\mathrm{L}_0$
Time ($\tilde{t}$)	$t = \mathrm{D}\tilde{t}/\mathrm{L}_0^2$
Concentration ($\tilde{c}$)	$c = \tilde{c}/\mathrm{c}_{\mathrm{max}}$
Flux ($\tilde{\boldsymbol{j}}$)	$\boldsymbol{j} = \mathrm{L}_0\tilde{\boldsymbol{j}}/(\mathrm{D}\mathrm{c}_{\mathrm{max}})$
Free energy density ($\tilde{\psi}^c$)	$\psi^c = \tilde{\psi}^c/(\mathrm{R}\mathrm{T}\mathrm{c}_{\mathrm{max}})$
Chemical potential ($\tilde{\mu}$)	$\mu = \tilde{\mu}/(\mathrm{R}\mathrm{T})$

Table 4.2. *Parameters used in the Cahn–Hilliard equation.*

Gas constant (R)	$8.32\,\mathrm{J\,mol^{-1}\,K^{-1}}$
Absolute temperature (T)	$283\,\mathrm{K}$
Diffusivity (D)	$7.08\times10^{-15}\,\mathrm{m^2\,s^{-1}}$
Maximum concentration ($\mathrm{c}_{\mathrm{max}}$)	$2.29\times10^{4}\,\mathrm{mol\,m^{-3}}$
Length scale (L_0)	$1\,\mu\mathrm{m}$

The evolution of the non-uniform mole fraction (or normalized concentration) of one component c is given by

$$\frac{\partial c}{\partial t} = -\nabla\cdot\boldsymbol{j}, \tag{4.1}$$

where the flux $\boldsymbol{j}$ is defined as

$$\boldsymbol{j} = -M\nabla\mu. \tag{4.2}$$

Here, M represents a degenerated mobility in the limit of $c\to1$ and $c\to0$, and $M = c(1-c)$ is used in this chapter. The chemical potential, defined as the variational derivative of the total free energy with respect to the species concentration,

$$\delta\Psi = \int_{\mathrm{B}} \mu\delta c\,\mathrm{dV}, \quad \mu = \delta_c\Psi = \delta_c\int_{\mathrm{B}} \psi^c + \frac{1}{2}\kappa|\nabla c|^2\,\mathrm{dV}, \tag{4.3}$$

where bulk chemical energy density ψ^c prescribes a double-well function, allowing for the co-existance of two phases. The term containing $\boldsymbol{\nabla} c$ represents an energetic penalty for the phase interface. The parameter κ related to the interfacial thickness. In the limit of $\kappa \rightarrow 0$, the interfacial thickness goes to 0. Since the variation

$$\delta\Psi = \delta \int_{\mathrm{B}} \psi^c + \frac{1}{2}\kappa|\boldsymbol{\nabla} c|^2 \,\mathrm{dV} = \int_{\mathrm{B}} \left(\frac{\mathrm{d}\psi^c}{\mathrm{d}c} - \kappa\Delta c\right)\delta c \,\mathrm{dV} + \int_{\partial\mathrm{B}} \kappa\boldsymbol{\nabla} c\cdot\boldsymbol{n}\,\delta c\,\mathrm{dS}, \tag{4.4}$$

by comparing Eq. (4.3) and Eq. (4.4), we can obtain the chemical potential as

$$\mu = \frac{\mathrm{d}\psi^c}{\mathrm{d}c} - \kappa\Delta c \tag{4.5}$$

and the surface integration of Eq. (4.4) as zero. Due to the randomness of δc, an additional boundary condition of $\kappa\boldsymbol{\nabla} c\cdot\boldsymbol{n} = 0$ should be fulfilled on the entire boundary $\partial\mathrm{B}$. In this thesis, we consider a regular solution model, the details of which can be found in the book by Guggenheim [109]. The bulk chemical free energy ψ^c is given as

$$\psi^c = \mu_0 c + c\ln c + (1-c)\ln(1-c) + \chi c(1-c), \tag{4.6}$$

where μ_0 is a reference value of the chemical potential of the diffusing species, set as 0 in the simulation since it will not influence the diffusion behavior; The next two terms represent the entropic contribution to the system for an ideal mixture; the last term, the enthalpic contribution, favors a separation of the system towards $c = 0$ and $c = 1$. The positive interchange-energetic parameter χ indicates the convexity of the energy. In particular, as shown in Fig. 4.1(a), the phase separation will not happen when $\chi \leq 2$, but happens when $\chi > 2$, where ψ^c_{R} is non-convex. In this chapter, $\chi = 2.5$ is taken for the two-phase system. We can then calculate the spinodal points (c^s_α, c^s_β) by solving the equation

$$\frac{\partial^2\psi^c}{\partial c^2} = \frac{1}{c(1-c)} - 2\chi = 0, \tag{4.7}$$

and the binodal points (c_α, c_β) by common tangent construction

$$\psi^c|_{c=c_\alpha} - \psi^c|_{c=c_\beta} = \left.\frac{\partial\psi^c}{\partial c}\right|_{c=c_\alpha}\left(c_\alpha - c_\beta\right), \tag{4.8}$$

$$\left.\frac{\partial\psi^c}{\partial c}\right|_{c=c_\alpha} - \left.\frac{\partial\psi^c}{\partial c}\right|_{c=c_\beta} = 0. \tag{4.9}$$

In Fig. 4.1(b), the black dashed line denotes, for different values of parameter χ, the spinodal points where the phase separation starts; the solid line represents the binodal points, i.e.,

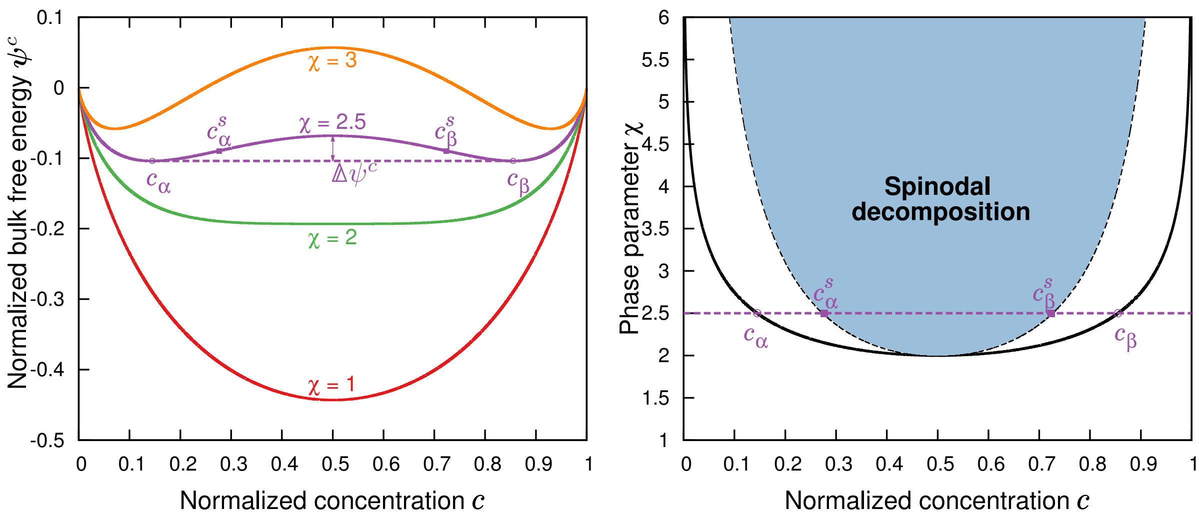

(a) (b)

FIGURE **4.1.** *(a) Normalized bulk free energy density* $\psi^c = c\ln c + (1-c)\ln(1-c) + \chi c(1-c)$ *and (b) the phase diagram with respect to the phase parameter* χ*.* c_α*,* c_β *are equilibrium concentrations;* c^s_α*,* c^s_β *are spinodals;* $\triangle\psi^c$ *is the difference between the specific free energy the free energy obtained as a mixture of the two equilibrium bulk phases, with* $\psi^c_{\max}$ *obtained at the middle concentration* $(c_\alpha + c_\beta)/2$.

the two respective equilibrium concentrations. The shaded area denotes an unstable region; here spinodal decomposition takes place, driving the system towards its corresponding equilibrium state. The interfacial properties can thus be analytically obtained through a variational study [31]. For a 1D problem, if the elastic influence is absent, we can obtain the interface thickness s as

$$s = \frac{\triangle c}{\tan\theta} = (c_\beta - c_\alpha)\sqrt{\frac{\kappa}{2\triangle\psi^c_{\max}}}, \tag{4.10}$$

where s is defined in Fig. 4.2. c_α, c_β and $\triangle\psi^c$ are shown in Fig. 4.1(a). The maximum value

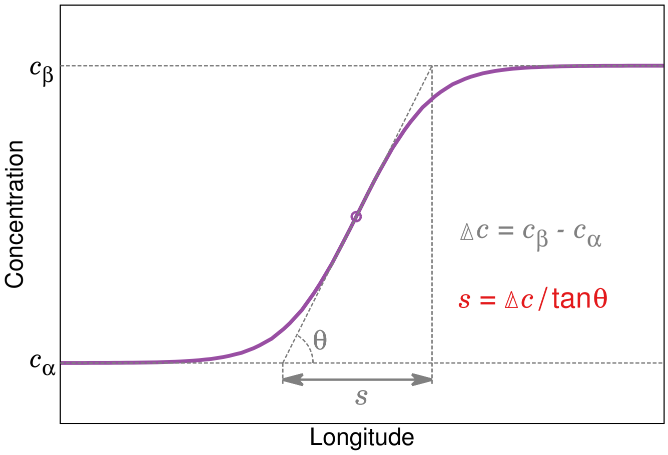

FIGURE **4.2.** *The definition of interface thickness for a 1D problem.*

$\Delta\psi^c_{\max}$ is $\Delta\psi^c$ computed at the middle concentration $(c_\alpha + c_\beta)/2$. The interfacial energy over the complete domain can be also obtained as

$$\Psi^i = \int_{-\infty}^{\infty} \psi^i \,\mathrm{d}x = \int_{-\infty}^{\infty} \frac{1}{2}\kappa\left(\frac{\partial c}{\partial x}\right)^2 \mathrm{d}x = \int_{c_\alpha}^{c_\beta} \sqrt{\frac{\kappa\Delta\psi^c}{2}}\,\mathrm{d}c. \tag{4.11}$$

We can see from Eq. (4.10) and Eq. (4.11) that, for a given bulk free energy density, the interface thickness is proportional to the square root of κ and the inverse of the maximum energy barrier $\Delta\psi^c_{\max}$; the interfacial energy is proportional to the square root of κ and the integrated square root of the energy barrier $\Delta\psi^c$, that is,

$$s \propto \sqrt{\frac{\kappa}{\Delta\psi^c_{\max}}}, \quad \Psi^i \propto \int_{c_\alpha}^{c_\beta} \sqrt{\kappa\Delta\psi^c}\,\mathrm{d}c. \tag{4.12}$$

It thus also holds that

$$\kappa \propto s\Psi^i, \quad \Delta\psi^c_{\max} \propto \frac{\Psi^i}{s}, \tag{4.13}$$

supposing

$$\sqrt{\Delta\psi^c_{\max}} \propto \int_{c_\alpha}^{c_\beta} \sqrt{\Delta\psi^c}\,\mathrm{d}c. \tag{4.14}$$

By Eq. (4.2), the corresponding flux $\boldsymbol{j}$ is then expressed as

$$\boldsymbol{j} = -\{[1-2\chi c(1-c)]\nabla c - c(1-c)\nabla(\kappa\Delta c)\}. \tag{4.15}$$

Finally, the Cahn–Hilliard equation is derived as

$$\frac{\partial c}{\partial t} = \nabla\cdot\{[1-2\chi c(1-c)]\nabla c - c(1-c)\nabla(\kappa\Delta c)\} \quad \text{in} \quad \mathrm{B}\times(0,\mathscr{T}). \tag{4.16}$$

The boundary conditions are summarized as

$$c = \hat{c} \qquad \text{on} \qquad \mathrm{S}_c\times(0,\mathscr{T}), \tag{4.17}$$

$$\{[1-2\chi c(1-c)]\nabla c - c(1-c)\nabla(\kappa\Delta c)\}\cdot\boldsymbol{n} = \hat{j} \qquad \text{on} \qquad \mathrm{S}_j\times(0,\mathscr{T}), \tag{4.18}$$

$$\kappa\nabla c\cdot\boldsymbol{n} = 0 \qquad \text{on} \qquad \partial\mathrm{B}\times(0,\mathscr{T}), \tag{4.19}$$

where S_c and S_j are two complimentary subsets of the complete boundary $\partial\mathrm{B}$. The constraint of Eq. (4.17) is built into the solution, and Eq. (4.18) can be directly satisfied in the weak formulation. Nevertheless, the additional essential boundary condition Eq. (4.19), which arises from the variational derivation in Eq. (4.4), does not fit in the weak formulation directly. Its physical interpretation is that the phase interface turns to be perpendicular to the boundary when it intersects with the latter. Only limited cases with special treatments are available if this boundary condition is to be enforced strongly ([70, 99, 100]). Therefore, we propose two methods to impose this boundary weakly: the Lagrange multiplier method and the Nitsche method.

Remark: To characterize different electrochemical properties of insertion materials, experiments are conducted under different conditions. These conditions need to be carefully treated in the simulation in order to reproduce the experimental results. To mimic galvanostatic charge/discharge, the Neumann boundary condition Eq. (4.18) is given on the electrode-electrolyte interface. The given flux $\hat{j}$ is computed from the relation $\hat{j} = \hat{\imath}/(z\mathrm{F})$, where $\hat{\imath}$ is the applied current, z the charge number of an inserted/extracted ion and F the Faraday constant. On the electrode-substrate interface, which is impermeable to the ions of active species, $\hat{j}$ in Eq. (4.18) is set to be zero. On the other hand, the Dirichlet boundary condition of Eq. (4.17) is often employed in simulations for potentiostatic charge/discharge process under the assumption that surface reaction is kinetically sufficiently fast that the equilibrium concentration of the active species is instantly reached on the surface and that lithium bulk diffusion governs the overall insertion/extraction rate (diffusion-limited dynamics). Alternatively, in Chapter 6 of this thesis, we propose a reaction-diffusion model, in which the lithium flux on the surface is governed by a modified Butler–Volmer equation, controlled by an applied electrostatic potential. In this approach, no assumptions of fast reaction is needed and numerical experiments can be carried out with different reaction-diffusion relations.

4.2 Variational formulation of Cahn–Hilliard equation with Lagrange multiplier

By the application of weighted residual and repeated integration by parts, we can derive the weak formulation of Eq. (4.16) as

$$\begin{aligned}
&\int_{\mathrm{B}} \frac{\partial c}{\partial t}\,\delta c\,\mathrm{dV} + \int_{\mathrm{B}} [1-2\chi c(1-c)]\,\boldsymbol{\nabla} c\cdot\boldsymbol{\nabla}\delta c\,\mathrm{dV} + \int_{\mathrm{B}} (1-2c)\,\kappa\Delta c\boldsymbol{\nabla} c\cdot\boldsymbol{\nabla}\delta c\,\mathrm{dV}\\
&+\int_{\mathrm{B}} c(1-c)\,\kappa\Delta c\,\Delta\delta c\,\mathrm{dV} - \int_{\partial\mathrm{B}} \{[1-2\chi c(1-c)]\,\boldsymbol{\nabla} c - c(1-c)\,\boldsymbol{\nabla}(\kappa\Delta c)\}\cdot\boldsymbol{n}\,\delta c\,\mathrm{dS}\\
&-\int_{\partial\mathrm{B}} \kappa c(1-c)\,\Delta c\,(\boldsymbol{\nabla}\delta c\cdot\boldsymbol{n})\,\mathrm{dS}\\
&=\delta\Pi - \int_{\partial\mathrm{B}} \{[1-2\chi c(1-c)]\,\boldsymbol{\nabla} c - c(1-c)\,\boldsymbol{\nabla}(\kappa\Delta c)\}\cdot\boldsymbol{n}\,\delta c\,\mathrm{dS}\\
&-\int_{\partial\mathrm{B}} \kappa c(1-c)\,\Delta c\,(\boldsymbol{\nabla}\delta c\cdot\boldsymbol{n})\,\mathrm{dS} = 0
\end{aligned} \tag{4.20}$$

where $\delta\Pi$ represents the volume integration of the weak form. As mentioned in the last section, the constraint of Eq. (4.17) is enforced strongly. The constraint of Eq. (4.18) is enforced by replacing the corresponding term in Eq. (4.20) directly. As for the boundary condition Eq. (4.19), a Lagrange multiplier is introduced in forming another functional $\bar{\Pi}$,

$$\bar{\Pi} = \Pi + \int_{\partial \mathrm{B}} \lambda \boldsymbol{\nabla} c \cdot \boldsymbol{n} \, \mathrm{dS} - \int_{\mathrm{B}} \frac{1}{2\alpha} \lambda^2 \, \mathrm{dV}, \tag{4.21}$$

so that

$$\delta \bar{\Pi} = \delta \Pi + \delta \int_{\partial \mathrm{B}} \lambda \boldsymbol{\nabla} c \cdot \boldsymbol{n} \, \mathrm{dS} - \delta \int_{\mathrm{B}} \frac{1}{2\alpha} \lambda^2 \, \mathrm{dV} = \int_{\mathrm{S}_j} \hat{j} \delta c \, \mathrm{dS}. \tag{4.22}$$

In Eq. (4.22), the second term is the weakly imposed constraint using the Lagrange multiplier λ. The term involving λ^2 is a perturbation to avoid numerical singularity, in which a proper choice of the parameter α is important for a good convergence of the computation. For more details, one can refer to the book of Zienkiewicz et al. [110]. By comparing Eq. (4.22) and Eq. (4.20), we identify the Lagrange multiplier λ as

$$\lambda = -c\,(1-c)\,\kappa \Delta c. \tag{4.23}$$

In the work of Anders et al. [101], the Lagrange multiplier was interpolated by standard Lagrangian linear basis functions on the surface, where a new set of function space was introduced. In this work, the Lagrange multiplier space is the same as that of the other solution fields. Since this higher-order Lagrange multiplier space on the surface can lead to over-constrained systems, we use the divergence theorem to transfer the surface integration into a volume integral:

$$\delta \bar{\Pi} = \delta \Pi + \delta \int_{\mathrm{B}} \mathrm{Div}(\lambda \boldsymbol{\nabla} c) \, \mathrm{dV} - \delta \int_{\mathrm{B}} \frac{1}{2\alpha} \lambda^2 \, \mathrm{dV}. \tag{4.24}$$

This approach is not only convenient to be implemented—as it introduces no new space for the Lagrange multiplier—but also computationally robust.

4.3 Numerical examples of the Lagrange multiplier method

As a benchmark test of the uncoupled Cahn–Hilliard equation, A bar with the dimensions 2 × 2 × 10, shown in the Fig. 4.3, is considered. The flux is given at one end, while on the four sides, as well as at the bottom, a flux-free boundary condition is defined. This flux is applied for a period of time; after its removal the system will evolve to the equilibrium state, as shown in Fig. 4.4. A two-phase system with a diffuse interface is formed. The energy

$$\psi = \psi^c + \psi^i = c \ln c + (1-c)\ln(1-c) + 2.5c(1-c) + \frac{1}{2}\kappa |\boldsymbol{\nabla} c|^2 \tag{4.25}$$

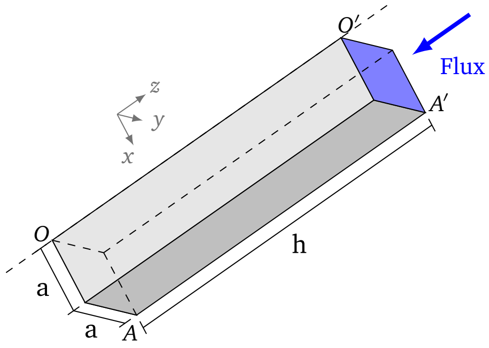

Flux $(\hat{j})$	0.064
Measurements $(a \times a \times h)$	$1 \times 1 \times 10$
Initial conc. (c_0)	0.25
Phase para. (χ)	2.5
Interface para. (κ)	0.04247

FIGURE 4.3. *Geometry and parameters of the bar under incoming flux at one end. Due to symmetry, only one quarter of the bar is modeled.* $\overline{OO'}$ *is the center line of the bar. All other parameters are given in Table 4.2.*

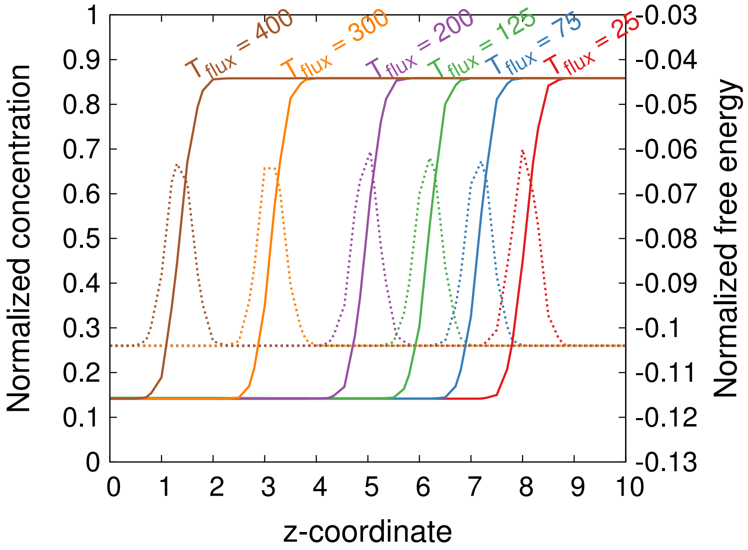

FIGURE 4.4. *The moving interface due to different amount of incoming flux. The distribution of concentration is plotted with solid line, while the energy* $\psi = \psi^c + \psi^i$ *is plotted with dashed line.*

peaks at the center of the interface. The normal gradient $\nabla c \cdot \boldsymbol{n}$ at the $O'A'$ end with respect to time is plotted in Fig. 4.5. The time applied in this problem is 5 normalized seconds. If the Lagrange multiplier is not used, this term fluctuates strongly even after the removal of the flux; however, the constraint is well fulfilled with the Lagrange multiplier ansatz. As we can see from this figure, when $\alpha > 10^6$, there is a satisfactory convergence. As a reference, the mixed formulation based on Miehe's approach [96] has also been implemented, where the chemical potential μ is introduced as an independent variable, and Eq. (4.16) is divided into two second-order partial differential equations

$$\frac{\partial c}{\partial t} = \nabla \cdot [c\,(1-c)\,\nabla \mu], \tag{4.26}$$

$$\mu = \ln c - \ln(1-c) + \chi\,(1-2c). \tag{4.27}$$

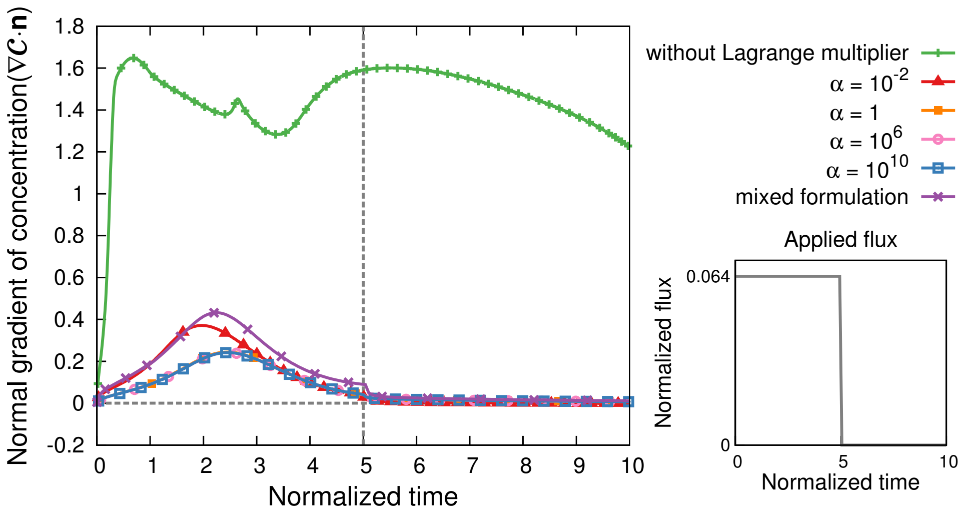

FIGURE 4.5. *Normal gradient of the concentration at the end of a bar under flux boundary condition. Constant flux is given for 5 normalized seconds and then removed, as shown in the small plot.*

From Fig. 4.5 we can see that a similar tendency between the Lagrange multiplier method and the mixed formulation is observed.

To check the interfacial thickness, the flux is applied for 200 normalized seconds and removed. As mentioned in Eq. (4.10), the interface thickness for a standard 1D problem is $s = (c_\beta - c_\alpha)\sqrt{\kappa/(2\triangle\psi^c)}$. For a 3D problem, the magnitude of $\mathbf{s}$ is defined in a similar way, with $\mathbf{s}$ being a vector parallel to ∇c. In the bar under consideration, it lies parallel to the z direction.

For ψ expressed as Eq. (4.25), we can obtain $c_\alpha = 0.1448$, $c_\beta = 0.8552$ and $\triangle\psi^c = 0.03585$ from common tangent construction. Substituting them into Eq. (4.10), we can plot $|\mathbf{s}|$ with different interface parameters κ, as shown in Fig. 4.6(b). The corresponding numerical results in equilibrium are also shown in Fig. 4.6(a,b). It can be seen that the simulation results have good agreement with the analytical predictions. However, one may notice from Fig. 4.6(b) that there is a deviation of the numerically measured interface thickness from the analytically predicted one when κ becomes very large (e.g. $\kappa = 3.3977$). The reason is that, as shown in Eq. (4.10), the interface thickness is influenced by two parts: the difference of the two equilibrium concentrations ($\triangle c$), and the slope of the tangent line at the interface center point ($\tan\theta$). In the analytical prediction, the bar is supposedly infinitely long; therefore $\triangle c$ will remain unchanged for a given bulk chemical free energy, and the slope, which is proportional to $\sqrt{\kappa}$, is the only contribution to different interface thicknesses. However, in the simulation, since the length of the bar is limited (10), apart from the slope, $\triangle c$ can also change with κ—when the interface evolves onto the surface, the interaction between the surface boundary condition $\nabla c \cdot \boldsymbol{n} = 0$ and the interface gradient will result in a smaller $\triangle c$. As a consequence, the interface thickness measured in the simulation will be smaller than that in the analytical solution. It is hence reasonable to predict that, when κ is further increased or the length of the bar is reduced,

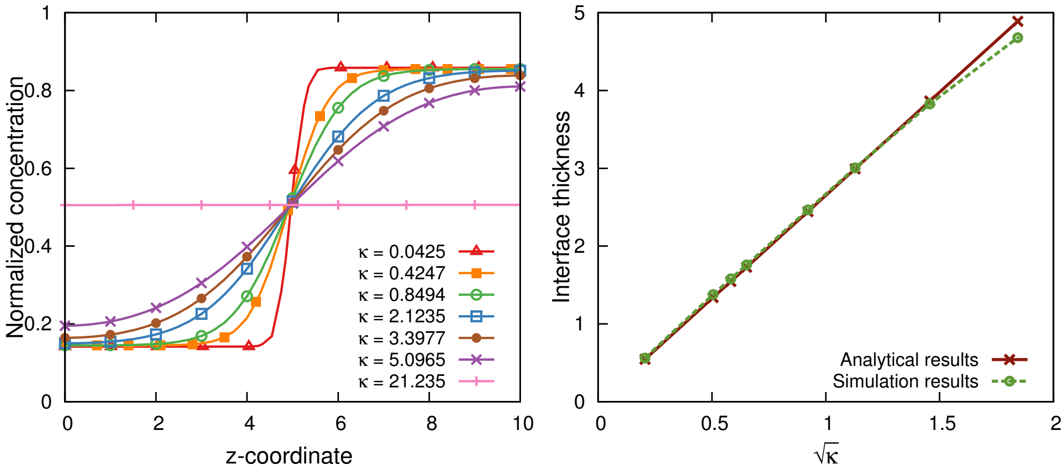

(a) (b)

Figure 4.6. *The dependence of the interface thickness on κ in the decoupled Cahn–Hilliard problem. In (a) the simulation results of the equilibrium concentration profile show that a larger κ results in a more diffusive interface, or even a suppression of the phase separation. (b) shows the consistency of the simulation results with the analytical predictions, and that both show a linear relationship $|\mathbf{s}| \propto \sqrt{\kappa}$, as long as κ is not too large.*

the two phases can merge into one phase, and the phase separation is suppressed due to this "surface effect". The suppression has been actually observed in the simulation, as shown in Fig. 4.6(a) when $\kappa = 21.235$.

4.4 Variational formulation of Cahn–Hilliard equation with Nitsche's method

While the Lagrange multiplier method is very easy to implement and shows promising applications in small problems, additional computational cost is not affordable when the problem becomes large. Therefore in this section we introduce another method based on Nitsche's method [102], which will not introduce any additional degrees of freedom yet variationally consistent.

4.4.1 Dirichlet and Neumann boundary conditions

Based on Nitsche's method, the weak formulation of Eqs. (4.16)–(4.19) is expressed as

$$\begin{aligned}
&\int_{B} \frac{\partial c}{\partial t}\,\delta c\,\mathrm{d}V + \int_{B} \left[1-2\chi c\,(1-c)\right] \nabla c\cdot\nabla\delta c\,\mathrm{d}V + \int_{B} (1-2c)\,\kappa\Delta c\nabla c\cdot\nabla\delta c\,\mathrm{d}V \\
&+ \int_{B} c\,(1-c)\,\kappa\Delta c\,\Delta\delta c\,\mathrm{d}V - \int_{S_c} \left\{\left[1-2\chi c\,(1-c)\right]\nabla c - c\,(1-c)\,\nabla\left(\kappa\Delta c\right)\right\}\cdot\boldsymbol{n}\,\delta c\,\mathrm{d}S \\
&- \int_{S_c} c\,\nabla\left(\kappa\Delta\delta c\right)\cdot\boldsymbol{n}\,\mathrm{d}S + \alpha_1 \int_{S_c} c\delta c\,\mathrm{d}S - \int_{\partial B} \kappa c\,(1-c)\,\Delta c\,\left(\nabla\delta c\cdot\boldsymbol{n}\right)\,\mathrm{d}S
\end{aligned}$$

$$
\begin{aligned}
&-\int_{\partial \mathrm{B}} \kappa c\,(1-c)\,(\boldsymbol{\nabla} c\cdot \boldsymbol{n})\;\Delta\delta c\,\mathrm{d}S+\alpha_2\int_{\partial \mathrm{B}}(\boldsymbol{\nabla} c\cdot \boldsymbol{n})\,(\boldsymbol{\nabla}\delta c\cdot \boldsymbol{n})\,\mathrm{d}S\\
&=\int_{\mathrm{S}_j} j\delta c\,\mathrm{d}S-\int_{\mathrm{S}_c}\hat{c}\,\boldsymbol{\nabla}(\kappa\Delta\delta c)\cdot \boldsymbol{n}\,\mathrm{d}S+\alpha_1\int_{\mathrm{S}_c}\hat{c}\,\delta c\,\mathrm{d}S. \qquad (4.28)
\end{aligned}
$$

The spaces spanned by the basis functions for approximation and weighting are the spaces of square integrable functions with square integrable first and second derivatives. The stabilization parameters α_1 and α_2 need to be chosen large enough in order to guarantee stability of Eq. (4.28). The terms defined on the Dirichlet boundary S_c and associated stabilization with α_1 weakly enforce a given concentration $\hat{c}$. The terms defined on the complete domain boundary $\partial\mathrm{B}$ and associated stabilization with α_2 weakly enforce that the normal derivative is zero. Comparing Eq. (4.22) and Eq. (4.28), one can observe that, the constraint of Nitsche's method is actually by replacing the Lagrange multiplier with the identified quantity in Eq. (4.23).

To show the consistency of the variational form Eq. (4.28) with the strong form of the boundary value problem Eqs. (4.16)–(4.19), we apply repeated integration by parts to Eq. (4.28). This results in

$$
\begin{aligned}
&\int_{\mathrm{B}}\frac{\partial c}{\partial t}\delta c\,\mathrm{d}V-\int_{\mathrm{B}}\boldsymbol{\nabla}\cdot\{[1-2\chi c\,(1-c)]\,\boldsymbol{\nabla} c-c\,(1-c)\,\boldsymbol{\nabla}(\kappa\Delta c)\}\,\delta c\,\mathrm{d}V\\
&+\int_{\mathrm{S}_j}(\{[1-2\chi c\,(1-c)]\,\boldsymbol{\nabla} c-c\,(1-c)\,\boldsymbol{\nabla}(\kappa\Delta c)\}\cdot\boldsymbol{n}-j)\,\delta c\,\mathrm{d}S\\
&-\int_{\mathrm{S}_c}(c-\hat{c})\,\boldsymbol{\nabla}(\kappa\Delta\delta c)\cdot\boldsymbol{n}\,\mathrm{d}S+\alpha_1\int_{\mathrm{S}_c}(c-\hat{c})\;\delta c\,\mathrm{d}S\\
&-\int_{\partial\mathrm{B}}\kappa c\,(1-c)\,(\boldsymbol{\nabla} c\cdot\boldsymbol{n})\,\Delta\delta c\,\mathrm{d}S+\alpha_2\int_{\partial\mathrm{B}}(\boldsymbol{\nabla} c\cdot\boldsymbol{n})(\boldsymbol{\nabla}\delta c\cdot\boldsymbol{n})\;\mathrm{d}S=0, \qquad (4.29)
\end{aligned}
$$

which will give us the equations Eqs. (4.16)–(4.19).

4.4.2 Periodic boundary condition

A typical simulation of Cahn–Hilliard equation is the evolution of concentration field from a random initial state under periodic boundary conditions. Let S^- and S^+ denote the entry and exit boundary of a periodic box B, which satisfies $\mathrm{S}^-\cup\mathrm{S}^+=\partial\mathrm{B}$ and $\mathrm{S}^-\cap\mathrm{S}^+=\emptyset$. $\boldsymbol{x}^-\in\mathrm{S}^-$ and $\boldsymbol{x}^+\in\mathrm{S}^+$ are two matching points with constituents $(\cdot)^-$ and $(\cdot)^+$, respectively. We note that we will use the condition

$$
\int_{\mathrm{S}^-}(\cdot)\,\mathrm{d}S=\int_{\mathrm{S}^+}(\cdot)\,\mathrm{d}S, \qquad (4.30)
$$

assuming that S^- and S^+ are geometrically symmetric.

We define the jump operator $[\![\cdot]\!]$ as

$$[\![a]\!] = a^- - a^+, \qquad a \in \mathrm{R}, \tag{4.31}$$

$$[\![\boldsymbol{a}]\!] = \boldsymbol{a}^- \cdot \boldsymbol{n}^- + \boldsymbol{a}^+ \cdot \boldsymbol{n}^+, \qquad \boldsymbol{a} \in \mathrm{R}^d, d = 2,3, \tag{4.32}$$

and the average operator $\langle \cdot \rangle$ as

$$\langle a \rangle = \frac{1}{2}\left(a^- + a^+\right), \qquad a \in \mathrm{R}, \tag{4.33}$$

$$\langle \boldsymbol{a} \rangle = \frac{1}{2}\left(\boldsymbol{a}^- \cdot \boldsymbol{n}^- - \boldsymbol{a}^+ \cdot \boldsymbol{n}^+\right), \qquad \boldsymbol{a} \in \mathrm{R}^d, d = 2,3. \tag{4.34}$$

The general set of boundary conditions Eqs. (4.17)–(4.19) can then be specified to the following set of periodic boundary conditions in strong form:

$$c^- - c^+ = [\![c]\!] = 0, \tag{4.35}$$

$$\boldsymbol{\nabla} c^- \cdot \boldsymbol{n}^- + \boldsymbol{\nabla} c^+ \cdot \boldsymbol{n}^+ = [\![\boldsymbol{\nabla} c]\!] = 0, \tag{4.36}$$

$$\kappa \Delta c^- - \kappa \Delta c^+ = [\![\kappa \Delta c]\!] = 0, \tag{4.37}$$

$$\boldsymbol{j}^- \cdot \boldsymbol{n}^- + \boldsymbol{j}^+ \cdot \boldsymbol{n}^+ = [\![\boldsymbol{j}]\!] = 0 \tag{4.38}$$

where $\boldsymbol{j}$ is given in Eq. (4.15). The boundary condition Eq. (4.35) is imposed strongly by setting two matching control values on the corresponding boundaries equal. Further, in analogy to Eq. (4.28), the boundary condition of Eqs. (4.36)–(4.38) are imposed weakly using the Nitsche method. The corresponding variational statement reads

$$\begin{aligned}
&\int_{\mathrm{B}} \frac{\partial c}{\partial t} \delta c \, \mathrm{dV} + \int_{\mathrm{B}} [1 - 2\chi c(1-c)] \boldsymbol{\nabla} c \cdot \boldsymbol{\nabla} \delta c \, \mathrm{dV} + \int_{\mathrm{B}} (1-2c) \kappa \Delta c \boldsymbol{\nabla} c \cdot \boldsymbol{\nabla} \delta c \, \mathrm{dV} \\
&+ \int_{\mathrm{B}} c(1-c) \kappa \Delta c \Delta \delta c \, \mathrm{dV} - \int_{\mathrm{S}^-} c(1-c) \langle \kappa \Delta c \rangle \, [\![\boldsymbol{\nabla} \delta c]\!] \, \mathrm{dS} \\
&- \int_{\mathrm{S}^-} c(1-c) [\![\boldsymbol{\nabla} c]\!] \, \langle \kappa \Delta \delta c \rangle \, \mathrm{dS} + \alpha_2 \int_{\mathrm{S}^-} [\![\boldsymbol{\nabla} c]\!] \, [\![\boldsymbol{\nabla} \delta c]\!] \, \mathrm{dS} = 0,
\end{aligned} \tag{4.39}$$

We again can show consistency with respect to the strong form Eq. (4.16) and Eqs. (4.35)–(4.38) by repeatedly applying integration by parts on Eq. (4.39), which leads to

$$\begin{aligned}
&\int_{\mathrm{B}} \frac{\partial c}{\partial t} \delta c \, \mathrm{dV} - \int_{\mathrm{B}} \boldsymbol{\nabla} \cdot \{[1 - 2\chi c(1-c)] \boldsymbol{\nabla} c - \kappa c(1-c) \boldsymbol{\nabla} \Delta c\} \, \delta c \, \mathrm{dV} \\
&- \int_{\mathrm{S}^-} [\![\boldsymbol{j}]\!] \, \delta c \, \mathrm{dS} + \int_{\mathrm{S}^-} c(1-c) [\![\kappa \Delta c]\!] \, \langle \boldsymbol{\nabla} \delta c \rangle \, \mathrm{dS} - \int_{\mathrm{S}^-} c(1-c) [\![\boldsymbol{\nabla} c]\!] \, \langle \kappa \Delta \delta c \rangle \, \mathrm{dS} \\
&+ \alpha_2 \int_{\mathrm{S}^-} [\![\boldsymbol{\nabla} c]\!] [\![\boldsymbol{\nabla} \delta c]\!] \, \mathrm{dS} = 0.
\end{aligned} \tag{4.40}$$

Making again use of the argument that Eq. (4.40) must hold for arbitrary weighting functions δc, we can identify the strong form of the boundary value problem Eq. (4.16) and the periodic boundary conditions Eqs. (4.36)–(4.38).

4.5 Numerical examples of Nitsche's method

4.5.1 Two coexisting phases with a flat interface—1D simulation

As a first example, we consider a bar with a lenghth L= 10. The initial conditions are set as

$$c(x,0) = \begin{cases} 0.2 & 0 \le x \le 5 \\ 0.8 & 5 < x \le 10, \end{cases} \tag{4.41}$$

and flux-free boundary conditions are given as

$$[1-2\chi c(1-c)]\frac{\partial c}{\partial x} - c(1-c)\kappa\frac{\partial^3 c}{\partial x^3} = 0, \qquad x = 0,\, \mathrm{L}, \quad t \in (0, \mathscr{T}), \tag{4.42}$$

$$\kappa\frac{\partial c}{\partial x} = 0, \qquad x = 0,\, \mathrm{L}, \quad t \in (0, \mathscr{T}). \tag{4.43}$$

In the simulation, $\chi = 2.5$, which indicates two homogeneous phases are $c_\alpha = 0.1448$ and $c_\beta = 0.8552$ in equilibrium. The interfacial parameter $\kappa = 0.01$.

For a first impression, we compute the solution of the Cahn–Hilliard equation with weakly imposed boundary conditions on 100 cubic B-spline elements with element size $h_e = 0.1$. Fig. 4.7 plots the corresponding concentration c and the free energy density ψ in equilibrium ($t \sim 10^{13}$), the latter being computed as

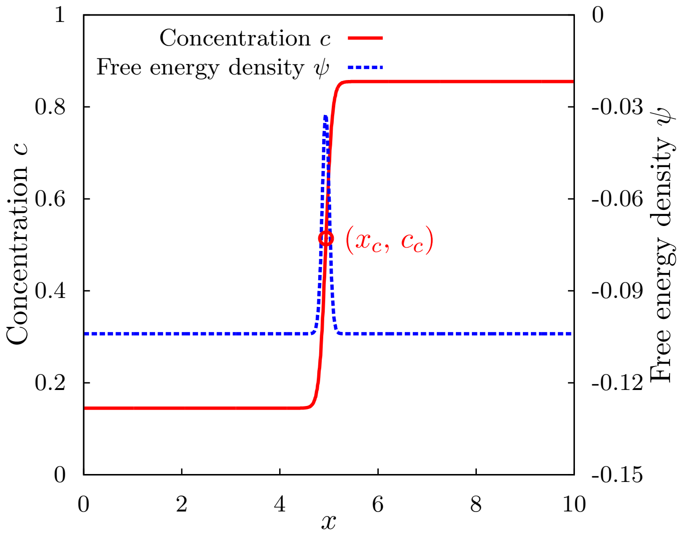

FIGURE 4.7. *The numerical solution of the distribution of the concentration c and the free energy ψ in equilibrium ($t \sim 1 \times 10^{13}$). The analytical solution for the two phases are $c_\alpha = 0.1448$ and $c_\beta = 0.8552$. The free energy ψ equals -0.1040 within homogeneous phases and peaks with the value -0.03229 when $c = c_c = 0.5$ in the middle of the interface. All numerical results agree well with the analytical results.*

$$\psi = \psi^c + \psi^i = c\ln c + (1-c)\ln(1-c) + 2.5\,c(1-c) + 5 \times 10^{-3}\left|\frac{\partial c}{\partial x}\right|^2. \tag{4.44}$$

There are two phases and a diffuse interface, with the energetic peak in the middle, where the largest concentration gradient occurs. The free energy ψ equals -0.1040 within homogeneous phases and peaks with the value -0.03229 when $c = c_c = 0.5$. All those values have been reproduced by the simulation.

In the next step, we perform a more rigorous convergence study. We know that in equilibrium, the exact chemical potential $\mu_{\text{ex}} = 0$ holds everywhere in the field, while there is no analytical solution for c. We therefore base our study on the chemical potential

$$\mu = \ln c - \ln(1-c) + 2.5\,(1-2c) - 1\times 10^{-2}\frac{\partial^2 c}{\partial x^2} \tag{4.45}$$

instead of the concentration c. Since this example does not involve a Dirichlet boundary condition, we only use the stabilization parameter α_2. Following the work of Wells et al. [97], the penalty parameter α_2 is taken as $5/h_e$, where h_e is the size of the element.

Table 4.3 and Fig. 4.8 show the convergence of the error in the L_2 norm, computed for μ.

Table 4.3. *Evolution of error* $\left[\int_0^L (\mu_{\text{FEM}} - \mu_{\text{ex}})^2 \,\mathrm{d}x\right]^{\frac{1}{2}}$.

$1/h_e$	Quadratics	Cubics	Quatics
10	$7.3845721536 \times 10^{-3}$	$1.5582188728 \times 10^{-3}$	$3.7061461505 \times 10^{-4}$
20	$1.4062186408 \times 10^{-3}$	$6.2066527184 \times 10^{-5}$	$1.7353482112 \times 10^{-5}$
40	$2.5452237937 \times 10^{-4}$	$2.5201024011 \times 10^{-6}$	$6.3594095903 \times 10^{-7}$
80	$4.5261342896 \times 10^{-5}$	$1.0874341541 \times 10^{-7}$	$2.6685542218 \times 10^{-8}$
160	$8.0130442296 \times 10^{-6}$	$4.7848784864 \times 10^{-9}$	$1.2567716120 \times 10^{-9}$

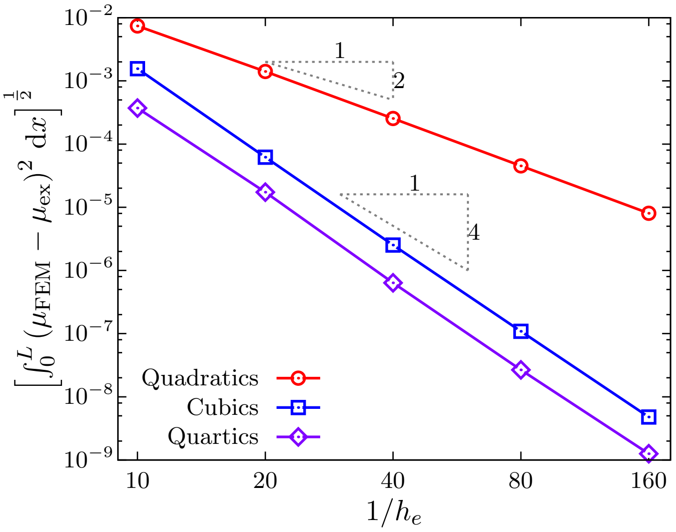

Figure 4.8. *Plot of the convergence of* $\left[\int_0^L (\mu_{\text{FEM}} - \mu_{\text{ex}})^2 \,\mathrm{d}x\right]^{\frac{1}{2}}$.

One can observe that for quadratic and quartic B-splines, the optimal convergence rate of two and four are achieved, respectively. For cubic basis functions, a superconvergent rate of four is achieved. This can be explained as follows: Inspection of the free energy ψ (Eq. (4.44)) indicates that, the distribution of c follows a sigmoid shape, which possesses rotational symmetry with respect to the middle point of the interface (x_c, c_c) by an angle of 180° (Fig. 4.7). This means, in the vicinity of (x_c, c_c), only odd power terms are non-zero in the Taylor expansion of the expression for c

$$c(x) = c(x_c) + \sum_{n=1,3,\ldots} A_n(x - x_c)^n = c_c + \sum_{n=1,3,\ldots} A_n(x - x_c)^n, \tag{4.46}$$

with A_n being the coefficients of the n-th term. Since μ is a function of c and $\mathrm{d}^2c/\mathrm{d}x^2$, the monomial components of the polynomial basis functions that have even power must have coefficients of zero and therefore do not contribute to the accuracy for μ in equilibrium. Therefore, odd degree cubics achieve the same accuracy as quartics in this special case.

We also consider a second scenario, where one of the flux boundary conditions is replaced by a corresponding Dirichlet boundary condition. The new set reads

$$c = 1.0, \qquad x = 0, \quad t \in (0, \mathscr{T}), \tag{4.47}$$

$$[1 - 2\chi c(1 - c)]\frac{\partial c}{\partial x} - c(1 - c)\kappa\frac{\partial^3 c}{\partial x^3} = 0, \qquad x = \mathrm{L}, \quad t \in (0, \mathscr{T}), \tag{4.48}$$

$$\kappa\frac{\partial c}{\partial x} = 0, \qquad x = 0,\, \mathrm{L}, \quad t \in (0, \mathscr{T}). \tag{4.49}$$

The initial condition is homogeneous distribution of concentration

$$c(x, 0) = 0.1, \quad x \in [0, \mathrm{L}]. \tag{4.50}$$

We enforce both conditions Eqs. (4.47) and (4.49) weakly, which involves two stabilization term. Following Ember et al. [104], we assume a stabilization parameter $\alpha_1 = 5000/h_e$, three orders of magnitude larger than α_2 in the simulation. Since the fixed concentration 1.0 at $x = 0$ is larger than the equilibrium concentrations $c_\alpha = 0.1448$ and $c_\beta = 0.8552$, it triggers a continuous influx until the overall domain reaches a homogeneous concentration of $c = 1.0$. Fig. 4.9 shows the concentration evolution in the bar. 500 cubic line elements are used for the simulation, $\alpha_1 = 2.5 \times 10^5$ and $\alpha_2 = 250$. We observe that the Dirichlet boundary condition is satisfied at all times.

4.5.2 Spinodal decomposition—2D simulation

In the second example, we consider spinodal decomposition on a unit square from a random distributed initial concentration field. We assume parameters are $\chi = 2.5$ and $\kappa = 1.42 \times 10^{-4}$, which leads to a characteristic interfacial thickness of 0.0316. The initial concentration is

$$c(\boldsymbol{x}, 0) = \bar{c} + r \tag{4.51}$$

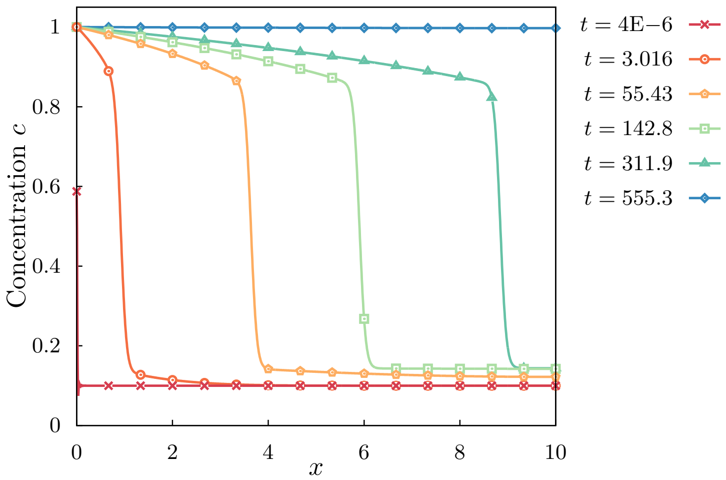

FIGURE 4.9. *The evolution of the concentration profile when a Dirichlet boundary condition* $x = 0$ *and zero first derivatives at both ends, all weakly enforced.*

where $\bar{c} = 0.63$ and r is a random variable with uniform distribution in the range $[-0.05, 0.05]$.

In a first step, we examine the evolution under a natural boundary condition. In this case, the flux and the normal gradient of concentration on all boundaries are zero, the latter being enforce by Nitsche's method. Fig. 4.10 shows the evolution of concentration field at different

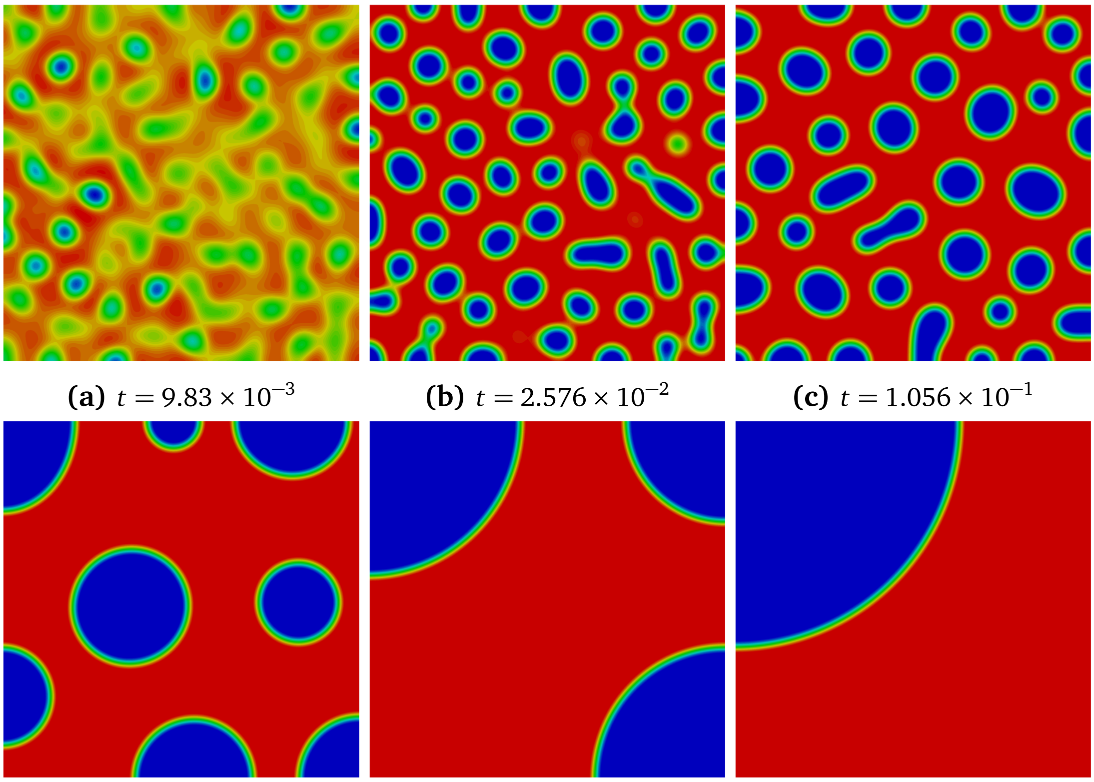

(a) $t = 9.83 \times 10^{-3}$ **(b)** $t = 2.576 \times 10^{-2}$ **(c)** $t = 1.056 \times 10^{-1}$

(d) $t = 5.57$ **(e)** $t = 62.01$ **(f)** *Equilibrium*

FIGURE 4.10. *Spinodal decomposition under natural boundary conditions. Due to the weakly enforced condition of zero normal gradient, all phase interfaces remain perpendicular to the border, when they intersect with the border.*

times, computed with 128×128 cubic B-spline elements. It is observed that phase interfaces are always perpendicular to the boundary when they intersect with the boundary. This indicates that the weakly enforced condition of zero normal gradient is accurately satisfied on the complete boundary.

As a second step, we simulated the evolution of the random field under weakly enforced periodic boundary conditions Eqs. (4.36)–(4.38). The constraint of Eq. (4.35) is imposed strongly by making the corresponding two control points on the edge coincide. We assume $\alpha_2 = 5.0/h_e$. Fig. 4.11 plots simulation results at different time instances, computed again with 128 × 128 cubic B-spline elements. In the simulation, the open knot vectors are used to build up the basis functions, unlike the treatment by Gomez et al. [70], which employed the periodic B-Splines to impose periodicity. The simulation results in Fig. 4.11 agree well with the results in [70]. We observe that phase interfaces now continue smoothly from one boundary to the opposite boundary. The final equilibrium state is complete circle. This is different from the previous case, where only one quarter of the complete sphere is reached at the equilibrium, and where it is energetically more favorable. This can be observed by computing the final energy. For both simulations, a monotonic decrease of the total free energy

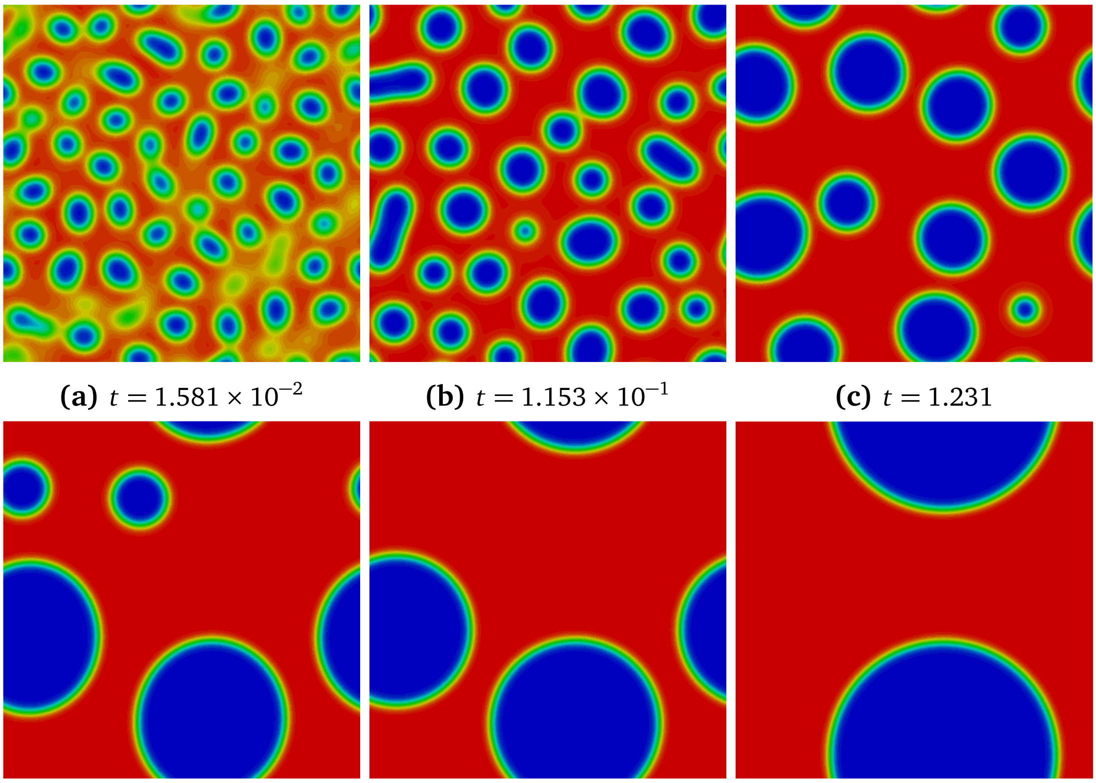
(a) $t = 1.581 \times 10^{-2}$ **(b)** $t = 1.153 \times 10^{-1}$ **(c)** $t = 1.231$

(d) $t = 10.28$ **(e)** $t = 20.41$ **(f)** *Equilibrium*

FIGURE **4.11.** *Spinodal decomposition under periodic boundary condition. The phase interfaces are not perpendicular but continued to the other side of the border when they are intersect with the box frame.*

$$\Psi = \int_B \psi \, \mathrm{dV} = \int_B \left[c \ln c + (1-c)\ln(1-c) + 2.5\, c\,(1-c) + 7.1 \times 10^{-5}\, |\nabla c|^2 \right] \mathrm{dV} \tag{4.52}$$

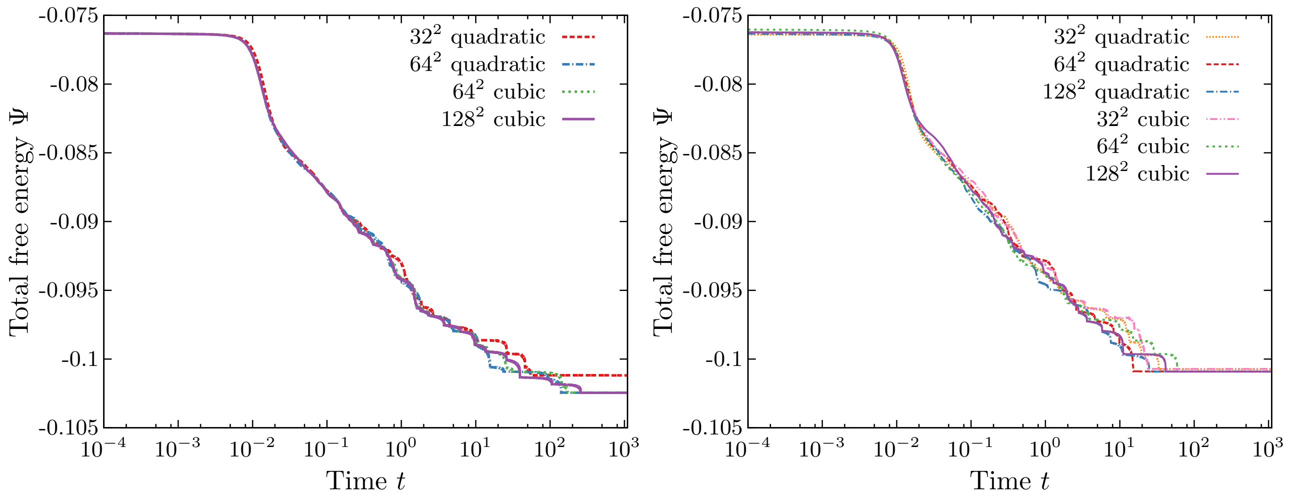

(a) *Evolution of Ψ under natural boundary condition.* **(b)** *Evolution of Ψ under periodic boundary condition.*

FIGURE 4.12. *Evolution of the total free energy Ψ with different quadratic and cubic elements under (a) natural and (b) periodic boundary conditions. Both simulations show that Ψ is monotonically decreasing, and the final energy under natural boundary conditions is lower than that under periodic boundary conditions.*

with time is observed. Moreover, the final total energy of the species under natural boundary conditions (Fig. 4.12(a)) is lower than that under periodic boundary conditions (Fig. 4.12(b)).

4.5.3 Spheroidal particles with incoming flux—3D simulation

As the third example, 3D spheroids with different aspect ratios are considered. Due to symmetry, only an octant of the whole spheroid is simulated. Homogeneous flux is applied on the surface for 2 normalized second and is removed afterwards. After removal of the flux, the species in the particle evolve towards equilibrium. All simulation parameters are listed in Table 4.4. For the simulation, quadratic NURBS shape functions are used. The IGA meshes of these three particles are shown in Fig. 4.13. With the examples in this section, we would like to demonstrate the ability of our method on constraining the boundary condition $\boldsymbol{\nabla} c \cdot \boldsymbol{n} = 0$, when the boundary is perturbed by an incoming flux.

TABLE 4.4. *Simulation parameters for the 3D spheroids*

Geometry	Sphere	Prolate	Oblate
Semi-axes (x, y, z)	(1, 1, 1)	(3/2, $\sqrt{2/3}$, $\sqrt{2/3}$)	(2/3, $\sqrt{3/2}$, $\sqrt{3/2}$)
Phase parameter χ	2.5		
Interface parameter κ	4.25×10^{-3}		
Flux per area $\hat{j}$	-0.1		
Time flux applied $\mathrm{T}_{\mathrm{flux}}$	2		
Initial concentration c_0	0.25		

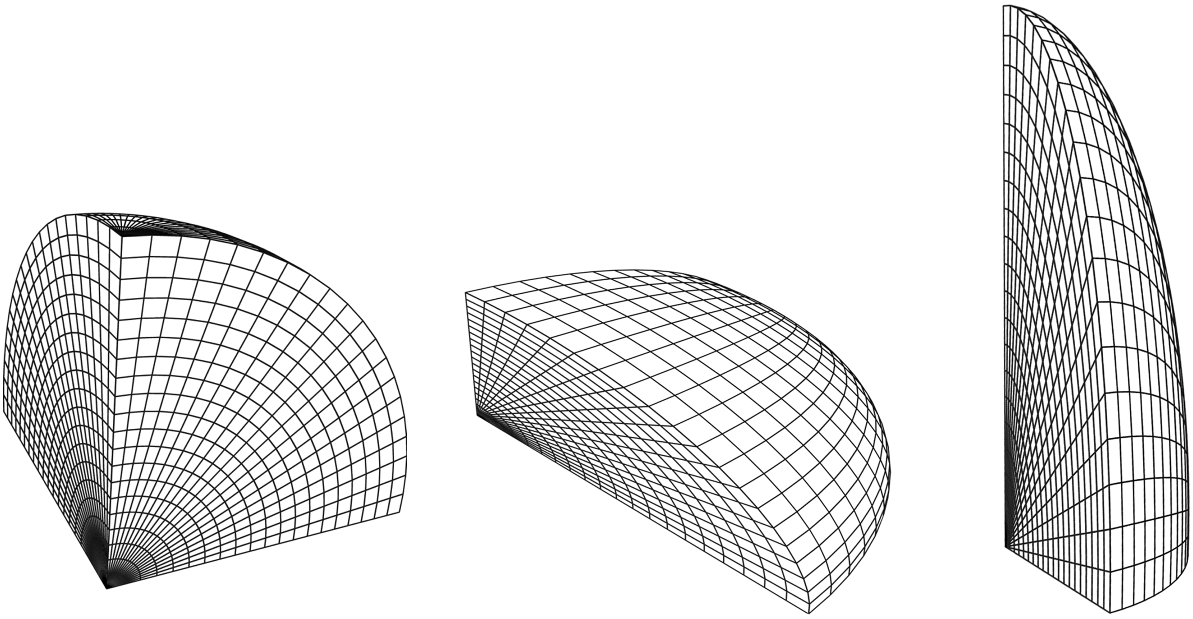

FIGURE 4.13. *The IGA meshes of the spherical and spheroidal particles in the simulation.*

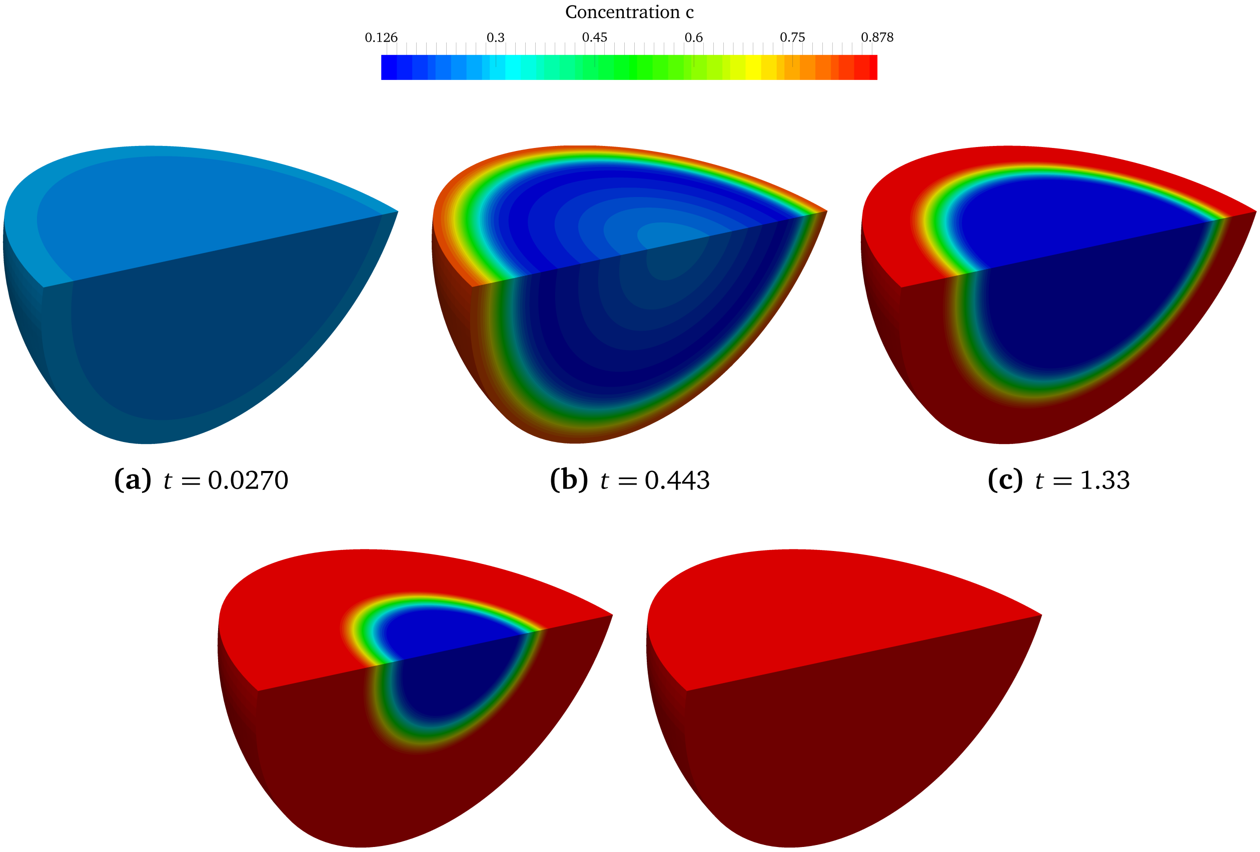

(a) $t = 0.0270$ **(b)** $t = 0.443$ **(c)** $t = 1.33$

(d) $t = 2.04$ **(e)** $t = 4.49$

FIGURE 4.14. *Evolution of the concentration in a spherical particle with an incoming flux simulated by boundary fitted isogeometric analysis.*

Fig. 4.14 shows the simulation results of a sphere. We can observe that a core-shell two-phase structure is maintained during the flux coming in. The phase interface stably marches towards the center until the total amount of flux is large enough to suppress the phase separation. In the prolate and oblate spheroids, since the the radial direction is not perpendicular to the circumferential direction, as shown in Fig. 4.15 for the case of a prolate spheroid, a strong imposition of $\nabla c \cdot \boldsymbol{n} = 0$ as described in the work of Liu et al. [99] is not possible.

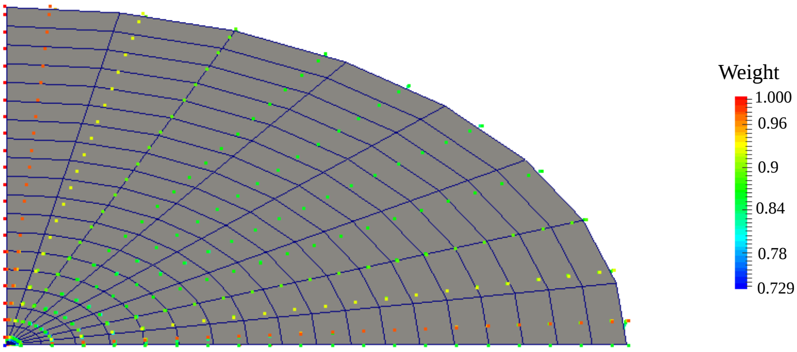

FIGURE 4.15. *The mesh and control points of one plane of symmetry of the prolate spheroid. The radial control lines are not perpendicular to the surface. A strong imposition of* $\nabla c \cdot \boldsymbol{n} = 0$ *is not possible. The weight of each control point is indicated by the color.*

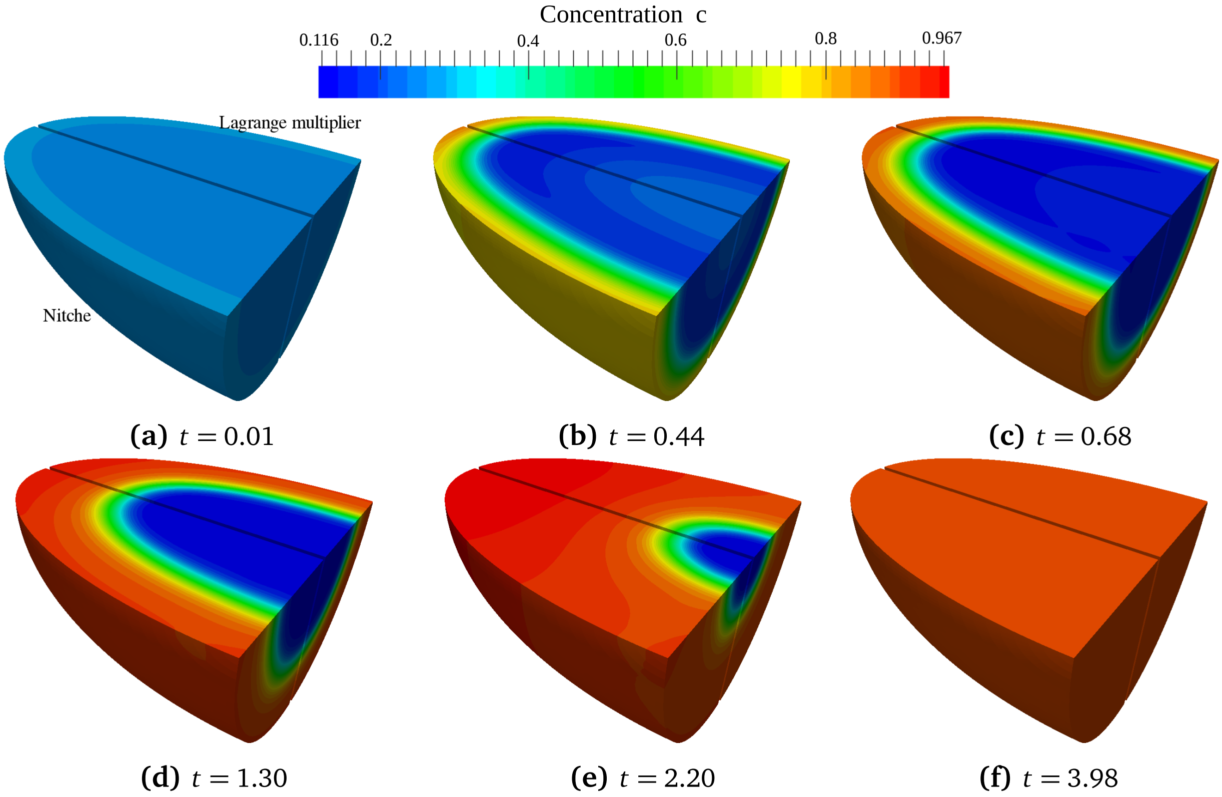

(a) $t = 0.01$ **(b)** $t = 0.44$ **(c)** $t = 0.68$

(d) $t = 1.30$ **(e)** $t = 2.20$ **(f)** $t = 3.98$

FIGURE 4.16. *Evolution of the concentration in a prolate spheroid with an incoming flux simulated by boundary fitted isogeometric analysis. The two octants are computed with different method: the lower left is with Nitsche's method, while the upper right octant is computed by the Lagrange multiplier method.*

Fig. 4.16 shows the simulation results at different time instants for the spheroid. As a comparison, the results with the Lagrange multiplier method described in the previous section is also plotted. For a better comparison, a fixed time step 0.01 is used here. It is shown that the two methods give the same evolutions of the concentration field. A core-shell two-phase structure is maintained during the flux comes in. The phase interface initiates on the surface and marches stably towards the center until the total amount of flux is large enough to suppress the phase separation. The phase interfaces are not spherical due to the geometry and the flux. To have a closer check of the weak constraint, the values of $\nabla c \cdot \boldsymbol{n}$ on the spheroidal surface are plotted, as shown in Fig. 4.17. In particular, the distribution of $\nabla c \cdot \boldsymbol{n}$ at $t = 0.48$ is plotted

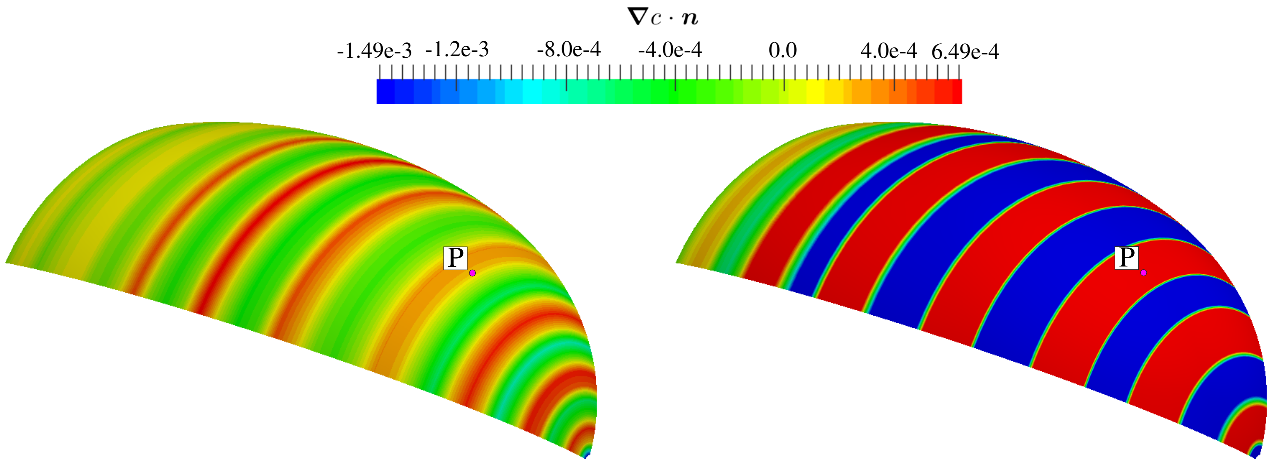

(a) *Nitsche*

(b) *Lagrange multiplier*

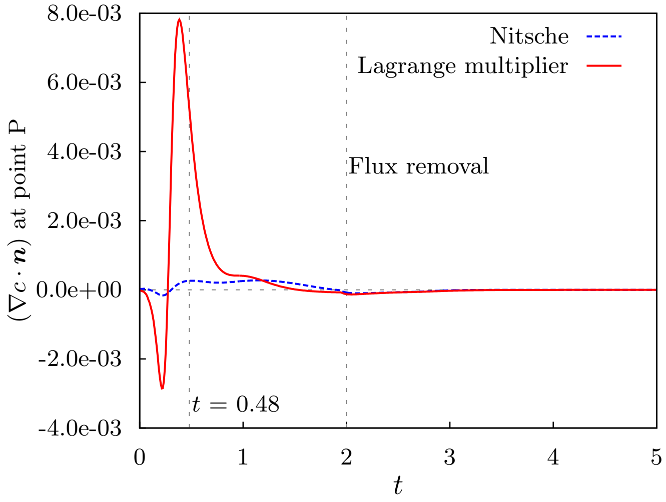

(c) *Evolution of* $\nabla c \cdot \boldsymbol{n}$ *at Point P.*

FIGURE 4.17. *The distribution of* $\nabla c \cdot \boldsymbol{n}$ *on the surface at* $t = 0.48$ *with Nitsche method (a) and Lagrange multiplier method (b). Both show similar pattern, while the Nitsche method gives a better constraint than Lagrange multiplier at that time. For a quantitative comparison, the evolution of* $\nabla c \cdot \boldsymbol{n}$ *at a representative point P (shown in (a) and (b)) is plotted in (c). The Lagrange multiplier method gives a stronger oscillation when the surface is perturbed by the incoming flux, but both methods bring* $\nabla c \cdot \boldsymbol{n}$ *to zero once the flux is removed.*

in Fig. 4.17(a) and Fig. 4.17(b). The evolution of $\nabla c \cdot \boldsymbol{n}$ with time at a representative point P (shown in Fig. 4.17(a)) is also plotted in Fig. 4.17(c). From the plots one can observe that both methods show similar behavior for the constraint, while the Lagrange multiplier method gives stronger oscillations of $\nabla c \cdot \boldsymbol{n}$, especially when the surface is strongly perturbed by the incoming flux. Finally, the phase separation is also simulated in the oblate spheroid. As shown in Fig. 4.18, it has the similar behavior as the prolate spheroid, where in general the core-shell structure is maintained, but not in a spherical shape.

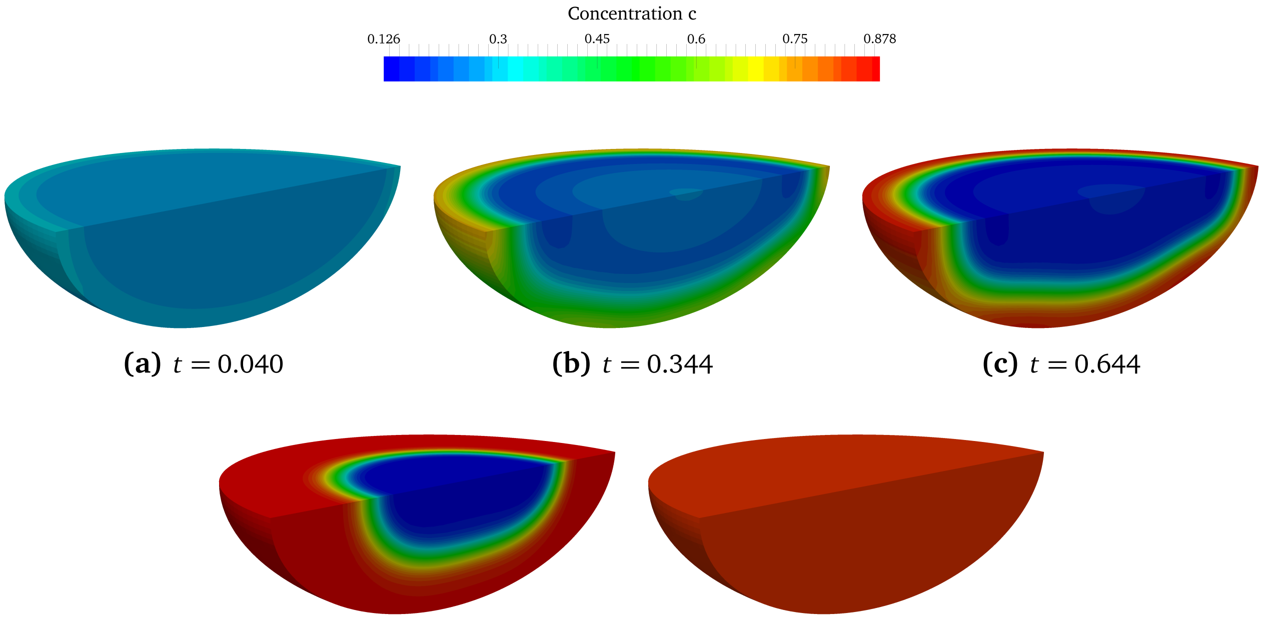

(a) $t = 0.040$ **(b)** $t = 0.344$ **(c)** $t = 0.644$

(d) $t = 1.64$ **(e)** $t = 5.44$

FIGURE **4.18.** *Evolution of the concentration in an oblate spheroid with an incoming flux simulated by boundary fitted isogeometric analysis.*

Remark: By virtue of their construction, the particle meshes become singular both in their center and along one of their semi-axes. Neither here nor in some previous work [111] did we experience adverse effects because of these mesh distortions. The Gauss points at which we evaluate the nodal residual vectors and the tangent matrices are always slightly offset from the singular regions of the mesh. Their respective contributions hence remain non-singular. Moreover, as has been shown by Lipton et al. [112], NURBS discretizations exhibit what is called a "variation-diminishing" property, rendering them robust against mesh distortions that would be fatal for isoparametric, C^0-continuous Finite Element discretizations.

4.5.4 Applications with the finite cell method

The finite cell method was recently developed to solve problems with non-boundary-fitted meshes, thus offering more geometric flexibility in the finite element method. The application will be, for instance, silicon-based composite electrodes in Lithium-ion batteries, where silicon particles experience phase transition during lithiation. In this case, the finite cell method is ideal for the simulation of composite electrodes based on their experimental images by characterization methods. In such a problem, the interface between the matrix and the active particle is introduced by a layer of Gauss quadrature points and weak imposition is necessary for the essential boundary conditions. As an attempt to integrate the Nitsche method into the finite cell method, we investigate the spherical example described in the previous section. Fig. 4.19 illustrates the numerical integration of intersected elements in the finite cell method. Quadratic B-splines were used as basis functions for the problem. Volume quadrature points were computed from an adaptive subdivision from the original Cartesian mesh. The number of degrees of freedom is only dependent on the mesh refinement, which has nothing to do with the subdivision level. The surface is represented by a fine triangulation generated and refined automatically from an open-source automatic 3d tetrahedral mesh generator NETGEN [113], where surface quadrature points are obtained from a standard 6-point formula [114]. Fig. 4.20 shows the results of the evolution of concentration distribution, which reproduce those in Fig. 4.14. Fig. 4.21 compares the concentration and the free energy obtained by the finite cell method with those by isogeometric method from the last subsection. It is observed that both methods yield a comparable concentration distribution. In addition, they also yield a comparable energy distribution, involving the first derivative of the primary degree of freedom.

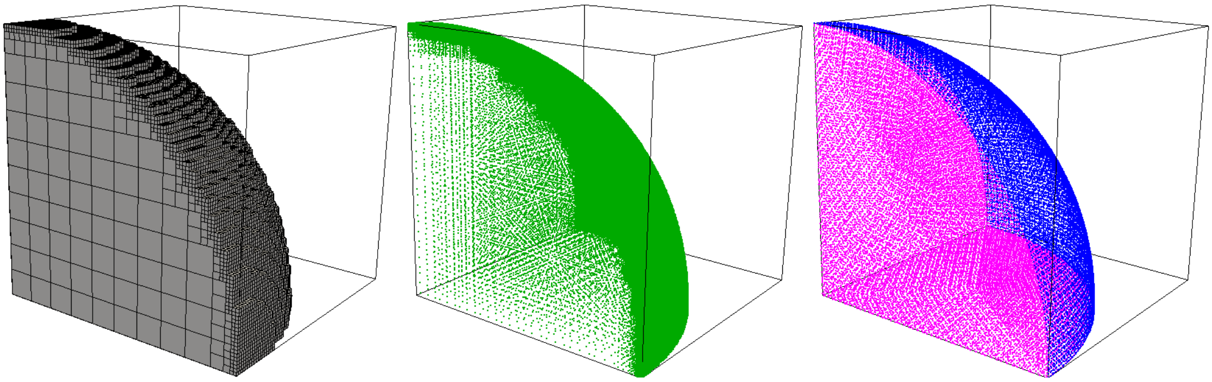

(a) *Sub-cells.* **(b)** *Volume quadrature points.* **(c)** *Surface quadrature points.*

FIGURE **4.19.** *Numerical scheme of the finite cell method. The integration volume quadrature points in (b) are computed based on an adaptive subdivision from the original* 10^3 *cartesian grids (a). The immersed surface is presented by the corresponding quadrature points. The additional flux is imposed on the spherical surface (blue points in (c)).*

Remark: Although the IGA mesh can reach desired accuracy for this problem with much less nodes thanks to its inherit rotational symmetry, FCM encounters no singularity in the solution field, as shown in Fig. 4.22.

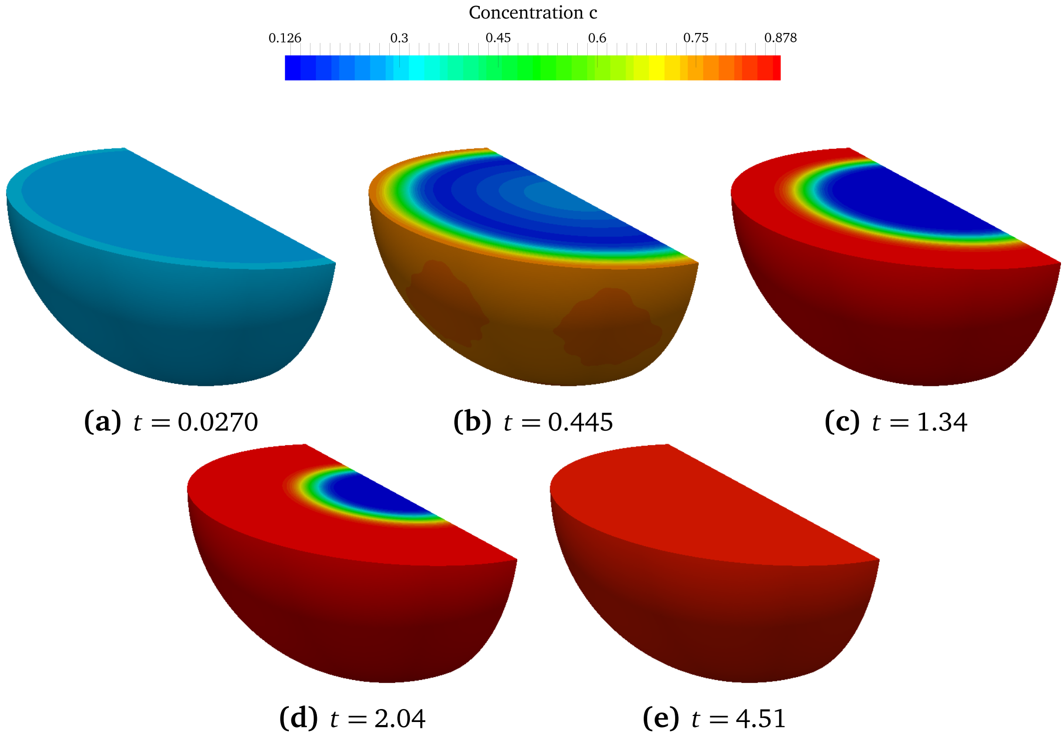

(a) $t = 0.0270$ **(b)** $t = 0.445$ **(c)** $t = 1.34$

(d) $t = 2.04$ **(e)** $t = 4.51$

Figure 4.20. *Evolution of concentration distribution in a sphere with an incoming flux simulated by the finite cell method.*

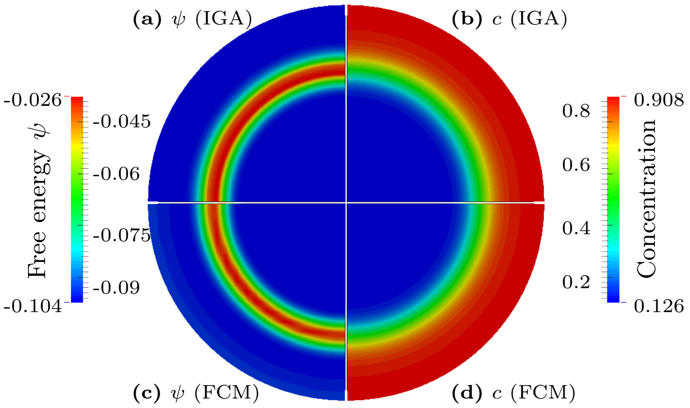

Figure 4.21. *The contour plot of free energy (a,c) and concentration (b,d) simulated by IGA and FCM at* $t = 1.34$. *For IGA,* 10^3 *quadratic elements with NURBS basis functions are given; for FCM,* 20^3 *elements with quadratic B-splines are used and the sub-cell level is 3. We can observe that, the concentration and free energy distributions obtained by two methods are the same.*

4.6 Summary

In this chapter, the Cahn–Hilliard equation was treated, which describes the diffusion of species in phase-separating materials. Since the Cahn–Hilliard equation is a fourth-order partial differential equation, shape functions that are globally C^1-continuous are needed for a straightforward treatment by the primary unknowns. There arises a difficulty of treating an additional

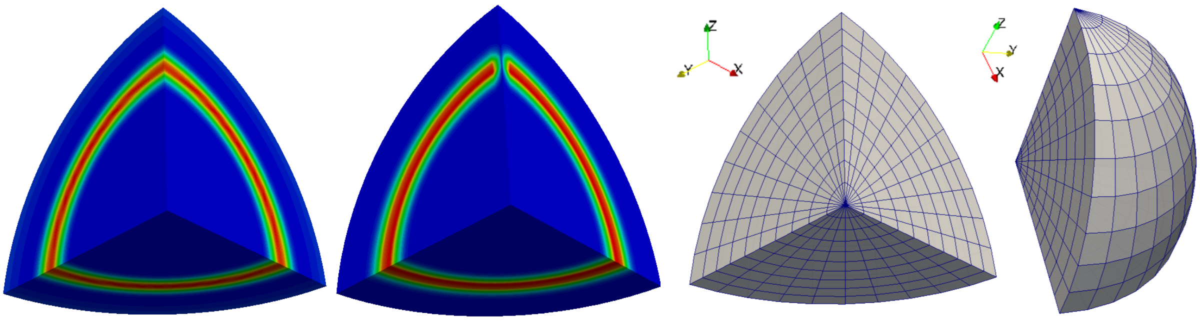

(a) *FCM solution* **(b)** *IGA solution* **(c)** *IGA mesh*

Figure 4.22. *The energy distribution simulated by FCM and IGA. The abnormal discontinuous energy is observed along z direction, where the singularity of the mesh is observed (Figure (c)).*

boundary term $\nabla c \cdot \boldsymbol{n} = 0$, which is essential but cannot directly fit into the weak formulation. Therefore, two methods were proposed in this chapter : the Lagrange multiplier and the Nitsche method. Firstly, we investigated the interfacial thickness with the Lagrange multiplier method, comparing the analytical solution with the numerical solution, which agree well with each other. Then, several characteristic examples were given based on Nitsche's method. In the 1D example, we gave a convergence study with regard to the chemical potential in equilibrium. A convergence rate of 2 with quardratic B-spline basis functions and rate of 4 with cubics and quartics were observed in the simulation. Another example shows that Nitsche's method can well enforce the Dirichlet boundary condition, which lays a basis for the implementation in the finite cell method. In the 2D example, we simulated the spinodal decomposition from an initial random field under natural and periodic boundary conditions. The resultant concentration profile showed that the constraints have been satisfactorily imposed. In the 3D example, the geometric flexibility was demonstrated through three spheroidal particles. The results agreed well with the results obtained by the Lagrange multiplier method. Finally in the last example, the proposed example was employed in the finite cell method, where the boundary was immersed in the mesh and the boundary condition can only be imposed on the surface quadrature points.

Chapter 5

Chemo-mechanical behavior of an electrode particle

In this chapter, chemical phase separation problem is coupled with mechanics issue. Alloy materials such as Si, Sn, and Sb have been introduced as alternative anode materials to graphite. However, those electrodes experience irreversible mechanical degradation already after few charge/discharge cycles due to high stresses. Those stresses arise from changes in lattice dimensions and crystal structures, which are associated with overall volume changes and phase transformation. For example, a volumetric expansion of more than 200% of Si particles has been observed during charge [6], which can result in particle cracking and contact loss. In addition, the formation of a two-phase system, which is observed in both cathode and anode materials [85, 115], can also lead to high stresses, in particular at the phase interface.

The need to understand the mechanical degradation in Li-ion batteries has motivated a number of continuum models of stress evolution in particles [111, 116–120], which presented intensive studies about the dependence of stresses on current density, particle size and geometry, charging mode, etc. However, in those studies the diffusion process was modeled as in a dilute solution, and phase separation was disregarded.

In order to account for phase transition, different models have been formulated. Huang et al. [121] prescribed a flexible sigmoid function for the two-phase concentration profile in respect of the interface position. Park et al. [122] modified the stress-strain relation by an additional volumetric strain due to phase transition in a thermal strain analogue. In the work of Bohn et al. [123], the driving force for diffusion was deduced from basic thermodynamics and statistical physics, to account for the non-ideal nature of lithium intercalation and a phase change. Drozdov [124] proposed a model which distinguishes the state of a guest atom as mobile and immobilized, and a sharp boundary between two phases was achieved by setting the diffusivity of mobile atoms increasing exponentially along with immobilized atom concentration. Zhang et al. [125, 126] used a reaction controlled diffusion model to describe the initial lithiation of crystalline silicon and the amorphous silicon.

Phase-field models based on the Cahn–Hilliard approach [31, 37] have recently found more applications for Li diffusion in Li-ion batteries, because this approach allows for a much simpler tracking of the phase interface. As for the phase-field models coupled with mechanical stresses, Huttin et al. [127] employed the Cahn–Hilliard model to investigate the stress generated in the spherical particle in the small deformation regime and compared it with the solution in a dilute model. Subsequently, Walk et al. [128] extended this model to the case of large deformation. Gladkov and Svendsen [129] derived thermodynamic models for inhomogeneous gradient continua with microstructure and formulated the corresponding initial boundary value problem in the light of rate variational methods. This general rate variational form can be recast into a numerical time incremental form via numerical time integration, whose application in the Cahn–Hilliard phase-field model can be found in the work of Miehe [96]. Concurrently, Anand [130] formulated a continuum model which coupled the Cahn–Hilliard-type diffusion with large elastic-plastic deformation, based on microforce balance theory, in which they introduced the Mandel stress as an additional source for the chemical potential. The simulation of the elastic part with a simplification of the drifting term was carried out later by Di Leo et al. [131].

In this chapter, the model is formulated based on the variational theorem in the line of the original Cahn–Hilliard model with no introduction of the Mandel stress for the chemical potential, and thus is thermodynamically consistent. In Section 5.1.4 it is shown that this model agrees with Anand's model [130].

Furthermore, none of the models introduced before has considered phase-dependent (concentration-dependent) elastic properties in the simulation, whose existence in both cathode and anode materials has been indicated by simulations of first-principles and molecular dynamics [19, 132–134]. In particular, Shenoy et al. [133] reported that elastic moduli of Li-Si alloys decrease in an approximately linear manner with increasing Li concentration in both crystalline and amorphous systems. In Anand's formulation [130], although the concentration-dependent elastic properties are mentioned, they are nevertheless not explicitly treated. Therefore in the numerical implementations [131] the related term was disregarded, together with the elastic chemical potential arising from the configurational change. However, the influence of the concentration-dependent elastic properties is not negligible; its impact becomes more profound as the mechanical stresses increase as shown in Section 5.3.2.

Therefore, in this chapter, an isotropic hyperelastic model coupled with Cahn–Hilliard phase-field diffusion with a full consideration of the phase-dependent elastic properties is formulated in Section 5.1. In Section 5.2, implementation details are given. The model and IGA implementation are tested on a benchmark example of a bar in Section 5.3, where the influence of phase-dependent elastic properties on phase separation and interfacial thickness is revealed. The calculated stress-dependent phase separation behavior in the bar agrees well with the results predicted by an analytical model. In Section 5.4, phase separation and stresses in spheroidal particles and circular plates are simulated. A short summary is given in Section 5.5.

5.1 Model

5.1.1 Free energy density

We now consider a free energy density comprised of three parts:

$$\psi_{\mathrm{R}}(c_{\mathrm{R}}, \boldsymbol{\nabla}_{\mathrm{R}} c_{\mathrm{R}}, \mathbf{C}) = \psi^{c}_{\mathrm{R}}(c_{\mathrm{R}}) + \psi^{i}_{\mathrm{R}}(\boldsymbol{\nabla}_{\mathrm{R}} c_{\mathrm{R}}) + \psi^{e}_{\mathrm{R}}(c_{\mathrm{R}}, \mathbf{C}), \tag{5.1}$$

where, $\psi^{c}_{\mathrm{R}}(c_{\mathrm{R}})$, $\psi^{i}_{\mathrm{R}}(\boldsymbol{\nabla}_{\mathrm{R}} c_{\mathrm{R}})$ and $\psi^{e}_{\mathrm{R}}(c_{\mathrm{R}}, \mathbf{C})$ are the bulk chemical free energy, the interface free energy and the elastic free energy, respectively. As mentioned in Section 2.2, entities with subscript R indicate those defined per volume of the reference configuration.

The bulk chemical free energy ψ^{c}_{R} only depends on the local concentration. As a simple case, we assume a regular solution model:

$$\psi^{c}_{\mathrm{R}}(c_{\mathrm{R}}) = \mathrm{RTc}_{\mathrm{max}}\left[c \ln c + (1-c)\ln(1-c)\right] + \mathrm{RTc}_{\mathrm{max}} \chi c (1-c). \tag{5.2}$$

Here, R and T are the gas constant and the reference temperature, respectively. The interface free energy ψ^{i}_{R} is a function of the concentration gradient:

$$\psi^{i}_{\mathrm{R}}(\boldsymbol{\nabla}_{\mathrm{R}} c_{\mathrm{R}}) = \frac{1}{2}\mathrm{c}_{\mathrm{max}} \kappa \left|\boldsymbol{\nabla}_{\mathrm{R}} c\right|^{2}, \tag{5.3}$$

with κ being an interface parameter. A detailed discussion on Eq. (5.2) and Eq. (5.3) has been given in Chapter 4.

The elastic free energy ψ^{e}_{R} represents the stored energy of elastic deformation. The influence of concentration field on displacement field is considered by analogy with thermal effects. On the other hand, since the chemical potential, which determines the concentration distribution in a system, incorporates contributions from the elastic free energy, this term also reveals the influence of displacement field on concentration field. Therefore, ψ^{e}_{R} can also be regarded as a coupling free energy. In general, for isotropic hyperelastic materials, the elastic free energy can be expressed with respect to the invariants of the elastic right Cauchy–Green stress tensor $\mathbf{C}^{e}$. Here we take a specific form of neo-Hookean solids comprised of a volumetric and a deviatoric part:

$$\psi^{e}_{\mathrm{I}}(c_{\mathrm{R}}, \mathbf{C}^{e}) = \frac{K_c}{2}(J^{e}-1)^{2} + \frac{G_c}{2}\left(\bar{I}^{e}_{1} - 3\right), \tag{5.4}$$

where J^{e} and $\bar{I}^{e}_{1}$ are defined in Eq. (2.41) and Eq. (2.44), respectively, and where K_c and G_c are the concentration-dependent elastic moduli. Since ψ^{e}_{I} is a density defined per unit volume in the intermediate configuration (Fig. 2.2), it is necessary to pull it back to the reference configuration. That yields

$$\psi^{e}_{\mathrm{R}}(c_{\mathrm{R}}, \mathbf{C}) = J^{c}\, \psi^{e}_{\mathrm{I}}(c_{\mathrm{R}}, \mathbf{C}^{e}) = J^{c}\left[\frac{K_c}{2}\left(\frac{J}{J^{c}} - 1\right)^{2} + \frac{G_c}{2}\left(\bar{I}_{1} - 3\right)\right], \tag{5.5}$$

where the relation $\bar{I}_{1} = \bar{I}^{e}_{1}$ is applied.

5.1.2 Chemical potential and mechanical stresses

Based on the work by Cahn and Hilliard [31, 37], the variation of the total free energy is

$$\delta\Psi = \int_{\mathrm{B_R}} \mu_{\mathrm{R}}\,\delta c_{\mathrm{R}}\,\mathrm{dV} + \int_{\mathrm{B_R}} \mathbf{S}_{\mathrm{R}} : \delta\mathbf{E}\,\mathrm{dV}, \tag{5.6}$$

in which, μ_{R} is the chemical potential, $\mathbf{S}_{\mathrm{R}}$ is the second Piola–Kirchhoff stress tensor, and Ψ is defined as the free energy over the whole body in the reference configuration $\mathrm{B_R}$,

$$\Psi = \int_{\mathrm{B_R}} \psi_{\mathrm{R}}(c_{\mathrm{R}}, \boldsymbol{\nabla}_{\mathrm{R}} c_{\mathrm{R}}, \mathbf{C})\,\mathrm{dV}. \tag{5.7}$$

Recalling Eq. (5.1) and the kinematic relations, the variation yields

$$\begin{aligned}
\delta\Psi &= \int_{\mathrm{B_R}} \frac{\mathrm{d}\psi^c_{\mathrm{R}}}{\mathrm{d}c_{\mathrm{R}}}\delta c_{\mathrm{R}} + \frac{\mathrm{d}\psi^i_{\mathrm{R}}}{\mathrm{d}\boldsymbol{\nabla}_{\mathrm{R}} c_{\mathrm{R}}} \cdot \delta \boldsymbol{\nabla}_{\mathrm{R}} c_{\mathrm{R}} + \frac{\partial \psi^e_{\mathrm{R}}}{\partial c_{\mathrm{R}}}\delta c_{\mathrm{R}} + \frac{\partial \psi^e_{\mathrm{R}}}{\partial \mathbf{C}} : \delta\mathbf{C}\,\mathrm{dV} \\
&= \int_{\mathrm{B_R}} \left(\frac{\mathrm{d}\psi^c_{\mathrm{R}}}{\mathrm{d}c_{\mathrm{R}}} - \kappa \Delta_R c_{\mathrm{R}} + \frac{\partial \psi^e_{\mathrm{R}}}{\partial c_{\mathrm{R}}} \right) \delta c_{\mathrm{R}} + \boldsymbol{\nabla}_{\mathrm{R}} \cdot (\kappa \boldsymbol{\nabla}_{\mathrm{R}} c_{\mathrm{R}} \delta c_{\mathrm{R}}) + \frac{2\partial \psi^e_{\mathrm{R}}}{\partial \mathbf{C}} : \delta\mathbf{E}\,\mathrm{dV} \\
&= \int_{\mathrm{B_R}} \left(\frac{\mathrm{d}\psi^c_{\mathrm{R}}}{\mathrm{d}c_{\mathrm{R}}} - \kappa \Delta_R c_{\mathrm{R}} + \frac{\partial \psi^e_{\mathrm{R}}}{\partial c_{\mathrm{R}}} \right) \delta c_{\mathrm{R}}\,\mathrm{dV} + \int_{\mathrm{B_R}} \frac{2\partial \psi^e_{\mathrm{R}}}{\partial \mathbf{C}} : \delta\mathbf{E}\,\mathrm{dV} \\
&+ \int_{\partial \mathrm{B_R}} \kappa \boldsymbol{\nabla}_{\mathrm{R}} c_{\mathrm{R}} \cdot \boldsymbol{n}_{\mathrm{R}}\,\delta c_{\mathrm{R}}\,\mathrm{dS}.
\end{aligned} \tag{5.8}$$

Here, Δ_{R} denotes the Laplace operator in the reference configuration. $\partial \mathrm{B_R}$ is the boundary surface of $\mathrm{B_R}$. Comparing Eq. (5.6) and Eq. (5.8), we obtain

$$\mu_{\mathrm{R}} = \frac{\mathrm{d}\psi^c_{\mathrm{R}}}{\mathrm{d}c_{\mathrm{R}}} - \kappa \Delta_R c_{\mathrm{R}} + \frac{\partial \psi^e_{\mathrm{R}}}{\partial c_{\mathrm{R}}}, \tag{5.9}$$

$$\mathbf{S}_{\mathrm{R}} = \frac{2\partial \psi^e_{\mathrm{R}}}{\partial \mathbf{C}}, \tag{5.10}$$

given that the last term of Eq. (5.8) equals zero. That requires an additional boundary condition to be fulfilled:

$$\boldsymbol{\nabla}_{\mathrm{R}} c_{\mathrm{R}} \cdot \boldsymbol{n}_{\mathrm{R}} = 0 \quad \text{on} \quad \partial \mathrm{B_R}. \tag{5.11}$$

The condition of Eq. (5.11), although it can be violated during diffusion, will nevertheless hold for a system in equilibrium state. Similar to Eq. (5.1), we can write the chemical potential as:

$$\mu_{\mathrm{R}} = \mu^c_{\mathrm{R}}(c_{\mathrm{R}}) + \mu^i_{\mathrm{R}}(\boldsymbol{\nabla}_{\mathrm{R}} c_{\mathrm{R}}) + \mu^e_{\mathrm{R}}(c_{\mathrm{R}}, \mathbf{C}), \tag{5.12}$$

in which,

$$\mu_{\mathrm{R}}^{c}=\frac{\mathrm{d}\psi_{\mathrm{R}}^{c}}{\mathrm{d}c_{\mathrm{R}}}=\mathrm{RT}\left[\ln c-\ln\left(1-c\right)+\chi\left(1-2c\right)\right] \tag{5.13}$$

$$\mu_{\mathrm{R}}^{i}=-\kappa\Delta_{\mathrm{R}}c \tag{5.14}$$

$$\begin{aligned}\mu_{\mathrm{R}}^{e}=\frac{\partial\psi_{\mathrm{R}}^{e}}{\partial c_{\mathrm{R}}}&=\frac{\Omega K_{c}}{2}\left[1-(J^{e})^{2}\right]+\frac{\Omega G_{c}}{2}\left(\bar{I}_{1}-3\right)\\&+\frac{J^{c}}{\mathrm{c}_{\max}}\left[\frac{K_{c}^{\prime}}{2}\left(J^{e}-1\right)^{2}+\frac{G_{c}^{\prime}}{2}\left(\bar{I}_{1}-3\right)\right]\end{aligned} \tag{5.15}$$

In Eq. (5.15), G_c' and K_c' denote $\mathrm{d}G_c/\mathrm{d}c$ and $\mathrm{d}K_c/\mathrm{d}c$, respectively. In the case of concentration-independent elastic moduli, both terms equal zero. From Eq. (5.10), we can obtain the second Piola–Kirchhoff stress tensor

$$\mathbf{S}_{\mathrm{R}}=\frac{2\partial\psi_{\mathrm{R}}^{e}}{\partial\mathbf{C}}=J^{c}\left[K_{c}J^{e}\left(J^{e}-1\right)\mathbf{C}^{-1}+G_{c}J^{-\frac{2}{3}}\left(\mathbf{1}-\frac{1}{3}I_{1}\mathbf{C}^{-1}\right)\right]. \tag{5.16}$$

The first Piola–Kirchhoff stress tensor is then

$$\mathbf{P}_{\mathrm{R}}=\mathbf{F}\,\mathbf{S}_{\mathrm{R}}. \tag{5.17}$$

5.1.3 Governing equations

As it is common for deformable solids, we use a Lagrangian description for the local force balance as well as for the diffusion equation:

$$\mathrm{Div}_{\mathrm{R}}\,\mathbf{P}_{\mathrm{R}}=\mathbf{0} \qquad \text{in} \quad \mathrm{B}_{\mathrm{R}}\times(0,\mathscr{T}), \tag{5.18}$$

$$\frac{\partial c_{\mathrm{R}}}{\partial t}=\mathrm{Div}_{\mathrm{R}}\left(M_{c}\boldsymbol{\nabla}_{\mathrm{R}}\mu_{\mathrm{R}}\right) \qquad \text{in} \quad \mathrm{B}_{\mathrm{R}}\times(0,\mathscr{T}), \tag{5.19}$$

$$\mathbf{u}=\hat{\mathbf{u}} \qquad \text{on} \quad \mathrm{S}_{\mathrm{R}\mathbf{u}}\times(0,\mathscr{T}), \tag{5.20}$$

$$\mathbf{P}_{\mathrm{R}}\cdot\boldsymbol{n}_{\mathrm{R}}=\hat{\mathbf{t}} \qquad \text{on} \quad \mathrm{S}_{\mathrm{R}\mathbf{t}}\times(0,\mathscr{T}), \tag{5.21}$$

$$\mathbf{j}_{\mathrm{R}}\cdot\boldsymbol{n}_{\mathrm{R}}=\hat{j}_{\mathrm{R}}=\frac{i_{\mathrm{R}}}{\mathrm{F}} \qquad \text{on} \quad \partial\mathrm{B}_{\mathrm{R}}\times(0,\mathscr{T}), \tag{5.22}$$

$$\boldsymbol{\nabla}_{\mathrm{R}}c_{\mathrm{R}}\cdot\boldsymbol{n}_{\mathrm{R}}=0 \qquad \text{on} \quad \partial\mathrm{B}_{\mathrm{R}}\times(0,\mathscr{T}), \tag{5.23}$$

$$c_{\mathrm{R}}(\mathbf{X},0)=c_{\mathrm{R}0}(\mathbf{X}) \qquad \text{in} \quad \mathrm{B}_{\mathrm{R}}. \tag{5.24}$$

Here, $\mathrm{Div}_{\mathrm{R}}$ denotes the divergence with respect to the material coordinates $\mathbf{X}$ in the reference configuration. $\mathrm{S}_{\mathrm{R}\mathbf{u}}$ and $\mathrm{S}_{\mathrm{R}\mathbf{t}}$ are two complementary parts on the surface, satisfying $\mathrm{S}_{\mathrm{R}\mathbf{u}}\cup\mathrm{S}_{\mathrm{R}\mathbf{t}}=\partial\mathrm{B}_{\mathrm{R}}$ and $\mathrm{S}_{\mathrm{R}\mathbf{u}}\cap\mathrm{S}_{\mathrm{R}\mathbf{t}}=\emptyset$. M_c is the concentration-dependent mobility. Here we follow the common assumption that $M_c=\mathrm{D}\mathrm{c}_{\max}c(1-c)$ for the degenerate mobility, in which D is the constant diffusivity and $c=c_{\mathrm{R}}/\mathrm{c}_{\max}$ is the relative concentration. For the flux boundary, i_{R} is the applied current density and F is Faraday's constant. In the diffusion equation Eq. (5.19), the species are driven by the flux defined in the reference configuration, which leads to a simplified implementation. A more physically sound model where the flux is defined in the current configuration will be presented in Chapter 6.

5.1.4 Comparison with microforce balance theory

In the theory of microforce balance [130], the free energy is defined as

$$\tilde{\psi}^e_\mathrm{R}(c_\mathrm{R}, \mathbf{C}^e) = J^c \psi^e_\mathrm{I}(c_\mathrm{R}, \mathbf{C}^e), \tag{5.25}$$

and the chemical potential reads as

$$\tilde{\mu}^e_\mathrm{R} = \frac{\partial \tilde{\psi}^e_\mathrm{R}(c_\mathrm{R}, \mathbf{C}^e)}{\partial c_\mathrm{R}} - \frac{1}{3}\Omega \operatorname{tr} \mathbf{M}^e, \tag{5.26}$$

in which $\mathbf{M}^e$ is the Mandel stress, given by

$$\mathbf{M}^e = \mathbf{C}^e \mathbf{T}^e, \quad \mathbf{T}^e = \frac{2\partial \psi^e_\mathrm{I}(c_\mathrm{R}, \mathbf{C}^e)}{\partial \mathbf{C}^e}. \tag{5.27}$$

As a result, the chemical potential is

$$\tilde{\mu}^e_\mathrm{R} = \Omega \psi^e_\mathrm{I}(c_\mathrm{R}, \mathbf{C}^e) + J^c \frac{\partial \psi^e_\mathrm{I}(c_\mathrm{R}, \mathbf{C}^e)}{\partial c_\mathrm{R}} - \frac{1}{3}\Omega \mathbf{C}^e : \frac{2\partial \psi^e_\mathrm{I}(c_\mathrm{R}, \mathbf{C}^e)}{\partial \mathbf{C}^e}. \tag{5.28}$$

In our approach, the coupling free energy is defined as

$$\psi^e_\mathrm{R}(c_\mathrm{R}, \mathbf{C}) = J^c \psi^e_\mathrm{I}[c_\mathrm{R}, \mathbf{C}^e(c_\mathrm{R}, \mathbf{C})]. \tag{5.29}$$

The difference is that here the elastic deformation $\mathbf{C}^e$ is not an independent variable, but a dependent one, which indicates the coupling between the displacement field and the concentration field. The chemical potential is then simply derived as

$$\mu^e_\mathrm{R} = \frac{\partial \psi^e_\mathrm{R}(c_\mathrm{R}, \mathbf{C})}{\partial c_\mathrm{R}} = \frac{\partial J^c}{\partial c_\mathrm{R}} \psi^e_I(c_\mathrm{R}, \mathbf{C}^e) + J^c \frac{\partial \psi^e_I(c_\mathrm{R}, \mathbf{C}^e)}{\partial c_\mathrm{R}} + J^c \frac{\partial \psi^e_I(c_\mathrm{R}, \mathbf{C}^e)}{\partial \mathbf{C}^e} : \frac{\partial \mathbf{C}^e}{\partial c_\mathrm{R}}, \tag{5.30}$$

leading to Eq. (5.15) when ψ^e_R is defined through Eq. (5.5). Referring to Eq. (2.42), we can obtain

$$\frac{\partial \mathbf{C}^e}{\partial c_\mathrm{R}} = -\frac{2\Omega}{3J^c} \mathbf{C}^e. \tag{5.31}$$

Thus the chemical potential yields

$$\mu^e_\mathrm{R} = \Omega \psi^e_\mathrm{I}(c_\mathrm{R}, \mathbf{C}^e) + J^c \frac{\partial \psi^e_\mathrm{I}(c_\mathrm{R}, \mathbf{C}^e)}{\partial c_\mathrm{R}} - \frac{1}{3}\Omega \frac{2\partial \psi^e_\mathrm{I}(c_\mathrm{R}, \mathbf{C}^e)}{\partial \mathbf{C}^e} : \mathbf{C}^e, \tag{5.32}$$

which is equivalent to Eq. (5.28). In other words, the chemical potential can be thermodynamically consistently obtained from the partial derivative of our coupling free energy with respect to c_R.

Remark: Both Eq. (5.28) and Eq. (5.32) are comprised of three parts: the first term arises due to the configurational change, i.e., from the reference configuration to the intermediate configuration; the second term is related to the concentration-dependent elastic moduli; the last term can be compared with the hyperelastic stress in the small deformation model. In the work of Di Leo et al. [131], only the last term was implemented for simplicity. However, since all three terms contribute equally to the elastic chemical potential, they should be fully considered in the numerical simulation.

5.1.5 Concentration-dependent elastic moduli

To take the concentration-dependent elastic moduli into account, a linear dependence of the shear modulus and the bulk modulus on concentration is proposed:

$$K_c = \mathrm{K}_0(\mathrm{c}_{\mathrm{in}} - c), \quad G_c = \mathrm{G}_0(\mathrm{c}_{\mathrm{in}} - c), \tag{5.33}$$

where G_0, K_0 and c_{in} are constants, which can be determined by a linear fit of measurements of the elastic moduli at different concentrations. Please note that c_{in} is the intercept on the axis of concentration in a K_c-c (or G_c-c) plot, with K_0 and G_0 being their corresponding slope. In particular, $\mathrm{c}_{\mathrm{in}} > 1$ indicates that the material softens as Li concentration increases, whereas $\mathrm{c}_{\mathrm{in}} < 0$ means that the material strengthens with an increasing Li concentration. For example, for cathode materials such as $\mathrm{Li}_x\mathrm{Mn}_2\mathrm{O}_4$, the elastic moduli can reduce as much as 10% when x, the mole proportion of Li, increases from 0 to 1 [132]. In this case, we get $\mathrm{c}_{\mathrm{in}} = 10$. Another example is the anode material Silicon, whose Young's modulus can reduce as much as 75% as the Li fraction increases from 0 to 1 [133], hence $\mathrm{c}_{\mathrm{in}} = 1.33$. On the other hand, Qi et al [134] reported that the Young's modulus of a fully lithiated LiCoO_2 is 4.5 times as much as that of the fully delithiated CoO_2, which gives $\mathrm{c}_{\mathrm{in}} = -0.3$. In the following simulations, $\mathrm{c}_{\mathrm{in}} = 10$ will be used.

Inserting Eq. (5.33) into Eq. (5.15) yields

$$\mu_{\mathrm{R}}^e = \frac{\Omega}{2}\left(\bar{I}_1 - 3\right)\left(G_c - \frac{J^c}{\Omega^*}\mathrm{G}_0\right) - \frac{\Omega}{2}\left[K_c\left(J^e \cdot J^e - 1\right) + \frac{J^c}{\Omega^*}\mathrm{K}_0\left(J^e - 1\right)^2\right]. \tag{5.34}$$

This equation implies that the phase-dependent elastic moduli can influence the phase separation behavior. This influence involves not only the volumetric part, but also the deviatoric part. This issue is numerically and analytically demonstrated later in Section 5.3 using the example of a bar.

5.2 Numerical treatment

5.2.1 Normalization

The dimensionless form is given by scaling each variable to its natural units. The relative Li concentration $c = c_{\mathrm{R}}/\mathrm{c}_{\mathrm{max}}$ has been already given. In addition, we introduce the non-dimensional space and time coordinates as:

$$\bar{\mathbf{X}} = \frac{\mathbf{X}}{\mathrm{L}_0}, \quad \bar{t} = \frac{\mathrm{D}}{\mathrm{L}_0^2}\,t. \tag{5.35}$$

Here, L_0 is a characteristic length scale, and D is the constant diffusivity. Quantities such as free energy density, chemical potential, flux, and stresses are given in the normalized form as:

$$\psi = \frac{\psi_\mathrm{R}}{\mathrm{RTc}_\mathrm{max}}, \quad \mu = \frac{\mu_\mathrm{R}}{\mathrm{RT}}, \quad \mathbf{j} = \frac{\mathrm{L}_0}{\mathrm{Dc}_\mathrm{max}} \mathbf{j}_\mathrm{R}, \quad \mathbf{S} = \frac{\mathbf{S}_\mathrm{R}}{\mathrm{RTc}_\mathrm{max}}. \tag{5.36}$$

The normalized elastic moduli are:

$$K_c^* = \frac{K_c}{\mathrm{RTc}_\mathrm{max}}, \quad G_c^* = \frac{G_c}{\mathrm{RTc}_\mathrm{max}}, \quad \mathrm{K}_0^* = \frac{\mathrm{K}_0}{\mathrm{RTc}_\mathrm{max}}, \quad \mathrm{G}_0^* = \frac{\mathrm{G}_0}{\mathrm{RTc}_\mathrm{max}}, \tag{5.37}$$

along with the normalized interface parameter $\kappa^* = \kappa/(\mathrm{RTL}_0^2)$. We can then write the governing equations in the dimensionless form as:

$$\operatorname{Div} \mathbf{P} = \mathbf{0} \qquad \text{in} \quad \mathrm{B} \times \left(0, \bar{\mathscr{T}}\right), \tag{5.38}$$

$$\dot{c} = \operatorname{Div}\left[c(1-c)\boldsymbol{\nabla}\mu\right] \qquad \text{in} \quad \mathrm{B} \times \left(0, \bar{\mathscr{T}}\right), \tag{5.39}$$

$$\bar{\mathbf{u}} = \hat{\bar{\mathbf{u}}} \qquad \text{on} \quad \mathrm{S}_{\bar{\mathbf{u}}} \times \left(0, \bar{\mathscr{T}}\right), \tag{5.40}$$

$$\mathbf{P} \cdot \boldsymbol{n} = \hat{\bar{\mathbf{t}}} \qquad \text{on} \quad \mathrm{S}_{\bar{\mathbf{t}}} \times \left(0, \bar{\mathscr{T}}\right), \tag{5.41}$$

$$\mathbf{j} \cdot \boldsymbol{n} = \hat{\bar{j}} \qquad \text{on} \quad \partial\mathrm{B} \times \left(0, \bar{\mathscr{T}}\right), \tag{5.42}$$

$$\boldsymbol{\nabla} c \cdot \boldsymbol{n} = 0 \qquad \text{on} \quad \partial\mathrm{B} \times \left(0, \bar{\mathscr{T}}\right), \tag{5.43}$$

$$c\left(\bar{\mathbf{X}}, 0\right) = c_0\left(\bar{\mathbf{X}}\right) \qquad \text{in} \quad \mathrm{B}, \tag{5.44}$$

with temporal and spatial derivatives with respect to normalized time and coordinates, respectively.

5.2.2 Implementation details

The model presented in Section 5.1 is implemented with the isogeometric finite element method. In the model, there exists a fourth-order spatial derivative of the concentration to account for the diffusive phase interface, and a third-order derivative of the displacements in the chemo-mechanical coupling term. Both require C^1-continuous shape functions if these high-order operators are to be dealt with straightforwardly. IGA allows to employ a wide range of smooth, higher-order basis functions, e.g., Non-uniform rational B-Splines (NURBS) or T-Splines, whose continuity can be adapted both in geometric modeling and during discretization. Moreover, during simulation we have observed that, in the spinodal region, the whole system is sensitive to infinitesimal concentration fluctuation, either due to compositional inhomogeneity or computational error. A discretization failing to give a solution with high precision will lead to incorrect results on phase separation. Compared to traditional FEM, IGA has the advantage of modeling curved boundary geometry precisely, even with coarse meshes. Thus, spurious numerical effects of the boundary discretization on phase separation can be avoided.

There are 5 DOFs at each node: the displacements $u_i\,(i=1,2,3)$, the concentration c, and the Lagrange multiplier λ. A backward-Euler integration scheme has been applied together with the Newton-Raphson iteration scheme at each time step. All the codes are implemented in FEAP [61].

We employ the isoparametric/isogeometric concept. The displacements, concentration and Lagrange multiplier are interpolated as

$$\mathbf{u}=N^{\mathrm{I}}\mathbf{u}^{\mathrm{I}},\quad c=N^{\mathrm{I}}c^{\mathrm{I}},\quad \lambda=N^{\mathrm{I}}\lambda^{\mathrm{I}} \tag{5.45}$$

where $(\cdot)^{\mathrm{I}}$ is the quantity at the I-th control point, and N^{I} is the NURBS shape function associated with the I-th control point. The repeated I invokes the Einstein summation, unless commented otherwise. If the Green-Lagrangian strain tensor $\mathbf{E}=(\mathbf{C}-\mathbf{I})/2$ is given in Voigt notation,

$$\underline{\mathbf{E}}=\left[\begin{array}{cccccc} \mathrm{E}_{11} & \mathrm{E}_{22} & \mathrm{E}_{33} & 2\mathrm{E}_{12} & 2\mathrm{E}_{23} & 2\mathrm{E}_{13}\end{array}\right]^{\mathrm{T}}, \tag{5.46}$$

we can obtain

$$\delta\underline{\mathbf{E}}=\mathbf{B}_u^{\mathrm{I}}\,\delta\mathbf{u}^{\mathrm{I}},\quad \nabla c=\mathbf{B}_c^{\mathrm{I}}\,c^{\mathrm{I}},\quad \nabla\lambda=\mathbf{B}_\lambda^{\mathrm{I}}\,\lambda^{\mathrm{I}}, \tag{5.47}$$

in which

$$\mathbf{B}_c^{\mathrm{I}}=\mathbf{B}_\lambda^{\mathrm{I}}=\left[\begin{array}{ccc} N_{,1}^{\mathrm{I}} & N_{,2}^{\mathrm{I}} & N_{,3}^{\mathrm{I}}\end{array}\right]^{\mathrm{T}}, \tag{5.48}$$

$$\mathbf{B}_u^{\mathrm{I}}=\left[\begin{array}{ccc}
F_{11}N_{,1}^{\mathrm{I}} & F_{21}N_{,1}^{\mathrm{I}} & F_{31}N_{,1}^{\mathrm{I}}\\
F_{12}N_{,2}^{\mathrm{I}} & F_{22}N_{,2}^{\mathrm{I}} & F_{32}N_{,2}^{\mathrm{I}}\\
F_{13}N_{,3}^{\mathrm{I}} & F_{23}N_{,3}^{\mathrm{I}} & F_{33}N_{,3}^{\mathrm{I}}\\
F_{11}N_{,2}^{\mathrm{I}}+F_{12}N_{,1}^{\mathrm{I}} & F_{21}N_{,2}^{\mathrm{I}}+F_{22}N_{,1}^{\mathrm{I}} & F_{31}N_{,2}^{\mathrm{I}}+F_{32}N_{,1}^{\mathrm{I}}\\
F_{12}N_{,3}^{\mathrm{I}}+F_{13}N_{,2}^{\mathrm{I}} & F_{22}N_{,3}^{\mathrm{I}}+F_{23}N_{,2}^{\mathrm{I}} & F_{32}N_{,3}^{\mathrm{I}}+F_{33}N_{,2}^{\mathrm{I}}\\
F_{13}N_{,1}^{\mathrm{I}}+F_{11}N_{,3}^{\mathrm{I}} & F_{23}N_{,1}^{\mathrm{I}}+F_{21}N_{,3}^{\mathrm{I}} & F_{33}N_{,1}^{\mathrm{I}}+F_{31}N_{,3}^{\mathrm{I}}
\end{array}\right]. \tag{5.49}$$

Here, $N_{,i}^{\mathrm{I}}$ denotes $\partial N^{\mathrm{I}}/\partial X_i$, and F_{ij} are the components of the deformation gradient $\mathbf{F}$.

Given these equations together with the construction details and the governing equations, as well as the Lagrange multiplier method mentioned above, the weak form of the problem can be written as

$$\delta\bar{\Pi}=(\delta\mathbf{u}^{\mathrm{I}})^{\mathrm{T}}\,\mathbf{R}_u^{\mathrm{I}}+\delta c^{\mathrm{I}}\,\mathrm{R}_c^{\mathrm{I}}+\delta\lambda^{\mathrm{I}}\,\mathrm{R}_\lambda^{\mathrm{I}}=0, \tag{5.50}$$

in which

$$\mathbf{R}_u^{\mathrm{I}}=-\int_{\mathrm{B}}(\mathbf{B}_u^{\mathrm{I}})^{\mathrm{T}}\underline{\mathbf{S}}\,\mathrm{dV}, \tag{5.51}$$

$$
\begin{aligned}
\mathrm{R}^{\mathrm{I}}_{c} = & \int_{\mathrm{B}} \dot{c}\, N^{\mathrm{I}}\, \mathrm{dV} + \int_{\mathrm{B}} [1-2\chi c\,(1-c)]\,(\mathbf{B}^{\mathrm{I}}_{c})^{\mathrm{T}} \boldsymbol{\nabla} c\, \mathrm{dV} \\
& + \int_{\mathrm{B}} c\,(1-c)\,\frac{\partial \mu^{e}}{\partial c}(\mathbf{B}^{\mathrm{I}}_{c})^{\mathrm{T}} \boldsymbol{\nabla} c\, \mathrm{dV} + \int_{\mathrm{B}} c\,(1-c)\,(\mathbf{G}^{\mathrm{I}})^{\mathrm{T}} \frac{2\partial \mu^{e}}{\partial \underline{\mathbf{C}}}\, \mathrm{dV} \\
& + \int_{\mathrm{B}} \kappa^{*}\,(1-2c)\,\Delta c\,(\mathbf{B}^{\mathrm{I}}_{c})^{\mathrm{T}} \boldsymbol{\nabla} c\, \mathrm{dV} + \int_{\mathrm{B}} \kappa^{*} c\,(1-c)\,\Delta c \Delta N^{\mathrm{I}}\, \mathrm{dV} \\
& + \int_{\mathrm{B}} (\mathbf{B}^{\mathrm{I}}_{c})^{\mathrm{T}} \boldsymbol{\nabla} \lambda\, \mathrm{dV} + \int_{\mathrm{B}} \lambda \Delta N^{\mathrm{I}}\, \mathrm{dV}, \qquad (5.52) \\
\mathrm{R}^{\mathrm{I}}_{\lambda} = & \int_{\mathrm{B}} \Delta c\, N^{\mathrm{I}}\, \mathrm{dV} + \int_{\mathrm{B}} (\mathbf{B}^{\mathrm{I}}_{c})^{\mathrm{T}} \boldsymbol{\nabla} c\, \mathrm{dV} - \frac{1}{\alpha} \int_{\mathrm{B}} \lambda\, N^{\mathrm{I}}\, \mathrm{dV}. \qquad (5.53)
\end{aligned}
$$

Here, $\underline{\mathbf{S}}$ is the normalized second Piola–Kirchhoff stress tensor in Voigt notation. For more details on $\partial \mu^{e}/\partial c$, $2\partial \mu^{e}/\partial \mathbf{C}$, $\mathbf{G}^{\mathrm{I}}$, and the tangent matrices, the reader is referred to Appendix A.

5.3 Benchmark test of a bar

A bar with the dimensions 2μm × 2μm × 10μm, shown in the Fig. 5.1, is considered. The flux is given at one end, while on the four sides, as well as at the bottom, a flux-free boundary condition is defined. This flux is applied for a period of 400 s, and after its removal the system will evolve to the equilibrium state. As for the mechanical part, apart from necessary boundary conditions to prevent a rigid-body translation, we discuss two special cases: a free standing and a fully constrained bar.

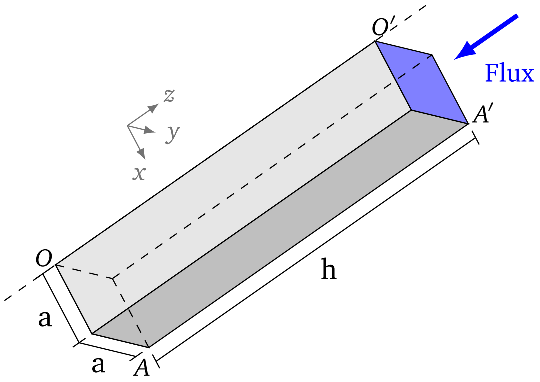

Current density (i)	$0.1\,\mathrm{A/m^2}$
Flux duration (t)	$400\,\mathrm{s}$
Measurements $(a \times a \times h)$	$1 \times 1 \times 10\,\mu\mathrm{m}^3$
Initial conc. (c_0)	0.25
Phase para. (χ)	2.5
Interface para. (κ)	$1.0 \times 10^{-10}\,\mathrm{J\,m^2/mol}$
Bulk mod. slope (K_0)	1 GPa (Default)
Reference conc. $(\mathrm{c}_{\mathrm{ref}})$	10.0

FIGURE 5.1. *Geometry and parameters of the bar under incoming flux at one end. For symmetry reasons, only one quarter of the bar is modeled.* $\overline{OO'}$ *is the center line of the bar. All other parameters are given in Table 5.1.*

5.3.1 Free standing case

Fig. 5.2 shows the distribution of the concentration and stresses at different instants of time when the bar is free to expand. After the flux comes in, phase separation initiates at the flux-end.

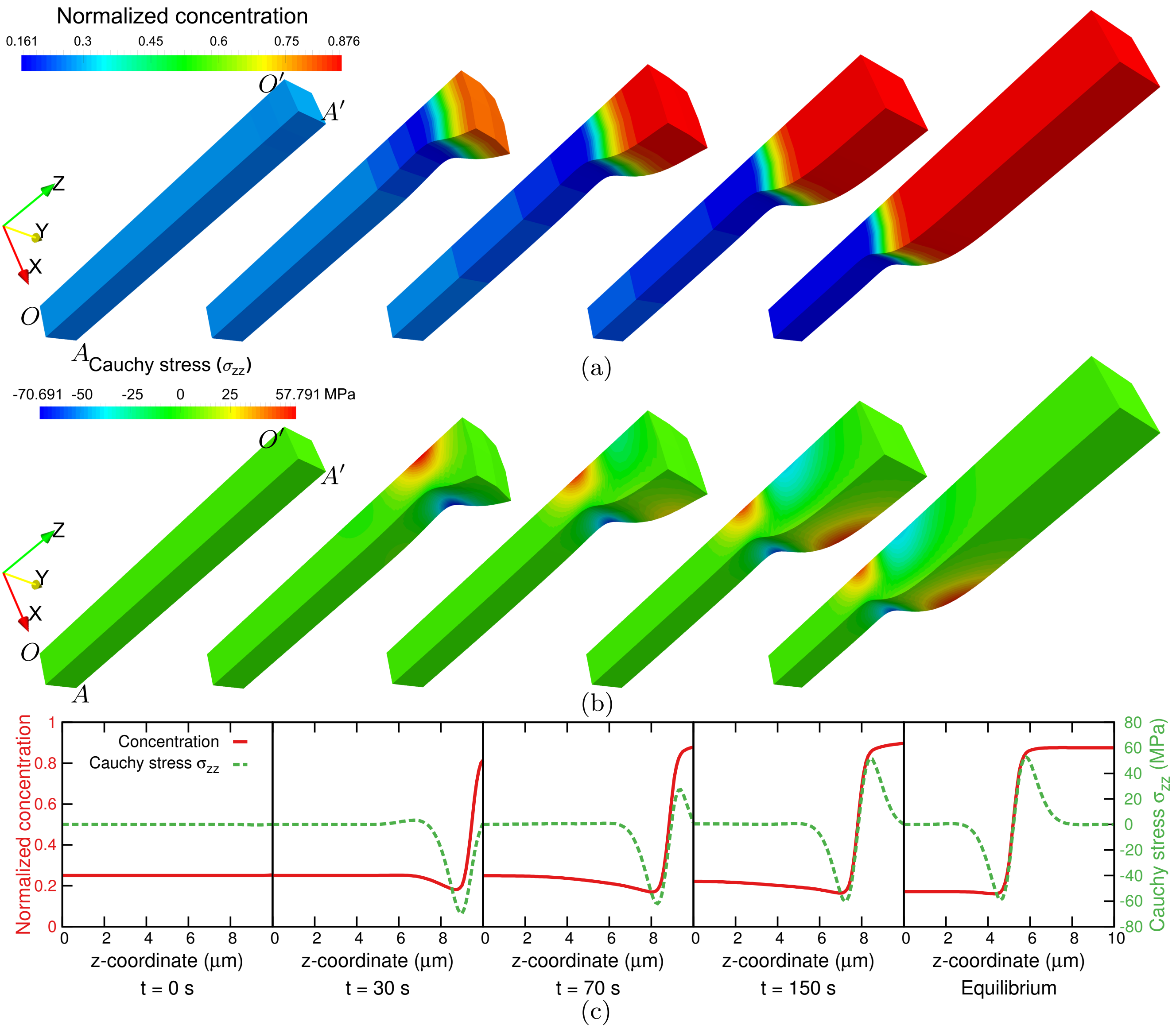

Figure 5.2. *Simulation results of the freestanding bar. (a) and (b) show snapshots of the contour plots of concentration and stresses, respectively, at different points in time. (c) shows the field distribution along outer edge* $\overline{AA'}$.

The interface moves towards the other end as the flux comes in continuously. The two-phase system can also be recognized by its deformation, which can be identified as a swollen top and a slim tail. The interface is slightly bent. The interior of each phase is stress-free. However, as shown in Fig. 5.2(b), intensified stresses are present at the interface due to an uneven chemically induced swelling. Along the center line $\overline{OO'}$, the interface experiences tensile stresses near the shrinking part and compressive stresses near the swelling part. Along the edge $\overline{AA'}$, we observe the opposite behavior: tensile stresses near the swelling part and compressive stresses near the shrinking part. Furthermore, as we can see from Fig. 5.2(c), along the corner edge $\overline{AA'}$, both tensile and compressive stresses peak at the point where the interface begins/ends.

5.3.2 Fully constrained case

In the free standing case, since stresses are only generated near the interface, mechanical contribution to phase separation is negligible. However, when the mechanical constraints are strong, phase separation can be diminished or even suppressed due to the high elastic energy.

The evolution of the species concentration is similar to that in the freestanding case. Here the concern is given to the equilibrium concentrations. Although it is difficult to find an analytical solution for the Cahn–Hilliard equation, especially when it is coupled with mechanical stresses, it is possible to obtain the concentrations within two homogeneous phases in equilibrium by solving Eqs. (B.1) and (B.10)–(B.13) in Appendix B, which are based on the common tangent construction. For a material with varying bulk modulus $K_c = \mathrm{K}_0(\mathrm{c}_{\mathrm{in}} - c)$, with $\mathrm{c}_{\mathrm{in}} = 10.0$, the equilibrium concentrations under different bulk modulus are plotted as solid line in Fig. 5.3(a). Note that the bulk modulus is concentration-dependent. The equilibrium concentrations are obtained at the intersection points of the green curve and the line of $K_c = \mathrm{K}_0(10.0 - c)$ instead of a horizontal line. For comparison, the results are also given to the model when the bulk modulus at all compositions remains constant. In both cases, the phase separation can be suppressed if K_c is large enough. However, there is a difference between these two curves before the suppression, which becomes more obvious as the bulk modulus increases. Particularly when $\mathrm{K}_0 = 1\,\mathrm{GPa}$, the model with varying elastic modulus leads to phase separation ($c_\alpha = 0.37$, $c_\beta = 0.67$). However, when the phase-dependency of the modulus is ignored, no phase separation can happen for the bulk modulus $K_{c_\alpha} = K_{c_\beta} = 9.63\,\mathrm{GPa}$, which is the corresponding modulus at $c = c_\alpha$ in the former model.

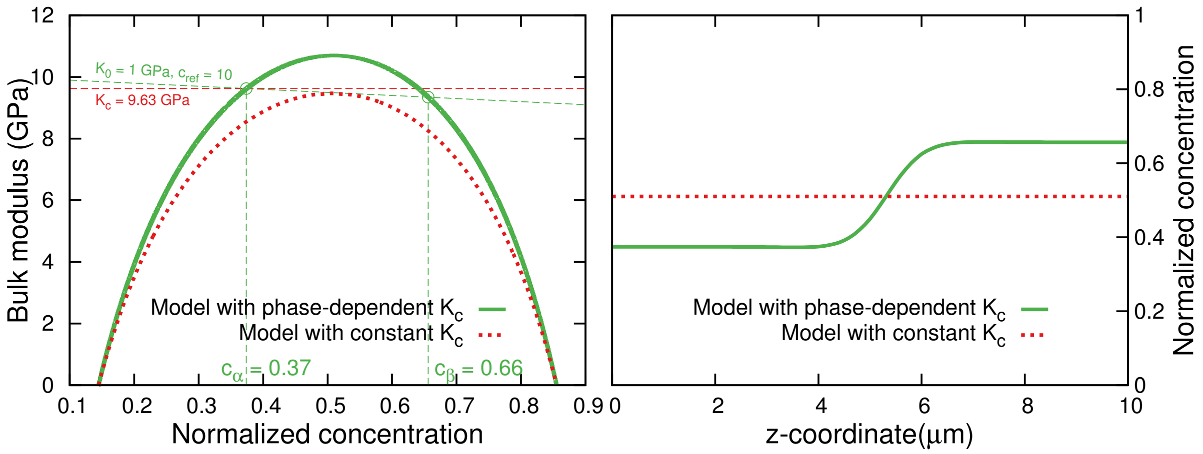

(a) (b)

Figure 5.3. *The influence of the bulk modulus on the phase separation under fixed displacement boundaries. (a) the analytical predictions. (b) the IGA simulation results of the equilibrium concentration profile along the longitude. The values of bulk concentrations in equilibrium reproduce the analytical predictions.*

Fig. 5.3(b) shows the corresponding IGA simulation results on the bar. It can be seen that the numerical results of the equilibrium concentrations in the model with varying modulus agree very well with the analytical results. Meanwhile, phase separation was not observed in the calculation results of the model with constant modulus, which agrees also with the analytical prediction. These agreements validate the mechanically coupled diffusion model presented in Section 5.1 and its IGA implementation. It also indicates that, for a more accurate study of phase separation behavior, it is necessary to take the phase-dependency of the elastic moduli into account.

5.3.3 Discussion of interface thickness

In Section 4.3, we have discussed the interface thickness in an uncoupled Cahn–Hilliard model, where the mechanical stresses are absent. If the mechanical coupling is taken into account, the interface thickness can be greatly influenced. Take the fully constrained bar as an example. Fig. 5.4(b) shows the simulation results of interface thickness versus $\sqrt{\kappa}$ for different bulk moduli. It can be observed that in general, the interface thickness increases first linearly with $\sqrt{\kappa}$ before the "surface effect" begins to slow down the growth. At a certain point, the line breaks because the phase separation is suppressed. Moreover, it can also be observed that the interface thickness in the materials with larger bulk modulus grows faster with increasing κ, and consequently the phases separation is suppressed earlier. Since the effective range of κ is smaller in those materials, we can conclude that it is easier for materials with larger bulk modulus to reach the phase suppression. This can be seen in Fig. 5.4(a), where we plot the concentration profile along the z-axis in equilibrium for different bulk moduli and a constant $\kappa = 6.0 \times 10^{-10}\,\mathrm{J\,m^2\,mol^{-1}}$.

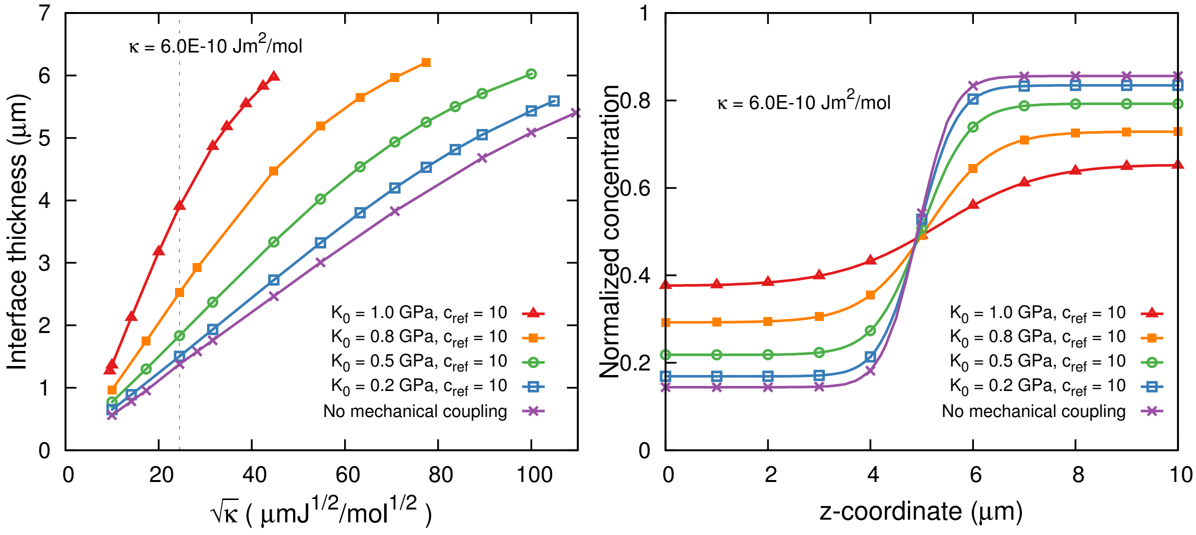

(a) (b)

Figure 5.4. *The influence of the bulk modulus on the thickness of the phase interface in a fully constrained bar. (a) the equilibrium concentration profile of materials with different bulk modulus when* $\kappa = 6.0 \times 10^{-10}\,\mathrm{J\,m^2\,mol^{-1}}$. *(b) shows that the interface thickness in materials with larger bulk modulus increases faster with increasing* κ .

A larger bulk modulus not only makes $\triangle c$ smaller, but also gives a more diffusive interface, namely, a smaller slope. In other words, compared to those with smaller bulk modulus, materials with larger bulk modulus will have a more diffusive and wider interface when κ is kept constant, and phase separation in those materials will be suppressed more easily.

5.4 Simulation results of spheroidal particles and a circular plate

As more general 3D cases, three spheroidal particles are considered in this section: a spherical particle with the radius $1\,\mu$m; an oblate spheroid with the semi-axes $1/2\,\mu$m, $\sqrt{2}\,\mu$m, $\sqrt{2}\,\mu$m; and a prolate spheroid with the semi-axes $2\,\mu$m, $1/\sqrt{2}\,\mu$m, $1/\sqrt{2}\,\mu$m. All of them share the same volume and boundary conditions as well as material law. Homogeneous normal flux is applied on the surface during the first 3 seconds. After removal of the flux, the system evolves towards its equilibrium. The particles are freestanding, therefore no further mechanical constraints are applied on the particle apart from those due to symmetry and restrictions of rigid-body movements. Parameters are given in Table 5.1. The mesh details are given in Chapter 4. Because of symmetry, only 1/8 of the whole particles are modeled. Please note that this symmetry will not always hold for a Cahn–Hilliard equation, even when a symmetric setup is given, as will be explained later; for those situations, models of full spheroids are needed for the simulation. Here we only focus on the symmetric solution.

TABLE 5.1. *The parameters for the simulation of spherical and spheroidal particles.*

Gas constant (R)	$8.32\,\mathrm{J\,mol^{-1}\,K^{-1}}$
Absolute temperature (T)	$283\,\mathrm{K}$
Diffusivity (D)	$7.08 \times 10^{-15}\,\mathrm{m^2\,s^{-1}}$
Faraday's constant (F)	$96\,485\,\mathrm{C\,mol^{-1}}$
Partial molar volume (Ω)	$3.497 \times 10^{-6}\,\mathrm{m^3\,mol^{-1}}$
Maximum concentration ($\mathrm{c_{max}}$)	$2.29 \times 10^{4}\,\mathrm{mol\,m^{-3}}$
Phase parameter (χ)	2.5
Interface parameter (κ)	$1.0 \times 10^{-10}\,\mathrm{J\,mol^{-1}\,m^2}$
Length scale ($\mathrm{L_0}$)	$1\,\mu\mathrm{m}$
Bulk modulus slope ($\mathrm{K_0}$)	100 MPa
Shear modulus slope ($\mathrm{G_0}$)	100 MPa
Reference concentration ($\mathrm{c_{in}}$)	10.0
Electric current density (i)	$2.0\,\mathrm{A\,m^{-2}}$
Charging duration ($\mathrm{T_{flux}}$)	3.0 s
Initial concentration (c_0)	0.25

5.4.1 Spherical particle

The spherical particle is a special case of spheroids which possesses symmetries in all directions. Therefore, one may expect—for a symmetric setup of initial and boundary conditions—a rotationally symmetric concentration profile, known as the "core-shell" structure. However, Huttin [135] has shown that this symmetry can be destroyed at the equilibrium state since an asymmetric concentration profile leads to a lower total free energy, and is thus more stable in the long run. However, if the flux rate is homogeneous on the surface and large enough compared to the diffusivity, the diffusion process is limited by the isotropic bulk transport and the dynamics of the shrinking core are achieved. A more detailed discussion of anisotropic diffusion and the transport in different limits is discussed in Chapter 6.

The simulation results of the spherical particle are shown in Fig. 5.5. When a homogeneous

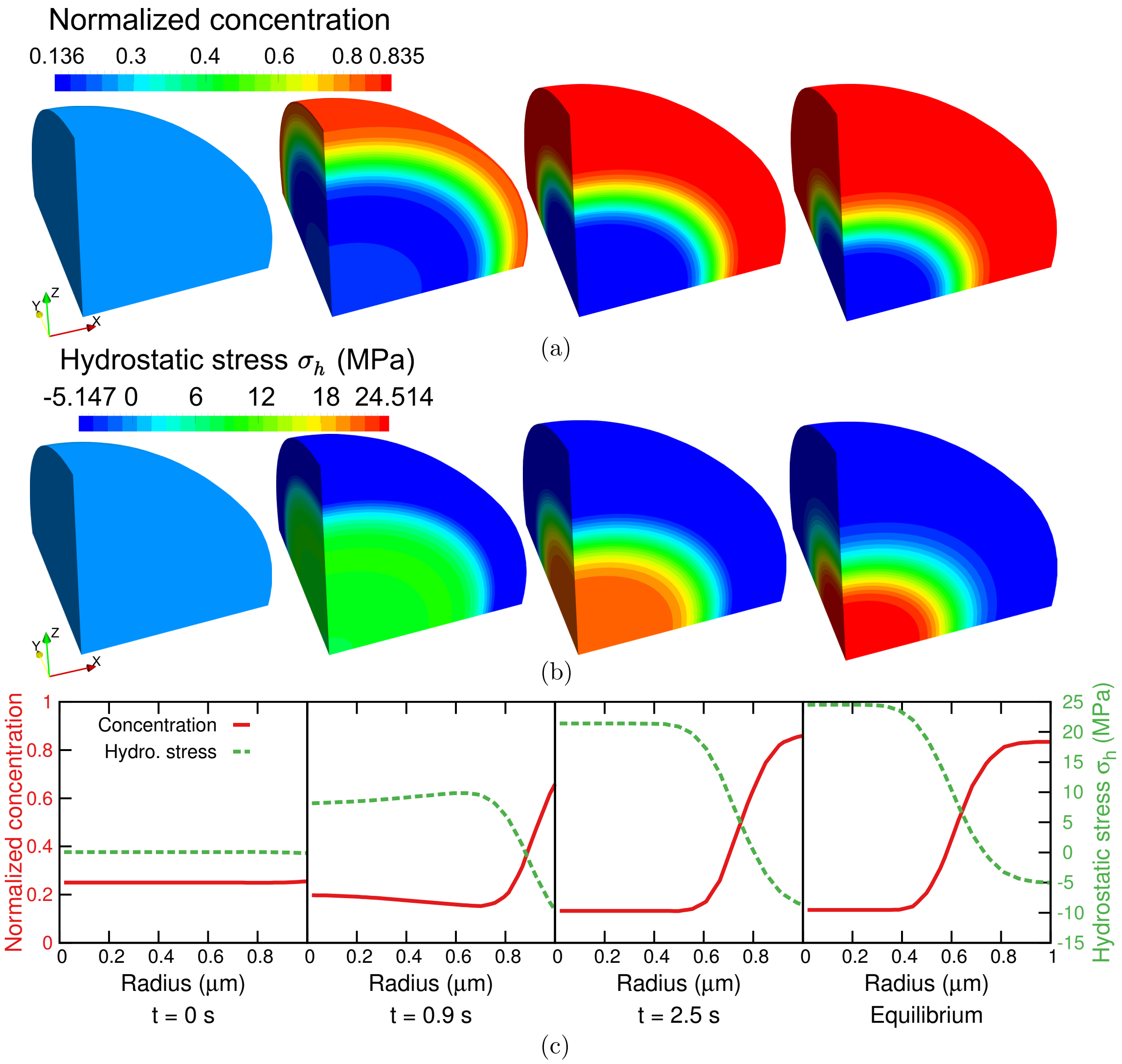

FIGURE 5.5. *The snapshots of the simulation results of a sphere at different times. (a) shows the concentration and (b) the hydrostatic stress distribution. (c) is the corresponding plot along the radius.*

flux is applied on the surface, the Li-rich phase initiates homogeneously from the surface. Thus a spherical core is formed, surrounded by a homogeneous shell. As the flux comes in continuously, the interface approaches the center, and the core shrinks. The lithiated outer layer expands stronger than the core, and a swelling of the outer layer is observed. Fig. 5.5(b) shows the contour plots of the hydrostatic stress. Although, from an engineering point of view, stress measures such as von Mises stress can give a better prediction of the failure of the material, the hydrostatic stress is plotted in this section since it is more relevant to the diffusion process and thus can be linked to the distribution of the concentration more easily. From Fig. 5.5(b) it can be observed that although it is a freestanding particle, there are compressive stresses built up in the outer layer and tensile stresses in the core region. The flux is only applied for 3 seconds, the particle is not fully lithiated, and there are two phases in equilibrium. However, if more flux is applied, the particle can be fully lithiated. As a consequence, in equilibrium there is only one phase left, and no stresses remain.

5.4.2 Oblate spheroidal particle

In spheroids other than spheres, the core-shell phase separation may not occur due to the geometric anisotropy. As shown in Fig. 5.6, the Li-rich phase initiates first around the particle's equator and subsequently appears around the semi-minor axis. The interface intersects with the particle surface, which resembles the behavior in a plate. After two Li-rich regions emerge, the interface on the surface vanishes and remains only within the particle. With further flux,

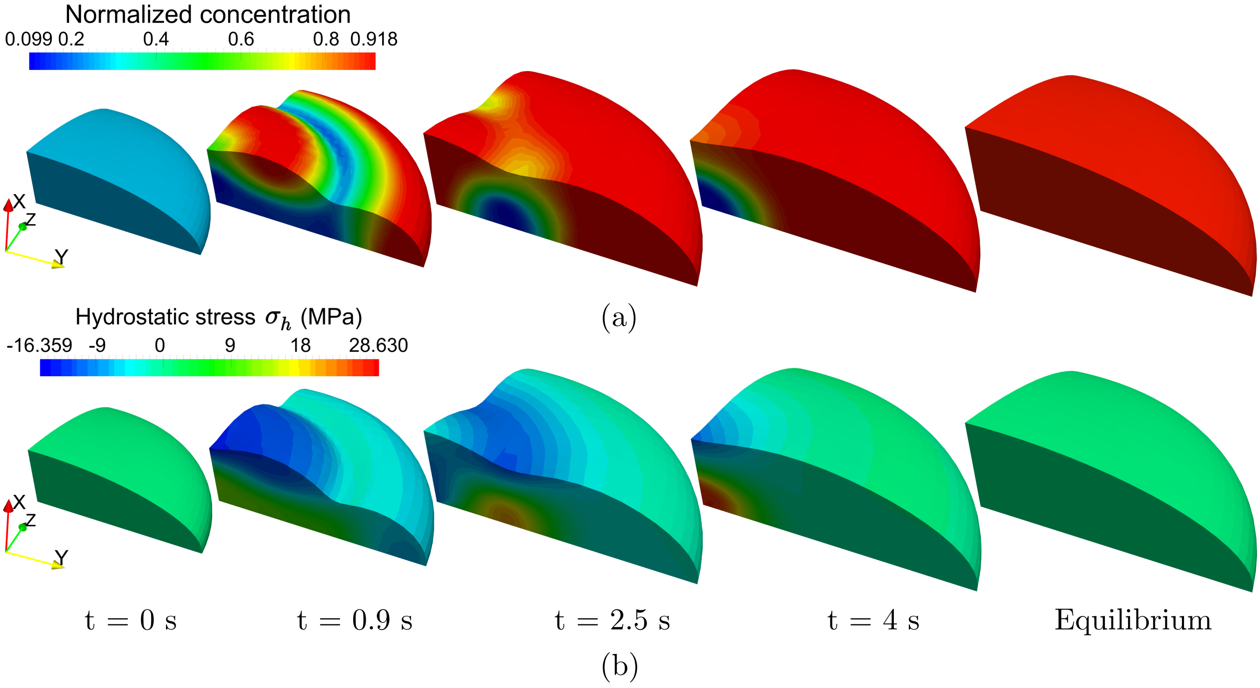

FIGURE 5.6. *The snapshots of the (a) concentration and (b) hydrostatic stress distribution of an oblate spheroid particle at different time.*

the interface moves to the center of the particle and disappears. In other words, there exists only the Li-rich phase. The particle is thus fully lithiated. In contrast, in the spherical particle two phases still coexist after the same charging time under the same flux density, as is shown in Fig. 5.5. This is due to the fact that the surface area of the oblate particle is larger than that of the spherical particle with the same volume. That is, the oblate particle will be lithiated further than the spherical particle of the same volume.

At the equator, the stresses are almost negligible. However, due to inhomogeneous deformation, the stress generated in the center part of the oblate spheroidal particle is higher than that in the spherical particle. After the single-phase stage is reached, the stress drops, and the particle eventually becomes stress-free.

5.4.3 Prolate spheroidal particle

For a needle-like particle as shown in Fig. 5.7, the Li-rich phase occurs first at the particle's tip, and subsequently at the equator. The two Li-rich regions emerge at the surface, and the interface leaves the surface. Thus, a core-shell type of phase separation appears. The shape of the core resembles first that of the particle geometry, and then evolves to a spherical type in order to minimize the interface area. After the same duration of the incoming flux, the equilibrium state consists of still two phases, unlike in the oblate particle, but the volume fraction of the Li-deficient phase is much smaller than that in the spherical particle. This can also be explained by the fact that the surface area of this prolate particle is less than that of the oblate particle, but larger than that of the spherical particle. In fact, for the particles with the indicated aspect ratios, the surface areas of the sphere, oblate spheroid, and the prolate spheroid are $12.5664\,\mu\mathrm{m}^2$, $15.4212\,\mu\mathrm{m}^2$ and $14.6303\,\mu\mathrm{m}^2$, respectively.

Due to relaxation, the tip remains almost stress free throughout the whole process. At the stage of the core-shell type of phase separation, the outer layer is compressed, while the inner layer is stretched, similar to the situation in the spherical particle. Nevertheless, the stress level is slightly higher than that in the spherical particle. Based on the comparison between the results shown in Fig. 5.5 and Fig. 5.7, one can see that the highest hydrostatic tensile stress in the prolate spheroid (26.44 MPa) is slightly higher than that in the sphere (24.514 MPa). The compression shows the same tendency (16.71 MPa v.s. 15.948 MPa). We also computed the von Mises stress in the different particles, supporting this observation. In particular, we have the maximum von Mises stress of 25.714 MPa in the sphere, 35.817 MPa in the oblate spheroid, and 26.1 MPa in the prolate spheroid. This is different from the results obtained by the dilute solution model [111], where it was concluded that usually slender particles exhibit lower overall stress levels. This discrepancy implies that the stress situation can be very different when phase separation is considered.

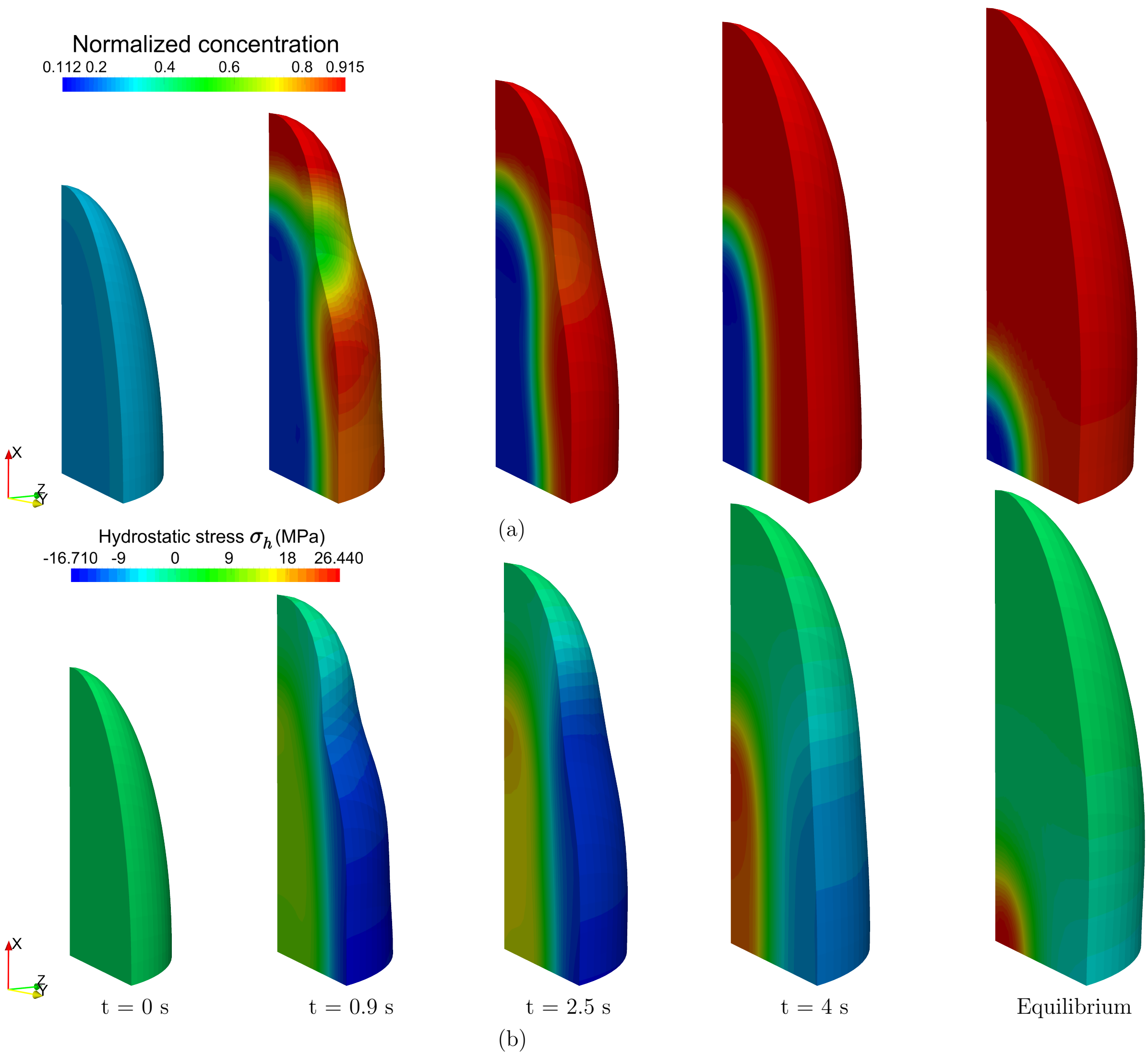

FIGURE 5.7. *The snapshots of (a) the concentration and (b) the hydrostatic stress distribution in a prolate spheroidal particle at different times.*

5.4.4 Circular disc

In this section, a disc shown in Fig. 5.8 is considered. Because of symmetry, only one eighth of the plate is simulated. xOy, yOz, xOz are the three planes of symmetry. Homogeneous flux comes into the disc from the side surface for a certain period. After removal of the flux, the system evolves to the equilibrium state. As for the mechanical part, the plate is not constraint, apart from necessary boundary conditions to prevent rigid-body translation and rotation, which are applied at the planes of symmetry.

The parameters which are different from Table 5.1 are shown in Table 5.2.

Simulation results are shown in Fig. 5.9. When the homogeneous flux is applied on the side surface, Li-rich phase initiates homogeneously from the curved surface. Thus a core-shell structure with a diffusive interface is formed. As the flux comes in continuously, phase interface

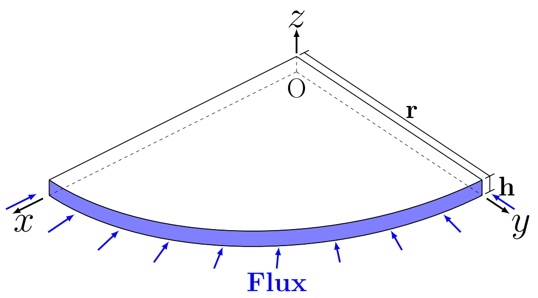

Figure 5.8. *Schematic of the simulated disc. Flux comes in homogeneously from the edge. Mechanical constraints are applied at the planes of symmetry (xOy, yOz, xOz) to prevent rigid-body translation and rotation.*

Table 5.2. *Parameters for the simulation of the disc. All other parameters are listed in Table 5.1.*

Radius (r)	$1\,\mu$m	Thickness (h)	$0.1\,\mu$m
Interface parameter (κ)	$3 \times 10^{-12}\,\mathrm{J\,m^2\,mol^{-1}}$	Initial concentration (c_0)	0.27
Flux density ($\hat{j}_R$)	$1.6 \times 10^{-6}\,\mathrm{mol\,m^{-2}\,s^{-1}}$	Flux duration (t)	2824 s

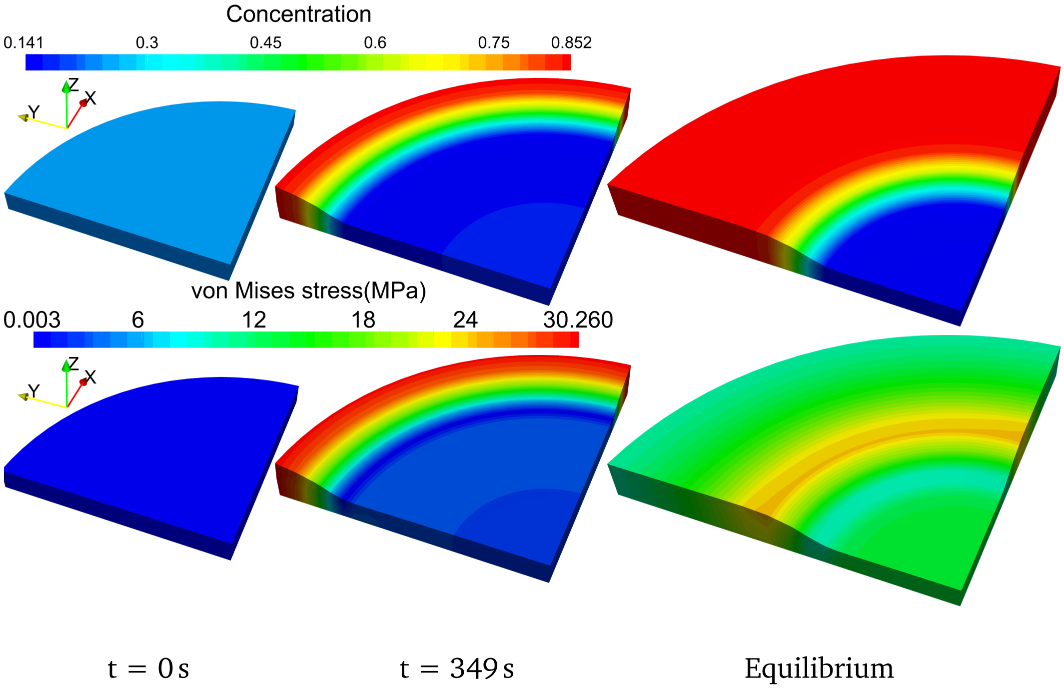

t = 0 s t = 349 s Equilibrium

Figure 5.9. *Simulation results of the concentration and the von Mises stress distribution at different time point in the disc.*

approaches the center of the plate. From the deformation one can observe a circular depression surrounded by a ring plateau. The formation of these two plateaus is the result of phase separation. The von Mises stress appears also from the edge, where the phase interface forms initially. High von Mises stress moves along with the interface and locates between the phase interface and the Li-rich phase. The highest von Mises stress of all time, however, occurs at t =

349 s, when the interface is forming at the surface, and as the interface approaches the center, the von Mises stress releases. This indicates that the plastic flow will most possibly occur during the formation of two phases at the surface.

5.5 Summary

A phase-field model for the mechanical response and a Cahn–Hilliard-type diffusion in hyperelastic solids was developed and implemented with the isogeometric finite element method. For the constitutive part, we took into account concentration-dependent elastic properties. Its influence on the phase separation was demonstrated.

For the numerical part, we employed isogeometric analysis to achieve the C^1-continuity required by the model. To deal with the additional boundary condition in the Cahn–Hilliard equation, we introduced a perturbed Lagrange multiplier as a weak constraint.

The models were applied for the analysis of the phase separation and stress generation in bars, spheroidal particles and a circular disc. The following conclusions are made. Firstly, phase separation with coexistent Li-rich and Li-poor phases is achieved in particles of different geometries. Secondly, phase separation can be suppressed by increasing elastic stresses and by reducing the particle size. Thirdly, the Li-rich phase will generally experience compressive stresses while the Li-poor phase is subject to tensile stresses. The stress state obtained by the phase-field model is very much different from those obtained by a dilute model, since the coexistence of the two phases will lead to inhomogeneous deformation and thus higher stresses. Lastly, given isotropy of the geometry as well as of the initial and boundary conditions, together with a proper value of flux versus diffusivity, the formation of a shrinking core in spherical particles can be achieved. In plate- and needle-like particles, on the other hand, although the interface intersects with the particle surface initially, it will leave the surface after a certain amount of flux and a core-shell structure can be observed before a full lithiation, when the whole system stays at the Li-rich phase. In the circular disc, similar phenomenon as in the sphere is observed, where the core-shell structure is retained.

Chapter 6

Electro-chemo-mechanical behavior of an electrode particle

As stated in Chapter 2, in the electrochemical system of a battery, the reaction rate is a key issue since it is directly related to the charge/discharge performance of a battery. A faithful mathematical description of the reaction process plays thus a key role in the modeling of the charge/discharge process in an electrode. In Chapter 5, Neumann boundary conditions are imposed to mimic the galvanostatic charge/discharge process. As for the potentiostatic charge/discharge, the application is not that straightforward. An intuitive treatment is the imposition of the Dirichlet boundary condition Eq. (4.17), as mentioned in Section 4.1, under the assumption that the whole process is limited by bulk diffusion and that no phase separation occurs during the insertion/extraction. As a more general description, the phenomenological Butler–Volmer-type reaction equation is proposed. However, since it is based on a dilute solution model, it may not be able to account for a separation of phases with different Li concentrations in materials such as silicon and $LiFePO_4$. In the work of Singh et al. [23], a generalized Butler–Volmer kinetics model was proposed, which includes the influence of the phase transition on the surface reaction in a 1D case. Based on this model, Bai et al. [24] discussed the suppression of phase separation under large reaction rate. The two dimensional case, which also coupled the Cahn–Hilliard bulk diffusion was studied by Dargaville and Farrell [25]. Using different limits of the 1D case, they discussed when the orthotropic diffusivity becomes more isotropic. More applications of Butler–Volmer equation in the coupled chemo-mechanical problems can be found in [131, 136].

Further, the mechanical degradation of the electrode particle is widely believed to be closely related to the failure of batteries. In the last chapter, it is concluded that intensified stresses accumulate at phase interface. This is already very much different from dilute diffusion models, where the concentration smoothly changes with the incoming/outgoing flux, accompanied by a homogeneous “breathing-like” expansion and shrinkage of particles, which will hardly lead to the failure of the electrode particles. Moreover, as Rohrer et al. [137, 138] pointed out from first principle calculations, the anisotropic volumetric expansion in silicon will indeed initiate cracking, especially in large particles, where the separation between amorphous and crystalline silicon phases can not be suppressed. Apart from silicon, in positive electrode materials such as $LiFePO_4$, striped phase boundaries have been observed by Chen et al. [139, 140] because of

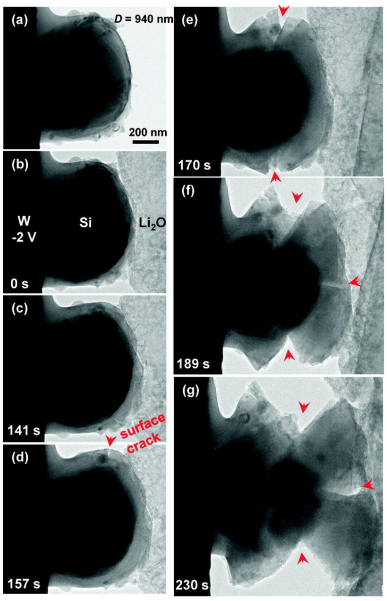

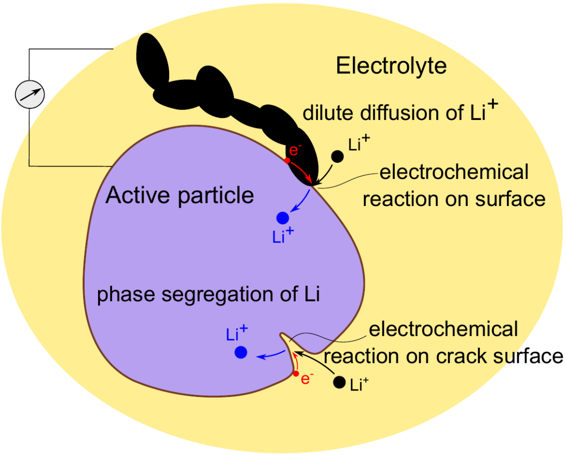

(a) *Phase separation and crack propagation in silicon nanoparticles during lithiation [141].*

(b) *Schematics of electro-chemo-mechanical model of the electrode active particle embedded in the composite electrode depicted in Fig. 2.1. The lithium ions diffuse through the electrolyte and insert into the electrode particle through an electrochemical reaction, which occurs on the particle surface and on the cracked surface.*

FIGURE **6.1.** *Fracture, phase separation and the reaction of the electrode particles.*

strong anisotropy and phase separation. It demonstrated the necessity to extend the chemo-mechanical model in Chapter 5 to the model incorporating the anisotropic diffusion and phase separation for describing the bulk behavior of the particle.

The cracks, as a result of chemo-mechanical interactions, initiate and propagate in the battery electrodes, leading to an irreversible capacity fade. In silicon nanoparticles, as shown in Fig. 6.1(a), amorphous silicon forms around the crystalline silicon during lithiation; the crack initiates from the surface and propagate into the core of the nanoparticle. The description of the dynamics of crack propagation in lithium ion battery electrode particles has long been a challenge. Only a few attempts are available in the literature, such as [142–144]. Recently, as the concept of phase-field modeling found more applications in different disciplines, phase-field methods have also been introduced to predict the crack propagation coupled with diffusion. In phase-field fracture models, the damaged and undamaged parts of the material are considered as two different phases, indicated by the distinct values of the order parameter. Schneider et al. [145] proposed a model coupling the mechanics with a general multiphase and multicomponent phase-field approach to describe the diffusion and crack propagation in brittle materials. Liang et al. [146] developed a phase-field model to predict the crack evolution in $LiFePO_4$ cathode nanoparticles in of Li-ion batteries. The phase-field fracture simulation in silicon anodes was also carried out by Zuo et al. [147] and Klinsmann et al. [148–150]. Recently, Miehe et al. [151] conducted a comprehensive study on chemo-mechanical induced fracture in the framework of phase-field fracture modeling, and considered the chemical reactions not only on exterior surfaces but also on fracture surfaces.

In this chapter, a phase-field model of the electrode particle illustrated in Fig. 6.1(b) is proposed, which accounts for electrochemical reactions on different interior and exterior surfaces of phases and crack surfaces based on the fully coupled Cahn–Hilliard diffusion–reaction model proposed in the work of Bazant [152]. We base our model in this chapter on that from the last chapter. Firstly, in Section 6.1, the electrochemical reactions on the particle surface is modeled through the modified Butler–Volmer equation, considering orthotropic Cahn–Hilliard diffusion and phase separation. Two corresponding examples with different particles are conducted in Section 6.2 to discuss the interaction between the reaction rate and the phase separation behavior. In Section 6.3, the model is further extended to simulate and predict fracture in the particle, by introducing a phase-field fracture order parameter ξ. The electrochemical reaction on the crack surface is thus also considered as a source in the diffusion equation. Finally, three examples are presented in Section 6.4 to discuss the crack propagation and branching during delithiation in the cylindric particles and spherical particles.

6.1 Electro-chemo-mechanical model of the electrode particle

In this section, we formulate a mechanically coupled reaction–diffusion model, taking into account orthotropic diffusion and phase separation. In this model, the flux that drives the species is defined in the current configuration, which is more physically sound than the model in Chapter 5, where the flux is defined in the undeformed configuration for numerical simplicity.

6.1.1 Free energy density and governing equations

The free energy density of this model is based on the one in Section 5.1, with an extension to incorporate orthotropic phase separation. As a short summary, the free energy density is

$$\psi_{\mathrm{R}}(c_{\mathrm{R}}, \boldsymbol{\nabla}_{\mathrm{R}} c_{\mathrm{R}}, \mathbf{C}) = \psi^{c}_{\mathrm{R}}(c_{\mathrm{R}}) + \psi^{i}_{\mathrm{R}}(\boldsymbol{\nabla}_{\mathrm{R}} c_{\mathrm{R}}) + \psi^{e}_{\mathrm{R}}(c_{\mathrm{R}}, \mathbf{C}), \tag{6.1}$$

where

$$\psi^{c}_{\mathrm{R}}(c_{\mathrm{R}}) = \mathrm{RTc_{max}}[c\ln c + (1-c)\ln(1-c)] + \mathrm{RTc_{max}}\chi c(1-c), \tag{6.2}$$

$$\psi^{i}_{\mathrm{R}}(\boldsymbol{\nabla}_{\mathrm{R}} c_{\mathrm{R}}) = \frac{1}{2}\mathrm{c_{max}}\boldsymbol{\nabla}_{\mathrm{R}} c \cdot \mathbf{K}\boldsymbol{\nabla}_{\mathrm{R}} c, \tag{6.3}$$

$$\psi^{e}_{\mathrm{R}}(c_{\mathrm{R}}, \mathbf{C}) = J^{c}\,\psi^{e}_{\mathrm{I}}(c_{\mathrm{R}}, \mathbf{C}^{e}) = J^{c}\left[\frac{K_{c}}{2}\left(\frac{J}{J^{c}} - 1\right)^{2} + \frac{G_{c}}{2}\left(\bar{I}_{1} - 3\right)\right]. \tag{6.4}$$

More details of this model please refer to Section 5.1. In Eq. (6.3), different from last chapter, $\mathbf{K}$ is a diagonal tensor which is defined as

$$\mathbf{K} = \begin{bmatrix} \kappa_x & & \\ & \kappa_y & \\ & & \kappa_z \end{bmatrix} \tag{6.5}$$

to exhibit the interfacial orthotropy. The parameters κ_x, κ_y and κ_z are related to the interfacial thickness in the corresponding directions. Recall Eq. (4.12), we know that, for a 1D case, if the elastic influence is absent, one have the following relation of the interfacial thickness s and energy Ψ^i

$$s \propto \sqrt{\frac{\kappa}{\triangle\psi^c_{\max}}}, \quad \Psi^i \propto \int_{c_\alpha}^{c_\beta} \sqrt{\kappa \triangle\psi^c}\,\mathrm{d}c. \tag{6.6}$$

It can be further concluded that, in the 3D case, if the interfacial parameter κ in one direction is much smaller than those in the other two directions, the interfacial thickness and the energy expended across the interface will be much smaller in this direction. For instance, $\kappa_x \ll \kappa_y = \kappa_z$ gives $s_1 \ll s_2 = s_3$ and $\Psi^i_1 \ll \Psi^i_2 = \Psi_3$. This relation will be used later to determine the mobility tensor. The second Piola–Kirchhoff stress tensor and the chemical potential are

$$\mathbf{S}_\mathrm{R} = J^c \left[K_c J^e \left(J^e - 1\right) \mathbf{C}^{-1} + G_c J^{-\frac{2}{3}} \left(\mathbf{1} - \frac{1}{3} I_1 \mathbf{C}^{-1} \right) \right], \tag{6.7}$$

$$\begin{aligned} \mu_\mathrm{R} = {} & \mathrm{RT}\left[\ln c - \ln(1-c) + \chi\left(1-2c\right)\right] - \boldsymbol{\nabla}_\mathrm{R} \cdot \mathbf{K} \boldsymbol{\nabla}_\mathrm{R} c \\ & + \frac{\Omega K_c}{2}\left[1 - (J^e)^2\right] + \frac{\Omega G_c}{2}\left(\bar{I}_1 - 3\right) + \frac{J^c}{\mathrm{c}_{\max}} \left[\frac{K_c'}{2}\left(J^e - 1\right)^2 + \frac{G_c'}{2}\left(\bar{I}_1 - 3\right) \right]. \end{aligned} \tag{6.8}$$

As for the governing equations. The mechanical local force balance is the same as last chapter, which reads

$$\boldsymbol{\nabla}_\mathrm{R} \cdot \mathbf{P}_\mathrm{R} = \mathbf{0} \quad \text{in} \quad \mathrm{B}_\mathrm{R} \times (0, \mathscr{T}), \tag{6.9}$$

where $\mathbf{P}_\mathrm{R}$ is the first Piola–Kirchhoff stress defined in Eqs. (5.17) and (6.7). And the corresponding Dirichlet and Neumann boundary conditions are

$$\mathbf{u} = \hat{\mathbf{u}} \qquad \text{on} \quad \mathrm{S}_{\mathrm{R}\mathbf{u}} \times (0, \mathscr{T}), \tag{6.10}$$

$$\mathbf{P}_\mathrm{R} \cdot \boldsymbol{n}_\mathrm{R} = \hat{\mathbf{t}} \quad \text{on} \quad \mathrm{S}_{\mathrm{R}\mathbf{t}} \times (0, \mathscr{T}). \tag{6.11}$$

The molar concentration c_R is a conserved order parameter and subject to the Cahn–Hilliard-type kinetics. In Eq. (5.19), the species are assumed to be driven by a flux defined in the reference configuration which leads to a simplification in the finite element implementation. In this chapter, a more physically based kinetics is employed which defines the flux by the gradient of chemical potential at the current configuration. More specifically,

$$\frac{\partial c_\mathrm{C}}{\partial t} = -\boldsymbol{\nabla}_\mathrm{C} \cdot \boldsymbol{j}_\mathrm{C} \quad \text{in} \quad \mathrm{B}_\mathrm{C} \times (0, \mathscr{T}), \tag{6.12}$$

with

$$\boldsymbol{j}_\mathrm{C} = -\boldsymbol{M}_c \boldsymbol{\nabla}_\mathrm{C} \mu_\mathrm{R}, \tag{6.13}$$

where the subscript C denotes quantities defined in the current configuration. The mobility tensor $\boldsymbol{M}_c$ in Eq. (6.13) is defined as

$$\boldsymbol{M}_c = c(1-c)\begin{bmatrix} \mathrm{M}_x & & \\ & \mathrm{M}_y & \\ & & \mathrm{M}_z \end{bmatrix} = c(1-c)\mathbf{M}, \tag{6.14}$$

with $c(1-c)$ representing a degenerated mobility towards $c = 0$ and $c = 1$. On the boundary surface $\partial \mathrm{B}_\mathrm{C}$, the flux boundary condition is imposed

$$\boldsymbol{j}_\mathrm{C} \cdot \boldsymbol{n}_\mathrm{C} = -\hat{j}_s \quad \text{on} \quad \partial \mathrm{B}_\mathrm{C} \times (0, \mathscr{T}), \tag{6.15}$$

where the flux $\hat{j}_s$ depends on the electrochemical reaction, described by a phenomenological Butler–Volmer equation. This is different from Eq. (5.22), where a constant flux is given to mimic the galvanostatic charge/discharge process. More details will follow in Section 6.1.2.

Based on density functional theory calculations, Rohrer et al. [138] have found that the anisotropy of mobility is a consequence of orientation-dependent interface energies and that high-energy interfaces are more mobile than low-energy interfaces. By recalling Eq. (6.6), it can be concluded that a higher κ leads to a larger M. For simplicity, a proportional relation is assumed, that is, $\mathrm{M}_x/\kappa_x = \mathrm{M}_y/\kappa_y = \mathrm{M}_z/\kappa_z$. The chemical potential μ_R expresses the free energy change for adding/extracting one mole lithium to/from the system, thus being the same for any configuration. The subscript R only indicates the fact that it is calculated by quantities in the reference configuration. Given the condition that the total mass should be conserved in different configurations,

$$\int_{\mathrm{B}_\mathrm{C}} \frac{\partial c_\mathrm{C}}{\partial t}\,\mathrm{dB} = \int_{\mathrm{B}_\mathrm{R}} \frac{\partial c_\mathrm{R}}{\partial t}\,\mathrm{dB}, \tag{6.16}$$

equation Eq. (6.12) can be pulled back straightforwardly to the reference configuration as

$$\frac{\partial c_\mathrm{R}}{\partial t} = \boldsymbol{\nabla}_\mathrm{R} \cdot \left[c(1-c)J\mathbf{F}^{-1}\mathbf{M}\mathbf{F}^{-\mathrm{T}}\boldsymbol{\nabla}_\mathrm{R}\mu_\mathrm{R}\right] \quad \text{in} \quad \mathrm{B}_\mathrm{R} \times (0, \mathscr{T}). \tag{6.17}$$

The corresponding boundary conditions and initial conditions are

$$\mathbf{j}_\mathrm{R} \cdot \boldsymbol{n}_\mathrm{R} = -\hat{j}_s \qquad \text{on} \quad \partial \mathrm{B}_\mathrm{R} \times (0, \mathscr{T}), \tag{6.18}$$

$$\mathbf{K}\boldsymbol{\nabla}_\mathrm{R} c \cdot \boldsymbol{n}_\mathrm{R} = 0 \qquad \text{on} \quad \partial \mathrm{B}_\mathrm{R} \times (0, \mathscr{T}), \tag{6.19}$$

$$c_\mathrm{R}(\mathbf{X}, 0) = c_{0\mathrm{R}}(\mathbf{X}) \quad \text{in} \quad \mathrm{B}_\mathrm{R}, \tag{6.20}$$

where

$$\mathbf{j}_\mathrm{R} = -c(1-c)J\mathbf{F}^{-1}\mathbf{M}\mathbf{F}^{-\mathrm{T}}\boldsymbol{\nabla}_\mathrm{R}\mu_\mathrm{R}. \tag{6.21}$$

For later discussion, a dimensionless activity a is introduced by

$$\mathrm{RT}\ln a = \mu_\mathrm{R}, \tag{6.22}$$

and an activity coefficient γ as the ratio $\gamma = a/c$. Note that, when $a = c$ and thus $\gamma = 1$, this model degenerates to an ideal dilute model.

6.1.2 Reaction on particle surfaces

On the particle surface, a Faradaic reaction

$$\mathrm{Li}^{+}_{(\mathrm{ely})} + \mathrm{e}^{-} + \mathrm{H} \rightleftharpoons \mathrm{LiH} \tag{6.23}$$

takes place, where H denotes the host material, as shown in Fig. 6.2. The resultant lithium inserts into the host material.

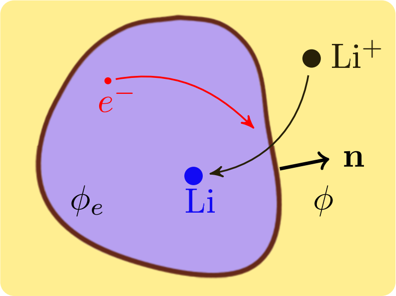

Figure 6.2. *Illustration of the electrochemical reaction on the surface*

The reaction rate is described by a phenomenological Butler–Volmer equation,

$$\hat{j}_s = \mathrm{c}_s \mathrm{R}_{\mathrm{BV}} = \mathrm{c}_s \frac{a_{+}^{1-\beta} a^{\beta}}{\tau_0 \gamma_{\mathrm{A}}} \left[\exp\left(-\beta \frac{\mathrm{F}\eta_{\mathrm{R}}^{s}}{\mathrm{RT}} \right) - \exp\left((1-\beta) \frac{\mathrm{F}\eta_{\mathrm{R}}^{s}}{\mathrm{RT}} \right) \right], \tag{6.24}$$

in which c_s with the unit of $\mathrm{mol\,m}^{-2}$ is the molar concentration of intercalation sites on the surface and R_{BV} is the reaction rate in unit s^{-1}. Moreover, τ_0 is the mean time for a single reaction step which will be set differently to mimic a slow or fast reaction process in the simulation. The parameter γ_{A} denotes the chemical activity coefficient of the activated state which is taken as $(1-c)^{-1}$, while β is a symmetry factor for a forward and backward reaction indicated in Eq. (6.23) and which is set to be 0.5. The Faraday constant F describes the amount of electric charge of one mole electrons. For more details on the coefficients of this model one can refer to the work of Bai et al. [24] and Dargaville et al. [25]. The definition of a has been introduced in Eq. (6.22). The parameters a_{+} and a are activities of lithium ion in the electrolyte and lithium in the host material, respectively. Since lithium diffuses in the electrolyte much faster than in the electrode [24], a_{+} is set to be unity for simplicity. For a similar reason, the activity of electrons a_{-} is also set to be 1. The surface overpotential η_{R}^{s} is defined as the electrostatic potential of the working electrode relative to a reference electrode of the same kind placed in the solution adjacent to the surface of the working electrode. It can be expressed in terms of the electrochemical potentials as

$$\mathrm{F}\eta_{\mathrm{R}}^{s} = \mu_{\mathrm{Li}} - \mu_{\mathrm{Li}^{+}} - \mu_{e^{-}}, \tag{6.25}$$

where μ_{Li}, μ_{Li^+}, μ_{e^-} are the electrochemical potentials of Li, Li$^+$ and e^-, respectively, which are expressed as

$$\mu_{\mathrm{Li}} = \mathrm{RT}\ln a = \mu_{\mathrm{R}}, \tag{6.26}$$

$$\mu_{\mathrm{Li}^+} = \mathrm{RT}\ln a_+ + \mathrm{F}\phi_e = \mathrm{F}\phi, \tag{6.27}$$

$$\mu_{e^-} = \mathrm{RT}\ln a_- - \mathrm{F}\phi = -\mathrm{F}\phi_e. \tag{6.28}$$

Here, ϕ_e denotes the electrostatic potential of the electrode and ϕ represents that of the electrolyte. Insertion of the last three equations into the surface overpotential given in Eq. (6.25) leads to

$$\mathrm{F}\eta^s_{\mathrm{R}} = \mu_{\mathrm{R}} + \mathrm{F}(\phi_e - \phi) = \mu_{\mathrm{R}} + \mathrm{F}\triangle\phi, \tag{6.29}$$

where $\triangle\phi = \phi_e - \phi$ is the voltage drop across electrode/electrolyte interface. In the expression, we assume the electrochemical potential of host material H remains unchanged. As mentioned, the subscript R in η is only to indicate that it is expressed by quantities in the reference configuration and it is free from the chosen configuration. On the other hand, the flux $\hat{j}_s$ is flow rate per unit area and thus it is dependent on the configuration. However, this dependence is fully described in the parameter c_s. Therefore Eq. (6.24), with the corresponding c_s, is valid for both configurations. The same applies for the later in this chapter, where the reaction on newly created crack surfaces is discussed.

By substituting Eq. (6.8) into Eq. (6.29), the normalized overpotential can be expressed as

$$\eta^s = \frac{\mathrm{F}\eta^s_{\mathrm{R}}}{\mathrm{RT}} = \ln\frac{c}{1-c} + \chi(1-2c) + \mu^e - \boldsymbol{\nabla}\cdot\mathbf{K}^*\boldsymbol{\nabla}c + \triangle\phi^*, \tag{6.30}$$

where $\mu^e = (1/\mathrm{RT})\partial\psi^e_{\mathrm{R}}/\partial c_{\mathrm{R}}$ is normalized elastic chemical potential, $\triangle\phi^* = \mathrm{F}\triangle\phi/(\mathrm{RT})$, $\mathbf{K}^* = \mathbf{K}/\left(\mathrm{RTL}_0^2\right)$ and $\boldsymbol{\nabla} = \mathrm{L}_0\boldsymbol{\nabla}_{\mathrm{R}}$. Here L_0 is a characteristic length.

Note that, insertion of Li takes place on the surface when $\eta^s < 0$, while extraction of Li occurs when $\eta^s > 0$. Thus, by choosing different voltage drop $\triangle\phi^*$, the reaction can be controlled as forward and backward. In particular, when the interfacial and elastic chemical potential is disregarded, $\eta^s = \mu^c + \triangle\phi^*$. As shown in Fig. 6.3(a), when $\triangle\phi^*$ is negative and large enough, electrode particles will take in Li until $c = c_1$ is reached. On the other hand, as shown in Fig. 6.3(c), when $\triangle\phi^*$ is positive and large enough, Li will be extracted from these particles until $c = c_5$. However, when $-\triangle\phi^*$ stays between two spinodal points, as shown in Fig. 6.3(b), it is highly probable that both insertion and extraction take place at the same time towards $c = c_2$ and $c = c_3$, since the whole system is unstable and subject to spinodal decomposition. Notice that c_2 and c_3 can be different from the concentrations in two phases c_α and c_β, which are the results of spinodal decomposition. The values of c_2 and c_3 depend not only on the chemical state of lithium but also on the applied voltage potential drop $\triangle\phi^*$. Implementation of surface

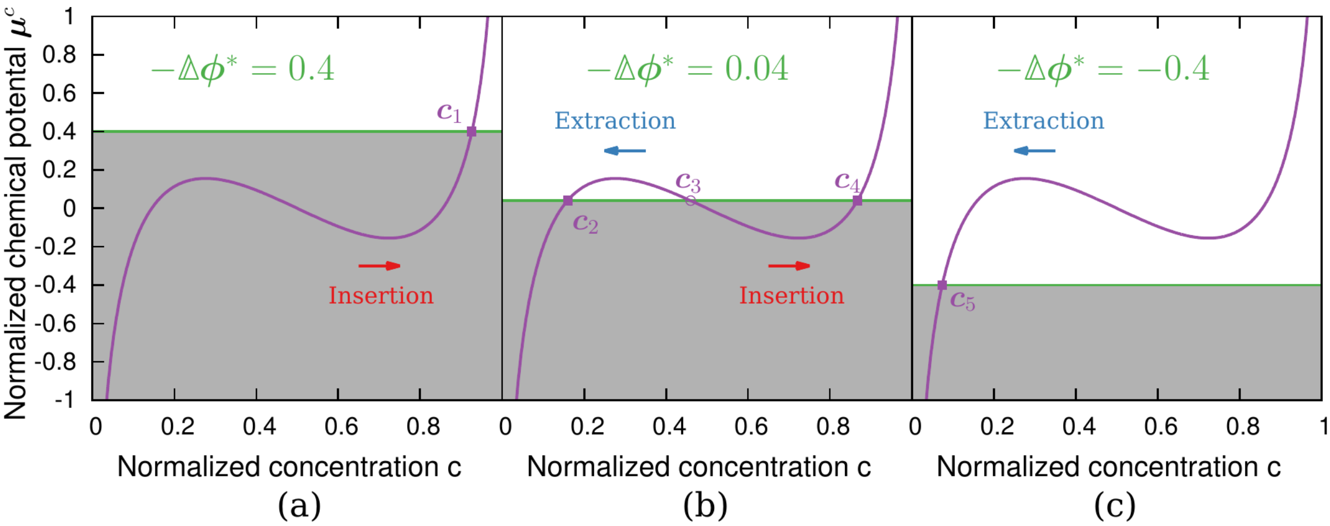

FIGURE 6.3. *Insertion/extraction of Li under different normalized voltage drop* $\Delta\phi^* = \mathrm{F}\Delta\phi/(\mathrm{RT})$*. The chemical potential* $\mu^c = \ln c - \ln(1-c) + 2.5\,(1-2c)$.

reaction can automatically constrain the concentration in the simulation domain so that it stays in the range from 0 to 1.

Substitution of Eq. (6.30) into Eq. (6.24) leads to

$$\hat{j}_s = \frac{c_s}{\tau_0}(1-c)\exp\left(-\frac{1}{2}\Delta\phi^*\right) - \frac{c_s}{\tau_0}\,c\exp\left[\chi\,(1-2c) + \mu^e - \nabla\cdot\mathbf{K}^*\nabla c + \frac{1}{2}\Delta\phi^*\right], \tag{6.31}$$

which gives the flux boundary condition in Eq. (6.18).

6.2 Simulation results: reaction on the particle surface and the phase interface

In this section, two numerical experiments based on the model presented in Section 6.1 are conducted to discuss the interaction between reaction rate and phase separation: reaction rate can influence the phase separation pattern; on the other hand, reaction rate is enhanced on phase interfaces.

6.2.1 Reaction on the particle surface

To study phase separation with different diffusion–reaction relations, a spherical particle with isotropic material is considered, where a homogeneous initial and boundary setup is furthermore given. Symmetric mechanical constraints are applied on the planes of symmetry, while the spherical surface is set free from stresses. The electrochemical reaction takes place on the surface of the sphere, across which a constant voltage drop $\Delta\phi$ is prescribed. It drives the reaction, such that the intercalating/intercalated lithium is produced/consumed until the particle is fully (dis-)charged. The reaction rate is controlled by the single reaction step time τ_0 which is given

TABLE 6.1. *Parameters for the simulation of the spherical particle.*

Gas constant (R)	$8.32\,\mathrm{J\,mol^{-1}\,K^{-1}}$
Absolute temperature (T)	283 K
Diffusivity (D)	$7.08\times10^{-15}\,\mathrm{m^2\,s^{-1}}$
Faraday's constant (F)	$96\,485\,\mathrm{C\,mol^{-1}}$
Partial molar volume (Ω)	$3.497\times10^{-6}\,\mathrm{m^3\,mol^{-1}}$
Maximum concentration (c_{max})	$2.29\times10^{4}\,\mathrm{mol\,m^{-3}}$
Phase parameter (χ)	2.5
Interface parameter (κ)	$1.0\times10^{-10}\,\mathrm{J\,mol^{-1}\,m^2}$
Length scale (L_0)	$1\,\mu$m
Bulk modulus slope (K_0)	100 MPa
Shear modulus slope (G_0)	100 MPa
Concentration intercept (c_{in})	10.0
Surface site concentration (c_s)	$6.78\times10^{-6}\,\mathrm{mol\,m^{-2}}$
Single reaction step time (τ_0)	0.01 s (fast)/1 s (slow)
Voltage drop electrode/electrolyte ($\Delta\phi$)	−4.88 mV
Initial normalized concentration (c_0)	0.25

as 0.01 s for a fast reaction and 1 s for a slow reaction. The parameters for the simulation are given in Table 6.1.

The state of charge (SOC) with respect to time is measured in the simulation by integrating all the lithium inside the particle at each current time compared with the amount in a full lithiation ($c_R = c_{max}$). The results are shown in Fig. 6.4. The solid lines describe the simulated SOC with respect to time. Both curves show the same tendency of the reaction, which is fairly fast at the beginning and slows down towards the end of the charge. Both of them show an acceleration of reaction when the particle is charged at roughly 30 % (A, E), because in both cases the phases start to form and the overpotential η^s increases rapidly as the concentration increases, which can be seen in Fig. 6.3 (a).

However, the phase-separation behaviors are very different in the two cases. The green line shows that, when the reaction is fast enough, a core-shell structure can be achieved. This is in agreement with the predictions in the work of Singh et al. [89], which stated that in an isotropic bulk-transport-limited case, where the bulk diffusion is much slower than the reaction, the phase boundary is driven largely by the incoming flux, thus a shrinking-core profile being formed. On the other hand, as shown by the red line, when the surface reaction is slow enough, the species can be always equilibrated by the bulk transport. In this case, the spinodal decomposition, or nucleation, initiates from the surface, where the dynamics of reaction can cause strong fluctuations in the species concentration. They are very unstable inside the spinodal region. The reaction in the core-shell structure slows down as the two phase region is finally formed (B, C),

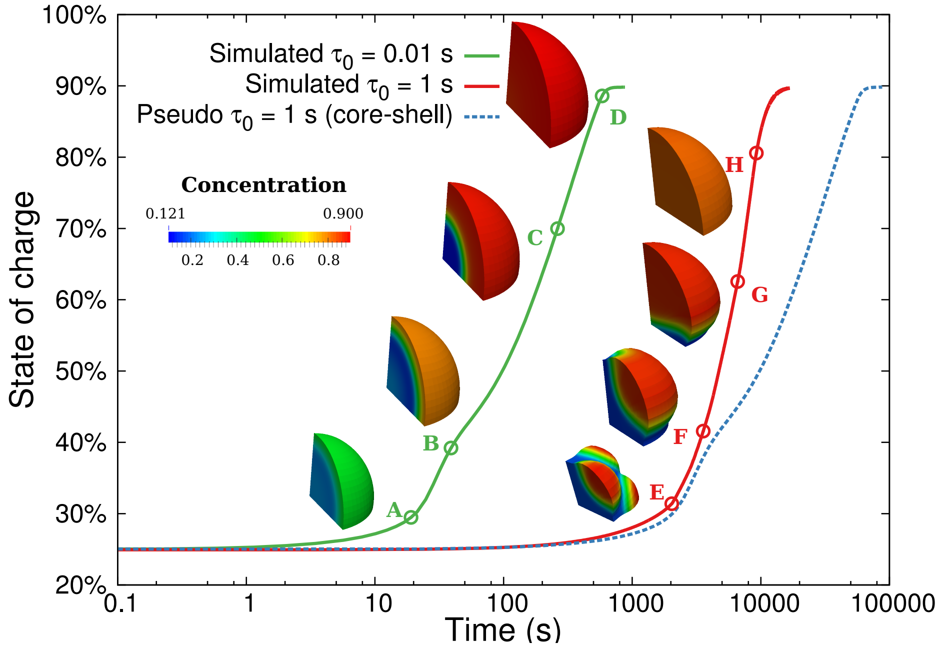

Figure 6.4. *The SOC and the corresponding concentration profile of the particle at different charge rate. A fast reaction (green line) can give a core-shell structure while a slow reaction (red line) will not preserve the core-shell. However, the latter can give a more robust reaction after the phase separation occurs. The pseudo plot is the curve when the core-shell structure is enforced when* $\tau_0 = 1\,\mathrm{s}$.

because the outer shell approaches a full lithiation. However, in the other case, the reaction maintains its rate (F, G) until the phase separation is suppressed. Based on the simulation results of the case $\tau_0 = 0.01\,\mathrm{s}$, one can predict the state of charge curve for $\tau_0 = 1s$ when the core-shell structure is enforced, simply by scaling the time of the fast case by a factor of 100. For comparison, this predicted result is shown by the curve in blue color in Fig. 6.4. It shows that if the core-shell structure is maintained, the lithiation process becomes slower than that in the case when the particle is free to adjust the phase pattern for a more robust reaction. This can be explained by the fact that the reaction rate is enhanced on the phase interface, which is discussed in more detail in the next example.

6.2.2 Reaction on the phase interface

To investigate the reaction in different phases and in the phase interface, a square plate with isotropic and anisotropic chemical properties is studied in this section. The geometry is given in Fig. 6.5. In this model, the mechanical part is disregarded. No preferred direction for the reaction is assumed. Therefore, in the simulation, the reaction will take place on all six surfaces of the plate and the reaction rate is governed by the chemical state at each position on the surface. The anisotropic interfacial parameter κ and diffusivity D in different directions are given in Table 6.2. In the isotropic case, as shown in Fig. 6.6, the flux is marching towards the interior from all four sides and the phase separation of a Li-rich frame and a Li-deficient center

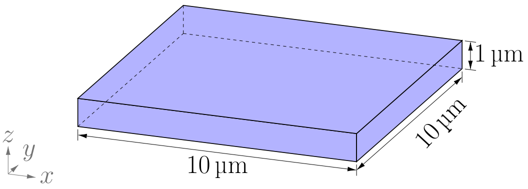

FIGURE 6.5. *Sketch and measurements of the square plate problem. All six surfaces of the plate are exposed to the electrolyte. Therefore electrochemical reaction can take place on all sides.*

Interfacial Parameter	κ_x	$1.0 \times 10^{-10}\,\mathrm{J\,mol^{-1}\,m^{-2}}$
	κ_y	$1000\,\kappa_x$
	κ_z	$1000\,\kappa_x$
Diffusivity	D_x	$7.08 \times 10^{-15}\,\mathrm{m^2\,s^{-1}}$
	D_y	$1000\,\mathrm{D}_x$
	D_z	$1000\,\mathrm{D}_x$
Sing. reac.	τ_0	1 s

TABLE 6.2. *Anisotropic interface and diffusivity parameters for the plate problem. For the isotropic case, the parameters for x direction are used for all three directions. All other parameters are given in Table 6.1.*

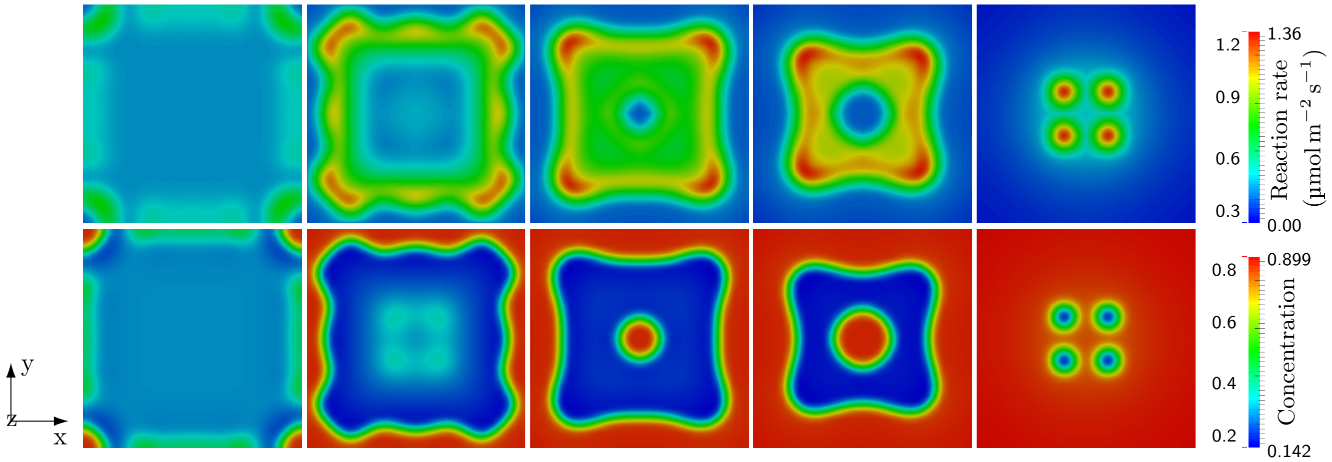

(a) SOC = 30 % (b) SOC = 40 % (c) SOC = 49 % (d) SOC = 61 % (e) SOC = 84 %

FIGURE 6.6. *Contour plot of the reaction rate and the concentration SOC in an isotropic diffusion process. The peak of the reaction will always take place near the interface.*

forms. As more flux comes in, there arises an island of Li-rich phase in the middle of the Li-poor phase. This can be explained by the dynamics of diffusion and reaction, where the whole system is perturbed strongly and it is easy to achieve a phase separation once the magnitude of fluctuation is large enough. As for the reaction, by comparing the concentration profile and the reaction rate, one can observe that the reaction peaks at the interface front, where the concentration gradient is very high. In the two homogeneous phases, the reaction is relatively slow, especially in the Li-rich phase, where the reaction almost stops. This low efficiency of reaction in the Li-rich phase explains again why the core-shell structure is lithiated much slower than the other, studied in the last subsection.

Fig. 6.7 shows the case of an anisotropic diffusion. As explained in the Section 6.1.1, the interfacial parameter is chosen in such a way that $\kappa_x/\mathrm{D}_x = \kappa_y/\mathrm{D}_y = \kappa_z/\mathrm{D}_z$. In the simulation, the diffusion in x direction is set to be slowest. Note that even though the diffusivity in y, z direction is the same, in z-direction lithium sites are filled faster than in y-direction. This is due

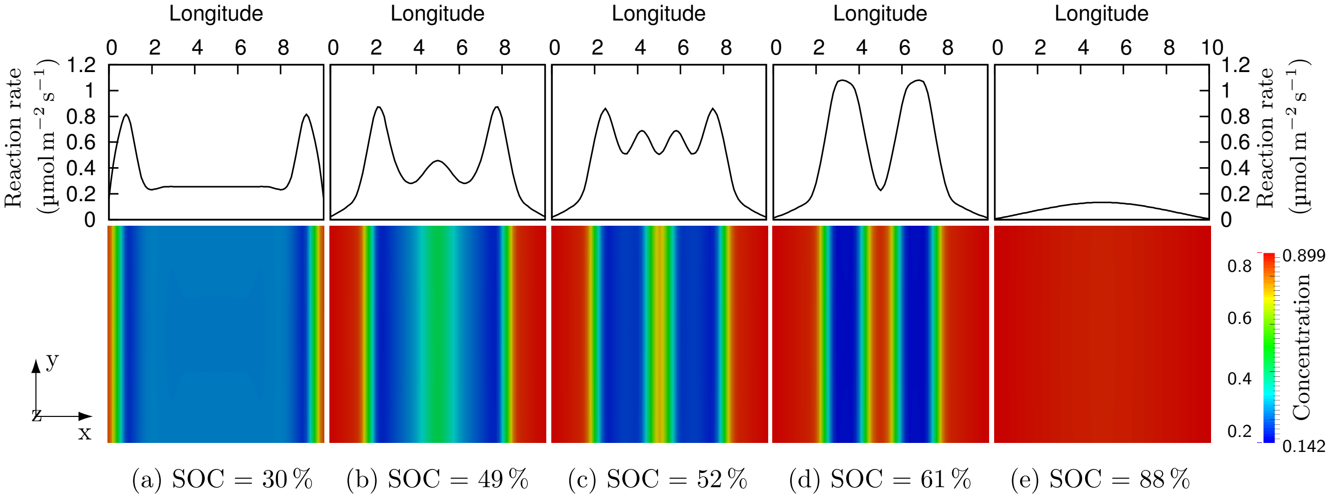

FIGURE 6.7. *Contour plot of the concentration and plot of the reaction rate along the direction of the slowest diffusion (x direction) at different SOC in an anisotropic diffusion process.*

to the fact that the dimension in z-direction is smaller than that in y-direction. In contrast to the isotropic case, phase separation initiates from the two ends although the reaction takes place in all six sides of x axis. As time goes on, the phase interface marches towards the center. A third Li-rich phase appears in the middle when SOC is approximately 50 %, thus the formation of stripes appears. This result supports the domino-cascade model of $LiFePO_4$, which was proposed in the work of Delma et al. [10]

These two cases are extreme. However, with a proper implementation of crystal anisotropy, by filling the diffusion matrix also in the off-diagonal entries, one can also achieve a core-shell structure with a polygonal core, as observed in the work of Liu et al. [141].

6.3 Electro-chemo-mechanical model of the electrode particle with fracture

6.3.1 Free energy density and governing equations

To describe fracture of particles, we employ the phase-field method, introducing a damage variable ξ, which bears the value of 1 where the material is unbroken and equals to 0 where it is fully broken, as shown in Fig. 6.8. The free energy density in this model is then modified from Eq. (6.1) as

$$\psi_\mathrm{R}(c_\mathrm{R}, \nabla_\mathrm{R} c_\mathrm{R}, \mathbf{C}, \xi, \nabla_\mathrm{R}\xi) = \psi^c_\mathrm{R}(c_\mathrm{R}) + \psi^i_\mathrm{R}(\nabla_\mathrm{R} c_\mathrm{R}) + \psi^f_\mathrm{R}(\xi, \nabla_\mathrm{R}\xi) + \psi^{ef}_\mathrm{R}(c_\mathrm{R}, \mathbf{C}, \xi), \tag{6.32}$$

where the bulk chemical free energy ψ^c_R and the phase interfacial free energy ψ^i_R are the same as in Eq. (6.1). Therefore we only introduce the fracture free energy ψ^f_R and the modified elastic free energyψ^{ef}_R here.

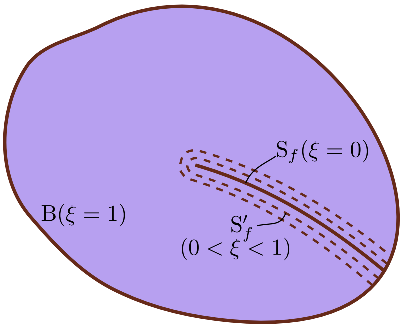

Figure 6.8. *Phase-field description of the fracture. The damage variable ξ has the value of 0 in the broken region and 1 in the unbroken region.*

According to Bourdin et al. [41], the fracture free energy density is given by,

$$\psi^{f}_{\mathrm{R}}(\xi, \boldsymbol{\nabla}_{\mathrm{R}}\xi) = \mathscr{G}_c\left[\epsilon|\boldsymbol{\nabla}_{\mathrm{R}}\xi|^2 + \frac{1}{4\epsilon}(1-\xi)^2\right]. \tag{6.33}$$

Here, $\mathscr{G}_c$ is the critical energy release rate and ϵ is a length scale which determines the width of the transition zone between the unbroken and the broken region.

For elastic energy density, we start from the material from Eq. (6.4) in the undamaged region, which reads as

$$\psi^{e}_{\mathrm{R}}(c_{\mathrm{R}}, \mathbf{C}) = J^c\left[\frac{K_c}{2}(J^e-1)^2 + \frac{G_c}{2}\left(\bar{I}_1 - 3\right)\right]. \tag{6.34}$$

Following Schneider et al. [145] and Zuo et al. [147], we ignore the direct influence of diffusion on the crack propagation. That is, the chemical field will not directly lead to fracture, but indirectly through the induced stress field. Moreover, to account for the fact that cracks will not propagate under hydrostatic compression, the elastic free energy can be split into a positive part ψ^{e+}_{R} and a negative part ψ^{e-}_{R}. The latter will not be involved in the coupling with the fracture. More specifically, the two parts take the form

$$\psi^{e+}_{\mathrm{R}}(c_{\mathrm{R}}, \mathbf{C}) = J^c\left[\frac{K_c}{2}\left(J^{e+}-1\right)^2 + \frac{G_c}{2}\left(\bar{I}_1 - 3\right)\right], \tag{6.35a}$$

$$\psi^{e-}_{\mathrm{R}}(c_{\mathrm{R}}, J) = J^c\frac{K_c}{2}\left(J^{e-}-1\right)^2 \tag{6.35b}$$

in which

$$\begin{cases} J^{e+} = J^e, \quad J^{e-} = 1, \quad \text{if} \quad J^e \geq 1; \\ J^{e+} = 1, \quad J^{e-} = J^e, \quad \text{if} \quad J^e < 1. \end{cases} \tag{6.36}$$

The elastic energy is defined as

$$\psi^{ef}_{\mathrm{R}}(c_{\mathrm{R}}, \mathbf{C}, \xi) = (\xi^2 + \eta)\psi^{e+}_{\mathrm{R}} + \psi^{e-}_{\mathrm{R}}, \tag{6.37}$$

in which $0 < \eta \ll 1$ is a constant introduced to prevent a singularity inside the broken phase when $\xi = 0$. This method has been successfully implemented in the works of Kuhn et al. [153, 154] and Schlüter et al. [155] with a careful choice of η.

In this model, there are three sets of field variables: a molar concentration c_R, the displacements $\boldsymbol{u}$ and a damage variable ξ. To derive the chemical potential, mechanical stresses and the driving force for the damage variable ξ, we perform the variation of the total free energy similar as Eq. (5.6)

$$\delta\Psi = \int_{\mathrm{B_R}} \mathbf{S}_\mathrm{R} : \delta\mathbf{E}\,\mathrm{dB} + \int_{\mathrm{B_R}} \mu_\mathrm{R}\,\delta c_\mathrm{R}\,\mathrm{dB} + \int_{\mathrm{B_R}} \zeta\,\delta\xi\,\mathrm{dB}, \tag{6.38}$$

in which $\mathbf{S}_\mathrm{R}$ is the second Piola-Kirchhoff stress tensor, μ_R is the chemical potential and ζ is the driving force for the fracture. Ψ is defined as the free energy over the whole body as

$$\Psi = \int_{\mathrm{B_R}} \psi_\mathrm{R}(c_\mathrm{R}, \boldsymbol{\nabla}_\mathrm{R} c_\mathrm{R}, \mathbf{C}, \xi, \boldsymbol{\nabla}\xi)\,\mathrm{dB}. \tag{6.39}$$

With ψ_R defined in Eq. (6.32), the variation of Ψ is given by

$$\begin{aligned}
\delta\Psi = &\int_{\mathrm{B_R}} \left[\frac{\mathrm{d}\psi^c_\mathrm{R}}{\mathrm{d}c_\mathrm{R}}\delta c_\mathrm{R} + \frac{\mathrm{d}\psi^i_\mathrm{R}}{\mathrm{d}\boldsymbol{\nabla}_\mathrm{R} c_\mathrm{R}} \cdot \delta\boldsymbol{\nabla}_\mathrm{R} c_\mathrm{R} + \frac{\partial\psi^e_\mathrm{R}}{\partial c_\mathrm{R}}\delta c_\mathrm{R} + \frac{\partial\psi^e_\mathrm{R}}{\partial\mathbf{C}} : \delta\mathbf{C} \right.\\
&\left. + \frac{\partial\psi^e_\mathrm{R}}{\partial\xi}\delta\xi + \frac{\partial\psi^f_\mathrm{R}}{\partial\xi}\delta\xi + \frac{\partial\psi^f_\mathrm{R}}{\partial\boldsymbol{\nabla}\xi} \cdot \delta\boldsymbol{\nabla}\xi \right] \mathrm{dB}\\
= &\int_{\mathrm{B_R}} \left\{ \left(\frac{\mathrm{d}\psi^c_\mathrm{R}}{\mathrm{d}c_\mathrm{R}} - \boldsymbol{\nabla}_\mathrm{R} \cdot \mathbf{K}\boldsymbol{\nabla}_\mathrm{R} c_\mathrm{R} + \frac{\partial\psi^e_\mathrm{R}}{\partial c_\mathrm{R}} \right) \delta c_\mathrm{R} + \boldsymbol{\nabla}_\mathrm{R} \cdot (\mathbf{K}\boldsymbol{\nabla}_\mathrm{R} c_\mathrm{R}\delta c_\mathrm{R}) + \frac{2\partial\psi^e_\mathrm{R}}{\partial\mathbf{C}} : \delta\mathbf{E} \right.\\
&\left. + \left[2\xi\psi^{e+}_\mathrm{R} + \frac{\mathscr{G}_c}{2\epsilon}(\xi - 1) - 2\mathscr{G}_c\epsilon\Delta_\mathrm{R}\xi \right] \delta\xi + \boldsymbol{\nabla}_\mathrm{R} \cdot (\boldsymbol{\nabla}_\mathrm{R}\xi\delta\xi) \right\} \mathrm{dB}\\
= &\int_{\mathrm{B_R}} \left(\frac{\mathrm{d}\psi^c_\mathrm{R}}{\mathrm{d}c_\mathrm{R}} - \boldsymbol{\nabla}_\mathrm{R} \cdot \mathbf{K}\boldsymbol{\nabla}_\mathrm{R} c_\mathrm{R} + \frac{\partial\psi^e_\mathrm{R}}{\partial c_\mathrm{R}} \right) \delta c_\mathrm{R}\,\mathrm{dB} + \int_{\mathrm{B_R}} \frac{2\partial\psi^e_\mathrm{R}}{\partial\mathbf{C}} : \delta\mathbf{E}\,\mathrm{dB}\\
&+ \int_{\mathrm{B_R}} \left[2\xi\psi^{e+}_\mathrm{R} + \frac{\mathscr{G}_c}{2\epsilon}(\xi - 1) - 2\mathscr{G}_c\epsilon\Delta_\mathrm{R}\xi \right] \delta\xi\,\mathrm{dB}\\
&+ \int_{\partial\mathrm{B_R}} \mathbf{K}\boldsymbol{\nabla}_\mathrm{R} c_\mathrm{R} \cdot \boldsymbol{n}_\mathrm{R}\,\delta c_\mathrm{R}\,\mathrm{dS} + \int_{\partial\mathrm{B_R}} \boldsymbol{\nabla}_\mathrm{R}\xi \cdot \boldsymbol{n}_\mathrm{R}\,\delta\xi\,\mathrm{dS}.
\end{aligned} \tag{6.40}$$

Comparing Eq. (6.38) and Eq. (6.40), $\mathbf{S}_\mathrm{R}$, μ_R and ζ can be written as

$$\mathbf{S}_\mathrm{R} = \frac{2\partial\psi_\mathrm{R}}{\partial\mathbf{C}} = \left(\xi^2 + \eta\right)\frac{2\partial\psi^{e+}_\mathrm{R}}{\partial\mathbf{C}} + \frac{2\partial\psi^{e-}_\mathrm{R}}{\partial\mathbf{C}}, \tag{6.41}$$

$$\mu_\mathrm{R} = \frac{\mathrm{d}\psi^c_\mathrm{R}}{\mathrm{d}c_\mathrm{R}} + \frac{\partial\psi^e_\mathrm{R}}{\partial c_\mathrm{R}} - \boldsymbol{\nabla}_\mathrm{R} \cdot \mathbf{K}\boldsymbol{\nabla}_\mathrm{R} c, \tag{6.42}$$

$$\zeta = 2\xi\psi_{\mathrm{R}}^{e+} - 2\mathcal{G}_c\epsilon\Delta_{\mathrm{R}}\xi + \frac{\mathcal{G}_c}{2\epsilon}(\xi - 1), \tag{6.43}$$

with two boundary conditions $\mathbf{K}\boldsymbol{\nabla}_{\mathrm{R}}c_{\mathrm{R}} \cdot \boldsymbol{n}_{\mathrm{R}} = 0$ and $\boldsymbol{\nabla}_{\mathrm{R}}\xi \cdot \boldsymbol{n}_{\mathrm{R}} = 0$ to be fulfilled on the boundary surface in the reference configuration $\partial\mathrm{B}_{\mathrm{R}}$, in addition to the Dirichlet and Neumann boundary conditions from physical constraints and fluxes.

The mechanical governing equations are the same as in Section 6.1

$$\begin{aligned}
&\boldsymbol{\nabla}_{\mathrm{R}} \cdot \mathbf{P}_{\mathrm{R}} = \mathbf{0} && \text{in} \quad \mathrm{B}_{\mathrm{R}} \times (0, \mathcal{T}), && (6.44)\\
&\mathbf{u} = \hat{\mathbf{u}} && \text{on} \quad \mathrm{S}_{\mathrm{R}\mathbf{u}} \times (0, \mathcal{T}), && (6.45)\\
&\mathbf{P}_{\mathrm{R}} \cdot \boldsymbol{n}_{\mathrm{R}} = \hat{\mathbf{t}} && \text{on} \quad \mathrm{S}_{\mathrm{R}\mathbf{t}} \times (0, \mathcal{T}), && (6.46)
\end{aligned}$$

where the first Piola–Kirchhoff stress $\mathbf{P}$ is defined by Eqs. (5.17) and (6.41).

As for the molar concentration c_{R}, the Cahn–Hilliard-type diffusion applies in the unbroken materials, while in the damaged region no diffusion is considered. It leads to a flux modified from Eq. (6.13) that

$$\boldsymbol{j}_{\mathrm{R}} = -\xi^2 c(1-c)J\mathbf{F}^{-1}\mathbf{M}\mathbf{F}^{-\mathrm{T}}\boldsymbol{\nabla}_{\mathrm{R}}\mu_{\mathrm{R}} \quad \text{in} \quad \mathrm{B}_{\mathrm{R}}. \tag{6.47}$$

The diffusion equation defined in the reference configuration is thus

$$\frac{\partial c_{\mathrm{R}}}{\partial t} = \boldsymbol{\nabla}_{\mathrm{R}} \cdot \left[\xi^2 c(1-c)J\mathbf{F}^{-1}\mathbf{M}\mathbf{F}^{-\mathrm{T}}\boldsymbol{\nabla}_{\mathrm{R}}\mu_{\mathrm{R}}\right] + S_R \quad \text{in} \quad \mathrm{B}_{\mathrm{R}} \times (0, \mathcal{T}), \tag{6.48}$$

where S_R is the source term, representing the reaction on the cracked surface S_f. The details of S_f will follow in Section 6.3.2. The boundary and initial conditions are

$$\begin{aligned}
&\mathbf{j}_{\mathrm{R}} \cdot \boldsymbol{n}_{\mathrm{R}} = -\hat{j}_s && \text{on} \quad \partial\mathrm{B}_{\mathrm{R}} \times (0, \mathcal{T}), && (6.49)\\
&\mathbf{K}\boldsymbol{\nabla}_{\mathrm{R}}c \cdot \boldsymbol{n}_{\mathrm{R}} = 0 && \text{on} \quad \partial\mathrm{B}_{\mathrm{R}} \times (0, \mathcal{T}), && (6.50)\\
&c_{\mathrm{R}}(\mathbf{X}, 0) = c_{0\mathrm{R}}(\mathbf{X}) && \text{in} \quad \mathrm{B}_{\mathrm{R}}, && (6.51)
\end{aligned}$$

with j_s defined in Eq. (6.31).

As for a non-conserved order parameter ξ, the evolution equation follows an Allen–Cahn-type equation

$$\frac{\partial \xi}{\partial t} = -\mathrm{M}_\xi \zeta = -\mathrm{M}_\xi \left[2\xi\psi_{\mathrm{R}}^{e+} - 2\mathcal{G}_c\epsilon\Delta_{\mathrm{R}}\xi + \frac{\mathcal{G}_c}{2\epsilon}(\xi - 1)\right] \tag{6.52}$$

with M_ξ as the mobility for the evolution of ξ. Following Miehe et al. [156, 157] and Borden et al. [158], to mimic the irreversibility of the crack, a strain-history field $\mathcal{H}_{\mathrm{R}}$ is introduced as a substitution of ψ_{R}^{e+}, which satisfies the Kuhn–Tucker conditions

$$\mathcal{H}_{\mathrm{R}} \geq \psi_{\mathrm{R}}^{e+}, \quad \dot{\mathcal{H}}_{\mathrm{R}} \geq 0, \quad \dot{\mathcal{H}}_{\mathrm{R}}\left(\psi_{\mathrm{R}}^{e+} - \mathcal{H}_{\mathrm{R}}\right) = 0. \tag{6.53}$$

The governing for ξ then reads

$$\frac{\partial \xi}{\partial t} = -\mathrm{M}_\xi \left[2\xi \mathscr{H}_\mathrm{R} - 2\mathscr{G}_c \epsilon \Delta_\mathrm{R} \xi + \frac{\mathscr{G}_c}{2\epsilon}(\xi - 1) \right] \quad \text{in} \quad \mathrm{B}_\mathrm{R} \quad \times (0, \mathscr{T}), \tag{6.54}$$

$$\nabla_\mathrm{R} \xi \cdot \boldsymbol{n}_\mathrm{R} = 0 \quad \text{on} \quad \partial \mathrm{B}_\mathrm{R} \quad \times (0, \mathscr{T}), \tag{6.55}$$

$$c_\mathrm{R}(\mathbf{X}, 0) = 0 \quad \text{on} \quad \mathrm{S}_f, \tag{6.56}$$

$$c_\mathrm{R}(\mathbf{X}, 0) = 1 \quad \text{in} \quad \mathrm{B}_\mathrm{R} \backslash \mathrm{S}_f. \tag{6.57}$$

For implementation details the readers are referred to Appendix C.

6.3.2 Reaction on crack surfaces

In the framework of phase-field fracture models, the crack interface can be tracked through $\xi(\xi - 1) \neq 0$ or $\nabla \xi \neq 0$. Therefore, the boundary flux can be weighted by functions containing either or both of these two terms, in order to consider the reaction at the crack interface.

As shown in Fig. 6.8, we denote the idealized crack surface by S_f (one crack will create two surfaces facing towards each other), and by S'_f the level surface in the phase-field model for a constant ξ. The damage variable gradient $\nabla \xi$ remains thus perpendicular to S'_f. Introduce a vector $\boldsymbol{s}$, which lies parallel to the damage variable gradient $\nabla \xi$. The flux on the crack surface can hence be approximated as the flux average across the interface

$$\int_{\mathrm{S}_f} \hat{j}_s \, \mathrm{dS} \approx \frac{1}{\epsilon} \int_s \int_{\mathrm{S}'_f} g(\xi, \nabla \xi) \hat{j}_s \, \mathrm{dS} \mathrm{d}s \approx \frac{1}{\epsilon} \int_\mathrm{B} g(\xi, \nabla \xi) \hat{j}_s \, \mathrm{dB}, \tag{6.58}$$

where ϵ is a length parameter which is related to the interface thickness. The weight function $g(\xi)$ contains either $\xi(\xi - 1)$ or $\nabla \xi$ as a factor. In this way, the reaction on the crack surface can be regarded as a bulk source term

$$S_R = \frac{1}{\epsilon} g(\xi, \nabla \xi) \hat{j}_s \tag{6.59}$$

in the diffusion equation Eq. (6.47). If the flux is kept constant across the interface or varies very little along the direction of $\nabla \xi$, we can observe the following relation

$$\frac{1}{\epsilon} \int_s \int_{\mathrm{S}'_f} g(\xi, \nabla \xi) \hat{j}_s \, \mathrm{dS} \mathrm{d}s \approx \frac{1}{\epsilon} \int_s g(\xi, \nabla \xi) \, \mathrm{d}s \int_{\mathrm{S}'_f} \hat{j}_s \mathrm{dS}. \tag{6.60}$$

It follows that the approximation of Eq. (6.58) is valid, if

$$\frac{1}{\epsilon} \int_s g(\xi, \nabla \xi) \, \mathrm{d}s = 1. \tag{6.61}$$

It should be commented that there will be several factors that can influence the accuracy of the approximation.

- The phase-field approximation of the cracked phase interface will determine the choice of $g(\xi)$. Usually $g(\xi)$ is chosen based on an uncoupled model for simplicity. However, when mechanical stresses come into play, the ξ profile can be different. The error can be even larger when $\xi(\xi-1)$ is used as its weighting term, since ξ might not be 0 and 1 in two homogeneous phases, depending on the boundary condition given (the reader is referred to [158] for more details). Therefore $g(\xi)$ needs to be modified accordingly when the influence of stresses is not negligible;
- The flux can vary strongly across phase interfaces, especially when diffusion is so slow that concentration varies strongly along the direction of $\boldsymbol{\nabla}\xi$, making electrochemical reaction in the interface highly fluctuating in a small range. In these cases, the equation Eq. (6.60) may not be accurate enough. One can, for instance, increase the polynomial order of $g(\xi)$, so that the fluctuation of the reaction will become negligible compared to $g(\xi)$.

As a simple case, we set $g(\xi) = \mathrm{A}\xi^2(1-\xi)^2$ with A being a coefficient to be determined. To this end, firstly, in the absence of stresses, the profile of $\tilde{\xi}(x)$ across the interface on one side can be obtained by solving the following uncoupled 1D problem at equilibrium

$$\begin{cases} 0 = 2\mathscr{G}_c\epsilon\tilde{\xi}'' + \dfrac{1}{2}\dfrac{\mathscr{G}_c}{\epsilon}\left(1-\tilde{\xi}\right), \quad (0 < x < \mathrm{L}) \\ \tilde{\xi}|_{x=0} = 0, \\ \tilde{\xi}'|_{x=\mathrm{L}} = 0. \end{cases} \tag{6.62}$$

The solution reads

$$\tilde{\xi}(x) = 1 - \cosh\left(\frac{x}{2\epsilon}\right) + \tanh\left(\frac{\mathrm{L}}{2\epsilon}\right)\sinh\left(\frac{x}{2\epsilon}\right) = 1 - \cosh^{-1}\left(\frac{\mathrm{L}}{2\epsilon}\right)\cosh\left(\frac{x-\mathrm{L}}{2\epsilon}\right). \tag{6.63}$$

With the influence of the stress state, the equilibrium solution is assumed to be $\xi = \xi_0\tilde{\xi}$, where ξ_0 is the value of the damage variable in the homogeneous region after relaxation but before charging process. Inserting Eq. (6.63) into $g(\xi)$ and integrating over the whole length L, one obtains

$$\begin{aligned} 1 &= \frac{1}{\epsilon}\mathrm{A}\int_0^{\mathrm{L}} (\xi_0\tilde{\xi})^2\left(\xi_0 - \xi_0\tilde{\xi}\right)^2 \,\mathrm{d}x \\ &= \frac{\xi_0^4}{\epsilon}\mathrm{A}\int_0^{\mathrm{L}} \left[1 - \cosh^{-1}\left(\frac{\mathrm{L}}{2\epsilon}\right)\cosh\left(\frac{x-\mathrm{L}}{2\epsilon}\right)\right]^2 \left[\cosh^{-1}\left(\frac{\mathrm{L}}{2\epsilon}\right)\cosh\left(\frac{x-\mathrm{L}}{2\epsilon}\right)\right]^2 \mathrm{d}x \\ &\approx \frac{\xi_0^4}{\epsilon}\mathrm{A}\cdot\frac{1}{6}\epsilon = \frac{\mathrm{A}}{6}\xi_0^4, \end{aligned} \tag{6.64}$$

which gives A$= 6/\xi_0^4$ and $g(\xi) = 6\xi^2(\xi_0-\xi)^2/\xi_0^4$. The evolution for concentration Eq. (6.48) then can be written as

$$\frac{\partial c_{\mathrm{R}}}{\partial t} = \boldsymbol{\nabla}_{\mathrm{R}}\cdot\left[\xi^2 c(1-c)J\mathbf{F}^{-1}\mathbf{M}\mathbf{F}^{-\mathrm{T}}\boldsymbol{\nabla}_{\mathrm{R}}\mu_{\mathrm{R}}\right] + \frac{6}{\epsilon\xi_0^4}\xi^2(\xi_0-\xi)^2\hat{j}_s \quad \text{in} \quad \mathrm{B}_{\mathrm{R}}\times(0,\mathscr{T}), \tag{6.65}$$

in which $\hat{j}_s$ is given in Eq. (6.31) to account for the flux due to electrochemical reaction.

6.4 Simulation results: crack propagation in different particles

6.4.1 Crack propagation in a cylindric particle

In this section, we simulate the model in Section 6.3 with an infinitely long cylinder with different initial cracks. The first cylinder is with two initial parallel longitudinal cracks on its exterior. The problem is illustrated in Fig. 6.9, and the corresponding parameters are given in Table 6.3. The electrode/electrolyte voltage drop is given such that Li is extracted from the cylinder. The reaction only takes place on the cylindrical surface and the crack surface. As explained in Section 6.3.2, the reaction on the crack surface is approximated by the weighted source in the phase-field theory. The initial crack is imposed through the strain history field $\mathscr{H}_\mathrm{R}$ such that an initial fracture order parameter ξ is determined. $\mathscr{H}_\mathrm{R}$ is given at initialization as

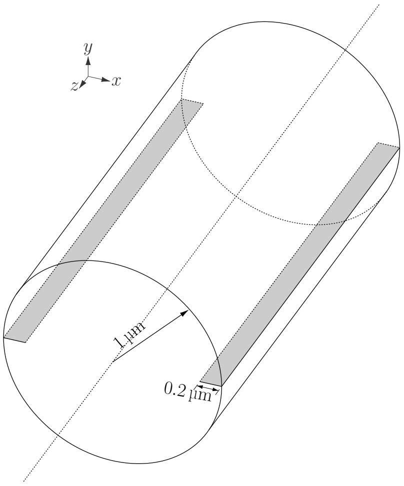

Figure 6.9. *Illustration and dimensions of an infinite cylinder with initial cracks. One quarter of a disc with a thickness of $1\,\mu$m under plane strain assumption is simulated.*

Voltage drop eld./ely. ($\Delta\phi$)	$4.88\,\mathrm{mV}$
Single reac. step time (τ_0)	$0.01\,\mathrm{s}$
Initial concentration (c_0)	0.8
Fracture resistance ($\mathscr{G}_c$)	$6\times10^{-2}\,\mathrm{N\,m^{-1}}$
Crack length scale (ϵ)	$0.05\,\mu\mathrm{m}$
Crack mobility (M_c)	$1.3\times10^{-3}\,\mathrm{J\,m^{-3}\,s^{-1}}$

Table 6.3. *Simulation parameters for the crack propagation problem. Others parameters can be found in Table 6.1.*

$$\mathscr{H}_\mathrm{R}\left(\bar{\mathbf{X}},0\right)=10^3\times\frac{\mathscr{G}_c^*}{4\epsilon^*}\left(1-\frac{d}{\epsilon^*}\right)\quad\text{with}\quad d=\min\left\{\mathrm{dist}(\bar{\mathbf{X}},\mathrm{S}_f),\epsilon^*\right\}\tag{6.66}$$

where $\mathrm{dist}(\bar{\mathbf{X}},\mathrm{S}_f)$ is the closest distance of a material point $\bar{\mathbf{X}}$ to the crack S_f. For more details the readers are referred to the work of Borden et al. [158]. In order to reach the diffusive profile for the initial crack, the reaction is set to be zero for the first 3 seconds.

The results of the crack propagation is shown in Fig. 6.10. Initially, the concentration field is homogeneous. As the outer layer loses more lithium, a two-phase profile appears. It should be noted that at the crack tip lithium can be supplied quickly from the unbroken material. In fact, due to the large tensile stresses at the crack tip, the drift effect of the mechanical field towards

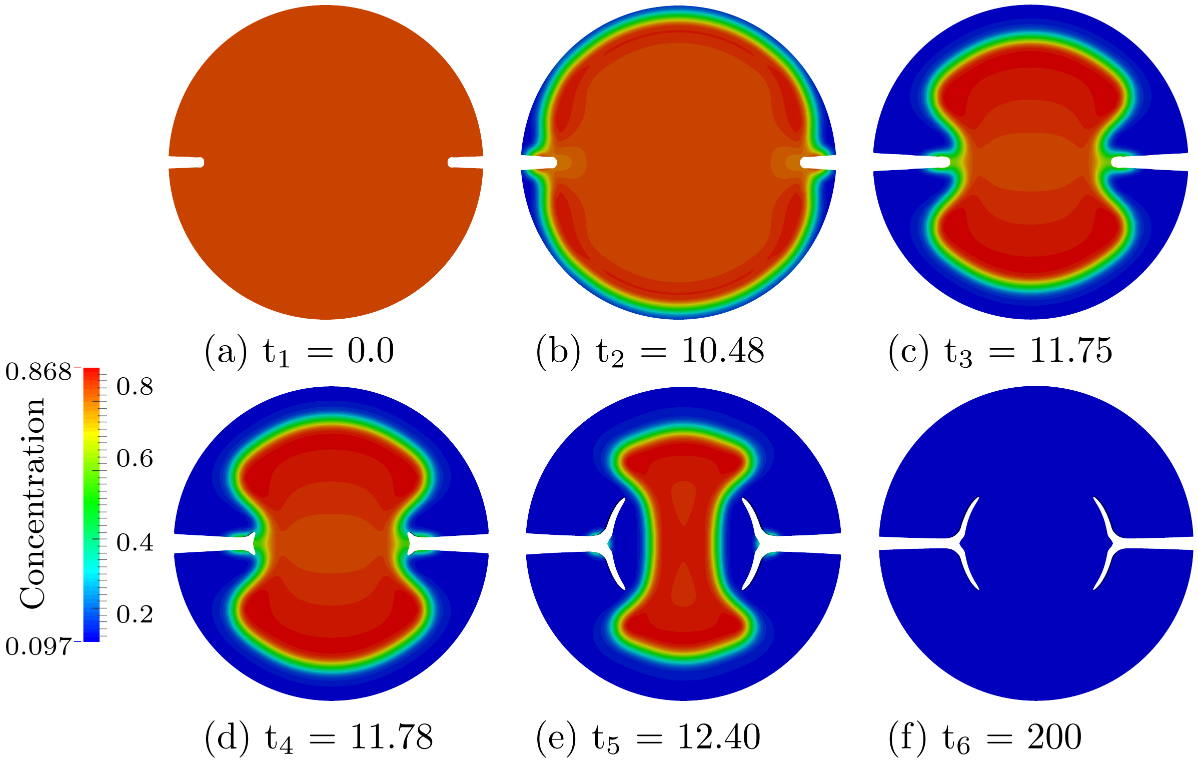

(a) $t_1 = 0.0$ (b) $t_2 = 10.48$ (c) $t_3 = 11.75$ (d) $t_4 = 11.78$ (e) $t_5 = 12.40$ (f) $t_6 = 200$

Figure 6.10. *Crack propagation under delithiation and phase separation. a) Initial homogeneous state. b) Formation of phase separation initiates the crack propagation. c) Intermediate stage when the phase interface catches up with the crack tip. d) Stage when the crack tip starts to branch at the phase interphase. e) Stage when phase interface leaves crack tip and moves towards center, the crack is perpendicular to the phase interface. d) Final stage when the reaction stops.*

the crack tip becomes prominent. The phase interface overtakes the crack tip and the fracture branching occurs at the interface, where there are intensified stresses. On the other hand, due to the loss of lithium, the outer layer turns to shrink. Because of this mismatch with the interior Li-rich phase, tensile circumferential stresses arise in the outer layer, which drive the crack to propagate. At the first stage, the crack propagates faster than the interface. It then slows down, until the phase interface runs over the crack tip. After the phase interface leaves the crack, the crack stops propagating due to the decreased driving force. The phase interface continues to move until the end of the simulation, when the whole material is almost fully delithiated and the reaction stops.

The state of charge (SOC) during the delithiation process is plotted over the time in Fig. 6.11, along with the reaction rate on a surface point away from the cracks. Immediately after the chemical reaction is permitted at $\bar{t} = 10$, there is sharp increase at the reaction rate on the surface. Note that the negative sign of the reaction rate indicates that lithium is distracted from the particle. It can also be observed on the SOC curve, indicated by the increase of the slop. After the phase interface is formed and moves into the particle interior, the reaction rate on the surface decreases rapidly, due to the overpotential drop. As it can be seen in Fig. 6.12,

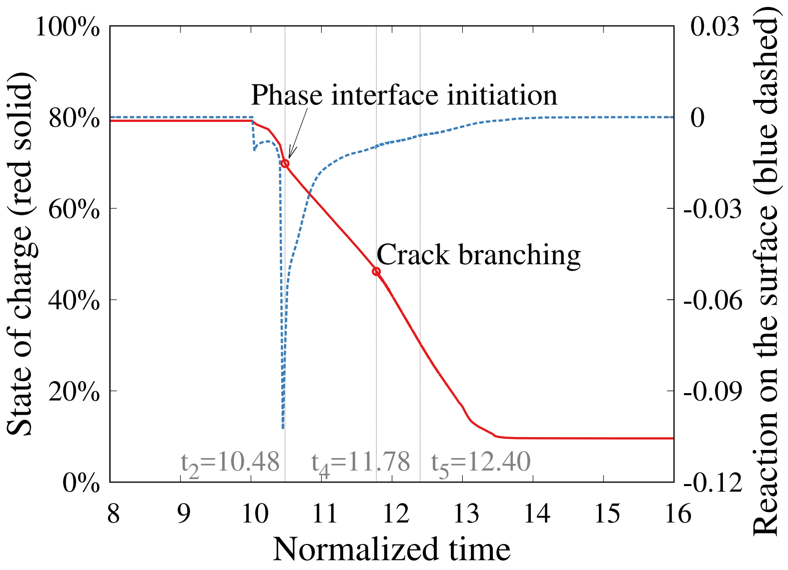

Figure 6.11. *State of charge (solid line, vertical label on r.h.s) during the simulated delithiation process. The delithiation starts from the 10th normalized time second. Two distinct time points can be recognized: the phase interface initiation along particle surface around* $\bar{t} = 10.48$, *and the crack branching around* $\bar{t} = 11.78$. *Accordingly, at* $\bar{t} = 10.48$ *the reaction rate on the surface (dashed line, vertical label on l.h.s) is significantly enhanced.*

the reaction rate around the crack tip is much more prominent. At $\bar{t} = 11.78$ when the phase interface induced crack bifurcates, the slop of the SOC curve is increased, because there are two crack tips with enhanced reaction rate. In order to examine the chemical reaction on the fracture surfaces in more details, snaps shots of the different fields are shown in Fig. 6.12 for the three time instances, respectively. Particularly, the chemical reaction rate along three different radial directions C_1, C_2 and C_3 is depicted. The radial direction C_1 lies in the horizontal direction, along which the initial crack is located, while the direction C_2 and C_3 has an angle of 31° and 45° against the horizontal direction, respectively. At $\bar{t} = 10.48$ when the phase interface is formed along the particle surfaces, an increased reaction rate at the crack tip on C_1 is noticeable, while along the other two directions no reaction takes places. At $\bar{t} = 11.78$, phase interface eventually reaches the crack tip and induces fracture branching. At crack front on the C_1 direction, an even more enhanced reaction is observed than that at $\bar{t} = 10.48$. Moreover, due to the presence of crack branch, along the radial direction C_2, two peaks of reaction rate appear. The reaction along C_2 is almost negligible. At $\bar{t} = 12.40$, phase interface has passed the fracture front, and the crack branch approaches the radial line C_3. Therefore, the reaction rate along C_3 become dominant, and two peaks can be observed. The radial line C_2 goes across the fracture surfaces. However, only one peak of the reaction rate is observed on the interior crack surface. This can be explained by the fact that the chemical potential and thus the overpotential of the material on the exterior side of the fracture surface decreases due to the presence of the Li-deficit phase. Thus the chemical reaction at the exterior crack surface almost vanishes. Along C_1, two peaks of reaction rate are also observed, which are resulted from different reasons other than that along

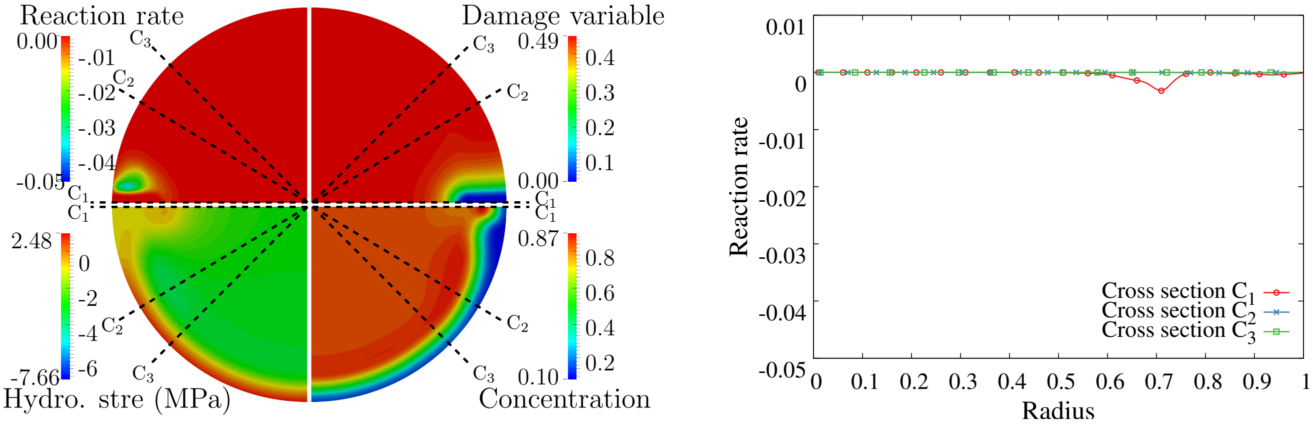

(a) *$\bar{t}_2 = 10.48$* **(b)** *$\bar{t}_2 = 10.48$*

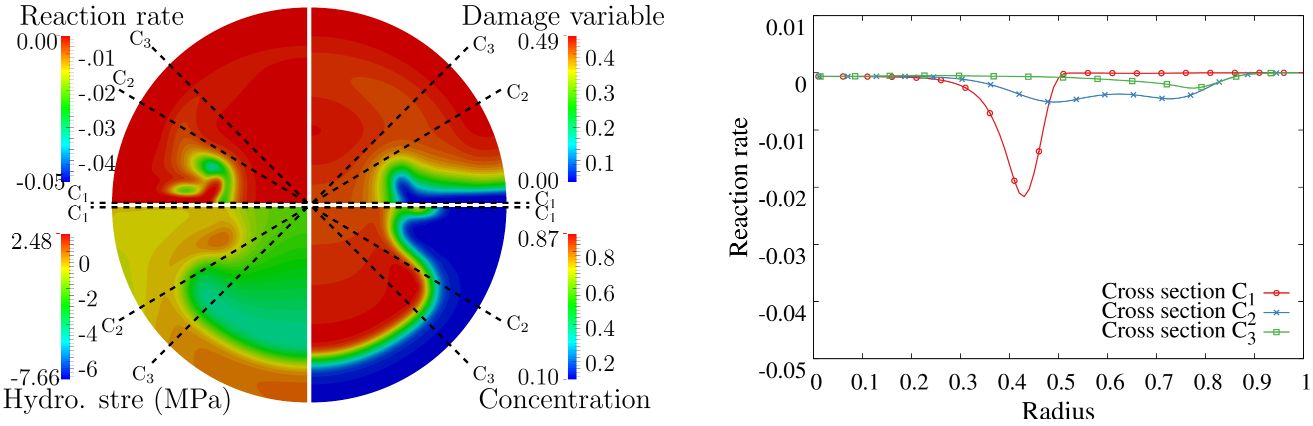

(c) *$\bar{t}_4 = 11.78$* **(d)** *$\bar{t}_4 = 11.78$*

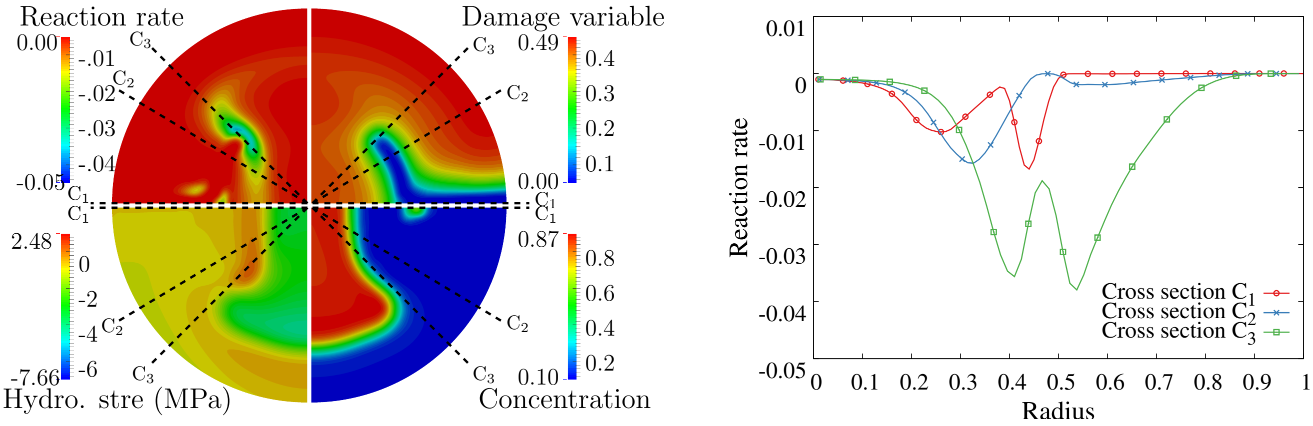

(e) *$\bar{t}_5 = 12.40$* **(f)** *$\bar{t}_5 = 12.40$*

FIGURE **6.12.** *Left: Contour plots of the damage-like order parameter, the concentration, the reaction rate, and the hydrostatic stress, for three different time instances. At $\bar{t} = 10.48$, phase interface is formed along the particle surfaces. At $\bar{t} = 11.78$, phase interface reaches the crack tip and induces fracture branching. At $\bar{t} = 12.40$, phase interface has passed the fracture front. Right: Plots of reaction rate along three different cuts for the corresponding time instances. The position of the cuts are denoted in the contour plots on the left side.*

C_3. As shown in the corresponding contour plot of the reaction rate in Fig. 6.12, the first peak on the interior side is due to the presence of phase interface, while the second peak is due to the crack front. It should be mentioned that the interplay between the phase separation and the crack propagation can strongly depend on the choice of the kinetic parameters.

As the second and third example, we consider the same cylinder, but with different initial cracks and pores. The existence of interior pores in the materials is inevitable, which makes the fracture behavior of the materials more complex. Two specimens with the same initial cracks are considered, as shown in Fig. 6.13 and Fig. 6.14. The sample in Fig. 6.14 contains pores in front of the initial cracks, while the sample in Fig. 6.13 is free from pores. The delithiation process and the accompanied phase and crack evolution of both samples are simulated, by using the same parameters listed in Table 6.3. The pores are assumed to be rather small, and exposed to electrolyte, since the electrolyte can diffuse into the pores through the ends of the considered cylinders. The phase and crack evolution in the sample without pores are shown in Fig. 6.13. Even though the initial cracks are placed pointing to each other, the electrochemical process induces crack branching in the direction almost perpendicular to the original crack surface. In the sample with pores, cracks form firstly from the prescribed pores during delithiation. These cracks propagate along both radial directions outwards until they meet the initial cracks, tearing the complete material apart.

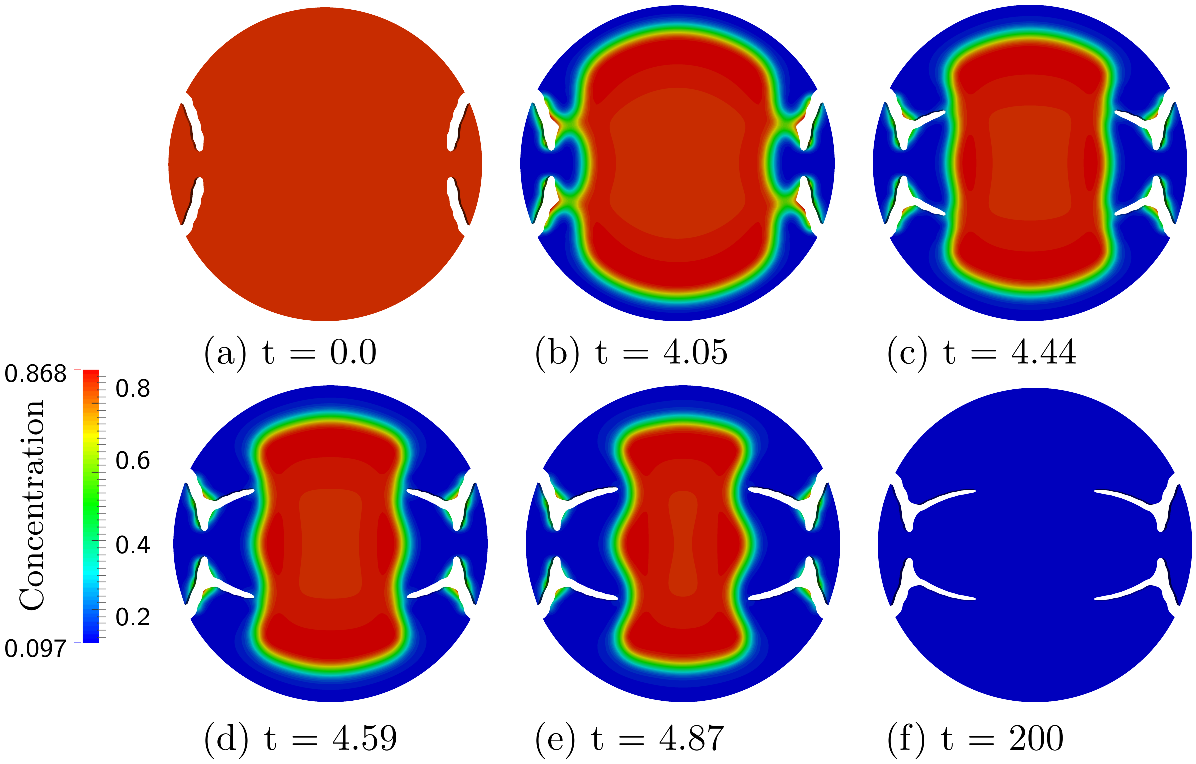

(a) t = 0.0 (b) t = 4.05 (c) t = 4.44

(d) t = 4.59 (e) t = 4.87 (f) t = 200

FIGURE 6.13. *Crack propagation on the cross section of the cylinder with initial curved cracks. A relaxation of 3 normalized seconds is applied before the reaction starts.*

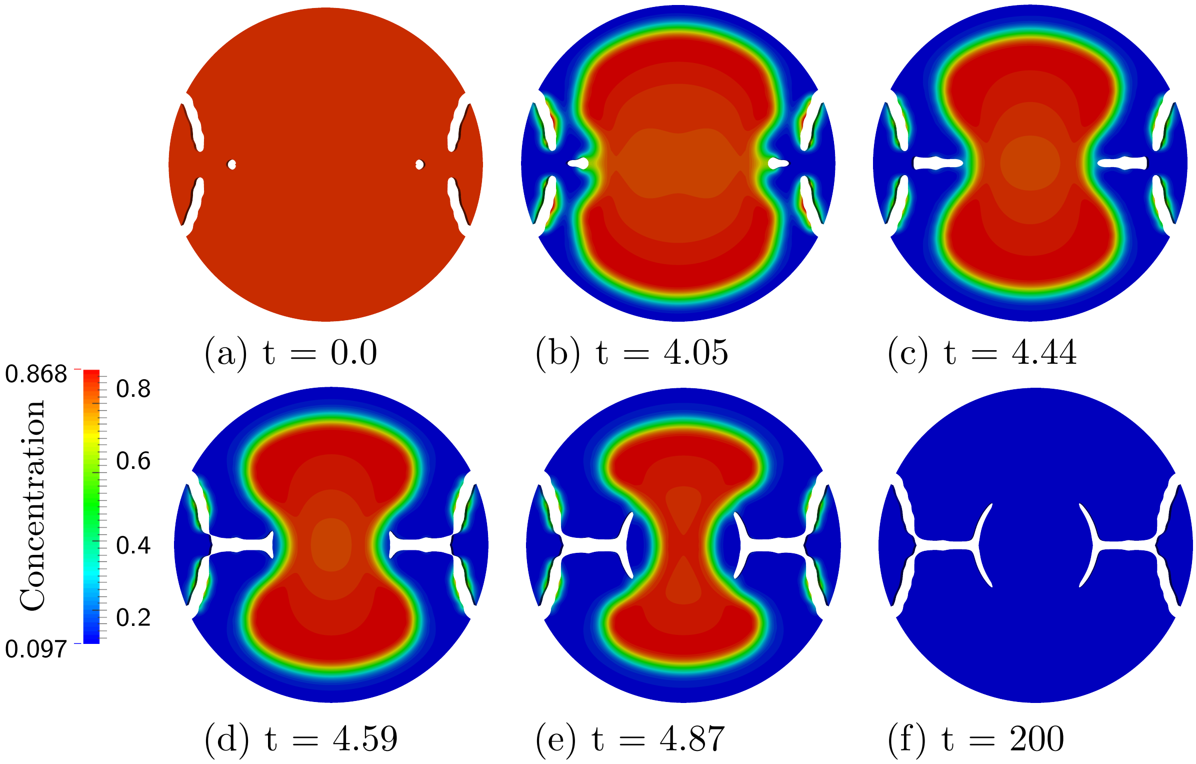

(a) t = 0.0 (b) t = 4.05 (c) t = 4.44

(d) t = 4.59 (e) t = 4.87 (f) t = 200

FIGURE 6.14. *Crack propagation on the cross section of the cylinder with initial curved cracks and interior pores in front. A relaxation of 3 normalized seconds is applied before the reaction starts.*

6.4.2 Crack propagation in the spherical particle

The last example is a spherical particle with a radius of $1\,\mu$m, where an initial a cut with a length of $0.2\,\mu$m through the equator is prescribed. All the material parameters remain the same as the previous cylinder. Fig. 6.15 shows a time sequence of the crack propagation during delithiation. The sphere shrinks during delithiation. The lithium-deficient phase initiates from neighborhoods of the crack since the lithium flows out from both the surface and the crack surface (Fig. 6.15 (a, b)). The phase interface initiates on the surface and soon overtakes the crack tip, when the crack starts to propagate along with the phase interface (Fig. 6.15 (c, d)). When the phase interface leaves the crack tip, propagation comes to an end (Fig. 6.15 (e, f)). From the stress distribution it is observed that tensile stresses—which drive the crack to propagate—follow the phase interface.

6.5 Summary

In this chapter, electrochemical reaction in lithium ion batteries was studied by using a phase-field model of fracture coupled with anisotropic Cahn–Hilliard-type diffusion in the large deformation regime.

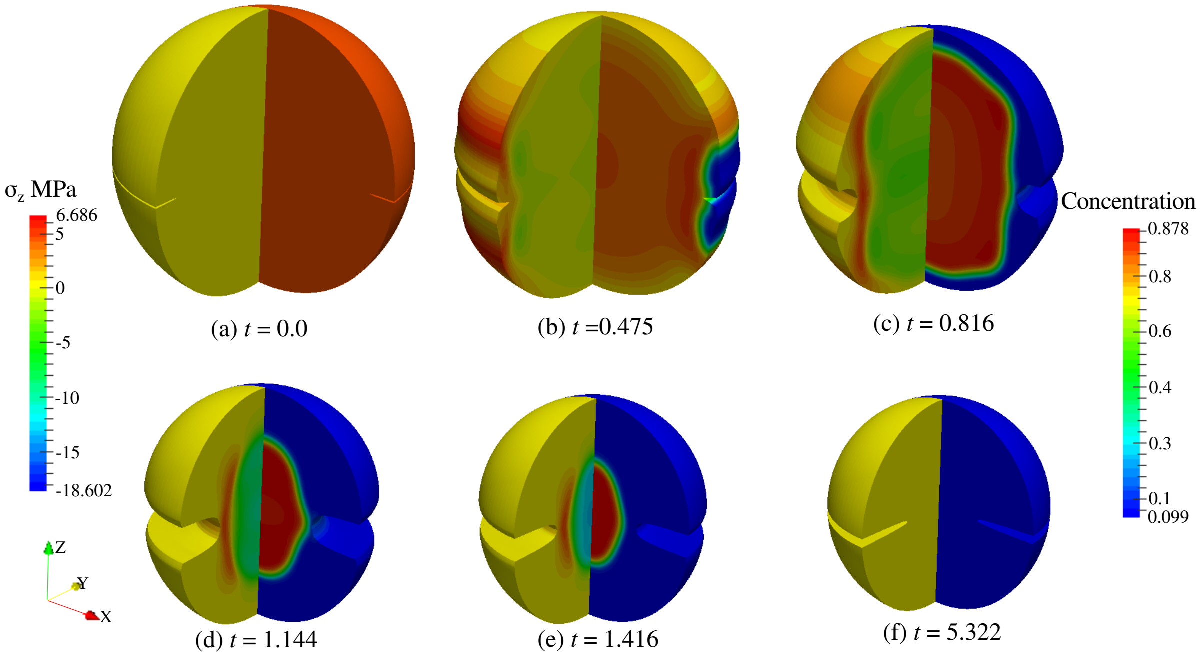

(a) $t = 0.0$ (b) $t = 0.475$ (c) $t = 0.816$

(d) $t = 1.144$ (e) $t = 1.416$ (f) $t = 5.322$

Figure 6.15. *Crack propagation in the sphere from an initial crack at the equator. A relaxation of 3 normalized seconds is applied before the reaction starts. The left hand side of the sphere shows the stress evolution along z direction, while the right hand side of the sphere shows the concentration distribution.*

The reaction on the surface is modeled through a modified Butler–Volmer equation, taking into account the influence of phase separation on the surface. The reaction on the crack surface is considered as a source term within the volume, regularized by a damage-variable-related term to constrain the reaction to take place within the transition zone between the unbroken and broken region.

Different numerical experiments were carried out to study different aspects. For the particles without fracture, two examples were conducted to study the interaction between reaction rate and phase separation. The first example of an isotropic sphere shows that the ratio of the reaction rate to the transport rate strongly influences the phase separation of the material: a fast reaction gives a “shrinking core”, while for a slow reaction two phases form on the surface early on. In turn, phase separation also influences the real reaction rate through the electrochemical potential on the surface. When a core-shell structure is formed, a homogeneous Li-rich phase on the surface prevents lithium from further inserting into the particle. However, an unevenly distributed concentration, although accompanied by a highly distorted surface, can give a much more robust reaction. In the second example, the reaction on the interface between two phases in isotropic and anisotropic materials is studied. The results show that, in both isotropic and anisotropic materials, reaction rate peaks near the interface, where there exists a large concentration gradient. Orthotropic diffusion as in the example has been observed in many cathode materials such as $LiFePO_4$ [10, 23].

Finally, we studied the crack propagation with the particle with fracture. We conducted the experiments in cylindric particles and a spherical particle. It is shown that crack evolution can be driven by an outflow of species when the material exhibits a phase separation behavior. The crack branches when the phase interface reaches the crack tip, since there are intensified stresses around the crack tip. Different initial cracks and pores will greatly influence the final crack pattern. Electrochemical reaction on particle surfaces and newly created crack surfaces was also discussed. We can clearly see a decreased reaction rate on particle surfaces after the formation of the core-shell phase separation since the outer layer is almost saturated; However, in phase interfaces and around crack tips enhanced reaction rate is observed.

Chapter 7

Modeling of composite electrode

Polymer binders and conductive additives, although not electrochemically active, provide mechanical and electronic support to active particles in composite electrodes [159–161]. Their amount of content plays a crucial rule in the performance of lithium-ion batteries [162]. However, the study on chemo-mechanical interaction between particles and binders is still in its infant, compared with the amount of study on single particles. The difficulty arises, when we want to move one step forward from single-particle models to the composite-electrode models, that the particle geometry varies greatly from one particle to another, the influence from binders is not negligible, more mechanisms are involved in the charging/discharging processes, and more importantly, the simulation scale is much larger than a single particle. Lu and Ni [163] discussed the effects of particle shape on stresses with interconnected multi-particle configuration. Doyle et al. [164] presented a cathode cell, which included a wide range of polymeric separator materials, lithium salts, and composite insertion cathodes. Bower et al. [20] formulated a continuum electro-chemo-mechanical half-cell model in the large deformation framework with plastic flow. Furthermore, there are also multi-scale models of the lithium-ion battery cells, where the particles embedded in polymer binders are taken care of at the micro-scale [165, 166]. For a fair representation of geometric irregularity, Lee et al. [166] generated a random microstructure. As a more faithful attempt, Roberts et al. [167] and Mendoza et al. [168] employed conformal decomposition finite element method introduce by Noble et al. [169] for a reconstruction of the microstructure. Orvananos et al. [170] considered the interaction among electrode nanoparticles. The interface condition between a particle and the electrolyte is modeled by a smoothed boundary method. However, all these models considered the electrode particles only without phase transformation. The lithium diffusion inside particles is modeled by stress-assisted Fick's law of diffusion, which is not applicable for particles made of phase-separating materials, such as crystalline silicon.

In this chapter, we present a chemo-mechanical model of the composite electrode, where the embedded particle experiences phase separation and the binder does not. Moreover, the numerical simulation is performed by the finite cell method, for a more flexible representation of irregular particle geometry. The remainder of the chapter is organized as follows. The material model is formulated in Section 7.1. Numerical details are given in Section 7.2, where the Nitsche method is employed not only for the boundary condition of the Cahn–Hilliard equation, but also for the mechanical and chemical interfacial conditions between the binder and the electrode particle. Examples of different embedding particles are presented in Section 7.3.

7.1 Material model

As a prototype, we consider a composite electrode shown in Fig. 7.1. The particle is embedded in the matrix, each occupying the domains $\mathrm{B}^{(1)}$ and $\mathrm{B}^{(2)}$, respectively. The interface between the two domains is denoted by $\mathrm{S}^{*} = \mathrm{B}^{(1)} \cap \mathrm{B}^{(2)}$. In each domain, there are two coupling fields: the displacement field $\boldsymbol{u}^{(p)}$ and the concentration field $c^{(p)}$. In this section, unless otherwise indicated, the superscript p runs from 1 to 2. Unlike previous models, the model in this chapter is in a small-deformation regime for simplicity. Therefore, an additive decomposition of the strain tensor $\boldsymbol{\epsilon}$ defined in Eq. (2.45) is assumed:

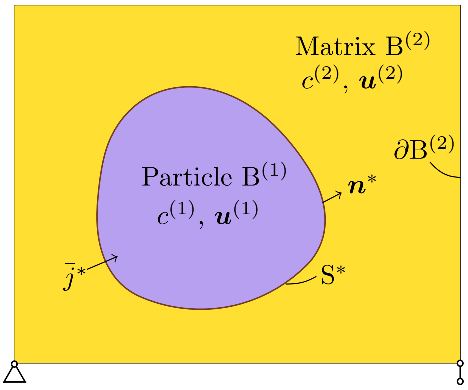

FIGURE 7.1. *Composite electrode configuration: the particle is constrained by a simply supported matrix. Different conditions are prescribed weakly at the interface* S^{*} *and the matrix boundary* $\partial\mathrm{B}^{(2)}$.

$$\boldsymbol{\epsilon}^{(p)} = \boldsymbol{\epsilon}^{e(p)} + \boldsymbol{\epsilon}^{c(p)}, \tag{7.1}$$

with

$$\boldsymbol{\epsilon}^{c(p)} = \frac{1}{3}\Omega^{(p)} c^{(p)} \mathbf{1}. \tag{7.2}$$

Here, $\Omega^{(p)}$ is the partial molar volume of lithium in the corresponding material. The model is presented in a normalized form. The chemical normalization can be found in Tables 4.1 and 4.2, while the mechanical part is given in Tables 7.1 and 7.2.

Following the same procedure in the previous chapters, we first build the free energy. We assume a regular solution model for both materials. Inside the particle, since there exists phase separation, the free energy density is expressed as

$$\begin{aligned}\psi^{(1)} = {} & c^{(1)} \ln c^{(1)} + \left(1 - c^{(1)}\right) \ln\left(1 - c^{(1)}\right) + \chi^{(1)} c^{(1)} \left(1 - c^{(1)}\right) \\ & + \frac{1}{2}\kappa^{(1)} \left|\boldsymbol{\nabla} c^{(1)}\right|^{2} + \frac{1}{2}\boldsymbol{\epsilon}^{e(1)} : \mathbb{C}^{(1)} : \boldsymbol{\epsilon}^{e(1)}\end{aligned} \tag{7.3}$$

Table 7.1. *Normalization of the mechanical quantities.*

Physical quantities	Normalization
Partial molar volume ($\tilde{\Omega}^{(p)}$)	$\Omega^{(p)} = \tilde{\Omega}^{(p)} \mathrm{c}_{\mathrm{max}}$
Stress ($\tilde{\boldsymbol{\sigma}}^{(p)}$)	$\boldsymbol{\sigma}^{(p)} = \tilde{\boldsymbol{\sigma}}^{(p)}/\tilde{\mathrm{E}}$
Shear modulus ($\tilde{\mathrm{G}}^{(p)}$)	$\mathrm{G} = \tilde{\mathrm{G}}^{(p)}/\tilde{\mathrm{E}}$
Bulk modulus ($\tilde{\mathrm{K}}^{(p)}$)	$\mathrm{K} = \tilde{\mathrm{K}}^{(p)}/\tilde{\mathrm{E}}$

Table 7.2. *Parameters used in the mechanical normalization.*

Reference Young's modulus ($\tilde{\mathrm{E}}$)	1.0 MPa
Maximum concentration ($\mathrm{c}_{\mathrm{max}}$)	$2.29 \times 10^4\,\mathrm{mol\,m^{-3}}$

In the matrix, only one phase is present, therefore the free energy density has no interfacial contribution

$$\psi^{(2)} = c^{(2)} \ln c^{(2)} + \left(1 - c^{(2)}\right) \ln\left(1 - c^{(2)}\right) + \chi^{(2)} c^{(2)} \left(1 - c^{(2)}\right) + \frac{1}{2} \boldsymbol{\epsilon}^{e(2)} : \mathbb{C}^{(2)} : \boldsymbol{\epsilon}^{e(2)} \tag{7.4}$$

The parameters $\chi^{(1)}$, $\chi^{(2)}$ and $\kappa^{(1)}$ in the Eq. (7.3) and Eq. (7.4) have been introduced already in Chapter 4. We take $\chi^{(1)} = 2.5$ and $\chi^{(2)} = 1.0$ to achieve the free energy allowing for two phases and one phase, respectively. The fourth-order elastic tensor $\mathbb{C}^{(p)}$ is given as

$$\mathbb{C}^{(p)} = 2\mathrm{G}^{(p)} \mathbb{I} + \left(\mathrm{K}^{(p)} - \frac{2}{3} \mathrm{G}^{(p)}\right) \mathbf{1} \otimes \mathbf{1}, \tag{7.5}$$

with $\mathrm{G}^{(p)}$ and $\mathrm{K}^{(p)}$ being the shear and bulk moduli, respectively. $\mathbb{I}$ is the fourth-order and $\mathbf{1}$ is the second-order unit tensor. The stress tensor and chemical potential can thus be derived from the free energy as

$$\boldsymbol{\sigma}^{(p)} = \mathbb{C}^{(p)} \boldsymbol{\epsilon}^{(p)} - \mathrm{K}^{(p)} \Omega^{(p)} \mathbf{1} \tag{7.6}$$

$$\mu^{(1)} = \ln c^{(1)} - \ln\left(1 - c^{(1)}\right) + \chi^{(1)} \left(1 - 2c^{(1)}\right) - \kappa^{(1)} \Delta c^{(1)} - \frac{1}{3} \Omega^{(1)} \mathrm{tr} \boldsymbol{\sigma}^{(1)} \tag{7.7}$$

$$\mu^{(2)} = \ln c^{(2)} - \ln\left(1 - c^{(2)}\right) + \chi^{(2)} \left(1 - 2c^{(2)}\right) - \frac{1}{3} \Omega^{(2)} \mathrm{tr} \boldsymbol{\sigma}^{(2)} \tag{7.8}$$

Based on the stress tensor and the chemical potential, we can construct the governing equation. In each domain, there are two sets of governing equations: the mechanical and chemical. For the mechanical part, the local force balance requires in each domain $\mathrm{B}^{(p)}$

$$\boldsymbol{\nabla} \cdot \boldsymbol{\sigma}^{(p)} = \boldsymbol{\nabla} \cdot \left(\mathbb{C}^{(p)} \boldsymbol{\epsilon}^{(p)}\right) - \mathrm{K}^{(p)} \Omega^{(p)} \boldsymbol{\nabla} c^{(p)} = \mathbf{0} \quad \text{in} \quad \mathrm{B}^{(p)} \times (0, \mathscr{T}). \tag{7.9}$$

For the chemical part, inside the particle, the diffusion process is governed by the stress-assisted Cahn–Hilliard equation

$$\begin{aligned}\frac{\partial c^{(1)}}{\partial t} &= \boldsymbol{\nabla}\cdot\left[c^{(1)}\left(1-c^{(1)}\right)\boldsymbol{\nabla}\mu^{(1)}\right]\\ &= \boldsymbol{\nabla}\cdot\left\{\left[1-2\chi^{(1)}c^{(1)}\left(1-c^{(1)}\right)\right]\boldsymbol{\nabla}c^{(1)}-c^{(1)}\left(1-c^{(1)}\right)\kappa^{(1)}\boldsymbol{\nabla}\Delta c^{(1)}\right\}\\ &\quad-\boldsymbol{\nabla}\cdot\left[c^{(1)}\left(1-c^{(1)}\right)\frac{1}{3}\Omega^{(1)}\boldsymbol{\nabla}\left(\operatorname{tr}\boldsymbol{\sigma}^{(1)}\right)\right] \quad \text{in} \quad \mathrm{B}^{(1)}\times(0,\mathscr{T})\,. \end{aligned} \tag{7.10}$$

In the matrix, the diffusion is driven by the gradient of the concentration and the hydrostatic stress

$$\begin{aligned}\frac{\partial c^{(2)}}{\partial t} &= \boldsymbol{\nabla}\cdot\left[c^{(2)}\left(1-c^{(2)}\right)\boldsymbol{\nabla}\mu^{(2)}\right]\\ &= \boldsymbol{\nabla}\cdot\left\{\left[1-2\chi^{(2)}c^{(2)}\left(1-c^{(2)}\right)\right]\boldsymbol{\nabla}c^{(2)}-c^{(2)}\left(1-c^{(2)}\right)\frac{1}{3}\Omega^{(2)}\boldsymbol{\nabla}\left(\operatorname{tr}\boldsymbol{\sigma}^{(2)}\right)\right\}\\ &\quad \text{in} \quad \mathrm{B}^{(2)}\times(0,\mathscr{T})\,. \end{aligned} \tag{7.11}$$

The initial condition in two materials are

$$c^{(1)} = c_0^{(1)} \quad \text{in} \quad \mathrm{B}^{(1)}, \tag{7.12}$$

$$c^{(2)} = c_0^{(2)} \quad \text{in} \quad \mathrm{B}^{(2)}. \tag{7.13}$$

On the interface S^* between two domains, traction equilibrium and displacement compatibility require that

$$\boldsymbol{u}^{(1)}-\boldsymbol{u}^{(2)} = [\![\boldsymbol{u}]\!] = \boldsymbol{0} \qquad \text{on} \quad \mathrm{S}^*\times(0,\mathscr{T})\,, \tag{7.14}$$

$$\boldsymbol{\sigma}^{(1)}\boldsymbol{n}^*-\boldsymbol{\sigma}^{(2)}\boldsymbol{n}^* = [\![\boldsymbol{\sigma}]\!] = \boldsymbol{0} \qquad \text{on} \quad \mathrm{S}^*\times(0,\mathscr{T})\,. \tag{7.15}$$

For the chemical part, mass conservation should also be fulfilled on the interface

$$-\left[c^{(1)}\left(1-c^{(1)}\right)\boldsymbol{\nabla}\mu^{(1)}\right]\cdot\boldsymbol{n}^* = -\bar{j}^* \qquad \text{on} \quad \mathrm{S}^*\times(0,\mathscr{T})\,, \tag{7.16}$$

$$-\left[c^{(2)}\left(1-c^{(2)}\right)\boldsymbol{\nabla}\mu^{(2)}\right]\cdot\boldsymbol{n}^* = -\bar{j}^* \qquad \text{on} \quad \mathrm{S}^*\times(0,\mathscr{T})\,, \tag{7.17}$$

$$\kappa^{(1)}\boldsymbol{\nabla}c^{(1)}\cdot\boldsymbol{n}^* = 0 \qquad \text{on} \quad \mathrm{S}^*\times(0,\mathscr{T})\,, \tag{7.18}$$

where $\bar{j}^*$ is determined by reaction rate, which in this chapter is given as constant. The additional condition Eq. (7.18) arises due to the Cahn–Hilliard equation Eq. (7.10).

The boundary conditions on the surface $\partial\mathrm{B}^{(2)}$ consist of two parts. Mechanically, minimum constraints as shown in Fig. 7.1 are applied to the matrix in order to prevent rigid-body movement. Chemically, Dirichlet boundary conditions are imposed

$$c^{(2)} = \bar{c} \quad \text{on} \quad \partial\mathrm{B}^{(2)}\times(0,\mathscr{T})\,. \tag{7.19}$$

7.2 Numerical treatments

In this section, we first give a weak formulation of the aforementioned model based on Nitsche's method. Then a short introduction to the numerical implementation by the finite cell method is illustrated.

The weak formulation of the problem is

$$
\begin{aligned}
0 = \sum_{p=1,2} \int_{B^{(p)}} \frac{\partial c^{(p)}}{\partial t} \delta c^{(p)} \, \mathrm{dV} + \sum_{p=1,2} \int_{B^{(p)}} \left[1 - 2\chi^{(p)} c^{(p)} \left(1 - c^{(p)}\right)\right] \boldsymbol{\nabla} c^{(p)} \cdot \boldsymbol{\nabla} \delta c^{(p)} \, \mathrm{dV} \\
- \sum_{p=1,2} \int_{B^{(p)}} \frac{1}{3} \Omega^{(p)} c^{(p)} \left(1 - c^{(p)}\right) \boldsymbol{\nabla} \left(\mathrm{tr} \boldsymbol{\sigma}^{(p)}\right) \cdot \boldsymbol{\nabla} \delta c^{(p)} \mathrm{dV} \\
+ \int_{B^{(1)}} \left(1 - 2c^{(1)}\right) \kappa^{(1)} \Delta c^{(1)} \boldsymbol{\nabla} c^{(1)} \cdot \boldsymbol{\nabla} \delta c^{(1)} \, \mathrm{dV} \\
+ \int_{B^{(1)}} c^{(1)} \left(1 - c^{(1)}\right) \kappa^{(1)} \Delta c^{(1)} \Delta \delta c^{(1)} \, \mathrm{dV} - \sum_{p=1,2} \int_{B^{(p)}} \boldsymbol{\sigma}^{(p)} : \delta \boldsymbol{\epsilon}^{(p)} \, \mathrm{dV} \\
- \int_{S^*} \bar{j}^* \, \delta c^{(1)} \, \mathrm{dS} + \int_{S^*} \bar{j}^* \, \delta c^{(2)} \, \mathrm{dS} + \int_{S^*} \langle \boldsymbol{\sigma} \rangle \cdot \llbracket \delta \boldsymbol{u} \rrbracket \, \mathrm{dS} - \int_{S^*} \llbracket \boldsymbol{u} \rrbracket \cdot \langle \delta \boldsymbol{\sigma} \rangle \, \mathrm{dS} \\
- \int_{S^*} c^{(1)} \left(1 - c^{(1)}\right) \kappa^{(1)} \Delta c^{(1)} \boldsymbol{n}^* \cdot \boldsymbol{\nabla} \delta c^{(1)} \, \mathrm{dS} \\
- \int_{S^*} c^{(1)} \left(1 - c^{(1)}\right) \boldsymbol{\nabla} c^{(1)} \cdot \boldsymbol{n}^* \kappa^{(1)} \Delta \delta c^{(1)} \, \mathrm{dS} + \alpha \int_{S^*} \left(\boldsymbol{\nabla} c^{(1)} \cdot \boldsymbol{n}^*\right) \left(\boldsymbol{\nabla} \delta c^{(1)} \cdot \boldsymbol{n}^*\right) \, \mathrm{dS},
\end{aligned}
\tag{7.20}
$$

where the additional mechanical coupling conditions Eq. (7.14) and Eq. (7.15) are imposed by the form

$$
0 = - \sum_{p=1,2} \int_{B^{(p)}} \boldsymbol{\sigma}^{(p)} : \delta \boldsymbol{\epsilon}^{(p)} \, \mathrm{dV} + \int_{S^*} \langle \boldsymbol{\sigma} \rangle \cdot \llbracket \delta \boldsymbol{u} \rrbracket \, \mathrm{dS} - \int_{S^*} \llbracket \boldsymbol{u} \rrbracket \cdot \langle \delta \boldsymbol{\sigma} \rangle \, \mathrm{dS}, \tag{7.21}
$$

proposed by Schillinger et al. [171] as the non-symmetric Nitsche method, offering a parameter-free weak constraint.

Remark: The classical Nitsche formulation is symmetric, expressed for the linear elastic problem as

$$
0 = - \sum_{p=1,2} \int_{B^{(p)}} \boldsymbol{\sigma}^{(p)} : \delta \boldsymbol{\epsilon}^{(p)} \, \mathrm{dV} + \int_{S^*} \langle \boldsymbol{\sigma} \rangle \cdot \llbracket \delta \boldsymbol{u} \rrbracket \, \mathrm{dS} + \int_{S^*} \llbracket \boldsymbol{u} \rrbracket \cdot \langle \delta \boldsymbol{\sigma} \rangle \, \mathrm{dS} - \alpha_S \int_{S^*} \llbracket \boldsymbol{u} \rrbracket \llbracket \delta \boldsymbol{u} \rrbracket \, \mathrm{dS}, \tag{7.22}
$$

which has been widely applied in the discontinuous Galerkin method. However, its performance crucially depends on appropriate estimates of stabilization parameter α_S. An excessive α_S adversely influences consistency, accuracy and robustness of the method; on the other hand, an insufficient α_S can not guarantee the stability. In the non-symmetric Nitsche method, on the contrary, no parameter α_S is needed. Moreover, the non-symmetric contributions of our formulation do not affect the symmetry of the stiffness matrix, since in the chemo-mechanically coupled problem, the stiffness matrix is already non-symmetric.

Since there are two different materials in the problem, two background meshes are present, which will be coupled at the interface S^*, as illustrated in Fig. 7.2. The field variables of the particle and the matrix are stored in respective meshes. The two background meshes are not necessarily identical. In this thesis, for simplicity, we make the two meshes exactly the same, which requires only one mesh with information from both materials.

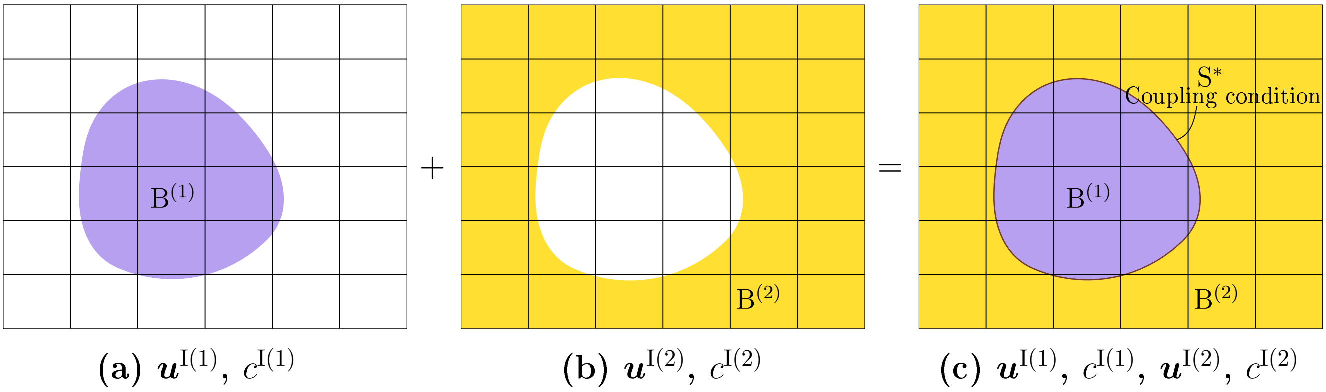

(a) $\boldsymbol{u}^{\mathrm{I}(1)}$, $c^{\mathrm{I}(1)}$ (b) $\boldsymbol{u}^{\mathrm{I}(2)}$, $c^{\mathrm{I}(2)}$ (c) $\boldsymbol{u}^{\mathrm{I}(1)}$, $c^{\mathrm{I}(1)}$, $\boldsymbol{u}^{\mathrm{I}(2)}$, $c^{\mathrm{I}(2)}$

FIGURE 7.2. *Illustration of the coupling of two materials. The mesh (a) with the information of the particle ($\boldsymbol{u}^{\mathrm{I}(1)}$, $c^{\mathrm{I}(1)}$) coincides with the mesh (b) with the information of the matrix ($\boldsymbol{u}^{\mathrm{I}(2)}$, $c^{\mathrm{I}(2)}$). The two meshes couple at the interface S^* in Figure (c). In this paper, the two meshes are identical.*

The procedure for an adaptive generation of the quadrature points has been illustrated in Chapter 2. Note that in this problem two sets of volume quadrature points need to be generated, as shown in Fig. 7.3. We generate the volume quadrature points based on an adaptive sub-cell division and the surface quadrature points based on a triangular mesh. Based on the spline order we are employing, different quadrature rules are employed [83, 114].

7.3 Simulation results

7.3.1 Composite electrodes with interconnected spherical particles

Firstly, we investigate composite electrode with interconnected spherical particles, whose geometry can be expressed analytically. Simulation parameters are listed in Table 7.3. The matrix is ten times softer than the particle. The flux across the interface is 0.01, flowing towards the particle and being applied for 5 seconds before removal.

The codes are parallelized at the assembly level by OpenMP in the finite element tool FEAP [61, 172]. To test the scalability of the parallelization, four Newton iterations during first time step of the benchmark example shown in Fig. 7.5 were computed. Fig. 7.4 shows the

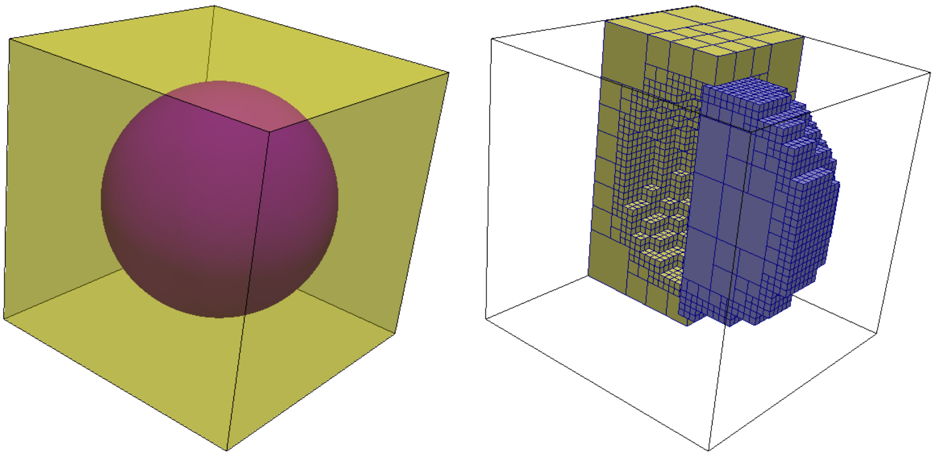

(a) *Geometry* **(b)** *Sub-cells*

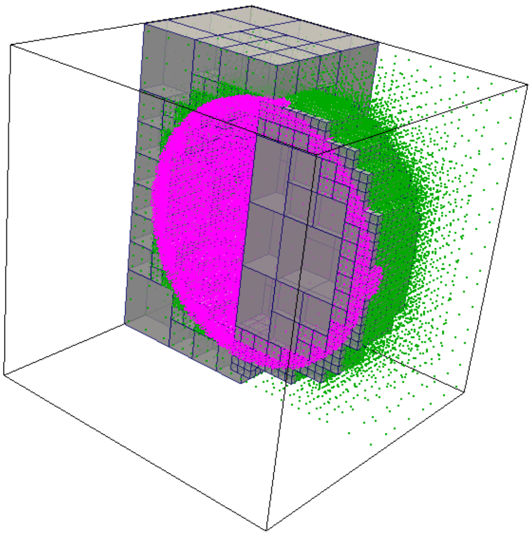

(c) *Quadratures (V)*

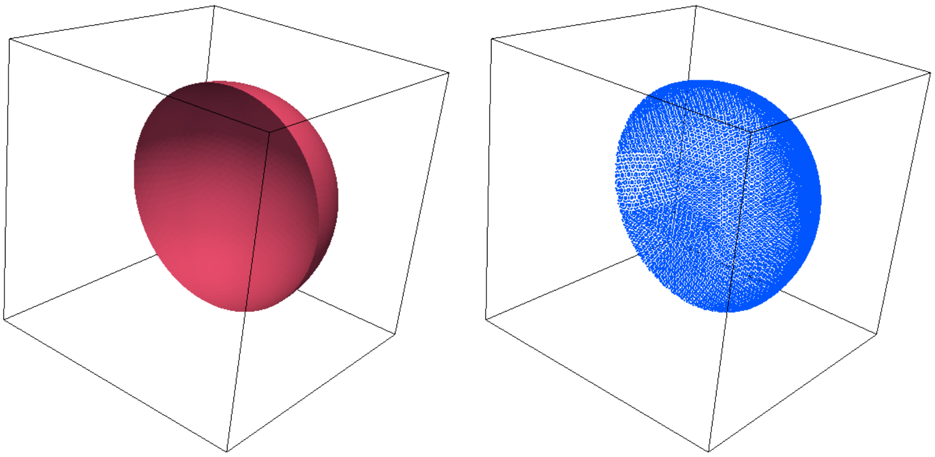

(d) *Surface* **(e)** *Quadratures (S)*

FIGURE 7.3. *Work-flow of producing integration points for the volume and the interface of a composite electrode. A spherical particle is embedded in a cubic matrix (a). Based on the geometry, an adaptive subdivision of level 3 is performed for both the matrix and the particle (b). The corresponding Gaussian quadrature points are then produced (c). For the interface (d), the surface quadrature points are produced based on a surface mesh generated by NETGEN (e).*

Table 7.3. *Materials parameters for the composite electrode. All the parameters are given in a dimensionless form.*

	Particle ($B^{(1)}$)	Matrix ($B^{(2)}$)
Bulk modulus (K)	1	0.1
Shear modulus (G)	1	0.1
Molar volume (V)	0.08	0.0001
Phase parameter (χ)	2.5	1.0
Interface parameter (κ)	1.247×10^{-3}	-
Initial concentration (c_0)	0.25	0.9
Boundary concentration ($\bar{c}$)	-	0.9

overall time spent on the assembly for different numbers of parallel processors. We observe that a speedup ratio of 8 could be achieved with 12 processors.

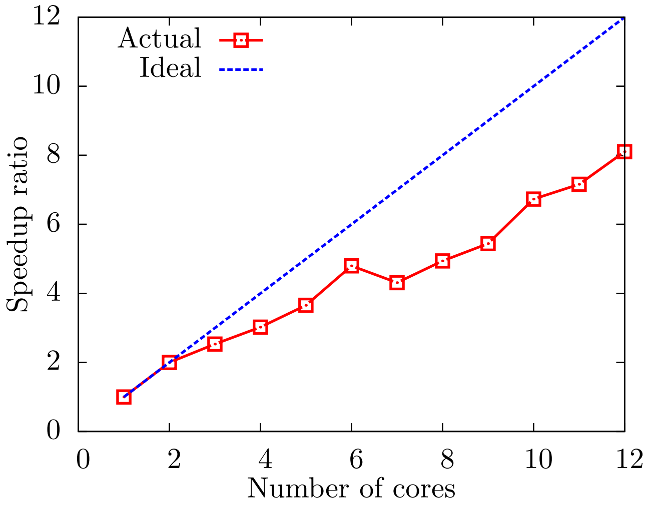

Figure 7.4. *Speedup ratio of parallelization of the assembly of the global matrix by OpenMP. The computation was performed at the Lichtenberg cluster hpb-nodes at Technical University Darmstadt. Every node consists of 2 processors, each with 12 cores.*

Figs. 7.5–7.7 show the simulation results of composite electrodes with different embedding particles. External mechanical constraints are applied on the matrix only to prevent rigid-body movements (Fig. 7.5(a)). When lithium flows from the matrix to the particle, in the matrix only a slight gradient of the concentration field is observed, while in the particles a more complex phenomenon is exhibited. For a sphere-shaped particle shown in Fig. 7.5, as the flux comes in, islands of Li-rich phase rise from the surface, surrounded by Li-deficit phase. Due to the unevenly distributed lithium concentration, the deformation on the particle is also inhomogeneous. As flux comes in continuously, Li-rich phases merge into larger domains until removal of the flux. For more geometrically complicated electrode particles such as merged two spheres

(Fig. 7.6) and merged three spheres (Fig. 7.7), the FCM shows great advantage since it represents the geometry only with adaptive quadrature points. In both cases, the Li-rich phases emerge from the ends, since the compressive stresses arising around the bottle necks drive the species towards the ends with tensile stresses. The Li-rich phase then marches towards the necks and join together. The remnant of Li-deficit phase is due to the incomplete charge. With longer incoming flux the particle can be finally fully charged. Fig. 7.8 shows the concentration distribution and the deformation of the matrix in the above three examples at $t = 3.0$. A homogeneous Dirichlet boundary was prescribed on the outer surface and a small flux is given. The concentration variation is not large, very different from what has been observed in the particle, where the phase-separation occurs. The unevenly distributed concentration profile on the interface is due to an uneven deformation and the consequent uneven stress distrubution.

7.3.2 Simulation based on scanned images

As a preliminary study, a model with particle geometries based on the scanned images is simulated. Since the geometry cannot be analytically described, a preprocessing is necessary. Fig. 7.9 illustrates the work-flow to identify each bulk and the interface between two bulk materials from an original image data. These data are obtained from Dr. Benedikt Peter [173] with scanning electron microscope (SEM). Images were taken along one direction with a fixed distance. Combination of them can give the voxel representation of the particles. Based on the voxel data, Allen–Cahn phase-field simulation is performed

$$\frac{\partial h}{\partial t} = \epsilon^2 \Delta h - \frac{\partial F(h)}{\partial h} \qquad \text{in} \quad \mathrm{B} \times (0, \mathscr{T}), \tag{7.23}$$

$$\boldsymbol{\nabla} h \cdot \boldsymbol{n} = 0 \qquad \text{on} \quad \partial \mathrm{B} \times (0, \mathscr{T}), \tag{7.24}$$

$$h(\boldsymbol{x}, 0) = H_0(\boldsymbol{x}) \qquad \text{in} \quad \mathrm{B}, \tag{7.25}$$

where $h(\boldsymbol{x}, t)$ is an order parameter, indicating if a position $\boldsymbol{x}$ is inside the particle or outside. The initial condition $H_0(\boldsymbol{x})$ is from the image data. With the distribution of h in equilibrium, one can perform the signed distance function

$$\frac{\partial d}{\partial t} + \operatorname{sgn}\left(d^0\right) \boldsymbol{n} \cdot \boldsymbol{\nabla} d = \operatorname{sgn}(d_0) \qquad \text{in} \quad \mathrm{B} \times (0, \mathscr{T}), \tag{7.26}$$

$$d(\boldsymbol{x}, 0) = d_0(\boldsymbol{x}) \qquad \text{in} \quad \mathrm{B}, \tag{7.27}$$

where $d_0(\boldsymbol{x})$ is obtained from the equilibrium $h(\boldsymbol{x}, \mathscr{T})$. The equilibrium distribution of d is passed to DistMesh [174] for a surface triangulation of interface between the particle and the matrix. The abovementioned preprocessing is done by Lam Nguyen from University of Minnesota.

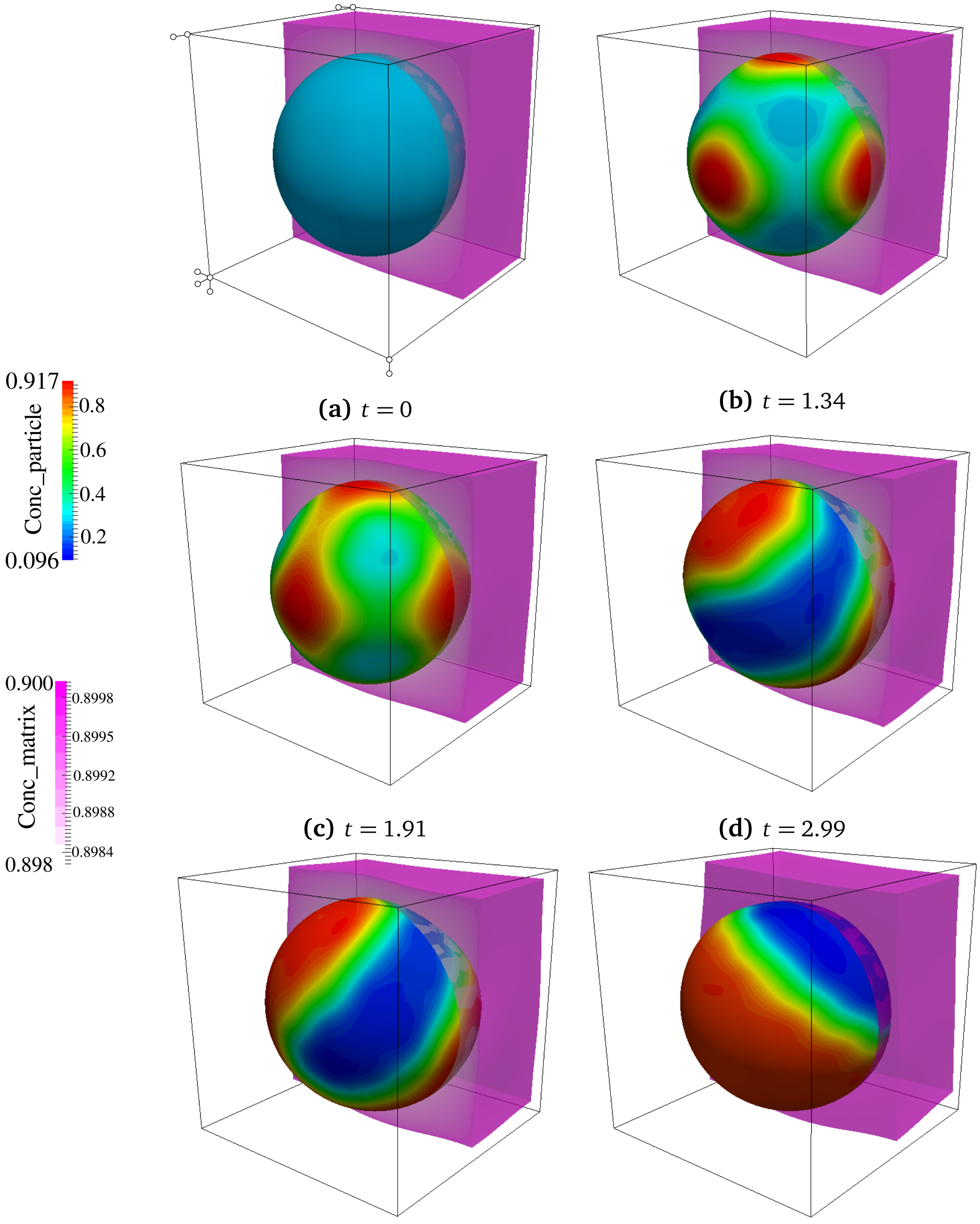

(a) $t = 0$ (b) $t = 1.34$

(c) $t = 1.91$ (d) $t = 2.99$

(e) $t = 4.06$ (f) $t = 9.74$

FIGURE 7.5. *Concentration distribution of the composite electrode with one sphere embedded in a matrix at different time. The mechanical constraints are only applied on the matrix to prevent the rigid body movements (Figure (a)). After the flux flows into the particle, two phases emerged from the surface. As the flux comes in continuously, islands of Li-rich phases merge together and reaches the final state.*

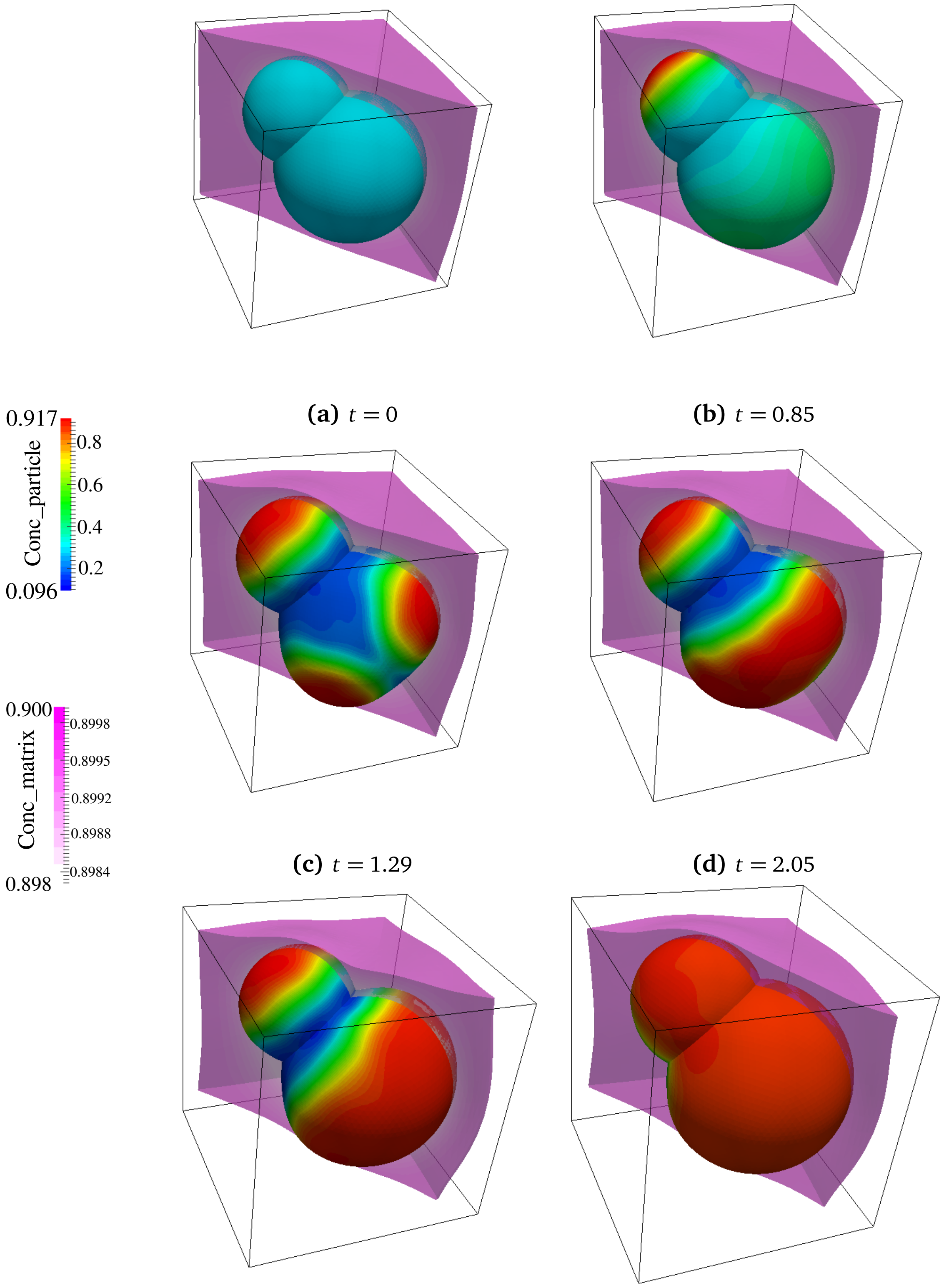

(a) $t = 0$ **(b)** $t = 0.85$

(c) $t = 1.29$ **(d)** $t = 2.05$

(e) $t = 3.94$ **(f)** $t = 31.13$

FIGURE 7.6. *Concentration evolution of the composite electrode with two merged spheres embedded in the matrix. The Li-rich phases emerge from the two ends and finally join at the neck.*

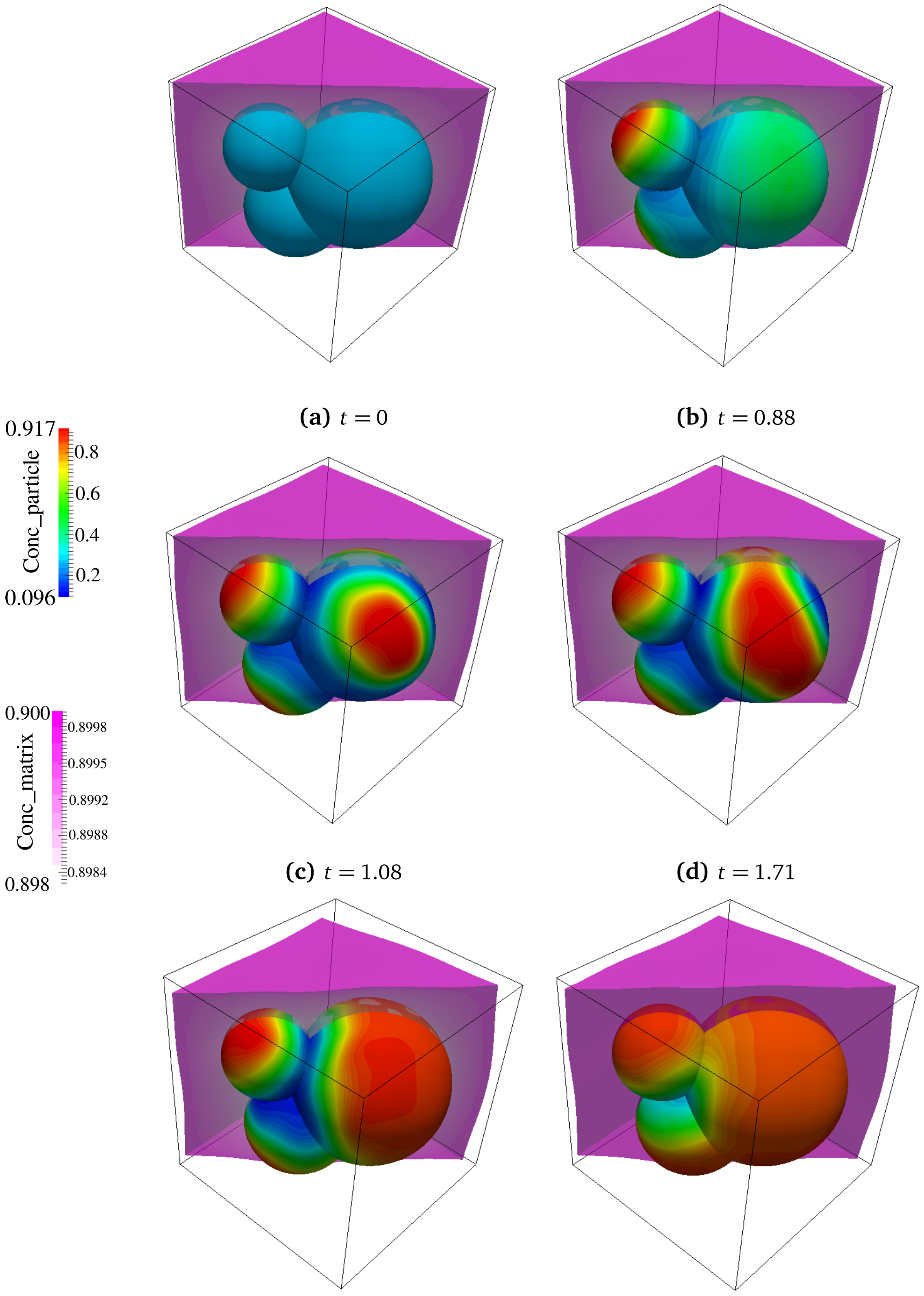

(a) $t = 0$ **(b)** $t = 0.88$

(c) $t = 1.08$ **(d)** $t = 1.71$

(e) $t = 4.66$ **(f)** $t = 6.25$

FIGURE 7.7. *Concentration evolution of the composite electrode with three merged spheres embedded in the matrix. Similar as the case with two particles in Fig. 7.6, the Li-rich phases emerge from the three ends and finally integrate at the necks.*

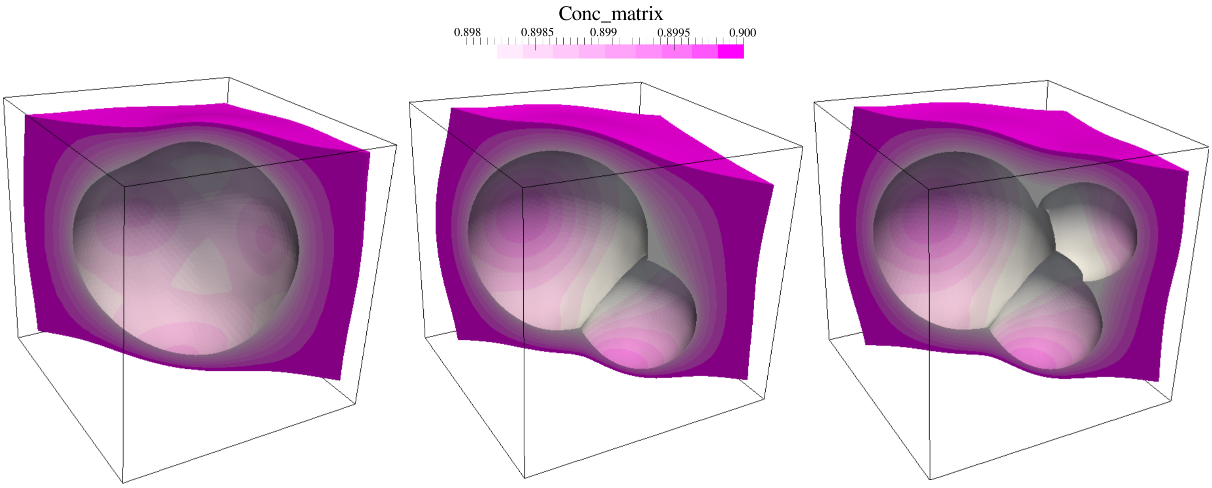

(a) *Single sphere.* **(b)** *Two spheres.* **(c)** *Three spheres.*

Figure 7.8. *The concentration and deformation in the matrix at* $t = 3.00$ *with different-shaped embedding particles. On the surface of the particle, a Dirichlet boundary* $c = 0.9$ *is prescribed, and only minimum points are constraint to prevent mechanical rigid body movements. On the interface, an out-going flux is given.*

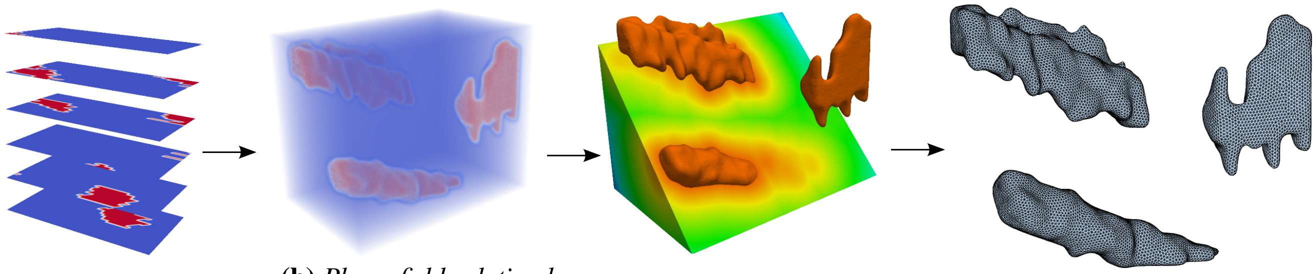

(a) *Original image data* **(b)** *Phase-field solution by Allen—Cahn equation* **(c)** *Signed distance function* **(d)** *Surface mesh by Distmesh*

Figure 7.9. *Workflow of image processing. From the original SEM scanned image [173] at each layer we can perform a phase-field simulation in order to extract the interface between the particle and the polymer surroundings (b). Afterwards the signed distance function is performed (c), whose results are passed to DistMesh [174] for the triangulation of the surface mesh. This work is done by Lam H. Nguyen from University of Minnesota.*

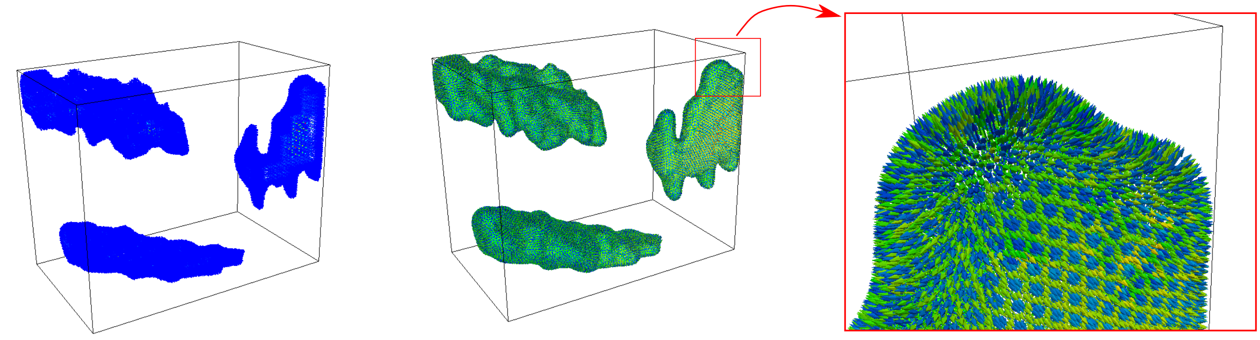

(a) *Volume quadrature points and weights*

(b) *Surface quadrature points, weights and normal vectors*

FIGURE 7.10. *Quadrature points in the volume and on the interface between the particle and the matrix. The color denotes the weight of the quadrature points. The arrows denote the normal vectors of the surface.*

Based on the phase-field result $h(\boldsymbol{x}, \mathscr{T})$, the volume integration points are produced, as shown in Fig. 7.10(a). The surface quadrature points, weights and the corresponding normal vectors are computed from the surface triangulation, as shown in Fig. 7.10(b). The preliminary results of the concentration distribution after the first several time steps is plotted in Fig. 7.11. Lithium accumulates at particle tips, where the surface curvature is larger; In the flat area, the concentration is lower.

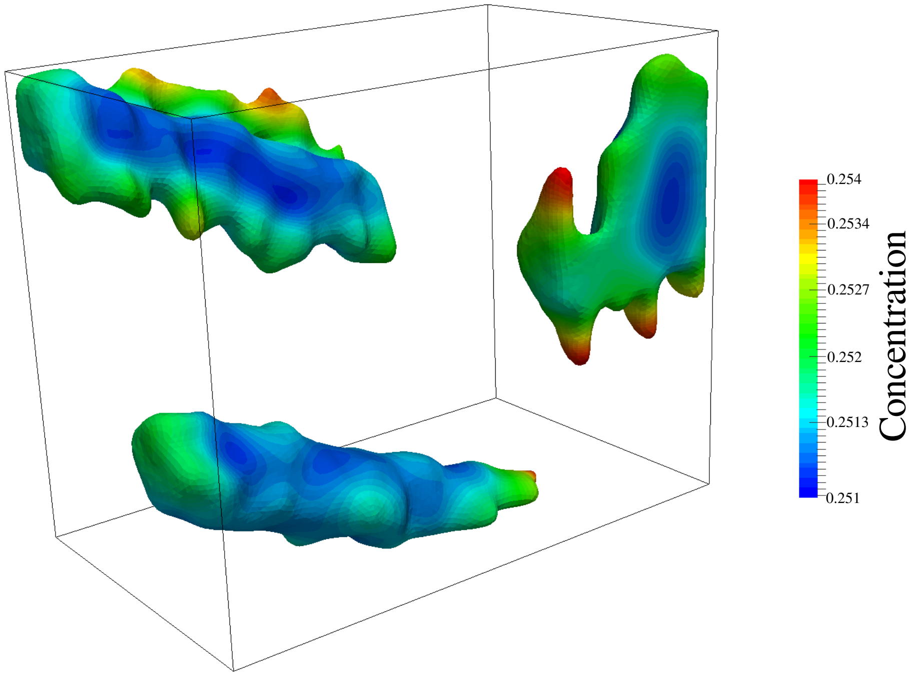

FIGURE 7.11. *Preliminary results of the concentration distribution of the lithium in the particles.*

7.4 Summary

In this chapter, a chemical-mechanical coupled two-material composite electrode model in lithium-ion batteries was formulated.

The model incorporates different chemical and mechanical properties in particles and matrix. Particles experience phase transformation. Moreover, different mechanical properties are allowed in two materials. Chemical and mechanical boundary conditions are applied on the interface between the particle and the matrix, which enforces that between the two materials, the mass is conserved, tractions equilibrate, and displacements are compatible.

The proposed model was simulated by the finite cell method. Different materials are represented by different sets of quadrature points, which are subject to different governing equations. The interface conditions are imposed weakly on interfacial quadrature points. In particular, for Dirichlet boundary conditions on the interface, non-symmetric Nitsche's method is employed. Volume quadrature points are computed through a recursive subdivision of the cells in each element based on the geometry given. The particle geometry can be described by an analytical expression, or by a voxel representation from scanned images. As examples of analytical expressed geometry, composites with different embedding interconnected spherical particles were simulated. Results show that mechanical stresses influence the phase separation in particles. The flux is driven by the compression towards regions with tensile stresses, which gives rise to the phenomenon that flux flows from heads towards necks of merged spheres. Lastly, the voxel representation based simulation was briefly introduced, the preliminary results were obtained.

Chapter 8

Concluding remarks

This thesis is dedicated to a deeper understanding of the electro-chemo-mechanical behavior of lithium-ion battery electrodes. Although there has been an everlasting interests and efforts on modeling, which has fertilized a handful of excellent dissertations [135, 175–177], the present thesis has its innovations in terms of both modeling and numerical treatments.

From the modeling point of view, we have formulated different mechanically coupled models summarized as follows.

1) A chemo-mechanical model with phase separation is formulated in a large-deformation regime. It is based on variational formulations, and proved to be consistent with the model derived from a microforce balance.

2) Concentration-dependent elastic properties are taken into account, which, as revealed in the thesis, can have significant influences on phase separation. In certain circumstances, models with concentration-dependent elastic properties predict the occurrence of phase separation while models without predict the opposite.

3) Electrochemical reaction is based on a modified Butler–Volmer equation, which involves not only electrostatic potential, but also chemical and mechanical properties of reactants. Concentration and mechanical stresses influence reaction rate and equilibrium states. In this way, flux on a surface is controlled during simulations and reaction-diffusion process stops when a desired equilibrium state is achieved.

4) Crack propagation in a particle is modeled by a phase-field approach. A fracture order parameter with values 0 and 1 denotes a cracked region and an unbroken region, respectively. The reaction on a crack surface is also considered in this model through a source term in the diffusion equation regularized by the fracture order parameter.

5) A composite-electrode model is formulated, considering different chemical and mechanical properties in particles and in matrix. In particles, phase separation occurs, while in matrix, only one phase exists. The two materials couple at the interface, where both chemical and mechanical conditions need to be imposed. Chemically, mass is conserved; Mechanically, traction equilibrium and displacement compatibility are fulfilled.

From the numerical point of view, different novel computational methods are explored in this thesis to achieve desired simulation results for the aforementioned models.

1) Single-particle models are simulated by isogeometric analysis, which employs a wide range of higher-order spline functions as basis functions. This can achieve higher continuity and faster convergence.

2) The additional boundary term arising from the Cahn–Hilliard equation is dealt with weakly by two methods: the Lagrange multiplier method and the Nitsche method. In contrast to strong enforcement, the new boundary condition formulation can be naturally applied to any mapped isogeometric parametrization of any polynomial degree.

3) The finite cell method is employed to simulate a composite-electrode model, because it has high flexibility to perform simulations with almost any geometries, ranging from boundary representations in computer aided geometric design to voxel representations obtained from scanned images.

Examples in this thesis are designed to understand mechanisms in lithium ion battery electrode particles with different geometry, charging rate, mechanical properties and phase interfaces properties. Following conclusions can be made from these numerical experiments:

1) Phase separation can be suppressed by reducing particle sizes, increasing stress level, or making materials stiffer.

2) Core-shell structure can be observed in spherical and spheroidal particles made of phase-separating materials, given that surface charging rate is fast compared with bulk diffusion. If charging rate is slow, spinodal decomposition on the surface leads to an uneven swelling already from the surface.

3) Even for rapid charge, if mechanical support from the matrix to the particle is unevenly given, the core-shell structure can not be achieved.

4) Crack in freestanding particles with initial notches on the edge will propagate during delithiation, when intensified tensile stresses accumulate at crack tips. Moreover, when phase interfaces overtake crack tips, crack branching can occur.

5) Reaction rate is enhanced on phase interfaces due to high concentration gradient and strain mismatch. Further, crack propagation and branching are also beneficial to a faster reaction, if broken regions are still electronically connected to each other and exposed to the electrolyte, since more surfaces are involved in electrochemical reaction.

Based on the work in this thesis, further efforts can be made to gain more understandings of lithium-ion battery systems.

1) The model in the present thesis can be adapted to describe electro-chemo-mechanical behavior of electrodes made of different materials. Chemical energy density can take the form from CALPHAD [56, 57]. Parameters such as diffusivity, interfacial energy, as well as elastic moduli can be measured by first principle calculations or experiments.

2) The model of the electrode particles can be further developed to incorporate visco-plastic and anisotropic behaviors of electrode materials. It is reported in materials such as silicon, plastic deformation is crucial in explaining capacity fade [118]. Further, anisotropic deformation with phase separation is also very much likely to lead to crack and contact loss in electrodes, which can result in an irreversible capacity fade.

3) The composite electrode model present in Chapter 7 has the potential to be carried out in a larger scale to simulate lithium-ion battery composite electrodes based on real scanned geometry, whose preliminary work has been already carried out.

4) This model is capable to describe the meso-scale behavior of a battery, which can fit in a multi-scale study to simulate a complete functionality of a lithium-ion battery in a cell phone or in an electric vehicle.

Appendix A

Tangent matrix for the chemo-mechanical model

The stiffness tangent matrices in Chapter 5 are (tensors with underlines denote those in Voigt notation):

$$\mathbf{K}_{uu}^{\mathrm{IJ}} = \int_{\mathrm{B}} (\boldsymbol{\nabla} N^{\mathrm{J}})^{\mathrm{T}} \mathbf{S} \, (\boldsymbol{\nabla} N^{\mathrm{I}}) \, \mathrm{dV} + \int_{\mathrm{B}} (\mathbf{B}_u^{\mathrm{I}})^{\mathrm{T}} \frac{2\partial \underline{\mathbf{S}}}{\partial \underline{\mathbf{C}}} \mathbf{B}_u^{\mathrm{J}} \, \mathrm{dV}, \tag{A.1}$$

$$\mathbf{K}_{uc}^{\mathrm{IJ}} = \int_{\mathrm{B}} (\mathbf{B}_u^{\mathrm{I}})^{\mathrm{T}} \frac{\partial \underline{\mathbf{S}}}{\partial c} N^{\mathrm{J}} \mathrm{dV}, \tag{A.2}$$

$$\begin{aligned}
\mathbf{K}_{cu}^{\mathrm{IJ}} = & -\int_{\mathrm{B}} c\,(1-c)\,(\mathbf{B}_c^{\mathrm{I}})^{\mathrm{T}} \boldsymbol{\nabla} c \frac{2\partial^2 \mu^e}{\partial c\,\partial \underline{\mathbf{C}}} \mathbf{B}_u^{\mathrm{J}} \, \mathrm{dV} \\
& -\int_{\mathrm{B}} c\,(1-c)\,(\mathbf{G}^{\mathrm{I}})^{\mathrm{T}} \frac{4\partial^2 \mu^e}{\partial \underline{\mathbf{C}} \partial \underline{\mathbf{C}}} \mathbf{B}_u^{\mathrm{J}} \, \mathrm{dV} - \int_{\mathrm{B}} c\,(1-c)\,(\frac{2\partial \mu^e}{\partial \underline{\mathbf{C}}})^{\mathrm{T}} \mathbf{G}^{\mathrm{IJ}} \, \mathrm{dV},
\end{aligned} \tag{A.3}$$

$$\begin{aligned}
\mathrm{K}_{cc}^{\mathrm{IJ}} = & \int_{\mathrm{B}} 2\chi\,(1-2c)\,N^{\mathrm{J}} (\mathbf{B}_c^{\mathrm{I}})^{\mathrm{T}} \boldsymbol{\nabla} c \, \mathrm{dV} - \int_{\mathrm{B}} [1 - 2\chi c\,(1-c)]\,(\mathbf{B}_c^{\mathrm{I}})^{\mathrm{T}} \mathbf{B}_c^{\mathrm{J}} \, \mathrm{dV} \\
& - \int_{\mathrm{B}} (1-2c)\,N^{\mathrm{J}} \frac{\partial \mu^e}{\partial c} (\mathbf{B}_c^{\mathrm{I}})^{\mathrm{T}} \boldsymbol{\nabla} c \, \mathrm{dV} - \int_{\mathrm{B}} c\,(1-c)\,\frac{\partial^2 \mu^e}{\partial c\,\partial c} N^{\mathrm{J}} (\mathbf{B}_c^{\mathrm{I}})^{\mathrm{T}} \boldsymbol{\nabla} c \, \mathrm{dV} \\
& - \int_{\mathrm{B}} c\,(1-c)\,\frac{\partial \mu^e}{\partial c} (\mathbf{B}_c^{\mathrm{I}})^{\mathrm{T}} \mathbf{B}_c^{\mathrm{J}} \, \mathrm{dV} \\
& - \int_{\mathrm{B}} (1-2c)\,N^{\mathrm{J}} (\mathbf{G}^{\mathrm{I}})^{\mathrm{T}} \frac{2\partial \mu^e}{\partial \underline{\mathbf{C}}} \, \mathrm{dV} - \int_{\mathrm{B}} c\,(1-c)\,(\mathbf{G}^{\mathrm{I}})^{\mathrm{T}} \frac{2\partial^2 \mu^e}{\partial \underline{\mathbf{C}} \partial c} N^{\mathrm{J}} \, \mathrm{dV} \\
& + \int_{\mathrm{B}} \kappa^* \cdot 2N^{\mathrm{J}} \Delta c\,(\mathbf{B}_c^{\mathrm{I}})^{\mathrm{T}} \boldsymbol{\nabla} c \, \mathrm{dV} - \int_{\mathrm{B}} \kappa^* (1-2c)\,\Delta N^{\mathrm{J}}\,(\mathbf{B}_c^{\mathrm{I}})^{\mathrm{T}} \boldsymbol{\nabla} c \, \mathrm{dV} \\
& - \int_{\mathrm{B}} \kappa^* (1-2c)\,\Delta c\,(\mathbf{B}_c^{\mathrm{I}})^{\mathrm{T}} \mathbf{B}_c^{\mathrm{J}} \, \mathrm{dV} \\
& - \int_{\mathrm{B}} \kappa^* (1-2c)\,N^{\mathrm{J}}\,\Delta c\,\Delta N^{\mathrm{I}} \, \mathrm{dV} - \int_{\mathrm{B}} \kappa^* c\,(1-c)\,\Delta N^{\mathrm{J}}\,\Delta N^{\mathrm{I}} \, \mathrm{dV},
\end{aligned} \tag{A.4}$$

$$\mathrm{D}_{cc}^{\mathrm{IJ}} = -\int_{\mathrm{B}} N^{\mathrm{J}} N^{\mathrm{I}} \, \mathrm{dV}, \tag{A.5}$$

$$\mathrm{K}_{c\lambda}^{\mathrm{IJ}} = -\int_{\mathrm{B}} (\mathbf{B}_c^{\mathrm{I}})^{\mathrm{T}} \mathbf{B}_c^{\mathrm{J}} \, \mathrm{dV} - \int_{\mathrm{B}} N^{\mathrm{J}} \Delta N^{\mathrm{I}} \, \mathrm{dV}, \tag{A.6}$$

$$\mathrm{K}_{\lambda c}^{\mathrm{IJ}} = -\int_{\mathrm{B}} (\mathbf{B}_c^{\mathrm{I}})^{\mathrm{T}} \mathbf{B}_c^{\mathrm{J}} \, \mathrm{dV} - \int_{\mathrm{B}} \Delta N^{\mathrm{J}} N^{\mathrm{I}} \, \mathrm{dV}, \tag{A.7}$$

$$\mathrm{K}_{\lambda c}^{\mathrm{IJ}} = \frac{1}{\alpha}\int_{\mathrm{B}} N^{\mathrm{J}} N^{\mathrm{I}}\,\mathrm{dV}, \tag{A.8}$$

in which

$$\frac{\partial \mu^e}{\partial c} = \frac{K_c^*(\Omega^*)^2 J^2}{(J^c)^3} + \mathrm{K}_0^*\Omega^*\left[(J^e)^2 - 1\right] - \mathrm{G}_0^*\Omega^*\left(\bar{I}_1 - 3\right), \tag{A.9}$$

$$\begin{aligned}\frac{2\partial \mu^e}{\partial \underline{\mathbf{C}}} &= G_c^*\Omega^* J^{-\frac{2}{3}}\left(\underline{\mathbf{1}} - \frac{1}{3}I_1\underline{\mathbf{C}}^{-1}\right) - K_c^*\Omega^*(J^e)^2\,\underline{\mathbf{C}}^{-1}\\ &\quad - J^c\left[\mathrm{G}_0^* J^{-\frac{2}{3}}\left(\underline{\mathbf{1}} - \frac{1}{3}I_1\underline{\mathbf{C}}^{-1}\right) + \mathrm{K}_0^* J^e(J^e - 1)\,\underline{\mathbf{C}}^{-1}\right],\end{aligned} \tag{A.10}$$

$$\frac{\partial^2 \mu^e}{\partial c\,\partial c} = -\frac{3K_c^*(\Omega^*)^3 J^2}{(J^c)^4} - \frac{3\mathrm{K}_0^*(\Omega^*)^2 J^2}{(J^c)^3}, \tag{A.11}$$

$$\frac{2\partial^2 \mu^e}{\partial c\,\partial \underline{\mathbf{C}}} = \frac{2K_c^*(\Omega^*)^2 J^2}{(J^c)^3}\underline{\mathbf{C}}^{-1} + 2\mathrm{K}_0^*\Omega^*(J^e)^2\,\underline{\mathbf{C}}^{-1} - 2\mathrm{G}_0^*\Omega^* J^{-\frac{2}{3}}\left(\underline{\mathbf{1}} - \frac{1}{3}I_1\underline{\mathbf{C}}^{-1}\right) = \frac{2\partial^2 \mu^e}{\partial \underline{\mathbf{C}}\partial c}, \tag{A.12}$$

$$\begin{aligned}\frac{4\partial^2 \mu^e}{\partial \underline{\mathbf{C}}\partial \underline{\mathbf{C}}} &= 2G_c^*\Omega^* J^{-\frac{2}{3}}\left(\frac{1}{3}I_1\underline{\mathbf{C}}^{-1}\odot\underline{\mathbf{C}}^{-1} - \frac{1}{3}\underline{\mathbf{C}}^{-1}\otimes\underline{\mathbf{1}} - \frac{1}{3}\underline{\mathbf{1}}\otimes\underline{\mathbf{C}}^{-1} + \frac{1}{9}I_1\underline{\mathbf{C}}^{-1}\otimes\underline{\mathbf{C}}^{-1}\right)\\ &\quad - 2K_c^*\Omega^*(J^e)^2\underline{\mathbf{C}}^{-1}\otimes\underline{\mathbf{C}}^{-1} + 2K_c^*\Omega^*(J^e)^2\underline{\mathbf{C}}^{-1}\odot\underline{\mathbf{C}}^{-1}\\ &\quad - 2\mathrm{G}_0^* J^c J^{-\frac{2}{3}}\left(\frac{1}{3}I_1\underline{\mathbf{C}}^{-1}\odot\underline{\mathbf{C}}^{-1} - \frac{1}{3}\underline{\mathbf{C}}^{-1}\otimes\underline{\mathbf{1}} - \frac{1}{3}\underline{\mathbf{1}}\otimes\underline{\mathbf{C}}^{-1} + \frac{1}{9}I_1\underline{\mathbf{C}}^{-1}\otimes\underline{\mathbf{C}}^{-1}\right)\\ &\quad - \mathrm{K}_0^* J(2J^e - 1)\,\underline{\mathbf{C}}^{-1}\otimes\underline{\mathbf{C}}^{-1} + 2\mathrm{K}_0^* J(J^e - 1)\,\underline{\mathbf{C}}^{-1}\odot\underline{\mathbf{C}}^{-1},\end{aligned} \tag{A.13}$$

$$\underline{\mathbf{S}} = J^c\left[G_c^* J^{-\frac{2}{3}}\left(\underline{\mathbf{1}} - \frac{1}{3}I_1\underline{\mathbf{C}}^{-1}\right) + K_c^* J^e(J^e - 1)\,\underline{\mathbf{C}}^{-1}\right], \tag{A.14}$$

$$\frac{\partial \underline{\mathbf{S}}}{\partial c} = G_c^*\Omega^* J^{-\frac{2}{3}}\left(\underline{\mathbf{1}} - \frac{1}{3}I_1\underline{\mathbf{C}}^{-1}\right) - K_c^*\Omega^*(J^e)^2\underline{\mathbf{C}}^{-1}, \tag{A.15}$$

$$-J^c\left[\mathrm{G}_0^* J^{-\frac{2}{3}}\left(\underline{\mathbf{1}} - \frac{1}{3}I_1\underline{\mathbf{C}}^{-1}\right) + \mathrm{K}_0^* J^e(J^e - 1)\,\underline{\mathbf{C}}^{-1}\right], \tag{A.16}$$

$$\begin{aligned}\frac{2\partial \underline{\mathbf{S}}}{\partial \underline{\mathbf{C}}} &= 2G_c^* J^c J^{-\frac{2}{3}}\left(\frac{1}{3}I_1\underline{\mathbf{C}}^{-1}\odot\underline{\mathbf{C}}^{-1} - \frac{1}{3}\underline{\mathbf{C}}^{-1}\otimes\underline{\mathbf{1}} - \frac{1}{3}\underline{\mathbf{1}}\otimes\underline{\mathbf{C}}^{-1} + \frac{1}{9}I_1\underline{\mathbf{C}}^{-1}\otimes\underline{\mathbf{C}}^{-1}\right)\\ &\quad + K_c^* J(2J^e - 1)\,\underline{\mathbf{C}}^{-1}\otimes\underline{\mathbf{C}}^{-1} - 2K_c^* J(J^e - 1)\,\underline{\mathbf{C}}^{-1}\odot\underline{\mathbf{C}}^{-1}.\end{aligned} \tag{A.17}$$

Here, $\otimes$ is the dyad tensor operator and $\odot$ is defined as a tensor product following the rule

$$(\mathbf{A}\odot\mathbf{A})_{IJKL} = \frac{1}{2}\left(\mathrm{A}_{IK}\mathrm{A}_{JL} + \mathrm{A}_{IL}\mathrm{A}_{JK}\right). \tag{A.18}$$

$\mathbf{G}^{\mathrm{I}} = \mathbf{GrC}\cdot\mathbf{B}_c^{\mathrm{I}}$, in which $\mathbf{B}_c^{\mathrm{I}}$ has been given in Eq. (5.48) and **GrC** is

$$\mathbf{GrC} = \begin{bmatrix} F_{i1}H2_{i1} & F_{i1}H2_{i4} & F_{i1}H2_{i6}\\ F_{i2}H2_{i4} & F_{i2}H2_{i2} & F_{i2}H2_{i5}\\ F_{i3}H2_{i6} & F_{i3}H2_{i5} & F_{i3}H2_{i3}\\ F_{i1}H2_{i4} + F_{i2}H2_{i1} & F_{i1}H2_{i2} + F_{i2}H2_{i4} & F_{i1}H2_{i5} + F_{i2}H2_{i6}\\ F_{i2}H2_{i6} + F_{i3}H2_{i4} & F_{i2}H2_{i5} + F_{i3}H2_{i2} & F_{i2}H2_{i3} + F_{i3}H2_{i5}\\ F_{i1}H2_{i6} + F_{i3}H2_{i1} & F_{i1}H2_{i5} + F_{i3}H2_{i4} & F_{i1}H2_{i3} + F_{i3}H2_{i6} \end{bmatrix} \tag{A.19}$$

with

$$\mathbf{H2} = \begin{bmatrix} u_1^{\mathrm{I}} N_{,11}^{\mathrm{I}} & u_1^{\mathrm{I}} N_{,22}^{\mathrm{I}} & u_1^{\mathrm{I}} N_{,33}^{\mathrm{I}} & u_1^{\mathrm{I}} N_{,12}^{\mathrm{I}} & u_1^{\mathrm{I}} N_{,23}^{\mathrm{I}} & u_1^{\mathrm{I}} N_{,31}^{\mathrm{I}} \\ u_2^{\mathrm{I}} N_{,11}^{\mathrm{I}} & u_2^{\mathrm{I}} N_{,22}^{\mathrm{I}} & u_2^{\mathrm{I}} N_{,33}^{\mathrm{I}} & u_2^{\mathrm{I}} N_{,12}^{\mathrm{I}} & u_2^{\mathrm{I}} N_{,23}^{\mathrm{I}} & u_2^{\mathrm{I}} N_{,31}^{\mathrm{I}} \\ u_3^{\mathrm{I}} N_{,11}^{\mathrm{I}} & u_3^{\mathrm{I}} N_{,22}^{\mathrm{I}} & u_3^{\mathrm{I}} N_{,33}^{\mathrm{I}} & u_3^{\mathrm{I}} N_{,12}^{\mathrm{I}} & u_3^{\mathrm{I}} N_{,23}^{\mathrm{I}} & u_3^{\mathrm{I}} N_{,31}^{\mathrm{I}} \end{bmatrix} \tag{A.20}$$

and $\mathbf{F}$ the deformation gradient.

As for $\mathbf{G}^{\mathrm{IJ}}$, $G_{MNj}^{\mathrm{IJ}} = 1/2\left(N_{,ML}^{\mathrm{J}} F_{jN} + u_{j,ML} N_{,N}^{\mathrm{J}} + N_{,NL}^{\mathrm{J}} F_{jM} + u_{j,NL} N_{,M}^{\mathrm{J}}\right) N_{,L}^{\mathrm{I}}$. In Voigt notation, each component of the matrix is

$$\begin{aligned}
G^{\mathrm{IJ}}(1,i) &= N^2(1,\mathrm{J})F(i,1)N(1,\mathrm{I}) + N^2(4,\mathrm{J})F(i,1)N(2,\mathrm{I}) + N^2(6,\mathrm{J})F(i,1)N(3,\mathrm{I}) \\
&+ H2(i,1)N(1,\mathrm{J})N(1,\mathrm{I}) + H2(i,4)N(1,\mathrm{J})N(2,\mathrm{I}) + H2(i,6)N(1,\mathrm{J})N(3,\mathrm{I}), \\
G^{\mathrm{IJ}}(2,i) &= N^2(4,\mathrm{J})F(i,2)N(1,\mathrm{I}) + N^2(2,\mathrm{J})F(i,2)N(2,\mathrm{I}) + N^2(5,\mathrm{J})F(i,2)N(3,\mathrm{I}) \\
&+ H2(i,4)N(2,\mathrm{J})N(1,\mathrm{I}) + H2(i,2)N(2,\mathrm{J})N(2,\mathrm{I}) + H2(i,5)N(2,\mathrm{J})N(3,\mathrm{I}), \\
G^{\mathrm{IJ}}(3,i) &= N^2(6,\mathrm{J})F(i,3)N(1,\mathrm{I}) + N^2(5,\mathrm{J})F(i,3)N(2,\mathrm{I}) + N^2(3,\mathrm{J})F(i,3)N(3,\mathrm{I}) \\
&+ H2(i,6)N(3,\mathrm{J})N(1,\mathrm{I}) + H2(i,5)N(3,\mathrm{J})N(2,\mathrm{I}) + H2(i,3)N(3,\mathrm{J})N(3,\mathrm{I}), \\
G^{\mathrm{IJ}}(4,i) &= N^2(1,\mathrm{J})F(i,2)N(1,\mathrm{I}) + N^2(4,\mathrm{J})F(i,2)N(2,\mathrm{I}) + N^2(6,\mathrm{J})F(i,2)N(3,\mathrm{I}) \\
&+ H2(i,1)N(2,\mathrm{J})N(1,\mathrm{I}) + H2(i,4)N(2,\mathrm{J})N(2,\mathrm{I}) + H2(i,6)N(2,\mathrm{J})N(3,\mathrm{I}) \\
&+ N^2(4,\mathrm{J})F(i,1)N(1,\mathrm{I}) + N^2(2,\mathrm{J})F(i,1)N(2,\mathrm{I}) + N^2(5,\mathrm{J})F(i,1)N(3,\mathrm{I}) \\
&+ H2(i,4)N(1,\mathrm{J})N(1,\mathrm{I}) + H2(i,2)N(1,\mathrm{J})N(2,\mathrm{I}) + H2(i,5)N(1,\mathrm{J})N(3,\mathrm{I}), \\
G^{\mathrm{IJ}}(5,i) &= N^2(4,\mathrm{J})F(i,3)N(1,\mathrm{I}) + N^2(2,\mathrm{J})F(i,3)N(2,\mathrm{I}) + N^2(5,\mathrm{J})F(i,3)N(3,\mathrm{I}) \\
&+ H2(i,4)N(3,\mathrm{J})N(1,\mathrm{I}) + H2(i,2)N(3,\mathrm{J})N(2,\mathrm{I}) + H2(i,5)N(3,\mathrm{J})N(3,\mathrm{I}) \\
&+ N^2(6,\mathrm{J})F(i,2)N(1,\mathrm{I}) + N^2(5,\mathrm{J})F(i,2)N(2,\mathrm{I}) + N^2(3,\mathrm{J})F(i,2)N(3,\mathrm{I}) \\
&+ H2(i,6)N(2,\mathrm{J})N(1,\mathrm{I}) + H2(i,5)N(2,\mathrm{J})N(2,\mathrm{I}) + H2(i,3)N(2,\mathrm{J})N(3,\mathrm{I}), \\
G^{\mathrm{IJ}}(6,i) &= N^2(6,\mathrm{J})F(i,1)N(1,\mathrm{I}) + N^2(5,\mathrm{J})F(i,1)N(2,\mathrm{I}) + N^2(3,\mathrm{J})F(i,1)N(3,\mathrm{I}) \\
&+ H2(i,6)N(1,\mathrm{J})N(1,\mathrm{I}) + H2(i,5)N(1,\mathrm{J})N(2,\mathrm{I}) + H2(i,3)N(1,\mathrm{J})N(3,\mathrm{I}) \\
&+ N^2(1,\mathrm{J})F(i,3)N(1,\mathrm{I}) + N^2(4,\mathrm{J})F(i,3)N(2,\mathrm{I}) + N^2(6,\mathrm{J})F(i,3)N(3,\mathrm{I}) \\
&+ H2(i,1)N(3,\mathrm{J})N(1,\mathrm{I}) + H2(i,4)N(3,\mathrm{J})N(2,\mathrm{I}) + H2(i,6)N(3,\mathrm{J})N(3,\mathrm{I}),
\end{aligned} \tag{A.21}$$

with $\mathbf{N}^2$ the second derivative of the shape functions

$$\mathbf{N}^2(:,\mathrm{I}) = \begin{bmatrix} N_{,11}^{\mathrm{I}} & N_{,22}^{\mathrm{I}} & N_{,33}^{\mathrm{I}} & N_{,12}^{\mathrm{I}} & N_{,23}^{\mathrm{I}} & N_{,31}^{\mathrm{I}} \end{bmatrix}^{\mathrm{T}} \tag{A.22}$$

and $\mathbf{N}$ the first derivative

$$\mathbf{N}(:,\mathrm{I}) = \begin{bmatrix} N_{,1}^{\mathrm{I}} & N_{,2}^{\mathrm{I}} & N_{,3}^{\mathrm{I}} \end{bmatrix}^{\mathrm{T}}. \tag{A.23}$$

Appendix B

Mechanical influence on the bulk phases

In this appendix, the analytical solution for the example presented in Section 5.3.2 is derived. Now we focus our attention on the two homogeneous phases, α and β phase respectively. Then the concentrations c_α and c_β are constants and no gradient term comes into play at equilibrium.

At equilibrium, the chemical potential should be everywhere constant [31], and they follow common tangent construction of the free energy functional, which means

$$\begin{cases} \mu_\alpha - \mu_\beta = 0, \\ \psi_\alpha - \psi_\beta - \mu_\alpha\left(c_\alpha - c_\beta\right) = 0, \end{cases} \tag{B.1}$$

in which

$$\begin{aligned} \mu_\alpha = {} & \ln c_\alpha - \ln(1-c_\alpha) + \chi(1-2c_\alpha) + \frac{G^*_{c_\alpha}\Omega^*}{2}\left((\bar{I}_1)_\alpha - 3\right) \\ & - \frac{K^*_{c_\alpha}\Omega^*}{2}\left[\left(J^e_\alpha\right)^2 - 1\right] - J^c_\alpha\left[\frac{\mathrm{G}^*_0}{2}\left((\bar{I}_1)_\alpha - 3\right) + \frac{\mathrm{K}^*_0}{2}\left(J^e_\alpha - 1\right)^2\right], \end{aligned} \tag{B.2}$$

$$\begin{aligned} \mu_\beta = {} & \ln c_\beta - \ln\left(1-c_\beta\right) + \chi\left(1-2c_\beta\right) + \frac{G^*_{c_\beta}\Omega^*}{2}\left((\bar{I}_1)_\beta - 3\right) \\ & - \frac{K^*_{c_\beta}\Omega^*}{2}\left[\left(J^e_\beta\right)^2 - 1\right] - J^c_\beta\left[\frac{\mathrm{G}^*_0}{2}\left((\bar{I}_1)_\beta - 3\right) + \frac{\mathrm{K}^*_0}{2}\left(J^e_\beta - 1\right)^2\right], \end{aligned} \tag{B.3}$$

$$\begin{aligned} \psi_\alpha = {} & c_\alpha \ln c_\alpha + (1-c_\alpha)\ln(1-c_\alpha) + \chi c_\alpha(1-c_\alpha) \\ & + J^c_\alpha\left[\frac{G^*_{c_\alpha}}{2}\left((\bar{I}_1)_\alpha - 3\right) + \frac{K^*_{c_\alpha}}{2}\left(J^e_\alpha - 1\right)^2\right], \end{aligned} \tag{B.4}$$

$$\begin{aligned} \psi_\beta = {} & c_\beta \ln c_\beta + \left(1-c_\beta\right)\ln\left(1-c_\beta\right) + \chi c_\beta\left(1-c_\beta\right) \\ & + J^c_\beta\left[\frac{G^*_{c_\beta}}{2}\left((\bar{I}_1)_\beta - 3\right) + \frac{K^*_{c_\beta}}{2}\left(J^e_\beta - 1\right)^2\right]. \end{aligned} \tag{B.5}$$

Note that if the stress state is different in two different phases, the c_α and c_β will be different from those obtained without mechanical coupling.

For a hydrostatic stress loading, the two phases are subject to uniformly distributed pressure, which is only related to volumetric elastic deformation, given that $p_\mathrm{R} = \partial\psi/\partial J = K_c(J^e - 1)$. Substituting it into (B.2)-(B.5), we have

$$\mu_\alpha = \ln\frac{c_\alpha}{1-c_\alpha} + \chi(1-2c_\alpha) - \frac{\Omega^* p}{2}\left(\frac{p}{K^*_{c_\alpha}} + 2\right) - J^c_\alpha\frac{\mathrm{K}^*_0}{2}\left(\frac{p}{K^*_{c_\alpha}}\right)^2 \tag{B.6}$$

$$\mu_\beta = \ln\frac{c_\beta}{1-c_\beta} + \chi\left(1-2c_\beta\right) - \frac{\Omega^* p}{2}\left(\frac{p}{K^*_{c_\beta}} + 2\right) - J^c_\beta \frac{\mathrm{K}^*_0}{2}\left(\frac{p}{K^*_{c_\beta}}\right)^2 \tag{B.7}$$

$$\psi_\alpha = c_\alpha \ln c_\alpha + (1-c_\alpha)\ln(1-c_\alpha) + \chi c_\alpha (1-c_\alpha) + J^c_\alpha \frac{K^*_{c_\alpha}}{2}\left(\frac{p}{K^*_{c_\alpha}}\right)^2 \tag{B.8}$$

$$\psi_\beta = c_\beta \ln c_\beta + \left(1-c_\beta\right)\ln\left(1-c_\beta\right) + \chi c_\beta \left(1-c_\beta\right) + J^c_\beta \frac{K^*_{c_\beta}}{2}\left(\frac{p}{K^*_{c_\beta}}\right)^2 \tag{B.9}$$

in which $p = p_{\mathrm{R}}/\mathrm{RTc}_{\mathrm{max}}$ is the normalized pressure. For a free standing particle, $p = 0$ and there is no mechanical contribution to the two homogeneous phases. However, as we can see from Fig. 5.2, there is still stresses at the interface, and this will influence the interface behavior.

For particle subjected to the boundary condition that no displacement is allowed, $\mathbf{F} = \mathbf{I}$, and the bulk chemical potential and free energy are:

$$\mu_\alpha = \ln\frac{c_\alpha}{1-c_\alpha} + \chi(1-2c_\alpha) - \frac{K^*_{c_\alpha}\Omega^*}{2}\left[\frac{1}{(J^c_\alpha)^2} - 1\right] - \frac{J^c_\alpha \mathrm{K}^*_0}{2}\left(\frac{1}{J^c_\alpha} - 1\right)^2 \tag{B.10}$$

$$\mu_\beta = \ln\frac{c_\beta}{1-c_\beta} + \chi\left(1-2c_\beta\right) - \frac{K^*_{c_\beta}\Omega^*}{2}\left[\frac{1}{(J^c_\beta)^2} - 1\right] - \frac{J^c_\beta \mathrm{K}^*_0}{2}\left(\frac{1}{J^c_\beta} - 1\right)^2 \tag{B.11}$$

$$\psi_\alpha = c_\alpha \ln c_\alpha + (1-c_\alpha)\ln(1-c_\alpha) + \chi c_\alpha (1-c_\alpha) + \frac{J^c_\alpha K^*_{c_\alpha}}{2}\left(\frac{1}{J^c_\alpha} - 1\right)^2 \tag{B.12}$$

$$\psi_\beta = c_\beta \ln c_\beta + \left(1-c_\beta\right)\ln\left(1-c_\beta\right) + \chi c_\beta \left(1-c_\beta\right) + \frac{J^c_\beta K^*_{c_\beta}}{2}\left(\frac{1}{J^c_\beta} - 1\right)^2 \tag{B.13}$$

Substituting them into B.1 and solving it numerically using Newton iteration method, we obtain and plot the results as shown in Figure 5.3.

Appendix C

Numerical details for the coupled fracture model

This appendix gives the implementation details for the model presented in Section 6.3. For the convenience of finite element implementation, the model presented above is normalized first. The normalization is the same as in the last chapter. Here we only give the newly introduced variables. In the fracture model, the normalized strain-history field, fracture length scale, energy release rate and the mobility are

$$\mathcal{H} = \frac{\mathcal{H}_{\mathrm{R}}}{\mathrm{RTc_{max}}}, \quad \epsilon^* = \frac{\epsilon}{\mathrm{L_0}}, \quad \mathcal{G}_c^* = \frac{\mathcal{G}_c}{\mathrm{L_0RTc_{max}}}, \quad \mathrm{M}_\xi^* = \frac{\mathrm{M}_\xi \mathrm{L}_0^2\mathrm{RTc_{max}}}{\mathrm{D}}. \tag{C.1}$$

For the reaction, the normalized surface site concentration c_s^* and the single reaction time step τ_0^* are

$$\mathrm{c}_s^* = \frac{\mathrm{c}_s}{\mathrm{c_{max}L_0}}, \quad \tau_0^* = \frac{\mathrm{D}}{\mathrm{L}_0^2}\tau_0. \tag{C.2}$$

Thus, the normalized governing equations can be summarized as:

$$\nabla\cdot\mathbf{P} = \mathbf{0} \qquad \text{in} \quad \mathrm{B} \quad \times\left(0,\bar{\mathcal{T}}\right), \tag{C.3}$$

$$\dot{c} = \nabla\cdot\left[\xi^2 c(1-c)J\mathbf{F}^{-1}\mathbf{M}^*\mathbf{F}^{-\mathrm{T}}\nabla\mu\right] + \frac{6}{\epsilon^*\xi_0^4}\xi^2\left(\xi_0-\xi\right)^2\bar{\hat{j}}_s \qquad \text{in} \quad \mathrm{B} \quad \times\left(0,\bar{\mathcal{T}}\right), \tag{C.4}$$

$$\dot{\xi} = -M_\xi^*\left[2\xi\mathcal{H} - 2\mathcal{G}_c^*\epsilon^*\Delta\xi + \frac{\mathcal{G}_c^*}{2\epsilon^*}\left(\xi-1\right)\right] \qquad \text{in} \quad \mathrm{B} \quad \times\left(0,\bar{\mathcal{T}}\right), \tag{C.5}$$

$$\bar{\mathbf{u}} = \hat{\bar{\mathbf{u}}} \qquad \text{on} \quad \mathrm{S}_{\bar{\mathbf{u}}} \quad \times\left(0,\bar{\mathcal{T}}\right), \tag{C.6}$$

$$\mathbf{P}\cdot\boldsymbol{n} = \hat{\bar{\mathbf{t}}} \qquad \text{on} \quad \mathrm{S}_{\bar{\mathbf{t}}} \quad \times\left(0,\bar{\mathcal{T}}\right), \tag{C.7}$$

$$\mathbf{j}\cdot\boldsymbol{n} = -\bar{\hat{j}}_s \qquad \text{on} \quad \partial\mathrm{B} \quad \times\left(0,\bar{\mathcal{T}}\right), \tag{C.8}$$

$$\mathbf{K}\nabla c\cdot\boldsymbol{n} = 0 \qquad \text{on} \quad \partial\mathrm{B} \quad \times\left(0,\bar{\mathcal{T}}\right), \tag{C.9}$$

$$\nabla\xi\cdot\boldsymbol{n} = 0 \qquad \text{on} \quad \partial\mathrm{B} \quad \times\left(0,\bar{\mathcal{T}}\right), \tag{C.10}$$

$$c\left(\bar{\mathbf{X}},0\right) = c_0\left(\bar{\mathbf{X}}\right) \qquad \text{in} \quad \mathrm{B}, \tag{C.11}$$

$$\xi\left(\bar{\mathbf{X}},0\right) = 0 \qquad \text{on} \quad \mathrm{S}_f, \tag{C.12}$$

$$\xi\left(\bar{\mathbf{X}},0\right) = 1 \qquad \text{in} \quad \mathrm{B}\backslash\mathrm{S}_f, \tag{C.13}$$

with $\bar{\hat{j}}_s$ defined as

$$\bar{\hat{j}}_s = \frac{\mathrm{c}_s^*}{\tau_0^*}(1-c)\exp\left(-\frac{1}{2}\Delta\phi^*\right) - \frac{\mathrm{c}_s^*}{\tau_0^*}c\exp\left[\chi(1-2c)+\mu^e-\boldsymbol{\nabla}\cdot\mathbf{K}^*\boldsymbol{\nabla}c+\frac{1}{2}\Delta\phi^*\right]. \tag{C.14}$$

The model is implemented by using the finite element program FEAP [61] with Non-Uniform Rational B-Splines (NURBS) as shape functions for the spatial discretization, which allow for a straightforward treatment of the fourth-order Cahn–Hilliard equation. The displacements $\boldsymbol{u}$, the concentration c and the order parameter ξ are nodal degrees of freedom. In addition, as in Chapter 5, to deal with the additional boundary condition $\mathbf{K}\boldsymbol{\nabla}c\cdot\boldsymbol{n}=0$ arising along with the Cahn–Hilliard equation, a Lagrange multiplier λ is introduced as an additional degree of freedom for each node. A backward Euler method is employed for the time integration and the Newton-Raphson iteration scheme is used for the nonlinear system of equations at each time step.

The above mentioned 6 field variables are interpolated under an isoparametric/isogeometric concept as

$$\boldsymbol{u}=N^{\mathrm{I}}\boldsymbol{u}^{\mathrm{I}},\quad c=N^{\mathrm{I}}c^{\mathrm{I}},\quad \xi=N^{\mathrm{I}}\xi^{\mathrm{I}},\quad \lambda=N^{\mathrm{I}}\lambda^{\mathrm{I}}. \tag{C.15}$$

The gradient terms are thus given by

$$\delta\underline{\mathbf{E}}=\mathbf{B}_{\boldsymbol{u}}^{\mathrm{I}}\delta\boldsymbol{u}^{\mathrm{I}},\quad \boldsymbol{\nabla}c=\mathbf{B}_c^{\mathrm{I}}c^{\mathrm{I}},\quad \boldsymbol{\nabla}\xi=\mathbf{B}_\xi^{\mathrm{I}}\xi^{\mathrm{I}},\quad \boldsymbol{\nabla}\lambda=\mathbf{B}_\lambda^{\mathrm{I}}\lambda^{\mathrm{I}} \tag{C.16}$$

where $\underline{\mathbf{E}}$ is the Green-Lagrangian strain tensor in Voigt notation,

$$\mathbf{B}_c^{\mathrm{I}}=\mathbf{B}_\xi^{\mathrm{I}}=\mathbf{B}_\lambda^{\mathrm{I}}=\boldsymbol{\nabla}N^{\mathrm{I}}=\begin{bmatrix} N_{,1}^{\mathrm{I}} & N_{,2}^{\mathrm{I}} & N_{,3}^{\mathrm{I}} \end{bmatrix}^{\mathrm{T}}, \tag{C.17}$$

and $\mathbf{B}_{\boldsymbol{u}}$ has been already introduced in Eq. (5.49).

Thus, the discretized weak form of Eqs. (C.3)–(C.13) reads

$$\delta\Pi=(\delta\mathbf{u}^{\mathrm{I}})^{\mathrm{T}}\mathbf{R}_u^{\mathrm{I}}+\delta c^{\mathrm{I}}\mathrm{R}_c^{\mathrm{I}}+\delta\xi^{\mathrm{I}}\mathrm{R}_\xi^{\mathrm{I}}+\delta\lambda^{\mathrm{I}}\mathrm{R}_\lambda^{\mathrm{I}}=0, \tag{C.18}$$

in which the residuals are

$$\mathbf{R}_u^{\mathrm{I}}=-\int_{\mathrm{B}}(\mathbf{B}_u^{\mathrm{I}})^{\mathrm{T}}\left[\left(\xi^2+\eta\right)\frac{\partial\psi^{e+}}{\partial\underline{\mathbf{E}}}+\frac{\partial\psi^{e-}}{\partial\underline{\mathbf{E}}}\right]\mathrm{dB}, \tag{C.19a}$$

$$\begin{aligned}\mathrm{R}_c^{\mathrm{I}}=&\int_{\mathrm{B}}\dot{c}N^{\mathrm{I}}\,\mathrm{dB}+\int_{\mathrm{B}}\xi^2[1-2\chi c(1-c)]J\left(\boldsymbol{\nabla}c\cdot\mathbf{F}^{-1}\mathbf{M}^*\mathbf{F}^{-\mathrm{T}}\boldsymbol{\nabla}N^{\mathrm{I}}\right)\mathrm{dB}\\&+\int_{\mathrm{B}}\xi^2c(1-c)J\left(\boldsymbol{\nabla}\mu^e\cdot\mathbf{F}^{-1}\mathbf{M}^*\mathbf{F}^{-\mathrm{T}}\boldsymbol{\nabla}N^{\mathrm{I}}\right)\mathrm{dB}\end{aligned}$$

$$
\begin{aligned}
&+\int_{\mathrm{B}} 2\xi c\,(1-c)J(\boldsymbol{\nabla}\cdot\mathbf{K}^{*}\boldsymbol{\nabla}c)(\boldsymbol{\nabla}\xi\cdot\mathbf{F}^{-1}\mathbf{M}^{*}\mathbf{F}^{-\mathrm{T}}\boldsymbol{\nabla}N^{\mathrm{I}})\,\mathrm{dB}\\
&+\int_{\mathrm{B}} \xi^{2}(1-2c)J\,(\boldsymbol{\nabla}\cdot\mathbf{K}^{*}\boldsymbol{\nabla}c)(\boldsymbol{\nabla}c\cdot\mathbf{F}^{-1}\mathbf{M}^{*}\mathbf{F}^{-\mathrm{T}}\boldsymbol{\nabla}N^{\mathrm{I}})\,\mathrm{dB}\\
&+\int_{\mathrm{B}} \xi^{2}c\,(1-c)(\boldsymbol{\nabla}\cdot\mathbf{K}^{*}\boldsymbol{\nabla}c)(\boldsymbol{\nabla}J\cdot\mathbf{F}^{-1}\mathbf{M}^{*}\mathbf{F}^{-\mathrm{T}}\boldsymbol{\nabla}N^{-1})\,\mathrm{dB}\\
&+\int_{\mathrm{B}} \xi^{2}c\,(1-c)\,(\boldsymbol{\nabla}\cdot\mathbf{K}^{*}\boldsymbol{\nabla}c)\,\Delta N^{\mathrm{I}}\,\mathrm{dB}\\
&+\int_{\mathrm{B}} \xi^{2}c\,(1-c)J\,(\boldsymbol{\nabla}\cdot\mathbf{K}^{*}\boldsymbol{\nabla}c)\left[\left(\boldsymbol{\nabla}\cdot\mathbf{F}^{-1}\mathbf{M}^{*}\mathbf{F}^{-\mathrm{T}}\right)\cdot\boldsymbol{\nabla}N^{\mathrm{I}}\right]\mathrm{dB}\\
&+\int_{\mathrm{B}} \xi^{2}c\,(1-c)J\,(\boldsymbol{\nabla}\cdot\mathbf{K}^{*}\boldsymbol{\nabla}c)\left(\mathbf{F}^{-1}\mathbf{M}^{*}\mathbf{F}^{-\mathrm{T}}:\boldsymbol{\nabla}\boldsymbol{\nabla}N^{\mathrm{I}}\right)\mathrm{dB}\\
&-\int_{\mathrm{B}} \frac{6\xi^{2}(\xi_{0}-\xi)^{2}}{\epsilon^{*}\xi_{0}^{4}}\hat{j}_{s}N^{\mathrm{I}}\,\mathrm{dB}-\int_{\partial\mathrm{B}}\hat{j}^{s}\,N^{\mathrm{I}}\,\mathrm{dS}\\
&+\int_{\mathrm{B}} \boldsymbol{\nabla}\lambda\cdot\mathbf{K}^{*}\boldsymbol{\nabla}N^{\mathrm{I}}\,\mathrm{dB}+\int_{\mathrm{B}}\lambda\,\boldsymbol{\nabla}\cdot\mathbf{K}^{*}\boldsymbol{\nabla}N^{\mathrm{I}}\,\mathrm{dB},
\end{aligned}
\tag{C.19b}
$$

$$
\begin{aligned}
\mathrm{R}^{\mathrm{I}}_{\xi}=&\int_{\mathrm{B}}\dot{\xi}\,N^{\mathrm{I}}\,\mathrm{dB}-\int_{\mathrm{B}}\mathrm{M}^{*}_{\xi}\left[2\xi\,\mathscr{H}+\frac{\mathcal{G}^{*}_{c}}{2\epsilon^{*}}(\xi-1)\right]N^{\mathrm{I}}\,\mathrm{dB}\\
&-\int_{\mathrm{B}}\mathrm{M}^{*}_{\xi}\cdot2\mathcal{G}^{*}_{c}\epsilon^{*}\boldsymbol{\nabla}\xi\cdot\boldsymbol{\nabla}N^{\mathrm{I}}\,\mathrm{dB}
\end{aligned}
\tag{C.19c}
$$

$$
\mathrm{R}^{\mathrm{I}}_{\lambda}=\int_{\mathrm{B}}\boldsymbol{\nabla}\cdot\mathbf{K}^{*}\boldsymbol{\nabla}c\,N^{\mathrm{I}}\,\mathrm{dB}+\int_{\mathrm{B}}\mathbf{K}^{*}\boldsymbol{\nabla}c\cdot\boldsymbol{\nabla}N^{\mathrm{I}}\,\mathrm{dB}-\frac{1}{\alpha}\int_{\mathrm{B}}\lambda\,N^{\mathrm{I}}\,\mathrm{dB}.
\tag{C.19d}
$$

The construction of the corresponding tangent matrices are obtained in the same manner as in Appendix A.

References

[1] BP. Statistical review of world energy, 2016.

[2] International Electrotechnical Commission. Electrical energy storage, 2011.

[3] David Linden and Thomas Reddy. *Handbook of Batteries*. The McGraw-Hill Companies, Inc, New York, 3rd edition, 2001.

[4] J.-M. Tarascon and M. Armand. Issues and challenges facing rechargeable lithium batteries. *Nature*, 414(6861):359–367, November 2001.

[5] Wu Xu, Jiulin Wang, Fei Ding, Xilin Chen, Eduard Nasybulin, Yaohui Zhang, and Ji-Guang Zhang. Lithium metal anodes for rechargeable batteries. *Energy & Environmental Science*, 7(2):513–537, January 2014.

[6] Uday Kasavajjula, Chunsheng Wang, and A. John Appleby. Nano- and bulk-silicon-based insertion anodes for lithium-ion secondary cells. *Journal of Power Sources*, 163(2):1003–1039, 2007.

[7] Claus Daniel and Jürgen O. Besenhard. *Handbook of Battery Materials*. Wiley-VCH, Weinheim, 2nd edition, 2011.

[8] Wei-Jun Zhang. Lithium insertion/extraction mechanism in alloy anodes for lithium-ion batteries. *Journal of Power Sources*, 196(3):877–885, February 2011.

[9] Gholam-Abbas Nazri and Gianfranco Pistoia, editors. *Lithium Batteries: Science and Technology*. Springer, New York, 2009.

[10] C. Delmas, M. Maccario, L. Croguennec, F. Le Cras, and F. Weill. Lithium deintercalation in $LiFePO_4$ nanoparticles via a domino-cascade model. *Nature Materials*, 7(8):665–671, August 2008.

[11] Gerardine G. Botte, Venkat R. Subramanian, and Ralph E. White. Mathematical modeling of secondary lithium batteries. *Electrochimica Acta*, 45(15-16):2595–2609, May 2000.

[12] Parthasarathy M. Gomadam, John W. Weidner, Roger A. Dougal, and Ralph E. White. Mathematical modeling of lithium-ion and nickel battery systems. *Journal of Power Sources*, 110(2):267–284, August 2002.

[13] Gerbrand Ceder, Marc Doyle, Pankaj Arora, and Yuris Fuentes. Computational Modeling and Simulation for Rechargeable Batteries. *MRS Bulletin*, 27(08):619–623, August 2002.

[14] Myounggu Park, Xiangchun Zhang, Myoungdo Chung, Gregory B. Less, and Ann Marie Sastry. A review of conduction phenomena in Li-ion batteries. *Journal of Power Sources*, 195(24):7904–7929, December 2010.

[15] Alejandro A. Franco. Multiscale modelling and numerical simulation of rechargeable lithium ion batteries: concepts, methods and challenges. *RSC Advances*, 3(32):13027–13058, July 2013.

[16] D. Grazioli, M. Magri, and A. Salvadori. Computational modeling of Li-ion batteries. *Computational Mechanics*, pages 1–21, August 2016.

[17] Sidney Yip, editor. *Handbook of Materials Modeling*. Springer, Berlin, 2005.

[18] Rajlakshmi Purkayastha and Robert M. McMeeking. A Linearized Model for Lithium Ion Batteries and Maps for their Performance and Failure. *Journal of Applied Mechanics*, 79(3):031021–031021, April 2012.

[19] Kejie Zhao, Wei L. Wang, John Gregoire, Matt Pharr, Zhigang Suo, Joost J. Vlassak, and Efthimios Kaxiras. Lithium-assisted plastic deformation of silicon electrodes in lithium-ion batteries: A first-principles theoretical study. *Nano Letters*, 11(7):2962–2967, July 2011.

[20] A. F. Bower, P. R. Guduru, and V. A. Sethuraman. A finite strain model of stress, diffusion, plastic flow, and electrochemical reactions in a lithium-ion half-cell. *Journal of the Mechanics and Physics of Solids*, 59(4):804–828, April 2011.

[21] Christopher Marc Doyle. *Design and Simulation of Lithium Rechargeable Batteries*. PhD thesis, University of California at Berkeley, August 1995.

[22] John Newman and Karen E. Thomas-Alyea. *Electrochemical Systems*. John Willey & Sons, Inc., 3rd edition, 2004.

[23] Gogi K. Singh, Gerbrand Ceder, and Martin Z. Bazant. Intercalation dynamics in rechargeable battery materials: General theory and phase-transformation waves in $LiFePO_4$. *Electrochimica Acta*, 53(26):7599–7613, November 2008.

[24] Peng Bai, Daniel A. Cogswell, and Martin Z. Bazant. Suppression of Phase Separation in $LiFePO_4$ Nanoparticles During Battery Discharge. *Nano Letters*, 11(11):4890–4896, November 2011.

[25] S. Dargaville and T. W. Farrell. The persistence of phase-separation in $LiFePO_4$ with two-dimensional Li^+ transport: The Cahn-Hilliard-reaction equation and the role of defects. *Electrochimica Acta*, 94:143–158, April 2013.

[26] Gerhard A. Holzapfel, editor. *Nonlinear solid mechanics: a continuum approach for engineering*. John Wiley & Sons Ltd, Chichester, 2010.

[27] Morton E. Gurtin, Eliot Fried, and Lallit Anand, editors. *The Mechanics and Thermodynamics of Continua*. Cambridge University Press, New York, 2011.

[28] J. S. Rowlinson. Legacy of van der Waals. *Nature*, 244(5416):414–417, August 1973.

[29] L. Landau and Lifshitz E. On the theory of the dispersion of magnetic permeability in ferromagnetic bodies. *Ukr. J. Phys.*, 53:14–22, 2008.

[30] L. Landau and Lifshitz E. On the theory of superconductivity. In D. Ter Haar, editor, *Collected Papers of L.D. Landau*, pages 217–225. Gordon and Breach, Science Publishers Inc. and Pergamon Press Ltd., New York, London, Paris, 1965.

[31] John W. Cahn and John E. Hilliard. Free Energy of a Nonuniform System. I. Interfacial Free Energy. *The Journal of Chemical Physics*, 28(26):258–267, 1958.

[32] S.M. Allen and J.W. Cahn. A macroscopic theory for antiphase boundary motion and its application to antiphase domain coarsening. *Acta Metall.*, 27:1085–1095, 1979.

[33] Ryo Kobayashi. Modeling and numerical simulations of dendritic crystal growth. *Physica D: Nonlinear Phenomena*, 63(3):410–423, March 1993.

[34] Alessia Berti and Claudio Giorgi. A Phase-Field Model for Liquid–Vapor Transitions. *Journal of Non-Equilibrium Thermodynamics*, 34(3):219–247, 2009.

[35] Long-Qing Chen and Yunzhi Wang. The continuum field approach to modeling microstructural evolution. *JOM*, 48(12):13–18.

[36] Long-Qing Chen and Wei Yang. Computer simulation of the domain dynamics of a quenched system with a large number of nonconserved order parameters: The grain-growth kinetics. *Physical Review B*, 50(21):15752–15756, December 1994.

[37] John W Cahn. On spinodal decomposition. *Acta Metallurgica*, 9(9):795–801, September 1961.

[38] I. S. Aranson, V. A. Kalatsky, and V. M. Vinokur. Continuum Field Description of Crack Propagation. *Physical Review Letters*, 85(1):118–121, July 2000.

[39] Alain Karma, David A. Kessler, and Herbert Levine. Phase-Field Model of Mode III Dynamic Fracture. *Physical Review Letters*, 87(4):045501, July 2001.

[40] Alain Karma and Alexander E. Lobkovsky. Unsteady Crack Motion and Branching in a Phase-Field Model of Brittle Fracture. *Physical Review Letters*, 92(24):245510, June 2004.

[41] Blaise Bourdin, Gilles A. Francfort, and Jean-Jacques Marigo. The Variational Approach to Fracture. *Journal of Elasticity*, 91(1-3):5–148, March 2008.

[42] Blaise Bourdin, Christopher J. Larsen, and Casey L. Richardson. A time-discrete model for dynamic fracture based on crack regularization. *International Journal of Fracture*, 168(2):133–143, November 2010.

[43] Nikolas Provatas and Ken Elder. *Phase-Field Methods in Materials Science an Engineering*. Wiley-VCH, Weinheim, 2010.

[44] Long-Qing Chen. Phase-Field Models for Microstructure Evolution. *Annual Review of Materials Research*, 32(1):113–140, 2002.

[45] Katsuyo Thornton, John Ågren, and P. W. Voorhees. Modelling the evolution of phase boundaries in solids at the meso- and nano-scales. *Acta Materialia*, 51(19):5675–5710, November 2003.

[46] Ingo Steinbach. Phase-field models in materials science. *Modelling and Simulation in Materials Science and Engineering*, 17(7):073001, 2009.

[47] R. S. Qin and H. K. Bhadeshia. Phase field method. *Materials Science and Technology*, 26(7):803–811, July 2010.

[48] D. Schrade, R. Mueller, B.-X. Xu, and D. Gross. Domain evolution in ferroelectric materials: a continuum phase field model and finite element implementation. *Computer methods in applied mechanics and engineering*, 196(41):4365–4374, 2007.

[49] T. L. Gilbert. A phenomenological theory of damping in ferromagnetic materials. *IEEE Transactions on Magnetics*, 40(6):3443–3449, November 2004.

[50] Michael J. Borden, Thomas J. R. Hughes, Chad M. Landis, and Clemens V. Verhoosel. A higher-order phase-field model for brittle fracture: Formulation and analysis within the isogeometric analysis framework. *Computer Methods in Applied Mechanics and Engineering*, 273:100–118, 2014.

[51] Morton E. Gurtin. Generalized Ginzburg–Landau and Cahn–Hilliard equations based on a microforce balance. *Physica D: Nonlinear Phenomena*, 92(3):178–192, May 1996.

[52] J. F. Blowey and C. M. Elliott. The Cahn–Hilliard gradient theory for phase separation with non-smooth free energy Part I: Mathematical analysis. *European Journal of Applied Mathematics*, 2(3):233–280, September 1991.

[53] J. E. Guyer, W. J. Boettinger, J. A. Warren, and G. B. McFadden. Phase field modeling of electrochemistry. I. Equilibrium. *Physical Review E*, 69(2):021603, February 2004.

[54] JX Zhang and LQ Chen. Phase-field microelasticity theory and micromagnetic simulations of domain structures in giant magnetostrictive materials. *Acta Materialia*, 53(9):2845–2855, 2005.

[55] Min Yi and Bai-Xiang Xu. A constraint-free phase field model for ferromagnetic domain evolution. *Proc. R. Soc. A*, 470(2171):20140517, 2014.

[56] L. Kaufman and H. Bernstein. *Computer Calculation of Phase Diagrams with Special Reference to Refractory Metals*. Academic Press Inc, New York, 1970.

[57] Nigel Saunders and A Peter Miodownik. *CALPHAD (calculation of phase diagrams): a comprehensive guide*, volume 1. Elsevier, 1998.

[58] Ju Liu. *Thermodynamically Consistent Modeling and Simulation of Multiphase Flows*. PhD thesis, The University of Texas at Austin, 2014.

[59] Courant Richard and Hilbert D. *Methods of Mathematical Physics*, volume 2. John Willey & Sons, April 1989.

[60] J. Austin Cottrell, Thomas J. R. Hughes, and Yuri Bazilevs. *Isogeometric Analysis: Toward Integration of CAD and FEA*. Wiley Publishing, 1st edition, 2009.

[61] R. L. Taylor. FEAP – Finite Element Analysis Program, 2014.

[62] Intel(R) Parallel Studio XE Cluster Edition for Linux*, 2016.

[63] T.J.R. Hughes, J.A. Cottrell, and Y. Bazilevs. Isogeometric analysis: CAD, finite elements, NURBS, exact geometry and mesh refinement. *Computer Methods in Applied Mechanics and Engineering*, 194(39–41):4135–4195, October 2005.

[64] D. Grossmann, B. Jüttler, H. Schlusnus, J. Barner, and A.H. Vuong. Isogeometric simulation of turbine blades for aircraft engines. *Computer Aided Geometric Design*, 29(7):519–531, 2012.

[65] D. Schillinger, M. Ruess, N. Zander, Y. Bazilevs, A. Düster, and E. Rank. Small and large deformation analysis with the p- and B-spline versions of the Finite Cell Method. *Computational Mechanics*, 50(4):445–478, 2012.

[66] D. Schillinger, J.A. Evans, A. Reali, M.A. Scott, and T.J.R. Hughes. Isogeometric collocation: Cost comparison with Galerkin methods and extension to adaptive hierarchical NURBS discretizations. *Computer Methods in Applied Mechanics and Engineering*, 267:170–232, 2013.

[67] J.A. Cottrell, A. Reali, Y. Bazilevs, and T.J.R. Hughes. Isogeometric analysis of structural vibrations. *Computer Methods in Applied Mechanics and Engineering*, 195:5257–5296, 2006.

[68] T.J.R. Hughes, A. Reali, and G. Sangalli. Duality and unified analysis of discrete approximations in structural dynamics and wave propagation: Comparison of p-method finite elements with k-method NURBS. *Computer Methods in Applied Mechanics and Engineering*, 197:4104–4124, 2008.

[69] T.J.R. Hughes, J.A. Evans, and A. Reali. Finite element and NURBS approximations of eigenvalue, boundary-value, and initial-value problems. *Computer Methods in Applied Mechanics and Engineering*, 272(15):290–320.

[70] Héctor Gómez, Victor M. Calo, Yuri Bazilevs, and Thomas J. R. Hughes. Isogeometric analysis of the Cahn-Hilliard phase-field model. *Computer Methods in Applied Mechanics and Engineering*, 197(49-50):4333–4352, September 2008.

[71] C.V. Verhoosel, M.A. Scott, M.J. Borden, T.J.R. Hughes, and R. de Borst. Discretization of higher-order gradient damage models using isogeometric finite elements. *Computer Methods in Applied Mechanics and Engineering*, 197:2976–2988, 2008.

[72] J. Kiendl, F. Auricchio, T.J.R. Hughes, and A. Reali. Single-variable formulations and isogeometric discretizations for shear deformable beams. *Computer Methods in Applied Mechanics and Engineering*, 284:988–1004, 2015.

[73] F. Auricchio, L. Beirão da Veiga, T.J.R. Hughes, A. Reali, and G. Sangalli. Isogeometric collocation methods. *Mathematical Models and Methods in Applied Sciences*, 20(11):2075–1077, 2010.

[74] D. Schillinger, M.J. Borden, and H.K. Stolarski. Isogeometric collocation for phase-field fracture models. *Computer Methods in Applied Mechanics and Engineering*, 284:583–610, 2015.

[75] Peter Stein. *Procedurally Generated Models for Isogeometric Analysis: Prozedural Generierte Modelle Für Isogeometrische Analysen*. PhD thesis, Bauhaus-Universität Weimar, 2012.

[76] Dominik Schillinger and Martin Ruess. The Finite Cell Method: A Review in the Context of Higher-Order Structural Analysis of CAD and Image-Based Geometric Models. *Archives of Computational Methods in Engineering*, 22(3):391–455, May 2014.

[77] D. Schillinger, L. Dede', M.A. Scott, J.A. Evans, M.J. Borden, E. Rank, and T.J.R. Hughes. An isogeometric design-through-analysis methodology based on adaptive hierarchical refinement of NURBS, immersed boundary methods, and T-spline CAD surfaces. *Computer Methods in Applied Mechanics and Engineering*, 249-250:116–150, 2012.

[78] A. Düster, J. Parvizian, Z. Yang, and E. Rank. The finite cell method for three-dimensional problems of solid mechanics. *Computer Methods in Applied Mechanics and Engineering*, 197:3768–3782, 2008.

[79] F. Xu, D. Schillinger, D. Kamensky, V. Varduhn, C. Wang, and M.-C. Hsu. The tetrahedral finite cell method for fluids: Immersogeometric analysis of turbulent flow around complex geometries. *Computers & Fluids*, doi:10.1016/j.compfluid.2015.08.027, 2016.

[80] Vasco Varduhn, Ming-Chen Hsu, Martin Ruess, and Dominik Schillinger. The tetrahedral finite cell method: Higher-order immersogeometric analysis on adaptive non-boundary-fitted meshes. *International Journal for Numerical Methods in Engineering*, 107(12):1054–1079, September 2016.

[81] Sascha Duczek and Ulrich Gabbert. The finite cell method for polygonal meshes: poly-fcm. *Computational Mechanics*, pages 1–32, 2016.

[82] R. Cools. Monomial cubature rules since "Stroud": A compilation - Part 2. *Journal of Computational and Applied Mathematics*, 112(1):21–27, 1999.

[83] Carlos Felippa. Advanced Finite Element Methods. `http://www.colorado.edu/engineering/CAS/courses.d/AFEM.d/Home.html`. [Lecture notes].

[84] Matthew T. McDowell, Ill Ryu, Seok Woo Lee, Chongmin Wang, William D. Nix, and Yi Cui. Studying the Kinetics of Crystalline Silicon Nanoparticle Lithiation with In Situ Transmission Electron Microscopy. *Advanced Materials*, 24(45):6034–6041, November 2012.

[85] Martin Ebner, Federica Marone, Marco Stampanoni, and Vanessa Wood. Visualization and quantification of electrochemical and mechanical degradation in Li ion batteries. *Science*, 342(6159):716–720, November 2013.

[86] Jongwoo Lim, Yiyang Li, Daan Hein Alsem, Hongyun So, Sang Chul Lee, Peng Bai, Daniel A. Cogswell, Xuzhao Liu, Norman Jin, Young-sang Yu, Norman J. Salmon, David A. Shapiro, Martin Z. Bazant, Tolek Tyliszczak, and William C. Chueh. Origin and hysteresis of lithium compositional spatiodynamics within battery primary particles. *Science*, 353(6299):566–571, August 2016.

[87] A Van der Ven, C Marianetti, D Morgan, and G Ceder. Phase transformations and volume changes in spinel $\mathrm{Li}_x\mathrm{Mn}_2\mathrm{O}_4$. *Solid State Ionics*, 135(1–4):21–32, November 2000.

[88] B. C. Han, A. Van der Ven, D. Morgan, and G. Ceder. Electrochemical modeling of intercalation processes with phase field models. *Electrochimica Acta*, 49(26):4691–4699, October 2004.

[89] Gogi K. Singh, Gerbrand Ceder, and Martin Z. Bazant. Intercalation dynamics in rechargeable battery materials: General theory and phase-transformation waves in LiFePO_4. *Electrochimica Acta*, 53(26):7599–7613, November 2008.

[90] C. M. Elliott. The Cahn-Hilliard Model for the Kinetics of Phase Separation. In José Francisco Rodrigues, editor, *Mathematical Models for Phase Change Problems*, number 88 in International Series of Numerical Mathematics, pages 35–73. Birkhäuser Basel, 1989.

[91] C. Elliott and H. Garcke. On the Cahn–Hilliard Equation with Degenerate Mobility. *SIAM Journal on Mathematical Analysis*, 27(2):404–423, March 1996.

[92] Daisuke Furihata. A stable and conservative finite difference scheme for the Cahn–Hilliard equation. *Numerische Mathematik*, 87(4):675–699, February 2001.

[93] Jingzhi Zhu, Long-Qing Chen, Jie Shen, and Veena Tikare. Coarsening kinetics from a variable-mobility Cahn–Hilliard equation: Application of a semi-implicit Fourier spectral method. *Physical Review E*, 60(4):3564–3572, October 1999.

[94] Luis Cueto-Felgueroso and Jaume Peraire. A time-adaptive finite volume method for the Cahn-Hilliard and Kuramoto-Sivashinsky equations. *Journal of Computational Physics*, 227(24):9985–10017, 2008.

[95] R. L. J. M. Ubachs, P. J. G. Schreurs, and M. G. D. Geers. A nonlocal diffuse interface model for microstructure evolution of tin-lead solder. *Journal of the Mechanics and Physics of Solids*, 52(8):1763–1792, August 2004.

[96] C. Miehe, F. E. Hildebrand, and L. Böger. Mixed variational potentials and inherent symmetries of the Cahn-Hilliard theory of diffusive phase separation. *Proceedings of the Royal Society of London A: Mathematical, Physical and Engineering Sciences*, 470(2164):20130641, April 2014.

[97] Garth N. Wells, Ellen Kuhl, and Krishna Garikipati. A discontinuous Galerkin method for the Cahn–Hilliard equation. *Journal of Computational Physics*, 218(2):860–877, 2006.

[98] S. Kaessmair and P. Steinmann. Comparative computational analysis of the Cahn–Hilliard equation with emphasis on C^1-continuous methods. *Journal of Computational Physics*, 322:783–803, October 2016.

[99] Ju Liu, Luca Dedè, John A Evans, Micheal J Borden, and Thomas J. R. Hughes. Isogeometric analysis of the advective Cahn-Hilliard equation: Spinodal decomposition under shear flow. *Journal of Computational Physics*, 242:321–350, June 2013.

[100] L. Dalcin, N. Collier, P. Vignal, A. M. A. Côrtes, and V. M. Calo. PetIGA: A framework for high-performance isogeometric analysis. *Computer Methods in Applied Mechanics and Engineering*, 308:151–181, August 2016.

[101] Denis Anders, Christian Hesch, and Kerstin Weinberg. Computational modeling of phase separation and coarsening in solder alloys. *International Journal of Solids and Structures*, 49(13):1557–1572, June 2012.

[102] J. Nitsche. über ein Variationsprinzip zur Lösung von Dirichlet-Problemen bei Verwendung von Teilräumen, die keinen Randbedingungen unterworfen sind. *Abhandlungen aus dem Mathematischen Seminar der Universität Hamburg*, 36(1):9–15, November 1971.

[103] Chandrasekhar Annavarapu, Martin Hautefeuille, and John E. Dolbow. A robust Nitsche's formulation for interface problems. *Computer Methods in Applied Mechanics and Engineering*, 225–228:44–54, June 2012.

[104] Anand Embar, John Dolbow, and Isaac Harari. Imposing Dirichlet boundary conditions with Nitsche's method and spline-based finite elements. *International Journal for Numerical Methods in Engineering*, 83(7):877–898, August 2010.

[105] Wen Jiang, Chandrasekhar Annavarapu, John E. Dolbow, and Isaac Harari. A robust Nitsche's formulation for interface problems with spline-based finite elements. *International Journal for Numerical Methods in Engineering*, 104(7):676–696, November 2015.

[106] John Dolbow and Isaac Harari. An efficient finite element method for embedded interface problems. *International Journal for Numerical Methods in Engineering*, 78(2):229–252, April 2009.

[107] Dongsun Lee, Joo-Youl Huh, Darae Jeong, Jaemin Shin, Ana Yun, and Junseok Kim. Physical, mathematical, and numerical derivations of the Cahn–Hilliard equation. *Computational Materials Science*, 81:216–225, January 2014.

[108] Alain Miranville. Generalized Cahn-Hilliard equations based on a microforce balance. *Journal of Applied Mathematics*, 2003(4):165–185, 2003.

[109] E.A. Guggenheim. *Mixtures: The Theory of the Equlibrium Properties of Some Simple Classes of Mixtures Solutions and Alloys*. The International series of monographs on physics. Clarendon Press, 1952.

[110] O.C. Zienkiewicz, R.L. Taylor, and J.Z. Zhu. *The Finite Element Method: Its Basis & Fundamentals*. Butterworth-Heinemann, Oxford, 6th edition, 2005.

[111] P. Stein and B. Xu. 3D Isogeometric Analysis of intercalation-induced stresses in Li-ion battery electrode particles. *Computer Methods in Applied Mechanics and Engineering*, 268:225–244, January 2014.

[112] Scott Lipton, John A. Evans, Yuri Bazilevs, Thomas Elguedj, and T. J. R. Hughes. Robustness of isogeometric structural discretizations under severe mesh distortion. *Computer Methods in Applied Mechanics and Engineering*, 199(5-8):357 – 373, 2010.

[113] Joachim Schöberl. NETGEN An advancing front 2d/3d-mesh generator based on abstract rules. *Computing and Visualization in Science*, 1(1):41–52, July 1997.

[114] Thomas J. R. Hughes. *Isoparametric elements and elementary programming concepts*, pages 109–184. Dover, 2000.

[115] Charles Delacourt, Philippe Poizot, Jean-Marie Tarascon, and Christian Masquelier. The existence of a temperature-driven solid solution in Li_xFePO_4 for $0 \leq x \leq 1$. *Nature Materials*, 4(3):254–260, March 2005.

[116] John Christensen and John Newman. Stress generation and fracture in lithium insertion materials. *Journal of Solid State Electrochemistry*, 10(5):293–319, May 2006.

[117] Xiangchun Zhang, Wei Shyy, and Ann Marie Sastry. Numerical simulation of intercalation-induced stress in Li-ion battery electrode particles. *Journal of The Electrochemical Society*, 154(10):A910–A916, October 2007.

[118] Kejie Zhao, Matt Pharr, Shengqiang Cai, Joost J. Vlassak, and Zhigang Suo. Large plastic deformation in high-capacity lithium-ion batteries caused by charge and discharge. *Journal of the American Ceramic Society*, 94:s226–s235, 2011.

[119] Zhiwei Cui, Feng Gao, and Jianmin Qu. A finite deformation stress-dependent chemical potential and its applications to lithium ion batteries. *Journal of the Mechanics and Physics of Solids*, 60(7):1280–1295, July 2012.

[120] H. L. Cheng, J. Wang, and Z. P. Huang. A thermo-viscoelastic constitutive model for compressible amorphous polymers. *Mechanics of Time-Dependent Materials*, 14(3):261–275, August 2010.

[121] S. Huang, F. Fan, J. Li, S. Zhang, and T. Zhu. Stress generation during lithiation of high-capacity electrode particles in lithium ion batteries. *Acta Materialia*, 61(12):4354–4364, July 2013.

[122] Jonghyun Park, Wei Lu, and Ann Marie Sastry. Numerical simulation of stress evolution in lithium manganese dioxide particles due to coupled phase transition and intercalation. *Journal of The Electrochemical Society*, 158(2):A201–A206, 2011.

[123] Esther Bohn, Thomas Eckl, Marc Kamlah, and Robert McMeeking. A model for lithium diffusion and stress generation in an intercalation storage particle with phase change. *Journal of The Electrochemical Society*, 160(10):A1638–A1652, 2013.

[124] A. D. Drozdov. A model for the mechanical response of electrode particles induced by lithium diffusion in Li-ion batteries. *Acta Mechanica*, 225(11):2987–3005, February 2014.

[125] Xiaoxuan Zhang, Seok Woo Lee, Hyun-Wook Lee, Yi Cui, and Christian Linder. A reaction-controlled diffusion model for the lithiation of silicon in lithium-ion batteries. *Extreme Mechanics Letters*, 4:61–75, September 2015.

[126] Xiaoxuan Zhang, Andreas Krischok, and Christian Linder. A variational framework to model diffusion induced large plastic deformation and phase field fracture during initial two-phase lithiation of silicon electrodes. *Computer Methods in Applied Mechanics and Engineering*, 312:51–77, December 2016.

[127] Magalie Huttin and Marc Kamlah. Phase-field modeling of stress generation in electrode particles of lithium ion batteries. *Applied Physics Letters*, 101(13):133902, September 2012.

[128] Ann-Christin Walk, Magalie Huttin, and Marc Kamlah. Comparison of a phase-field model for intercalation induced stresses in electrode particles of lithium ion batteries for small and finite deformation theory. *European Journal of Mechanics - A/Solids*, 48:74–82, November 2014.

[129] Svyatoslav Gladkov and Bob Svendsen. Thermodynamic and rate variational formulation of models for inhomogeneous gradient materials with microstructure and application to phase field modeling. *Acta Mechanica Sinica*, pages 1–11, May 2015.

[130] Lallit Anand. A Cahn–Hilliard-type theory for species diffusion coupled with large elastic-plastic deformations. *Journal of the Mechanics and Physics of Solids*, 60(12):1983–2002, dec 2012.

[131] Claudio V. Di Leo, Elisha Rejovitzky, and Lallit Anand. A Cahn-Hilliard-type phase-field theory for species diffusion coupled with large elastic deformations: Application to phase-separating Li-ion electrode materials. *Journal of the Mechanics and Physics of Solids*, 70:1–29, October 2014.

[132] Seungjun Lee, Jonghyun Park, Ann Marie Sastry, and Wei Lu. Molecular dynamics simulations of SOC-dependent elasticity of $\mathrm{Li}_x\mathrm{Mn}_2\mathrm{O}_4$ spinels in Li-ion batteries. *Journal of The Electrochemical Society*, 160(6):A968–A972, 2013.

[133] V. B. Shenoy, P. Johari, and Y. Qi. Elastic softening of amorphous and crystalline Li-Si phases with increasing Li concentration: A first-principles study. *Journal of Power Sources*, 195(19):6825–6830, October 2010.

[134] Yue Qi, Louis G. Hector, Christine James, and Kwang Jin Kim. Lithium concentration dependent elastic properties of battery electrode materials from first principles calculations. *Journal of The Electrochemical Society*, 161(11):F3010–F3018, January 2014.

[135] Magalie Huttin. *Phase-field modeling of the influence of mechanical stresses on charging and discharging processes in lithium ion batteries*. PhD thesis, Karlsruher Institut für Technologie, February 2014.

[136] Hüsnü Dal and Christian Miehe. Computational electro-chemo-mechanics of lithium-ion battery electrodes at finite strains. *Computational Mechanics*, 55(2):303–325, December 2014.

[137] Jochen Rohrer and Karsten Albe. Insights into Degradation of Si Anodes from First-Principle Calculations. *The Journal of Physical Chemistry C*, 117(37):18796–18803, September 2013.

[138] Jochen Rohrer, Ashkan Moradabadi, Karsten Albe, and Payam Kaghazchi. On the origin of anisotropic lithiation of silicon. *Journal of Power Sources*, 293:221–227, October 2015.

[139] Guoying Chen, Xiangyun Song, and Thomas J. Richardson. Electron Microscopy Study of the $LiFePO_4$ to $FePO_4$ Phase Transition. *Electrochemical and Solid-State Letters*, 9(6):A295–A298, June 2006.

[140] C. V. Ramana, A. Mauger, F. Gendron, C. M. Julien, and K. Zaghib. Study of the Li-insertion/extraction process in $LiFePO_4/FePO_4$. *Journal of Power Sources*, 187(2):555–564, February 2009.

[141] Xiao Hua Liu, Li Zhong, Shan Huang, Scott X. Mao, Ting Zhu, and Jian Yu Huang. Size-Dependent Fracture of Silicon Nanoparticles During Lithiation. *ACS Nano*, 6(2):1522–1531, February 2012.

[142] Yang-Tse Cheng and Mark W. Verbrugge. Diffusion-Induced Stress, Interfacial Charge Transfer, and Criteria for Avoiding Crack Initiation of Electrode Particles. *Journal of The Electrochemical Society*, 157(4):A508–A516, April 2010.

[143] Yuhang Hu, Xuanhe Zhao, and Zhigang Suo. Averting cracks caused by insertion reaction in lithium-ion batteries. *Journal of Materials Research*, 25(6):1007–1010, June 2010.

[144] Ill Ryu, Seok Woo Lee, Huajian Gao, Yi Cui, and William D. Nix. Microscopic model for fracture of crystalline Si nanopillars during lithiation. *Journal of Power Sources*, 255:274–282, June 2014.

[145] Daniel Schneider, Michael Selzer, Johannes Bette, Idoia Rementeria, Alexander Vondrous, Michael J. Hoffmann, and Britta Nestler. Phase-Field Modeling of Diffusion Coupled Crack Propagation Processes. *Advanced Engineering Materials*, 16(2):142–146, February 2014.

[146] Linyun Liang, Marius Stan, and Mihai Anitescu. Phase-field modeling of diffusion-induced crack propagations in electrochemical systems. *Applied Physics Letters*, 105(16):163903, October 2014.

[147] Peng Zuo and Ya-Pu Zhao. A phase field model coupling lithium diffusion and stress evolution with crack propagation and application in lithium ion batteries. *Physical Chemistry Chemical Physics*, 17(1):287–297, December 2014.

[148] Markus Klinsmann, Daniele Rosato, Marc Kamlah, and Robert M. McMeeking. An assessment of the phase field formulation for crack growth. *Computer Methods in Applied Mechanics and Engineering*, 294:313–330, September 2015.

[149] Markus Klinsmann, Daniele Rosato, Marc Kamlah, and Robert M. McMeeking. Modeling crack growth during Li insertion in storage particles using a fracture phase field approach. *Journal of the Mechanics and Physics of Solids*, 92:313–344, July 2016.

[150] Markus Klinsmann, Daniele Rosato, Marc Kamlah, and Robert M. McMeeking. Modeling Crack Growth during Li Extraction in Storage Particles Using a Fracture Phase Field Approach. *Journal of The Electrochemical Society*, 163(2):A102–A118, January 2016.

[151] C. Miehe, H. Dal, L.-M. Schänzel, and A. Raina. A phase-field model for chemo-mechanical induced fracture in lithium-ion battery electrode particles. *International Journal for Numerical Methods in Engineering*, 106(9):683–711, June 2016.

[152] Martin Z. Bazant. Theory of Chemical Kinetics and Charge Transfer based on Nonequilibrium Thermodynamics. *Accounts of Chemical Research*, 46(5):1144–1160, May 2013.

[153] Charlotte Kuhn and Ralf Müller. A continuum phase field model for fracture. *Engineering Fracture Mechanics*, 77(18):3625–3634, December 2010.

[154] Charlotte Kuhn, Alexander Schlüter, and Ralf Müller. On degradation functions in phase field fracture models. *Computational Materials Science*, 108, Part B:374–384, October 2015.

[155] Alexander Schlüter, Adrian Willenbücher, Charlotte Kuhn, and Ralf Müller. Phase field approximation of dynamic brittle fracture. *Computational Mechanics*, 54(5):1141–1161, June 2014.

[156] Christian Miehe, Martina Hofacker, and Fabian Welschinger. A phase field model for rate-independent crack propagation: Robust algorithmic implementation based on operator splits. *Computer Methods in Applied Mechanics and Engineering*, 199(45-48):2765 – 2778, 2010.

[157] Christian Miehe, Lisa-Marie Schänzel, and Heike Ulmer. Phase field modeling of fracture in multi-physics problems. Part I. Balance of crack surface and failure criteria for brittle crack propagation in thermo-elastic solids. *Computer Methods in Applied Mechanics and Engineering*, 294:449 – 485, 2015.

[158] Michael J. Borden, Clemens V. Verhoosel, Michael A. Scott, Thomas J. R. Hughes, and Chad M. Landis. A phase-field description of dynamic brittle fracture. *Computer Methods in Applied Mechanics and Engineering*, 217–220:77–95, April 2012.

[159] Byoungwoo Kang and Gerbrand Ceder. Battery materials for ultrafast charging and discharging. *Nature*, 458(7235):190–193, March 2009.

[160] Jing Li, Dinh-Ba Le, P. P. Ferguson, and J. R. Dahn. Lithium polyacrylate as a binder for tin–cobalt–carbon negative electrodes in lithium-ion batteries. *Electrochimica Acta*, 55(8):2991–2995, March 2010.

[161] Gao Liu, Shidi Xun, Nenad Vukmirovic, Xiangyun Song, Paul Olalde-Velasco, Honghe Zheng, Vince S. Battaglia, Linwang Wang, and Wanli Yang. Polymers with Tailored Electronic Structure for High Capacity Lithium Battery Electrodes. *Advanced Materials*, 23(40):4679–4683, October 2011.

[162] G. Liu, H. Zheng, X. Song, and V. S. Battaglia. Particles and Polymer Binder Interaction: A Controlling Factor in Lithium-Ion Electrode Performance. *Journal of The Electrochemical Society*, 159(3):A214–A221, January 2012.

[163] Yuyang Lu and Yong Ni. Effects of particle shape and concurrent plasticity on stress generation during lithiation in particulate Li-ion battery electrodes. *Mechanics of Materials*, 91, Part 2:372–381, December 2015.

[164] Marc Doyle, Thomas F. Fuller, and John Newman. Modeling of Galvanostatic Charge and Discharge of the Lithium/Polymer/Insertion Cell. *Journal of The Electrochemical Society*, 140(6):1526–1533, June 1993.

[165] A. Salvadori, D. Grazioli, and M. G. D. Geers. Governing equations for a two-scale analysis of Li-ion battery cells. *International Journal of Solids and Structures*, 59:90–109, May 2015.

[166] Sangmin Lee, Ann Marie Sastry, and Jonghyun Park. Study on microstructures of electrodes in lithium-ion batteries using variational multi-scale enrichment. *Journal of Power Sources*, 315:96–110, May 2016.

[167] Scott A. Roberts, Victor E. Brunini, Kevin N. Long, and Anne M. Grillet. A Framework for Three-Dimensional Mesoscale Modeling of Anisotropic Swelling and Mechanical Deformation in Lithium-Ion Electrodes. *Journal of The Electrochemical Society*, 161(11):F3052–F3059, January 2014.

[168] Hector Mendoza, Scott A. Roberts, Victor E. Brunini, and Anne M. Grillet. Mechanical and Electrochemical Response of a $LiCoO_2$ Cathode using Reconstructed Microstructures. *Electrochimica Acta*, 190:1–15, February 2016.

[169] David R. Noble, Elijah P. Newren, and Jeremy B. Lechman. A conformal decomposition finite element method for modeling stationary fluid interface problems. *International Journal for Numerical Methods in Fluids*, 63(6):725–742, June 2010.

[170] Bernardo Orvananos, Hui-Chia Yu, Aziz Abdellahi, Rahul Malik, Clare P. Grey, Gerbrand Ceder, and Katsuyo Thornton. Kinetics of Nanoparticle Interactions in Battery Electrodes. *Journal of The Electrochemical Society*, 162(6):A965–A973, January 2015.

[171] Dominik Schillinger, Isaac Harari, Ming-Chen Hsu, David Kamensky, Stein K. F. Stoter, Yue Yu, and Ying Zhao. The non-symmetric Nitsche method for the parameter-free imposition of weak boundary and coupling conditions in immersed finite elements. *Computer Methods in Applied Mechanics and Engineering*, 309:625–652, September 2016.

[172] P. Jarzebski, K. Wisniewski, and R. L. Taylor. On parallelization of the loop over elements in FEAP. *Computational Mechanics*, 56(1):77–86, May 2015.

[173] Benedikt Peter. *Einfluss der Trägermorphologie auf die 3D-Elektrodenstruktur von Kathoden in Polymerelektrolyt-Membran-Brennstoffzellen*. PhD thesis, Technische Universität Darmstadt, 2015.

[174] Per-Olof Persson. DistMesh – A Simple Mesh Generator in MATLAB, 2012.

[175] Feifei Fan. *Revealing novel degradation mechanisms in high-capacity battery materials by integrating predictive modeling with in-situ experiments*. PhD thesis, Georgia Institute of Technology, 2015.

[176] Claudio V. Di Leo. *Chemo-Mechanics of Lithium-Ion Battery Electrodes*. PhD thesis, Massachusetts Institute of Technology, 2015.

[177] Kejie Zhao. *Mechanics of Electrodes in Lithium-Ion Batteries*. PhD thesis, Harvard University, 2012.

List of Publications

Peer Reviewed Journal Publications

[1] **Y. Zhao**, P. Stein, and B.-X. Xu, “Isogeometric analysis of mechanically coupled Cahn–Hilliard phase segregation in hyperelastic electrodes of Li-ion batteries,” *Computer Methods in Applied Mechanics and Engineering*, vol. 297, pp. 325–347, Dec. 2015.

[2] **Y. Zhao**, B.-X. Xu, P. Stein, and D. Gross, “Phase-field study of electrochemical reactions at exterior and interior interfaces in Li-ion battery electrode particles,” *Computer Methods in Applied Mechanics and Engineering*, vol. 312, pp. 428–446, Dec. 2016.

[3] **Y. Zhao**, D. Schillinger, and B.-X. Xu, “Variational boundary conditions based on the Nitsche method for fitted and unfitted isogeometric discretizations of the mechanically coupled Cahn–Hilliard equation,” *Journal of Computational Physics*, vol. 340, pp. 177–199, July 2017.

[4] B.-X. Xu, **Y. Zhao**, and P. Stein, “Phase field modeling of electrochemically induced fracture in Li-ion battery with large deformation and phase segregation,” *GAMM-Mitteilungen*, vol. 39, no. 1, pp. 92–109, 2016.

[5] P. Stein, **Y. Zhao**, and B.-X. Xu, “Effects of surface tension and electrochemical reactions in Li-ion battery electrode nanoparticles,” *Journal of Power Sources*, vol. 332, pp. 154–169, Nov. 2016.

[6] D. Schillinger, I. Harari, M.-C. Hsu, D. Kamensky, S. K. F. Stoter, Y. Yu, and **Y. Zhao**, “The non-symmetric Nitsche method for the parameter-free imposition of weak boundary and coupling conditions in immersed finite elements,” *Computer Methods in Applied Mechanics and Engineering*, vol. 309, pp. 625–652, Sept. 2016.

[7] D. Eder-Goy, **Y. Zhao**, and B.-X. Xu, “Dynamic instability of prestretched viscous dielectric elastomer actuators,” *Acta Mechanica*, 2016. Submitted.

Peer Reviewed Conference Publications

[1] P. Stein, **Y. Zhao**, and B. Xu, “An analytical solution for the mechanically coupled diffusion problem in thin-film electrodes,” *Proceedings in Applied Mathematics and Mechanics*, vol. 13, no. 1, pp. 237–238, 2013.

[2] **Y. Zhao**, P. Stein, and B.-X. Xu, “Phase field simulation of the intercalation-induced stresses in the hyperelastic solids via isogeometric analysis,” *Proceedings in Applied Mathematics and Mechanics*, vol. 15, no. 1, pp. 443–444, 2015.

Oral Presentations

[1] **Y. Zhao**, D. Schillinger, and B.-X. Xu, “Chemo-mechanical modeling of Li-ion battery composite electrodes with the finite cell method.” Oral presention at WCCM XII & APCOM VI, Seoul, South Korea, 2016.

[2] **Y. Zhao**, D. Schillinger, and B.-X. Xu, “Modeling of lithium-ion battery composite electrodes using finite cell method.” Oral presention at Crete Island, Greece, 2016.

[3] **Y. Zhao**, P. Stein, and B.-X. Xu, “Phase-field modeling of phase-segregation induced crack propagation in Li-ion battery electrode particles.” Oral presention at Joint Annual Meeting of GAMM and DMV, Brunswick, Germany, 2016.

[4] **Y. Zhao**, P. Stein, and B.-X. Xu, “3d isogeometric analysis of phase segregation and mechanical stresses in li-ion battery electrode particles with anisotropy.” Oral presention at European Solid Mechanics Conference, Madrid, Spain, 2015.

[5] **Y. Zhao**, P. Stein, and B.-X. Xu, “Isogeometric analysis of mechanically coupled phase segregation in Li-ion battery electrode particles.” Oral presention at 86th Annual Meeting of the International Association of Applied Mathematics and Mechanics, Lecce, Italy, 2015.

[6] **Y. Zhao**, P. Stein, and B.-X. Xu, “Isogeometric analysis of Cahn–Hilliard phase field diffusion problem coupled with mechanical stresses in li-ion battery electrode.” Oral presention at Materials Science and Engineering Congress, Darmstadt, Germany, 2014.

[7] **Y. Zhao**, P. Stein, and B.-X. Xu, “Isogeometric analysis of Cahn-Hilliard phase field diffusion problem coupled with mechanical stresses in li-ion battery electrode.” Oral presention at 14th European Mechanics of Materials Conference, Gothenburg, Sweden, 2014.

[8] **Y. Zhao**, P. Stein, and B.-X. Xu, “Isogeometric analysis of the mechanically coupled Cahn-Hilliard phase-field model.” Oral presention at 85th Annual Meeting of the International Association of Applied Mathematics and Mechanics, Erlangen, Germany, 2014.

Curriculum Vitae

Personal

Ying Zhao.

Born on August 9, 1988.

From Dangyang, Hubei, China.

Chinese citizen.

Educational background

April, 2013 - January, 2017

Department of Materials and Earth Sciences, Technische Universität Darmstadt, Germany

Graduate School of Computational Engineering, Technische Universität Darmstadt, Germany

Doctoral student. Advisor: Prof. Bai-Xiang Xu

September, 2015 - December, 2015

Department of Civil, Environmental, and Geo- Engineering, University of Minnesota, Minneapolis, USA

Visiting student. Advisor: Dominik Schillinger, Assistant Professor

September, 2010 - March, 2013

Department of Aerospace Engineering and Applied Mechanics, Tongji University, Shanghai, China

Master of Engineering Mechanics. Advisor: Prof. Guo-Hua Nie

September, 2006 - June, 2010

Department of Aerospace Engineering and Applied Mechanics, Tongji University, Shanghai, China

Bachelor of Engineering. Grade-Point-Average (GPA): 4.62/5.0